

UNIVERSITY OF NOTTINGHAM



**University of
Nottingham**

UK | CHINA | MALAYSIA

Jing Pu

**Parametric Analysis of 3D Printing of Continuous
Carbon Fibre with Polyether Ether Ketone Matrix
Using the Fused Filament Fabrication Process**

**Submitted in Partial Fulfilment of the Requirements for
the Award of Doctor of Philosophy**

October 2020

Acknowledgements

Although this thesis has only one named author, it could not have been written without the input of many others to this work, directly and indirectly by collaboration. Here I would like to thank all who have contributed to this project. My special thanks goes out to:

Firstly, I am grateful for the China Scholarship Council (CSC) scholarship, which made it possible for me to do my research here.

I would wish to express my deepest gratitude to my supervisors Prof. Arthur Jones and Prof. Ian Ashcroft, who not just give me technical support but also encouraged me with my PhD research and gave valuable advice on my well-being.

I would also like to appreciate Dr. Ehab Saleh who used to be one of my supervisors and helped me to establish my research project at the beginning of my PhD. Although he moved to the University of Leeds, he still continued to provide me support whenever he was able to.

Thanks also goes to Dr. Gustavo F. Trindade for his help with the ToF-SIMS tests for my material characterisation, which helped me to carry out the further CF/PEEK filament analysis. Thanks to Dr. Claire McIlroy who shared her knowledge of crystallisation modelling of polymer, this insight in polymer crystallisation gave me a deeper theoretical understanding of the printing process.

I wish to express my gratitude to the technicians who have helped me during the PhD research. Especially to Mr. Joe White, formerly with the University of Nottingham, who has greatly contributed to this work with his assistance for building the pultrusion system.

Thanks to my colleagues from the Advanced Manufacturing Buildings for being there and for the fun time. Thanks to the office “Lunch club” for being good

friends, for our discussions on PhD life, regular sports events, game nights, group trips etc.

Finally, I would like to thank my family, who have always encouraged, supported and loved during my PhD. Lastly, thanks to my motherland, who cares and has given us the biggest support during the COVID19 pandemic.

Abstract

High performance applications in fields such as aerospace, medical and high volume automation are demanding products that have an ever lower weight, greater reliability, a faster time to market, and greater geometric complexity. However, light-weight structures with both high mechanical properties and complex geometries are challenging to manufacture. In order to meet these demands, the 3D printing of continuous carbon fibre reinforced polyether ether ketone (PEEK) materials is a promising prospect. The advantage of this manufacturing process is that the high stiffness and strength properties of the high-performance plastic PEEK reinforced with carbon fibre is paired with the manufacturing agility of the 3D printing process.

Fused filament fabrication FFF is the most suitable 3D printing process for such materials as it is capable of processing continuous filament. For the work presented in this thesis, a novel FFF processing method was developed based on a comprehensive experimental programme. The research method was guided by understanding of materials via characterisation and the development of a number of first-principles models. The overall aim of the work was firstly to develop a method of manufacturing continuous fibre reinforced feedstock material for FFF in order to enable the production of a wider range of products with enhanced printing; and secondly to optimise the FFF printing parameters to maximise polymer fusion. The project, therefore, includes two main parts: (i) composite material feedstock development; (ii) Printing strategy development to optimise the mechanical performances of the printed parts. This project delivered a methodology to fabricate a printable carbon fibre reinforced PEEK filament (CF/PEEK filament) with a fibre volume fraction higher than 57.4%. The value is significantly higher than the 5%, which has previously been reported in the literature of Stepashkin *et al.* [1]

In the first part of the work, a high fibre volume fraction commingled carbon fibre with PEEK (commingled CF/PEEK) was selected as the feedstock material

for the pultrusion process based on its high performances properties and the potential industrial relevant applications. Prior to the FFF feedstock development, characterisation of the material was undertaken for both PEEK and commingled CF/PEEK using Thermogravimetric Analysis (TGA), Differential Scanning Calorimetry (DSC), Scanning Electron Microscope (SEM) and optical microscopy. Based on the range of potentially viable processable temperatures revealed by the material characterisation, a comprehensive experimental programme was undertaken to determine the relevant ranges of other parameters within this range of temperatures. The optimal processing parameters were established using a specially constructed laboratory rig. The manufactured FFF feedstock material was subsequently characterised to determine the consolidated diameter measured from side view microscopy images. Porosity, the filament circularity, the PEEK area coverage and overall void content were estimated by processing microscopic cross sectional views using ImageJ and GIMP. Finally, the printability of the manufactured CF/PEEK filaments was demonstrated.

In the second part of the work, in order to understand the microstructure and mechanical properties of the 3D printed parts, the research was focused on the rheological aspects of the printing process. Both PEEK printing and carbon fibre with PEEK (CF/PEEK) printing were investigated, while only PEEK printing analysis could be accomplished in this project due to the time limitation. Using dynamic mechanical analysis (DMA), this part of the work investigated differences in the mechanical properties of a single filament wall of PEEK constructed using FFF under a range of different printing conditions. Since PEEK is a semi-crystalline polymer, a non-isothermal quiescent crystallisation model was employed to understand the findings. This model was informed by infra-red (IR)-imaging measurements. The predicted crystal fraction was correlated to a storage modulus from DMA using a classic composite solid theory. With a single model fitting parameter, it was possible to make reasonable predictions for the perpendicular and parallel storage moduli measured via DMA over a range of printing conditions. This work provides a

foundation for optimising crystallisation for the mechanical performance of the FFF printed PEEK.

Contents

| | |
|---|-----------|
| Acknowledgements..... | i |
| Abstract..... | iii |
| Contents..... | vi |
| List of Figures | xii |
| List of Tables | xix |
| Symbols..... | xx |
| Acronyms | xxiv |
| Publications..... | xxvi |
| CHAPTER 1..... | 1 |
| Introduction | 1 |
| 1.1 Background | 1 |
| 1.2 Aim and Objectives | 5 |
| 1.3 Research Methodology | 6 |
| 1.4 Contributions to Knowledge from this Research..... | 10 |
| 1.5 Thesis Structure | 12 |
| CHAPTER 2..... | 14 |
| Literature Review and Analytical Techniques..... | 14 |
| 2.1 Introduction | 14 |
| 2.2 Additive Manufacturing | 15 |
| 2.2.1 AM Process in General..... | 15 |
| 2.2.2 Different Types of AM Processes..... | 19 |
| 2.3 Fused Filament Fabrication (FFF) Process in Additive Manufacturing .. | 25 |
| 2.3.1 Introduction to Fused Filament Fabrication (FFF) Process..... | 25 |

| | |
|---|-----------|
| 2.3.2 Printing of PEEK..... | 27 |
| 2.3.3 Printing of Fibre Reinforced Polymers..... | 28 |
| 2.3.4 Description of Elements of Extrusion-based AM Machine..... | 33 |
| 2.3.5 Process Analysis | 38 |
| 2.4 Feedstock Material and Properties..... | 45 |
| 2.4.1 FFF Thermoplastic Polymer Filament | 45 |
| 2.4.2 Semi-crystalline Material Characteristics of PEEK | 46 |
| 2.4.3 Carbon Fibre Reinforced Polymer Filament..... | 51 |
| 2.5 Analytical Equipment | 52 |
| 2.5.1 Thermogravimetric Analysis (TGA) | 53 |
| 2.5.2 Differential Scanning Calorimetry (DSC)..... | 55 |
| 2.5.3 Scanning Electron Microscope (SEM) | 56 |
| 2.5.4 Time-of-Flight Secondary Ion Mass Spectrometry (ToF-SIMS)..... | 57 |
| 2.5.5 Thermography..... | 59 |
| 2.5.6 Dynamic Mechanical Analysis (DMA) | 60 |
| 2.6 Conclusion..... | 61 |
| CHAPTER 3..... | 63 |
| Material and Characterisation Prior to the Experiment | 63 |
| 3.1 Introduction | 63 |
| 3.2 Materials Selection | 64 |
| 3.2.1 Polyether Ether Ketone (PEEK) | 64 |
| 3.2.2 Commingled Carbon Fibre – Polyether ether Ketone (PEEK) Fibre | 65 |
| 3.3. Material Characterisation | 67 |
| 3.3.1 SEM and Optical Microscopy Experiment, Research and Discussion | 67 |
| 3.3.2 TGA Experiment, Results and Discussion..... | 69 |

| | |
|--|------------|
| 3.3.3 DSC Experiment, Results and Discussion | 73 |
| 3.4 Summary | 79 |
| CHAPTER 4 | 81 |
| Development of a CF/PEEK FFF Feedstock Production Process | 81 |
| 4.1 Introduction | 81 |
| 4.2 Selection of the HotEnd | 81 |
| 4.2.1 Introduction | 81 |
| 4.2.2 Ladder Network Model – Universal Model | 84 |
| 4.2.3 Model Verification | 97 |
| 4.2.4 Ladder Network Model on E3D All-metal HotEnd..... | 100 |
| 4.2.5 Experimental Verification of the Thermal Network Modelling with the Selected HotEnd | 103 |
| 4.2.6 Conclusions | 109 |
| 4.3 Design of the Pultrusion Apparatus..... | 110 |
| 4.3.1 Functional Analysis and System Architecture..... | 110 |
| 4.3.2 Conceptual Design and Its Evolution | 111 |
| 4.3.3 Calculation of the Pultrusion Die Diameter for Full Consolidation of the Filament..... | 112 |
| 4.3.4 Mechanical Design and Component Sizing..... | 114 |
| 4.3.5 Electronics and Controller Setup | 129 |
| 4.3.6 Initial Pultrusion Start-up Steps | 129 |
| 4.4 Conclusions | 135 |
| CHAPTER 5 | 136 |
| Characterisation of Composites Filaments..... | 136 |
| 5.1 Introduction | 136 |
| 5.2 Processing Conditions | 137 |

| | |
|---|------------|
| 5.3 Filament Diameter Analysis | 137 |
| 5.4 Filament Porosity Study | 139 |
| 5.4.1 Cross Section Analysis | 139 |
| 5.4.2 Density Measurement | 149 |
| 5.5 Discussion..... | 156 |
| 5.6 Conclusion..... | 159 |
| CHAPTER 6..... | 161 |
| Development of FFF Printing Process | 161 |
| 6.1 Introduction | 161 |
| 6.2 Design of the Samples and FFF Printing Parameters..... | 162 |
| 6.3 Parametric Study of PEEK FFF Printing Process | 165 |
| 6.3.1 Infrared Thermography Measurement..... | 165 |
| 6.3.2 DMA Tension Tests as Quantitative Measurement..... | 168 |
| 6.3.3 Microscopy of the Sample Surface | 172 |
| 6.4 Carbon Fibre Reinforced PEEK FFF Printing Process..... | 172 |
| 6.4.1 Adaptation of Traditional 3D Printing Process | 173 |
| 6.4.2 Preliminary CF/PEEK Printing tests | 174 |
| 6.4.3 Temperature Control for Printing Carbon Fibre with PEEK Filament | 176 |
| 6.5 Modelling of PEEK Crystal Growth..... | 202 |
| 6.6 Summary | 205 |
| CHAPTER 7..... | 207 |
| Discussion..... | 207 |
| 7.1 Introduction | 207 |
| 7.2 Contributions | 207 |
| 7.2.1. Identified Knowledge Gaps..... | 207 |

| | |
|--|------------|
| 7.2.2 Workflow and Methodology..... | 208 |
| 7.2.3 Contributions in the Work | 209 |
| 7.3 Limitations of Current Work | 213 |
| 7.4 Summary | 214 |
| CHAPTER 8..... | 216 |
| Conclusions and Future Work..... | 216 |
| 8.1 Introduction | 216 |
| 8.2 Conclusions | 216 |
| 8.3 Recommendations for Future Work | 218 |
| References | 222 |
| Appendix A..... | 252 |
| Cross Sectional Images of CF/PEEK Filament..... | 252 |
| Appendix B | 267 |
| A Numerical Model Theory of Crystal Growth | 267 |
| B.1 Overview | 267 |
| B.2 Modelling Quiescent Crystallisation | 268 |
| B.3 Modelling Temperature Profile | 268 |
| Appendix C | 269 |
| IR-Imaging Measurement Results..... | 269 |
| C.1 Temperature profile loaded with PEEK | 269 |
| C.2 Temperature profile without load..... | 274 |
| C.3 Temperature profile with correction..... | 280 |
| Appendix D..... | 286 |
| Temperature Control Correction of CF/PEEK | 286 |
| Appendix E | 288 |

| | |
|---|-----|
| On the Nielsen Model for the Prediction of Thermal Conductivity of Composites | 288 |
| Appendix F | 289 |
| Halpin & Kardos Theory | 289 |

List of Figures

| | |
|---|----|
| FIGURE 1.1: CURRENT STATUS AND FUTURE VISION FOR POLYMER BASED (PB) ADDITIVE MANUFACTURING [5] | 3 |
| FIGURE 1.2: OVERALL RESEARCH METHODOLOGY | 9 |
| FIGURE 2.1: THE THREE AGES OF INDUSTRIAL 3D PRINTING [11] | 15 |
| FIGURE 2.2: ADDITIVE MANUFACTURING (AM) PROCESS FLOW CHART [16] | 17 |
| FIGURE 2.3: MANUFACTURING SYSTEM INTEGRATION OF THE FOUR KEY PROCESSING TECHNOLOGY AREAS TO ENABLE VIABLE AM [18] | 18 |
| FIGURE 2.4: THE EVOLUTION OF 3D PRINTING TECHNIQUES: RESOLUTIONS AND COMPATIBLE MATERIALS [23] | 20 |
| FIGURE 2.5: FUSED FILAMENT FABRICATION. FROM [12] | 26 |
| FIGURE 2.6: THE SCHEMATIC OF A DESIGNED CO-EXTRUSION DEVICE TO PRINT CONTINUOUS CARBON FIBRE REINFORCED POLYMER [30] | 33 |
| FIGURE 2.7: PULTRUSION MECHANISM FOR THE COMMINGLED YARNS OF E-GLASS AND POLYPROPYLENE FILAMENTS PRODUCTION, SOURCE: [37] | 35 |
| FIGURE 2.8: DETAILED VIEW OF THE DIE IN THE HEATER WITH THE COMMINGLE YARN ENTERING FROM ABOVE AND THE FILAMENT LEAVING AT THE BOTTOM FOR THE COMMINGLED YARNS OF E-GLASS AND POLYPROPYLENE FILAMENTS PRODUCTION [37] | 35 |
| FIGURE 2.9: (A) SCHEMATIC ILLUSTRATION OF CFLF PROCESSING HEAD, (B) CFLF PROTOTYPING MACHINE [38] | 36 |
| FIGURE 2.10: SCHEMATIC OF A LIQUEFIER REPRESENTATION IN THE FUSED FILAMENT FABRICATION PROCESS [100]. | 37 |
| FIGURE 2.11: FFF PROCESS ILLUSTRATION AND ITS RELATED PHYSICAL PHENOMENA [3]. | 38 |
| FIGURE 2.12: BOND FORMATION ILLUSTRATION DURING PROCESS BETWEEN TWO ADJACENT FILAMENTS [106]. | 41 |
| FIGURE 2.13: REPEAT MONOMER UNIT OF PEEK [159] | 46 |
| FIGURE 2.14: THERMAL DECOMPOSITION OF PEEK AND PEEK-GL30 AND CARBON-CA30 COMPOSITES UNDER NITROGEN [166] | 48 |
| FIGURE 2.15: THERMAL DECOMPOSITION OF PEEK AND PEEK-GL30 AND PEEK-CA30 COMPOSITES IN AIR [166]. | 48 |
| FIGURE 2.16: DSC HEATING SCAN OF REPROCESSED AMORPHOUS 150PF PEEK [166]. | 50 |
| FIGURE 2.17: DSC HEATING SCAN OF REPROCESSED AMORPHOUS 150CA30 PEEK [166]. | 50 |
| FIGURE 2.18: GENERAL COMPONENTS IN A THERMOBALANCE [196]. | 54 |
| FIGURE 2.19: SCHEMATIC OF DSC [199]. | 56 |

| | |
|--|----|
| FIGURE 2.20:EXAMPLE PLOT OF A HEAT FLOW VS. TEMPERATURE PLOT FOR A POLYMER THAT UNDER GOES T_g , T_c AND T_m . [200]. | 56 |
| FIGURE 2.21: SCHEMATIC OF THE COMPONENTS OF A DUAL BEAM TOF-SIMS INSTRUMENT [203]. | 58 |
| FIGURE 2.22: SCHEMATIC OF THE DMA 8000 ANALYTIC TRAIN [216] | 61 |
| FIGURE 3.1: CARBON FIBRE/PEEK COMMINGLED FIBRES (HEXCEL AS4C 3K/VICTREX 150G) [223]. | 66 |
| FIGURE 3.2: MICROSCOPY IMAGES OF COMMINGLED CF/PEEK (A) UNDER MAGNIFICATION FACTOR OF 50, (B) UNDER MAGNIFICATION FACTOR OF 20. | 67 |
| FIGURE 3.3: SEM IMAGE OF COMMINGLED CF/PEEK INDICATING RELATE FIBRE DIAMETERS. | 68 |
| FIGURE 3.4: CROSS-SECTIONAL VIEWS OF THE COMMINGLED CF/PEEK IN THE SAME BUNDLE: (A), (B) AND (C) ILLUSTRATIONS OF THE NON-HOMOGENEOUS DISTRIBUTION OF PEEK AND CARBON FIBRES IN CROSS-SECTIONAL VIEWS OF THE COMMINGLED CF/PEEK, WITH THE PEEK FIBRES CLEARLY VISIBLE AS THE LARGER WHITE "DOTS". (D) CLOSE UP OF A SMALLER REGION IN A CROSS-SECTION SHOWS HOW CARBON AND PEEK FIBRES CAN BE READILY DISTINGUISHED BASED ON THEIR RADIAL SIZES. | 69 |
| FIGURE 3.5: THE TGA RESULT FOR PEEK. | 71 |
| FIGURE 3.6: THE TGA RESULT FOR COMMINGLED CF/PEEK. | 71 |
| FIGURE 3.7: (A) THE DSC RESULTS FOR THE PEEK WITH HEATING RATES OF 5°C/MIN, 10°C/MIN, AND 50°C/MIN IN THREE CYCLES WITH THE SAME SAMPLE. (B) THE DSC RESULT FOR THE PEEK WITH COOLING RATES OF 10°C/MIN, 50°C/MIN, AND 100°C/MIN IN THREE CYCLES WITH THE SAME SAMPLE. | 75 |
| FIGURE 3.8: (A) THE DSC RESULTS OF THE COMMINGLED CF/PEEK WITH HEATING RATES OF 5°C/MIN, 10°C/MIN, AND 50°C/MIN IN THREE CYCLES WITH THE SAME SAMPLE. (B) THE DSC RESULT OF THE COMMINGLED CF/PEEK WITH COOLING RATES OF 10°C/MIN, 50°C/MIN, AND 100°C/MIN IN THREE CYCLES WITH THE SAME SAMPLE | 76 |
| FIGURE 4.1: A SCALED SECTIONED VIEW OF THE HOTEND HEAT FLOW USING EXAMPLE OF E3D, MODIFIED FROM REF. [239]. | 83 |
| FIGURE 4.2: HEAT FLOW PATH OF HEATBREAK: SOURCE, REF [99]. | 85 |
| FIGURE 4.3: HEAT FLOW PATH OF THE HEATSINK: SOURCE, REF. [99]. | 85 |
| FIGURE 4.4: HEAT FLOW PATH OF HEATBREAK. | 88 |
| FIGURE 4.5: HEAT FLOW PATH OF THE HEATBREAK AND HEATSINK CONJUNCTION. | 89 |
| FIGURE 4.6: HEAT FLOW PATH OF THE HEATSINK REGION WHERE FORCED AIR CONVECTION OCCURS. | 90 |
| FIGURE 4.7: HEATBLOCK AND HEATSINK PART I THERMAL RESISTANCE CIRCUIT DIAGRAM. | 92 |
| FIGURE 4.8: HEATBREAK AND HEATSINK PART I THERMAL RESISTANCE CIRCUIT LADDER NETWORK MODEL VERSION. | 92 |

| | |
|--|-----|
| FIGURE 4.9: THERMAL RESISTANCE CIRCUIT OF THE HOTEND. | 93 |
| FIGURE 4.10: CIRCUIT AS MESH CURRENTS OF THE THERMAL RESISTANCE. | 93 |
| FIGURE 4.11: REPEATABLE PART OF THE MESH ANALYSIS MATRIX. | 96 |
| FIGURE 4.12: CIRCUIT AS MESH CURRENTS OF THE THERMAL RESISTANCE. | 96 |
| FIGURE 4.13: COMPARISON OF TEMPERATURE DISTRIBUTIONS ALONG THE NOZZLE FOR DIFFERENT FAN VELOCITIES LADDER NETWORK MODEL CALCULATED (COLOURED LINES) WITH THE EXPERIMENTAL RESULTS (GREY MARKERS) AND RDA RESULTS (GREY LINES) BY JEREZ MESA ET AL. [100]. | 98 |
| FIGURE 4.14: HOTEND IR MEASUREMENT EXPERIMENTAL SET-UP. | 103 |
| FIGURE 4.15: (A) INFRARED CAPTURE AND TEMPERATURE DISTRIBUTION OF HEATSINK AT NOZZLE 420°C. (B) MODELLING DOMAIN OF THE HOTEND, STARTING WITH THE HEATBLOCK ON THE LEFT TO THE HEATSINK ON THE RIGHT, ALL LENGTHS IN MM. (C) LADDER NETWORK MODEL RESULT AT NOZZLE HIGH TEMPERATURE TO COMPARE WITH THE IR MEASUREMENT RESULT (IN THICK PURPLE LINE). | 106 |
| FIGURE 4.16: LADDER NETWORK MODEL RESULT AT NOZZLE HIGH TEMPERATURE. | 107 |
| FIGURE 4.17: (A) INFRARED CAPTURE AND TEMPERATURE DISTRIBUTION OF HEATSINK AT NOZZLE 224°C. (B) LADDER NETWORK MODEL RESULT AT NOZZLE LOW TEMPERATURE TO COMPARE WITH THE IR MEASUREMENT RESULT (IN THICK RED LINE). | 108 |
| FIGURE 4.18: LADDER NETWORK MODEL RESULT AT NOZZLE LOW TEMPERATURE. | 109 |
| FIGURE 4.19: PULTRUSION SYSTEM DIAGRAM. | 111 |
| FIGURE 4.20: PULTRUDER PROTOTYPES. | 112 |
| FIGURE 4.21: CROSS SECTION OF PULTRUSION DIE (UNIT: MM). | 114 |
| FIGURE 4.22: SOURCES OF FRICTION TO BE OVERCOME BY THE DRIVING TORQUE. | 116 |
| FIGURE 4.23: VELOCITY PROFILE OF CF/PEEK FILAMENT IN THE PULTRUSION DIE (NOT TO SCALE). | 118 |
| FIGURE 4.24: UNIT CELL OF CONSOLIDATED MATERIAL. | 119 |
| FIGURE 4.25: SCHEMATIC SHOWING THE DIMENSION OF THE CONSOLIDATION DIE. | 121 |
| FIGURE 4.26: DIAGRAM OF FRICTION MOMENT FOR BEARING CALCULATION. | 123 |
| FIGURE 4.27: SCHEMATIC CROSS SECTION OF SUPPORT AND SPOOL. | 126 |
| FIGURE 4.28: DRAWING OF PULTRUSION SYSTEM SUPPORTS. | 128 |
| FIGURE 4.29: FINAL PULTRUSION SYSTEM SETUP. | 128 |
| FIGURE 4.30: DIFFERENT TYPES OF NOZZLES FOR STARTING PROCESS. | 130 |
| FIGURE 4.31: 0.8 MM NOZZLE SHOWING CF/PEEK FIBRES BEFORE AND AFTER CONSOLIDATION, ALONG WITH MICROGRAPH OF CONSOLIDATED CF/PEEK FILAMENT. | 131 |
| FIGURE 4.32: 0.6 MM NOZZLE SHOWING CF/PEEK FIBRES BEFORE AND AFTER CONSOLIDATION, ALONG WITH MICROGRAPH OF CONSOLIDATED CF/PEEK FILAMENT. | 131 |

| | |
|--|-----|
| FIGURE 4.33: 0.5 MM NOZZLE SHOWING CF/PEEK FIBRES BEFORE AND AFTER CONSOLIDATION, ALONG WITH MICROGRAPH OF CONSOLIDATED CF/PEEK FILAMENT. ----- | 132 |
| FIGURE 4.34: DESIGNED PULTRUSION DIE SHOWING CF/PEEK FIBRES BEFORE AND AFTER CONSOLIDATION, ALONG WITH MICROGRAPH OF CONSOLIDATED CF/PEEK FILAMENT. ----- | 132 |
| FIGURE 4.35: ERROR PLOT OF CF/PEEK SIZE BASED ON DIFFERENT NOZZLES. ----- | 134 |
| FIGURE 4.36: MICROSCOPY IMAGE OF THE CF/PEEK FILAMENT CONSOLIDATED BY (A) 0.5 MM BRASS NOZZLE AND (B) SPECIALLY DESIGNED PULTRUSION DIE. BOTH IMAGES WERE TAKEN WITH A MAGNIFICATION FACTOR 10.----- | 135 |
| FIGURE 5.1: DIAMETERS OF THE CF/PEEK FILAMENTS AS A FUNCTION OF TEMPERATURE AND PULTRUSION SPEED. ----- | 138 |
| FIGURE 5.2: TOF-SIMS MAPPING OF FILAMENT CROSS SECTIONS BEFORE AND AFTER PROCESSING TO UNAMBIGUOUSLY IDENTIFY VOIDS IN A PROCESSED FILAMENT. CHARACTERISTIC SIGNALS FOR EACH COMPOUND (CARBON FIBRE, PEEK AND EMBEDDING RESIN) WERE IDENTIFIED BY MEANS OF UNSUPERVISED MACHINE LEARNING. (A) OVERLAYS OF MAPS FOR UNPROCESSED FIBRES (LEFT), PROCESSED FILAMENT (CENTRE) AND PURE RESIN (RIGHT) WITH THE RELATIVE INTENSITIES IDENTIFIED FOR THREE COMPOUNDS: RESIN (RED), CARBON FIBRE (GREEN) AND PEEK (BLUE). (B) CHARACTERISTIC MASS SPECTROMETRY SIGNAL IDENTIFIED FOR EACH COMPOUND (LEFT) AND THEIR INDIVIDUAL INTENSITY MAPS (RIGHT) USED TO CREATE THE OVERLAY MAP IN (A). ----- | 141 |
| FIGURE 5.3: (A) VISUAL CORRELATION BETWEEN LIGHT MICROSCOPY IMAGES, (B) THE TOF-SIMS MAPS FOR THE IDENTIFICATION OF DISTRIBUTION OF FILAMENT MATERIALS. - | 142 |
| FIGURE 5.4: CROSS-SECTIONAL VIEW OF FILAMENT UNDER PROCESSING CONDITION OF 1 mm/s PULTRUSION SPEED AND 400°C OPERATION TEMPERATURE. ----- | 143 |
| FIGURE 5.5: (A) IMAGE OF FILAMENT, (B) THE BINARY BLACK AND WHITE OF THE WHOLE FILAMENT AREA, (C) PEEK AREA COVERAGE, (D) THE WHOLE VOIDS AREA, (E) THE AIR VOIDS AREA. THIS FILAMENT IS UNDER PROCESSING CONDITION OF 400°C DIE TEMPERATURE AT 1MM/S PULTRUSION SPEED. ----- | 145 |
| FIGURE 5.6: FILAMENT CIRCULARITY.----- | 146 |
| FIGURE 5.7: FILAMENT ROUNDNESS. ----- | 146 |
| FIGURE 5.8: THE FILAMENT PEEK AREA COVERAGE.----- | 147 |
| FIGURE 5.9: THE FILAMENT OVERALL VOID CONTENT. ----- | 148 |
| FIGURE 5.10: CARBON FIBRE DISTRIBUTION COMPARISON BY DIFFERENT PEEK IMPREGNATION: (A) IS UNDER 0.5 MM/S 360°C TEMPERATURE, (B) IS UNDER 0.5 MM/S 380°C. ----- | 149 |

| | |
|--|-----|
| FIGURE 5.11: SCHEMATIC OF THE PULTRUSION PROCESS. COMMINGLED FIBRES BECOME CONSOLIDATED (FULLY COMPACTED) AFTER THE PULTRUSION PROCESS. IT LEADS TO A THEORETICAL CONSOLIDATED DIAMETER D OF THE FILAMENT.----- | 152 |
| FIGURE 5.12: SCHEMATIC OF A FILAMENT. THE ACTUAL CROSS-SECTION OF THE PRODUCED FILAMENTS IS CLOSER TO AN ELLIPSE (OVAL) SHAPE THAN A CIRCULAR SHAPE. THE HYPOTHESIS OF THE DENSITY ANALYSIS ASSUMES THE CROSS-SECTION IS CIRCULAR. THE FILAMENT MEAN DIAMETER d_m IS OBTAINED BY MICROSCOPY MEASUREMENT BASED ON THIS ASSUMPTION. THE FILAMENT REAL LENGTH l_r IS THE MEASURED LENGTH.----- | 153 |
| FIGURE 5.13: SCHEMATIC OF THE FILAMENT VOLUME DIFFERENCES. ΔV IS CALCULATED BY THE VOLUME DIFFERENCES OF THE REAL FILAMENT (LIGHT BLUE) AND THE THEORETICAL CONSOLIDATED FILAMENT (WHITE). ----- | 153 |
| FIGURE 5.14: THE VOID CONTENT e_c (EQ. 5.6) BASED ON THE MEAN CONSOLIDATION d_c | 154 |
| FIGURE 5.15: VOID PERCENTAGE e_m (EQ. 5.9) BASED ON OPTICAL IMAGE MEASURED MEAN DIAMETER IN FIGURE 5.1. ----- | 154 |
| FIGURE 5.16: THE RELATIVE DENSITY RD (EQ. 5.10) OF THE FILAMENTS. ----- | 155 |
| FIGURE 5.17: THE DENSITY ρ_r (EQ. 5.11) OF THE FILAMENTS.----- | 155 |
| FIGURE 6.1: FABRICATION OF DMA TEST SAMPLES FROM A PRINTED BOX WITH WALLS THAT ARE A SINGLE FILAMENT THICK, WITH (A) THE PRINTING DIRECTION, (B) CUTTING LINES, AND (C) FINAL SAMPLE DIMENSIONS. ----- | 164 |
| FIGURE 6.2: AN ILLUSTRATION OF PRINTED SAMPLE IN THE DESIGNED GEOMETRY: (A) THE TOP VIEW; (B) THE SIDE VIEW.----- | 164 |
| FIGURE 6.3: IR CAMERA SETUP. ----- | 166 |
| FIGURE 6.4: IR IMAGE OF PRINTING (A) PRINTING WITH LOADED NOZZLE (B) PRINTING WITHOUT LOADED NOZZLE ----- | 167 |
| FIGURE 6.5: CORRECTED TEMPERATURE PROFILE OF PEEK AT 18 mm/s 410°C .----- | 168 |
| FIGURE 6.6: SCHEMATIC OF DMA TEST SAMPLES. THE VALID TEST SIZE IS LESS THAN 5 MM WIDTH AND 10 MM LENGTH. (A) TEST SAMPLE WITH PARALLEL LOAD DIRECTION. (B) TEST SAMPLE WITH PERPENDICULAR LOAD DIRECTION.----- | 169 |
| FIGURE 6.7: STORAGE MODULUS FOR PEEK DMA TESTED IN PERPENDICULAR DIRECTION. THIS CORRESPONDS TO E_{perp} . THE PRINTABLE CONDITIONS ARE: 3 mm/s , 6 mm/s AND 18 mm/s AT 420°C ; 3 mm/s AND 6 mm/s AT 410°C ; 3 mm/s AT 400°C .----- | 170 |
| FIGURE 6.8: STORAGE MODULUS FOR PEEK DMA TESTED IN PARALLEL DIRECTION. THIS CORRESPONDS TO E_{par} . THE PRINTABLE CONDITIONS ARE: 3 mm/s , 6 mm/s AND 18 mm/s AT 420°C ; 3 mm/s , 6 mm/s AND 18 mm/s AT 410°C ; 3 mm/s , 6 mm/s AND 18 mm/s AT 400°C ; 3 mm/s AND 6 mm/s AT 390°C .----- | 170 |
| FIGURE 6.9: DISABLED FILAMENT DETECTOR SENSOR TO ENSURE THE PRINTER WORK PROPERLY WITH AN OVERSIZED NOZZLE. ----- | 173 |

| | |
|--|-----|
| FIGURE 6.10: ILLUSTRATION OF A PRINTED CF/PEEK PART IN THE FINAL STEP. ----- | 174 |
| FIGURE 6.11: FFF CF/PEEK PRINTED PART. ----- | 176 |
| FIGURE 6.12:DSC RESULTS BY TRADITIONAL 2-CURVE METHOD, WHICH PROVIDES A VALUE OF SPECIFIC HEAT CAPACITY AS $1.5 J/gK$. ----- | 178 |
| FIGURE 6.13:PREDICTED THERMAL CONDUCTIVITY CF/PEEK IN LATERAL DIRECTION AS FUNCTION OF FIBRE VOLUME FRACTION. ----- | 180 |
| FIGURE 6.14:TEMPERATURE VARIATIONS IN AXIAL DIRECTION FOR HEAT TRANSFER IN A PIPE WITH CONSTANT SURFACE TEMPERATURE. SOURCE REF. [240], FIG. 8.7 (NOTATIONS HAVE BEEN ADAPTED). ----- | 181 |
| FIGURE 6.15:SCHEMATIC CROSS SECTIONAL VIEW OF NOZZLE AND FILAMENT, NOT TO SCALE. ----- | 182 |
| FIGURE 6.16:CYLINDRICAL CONTROL VOLUME OF A CYLINDER WITH INFINITESIMAL THICKNESS Dz IN THE CYLINDRICAL COORDINATE SYSTEM, WITH T_N (AS THE SET TEMPERATURE AS THE SURFACE), $T_a(z)$ (THE LOCAL AVERAGE TEMPERATURE OF THE CROSS SECTION, AND T_o THE CENTRELINE TEMPERATURE ----- | 184 |
| FIGURE 6.17:COMPARISON OF NORMALIZED LINEAR AND PARABOLIC TEMPERATURE DISTRIBUTION. ----- | 186 |
| FIGURE 6.18:VOLUME OF A PARABOLOID, ADAPTED FROM [280].----- | 187 |
| FIGURE 6.19: ASSUMED MODE OF HEAT TRANSFER FROM OVERSIZED NOZZLE TO CF/PEEK FILAMENT: (A) GEOMETRY, (B) EQUIVALENT THERMAL CIRCUIT.----- | 188 |
| FIGURE 6.20:FREE CONVECTION FLOW PATTERN IN THE AIR GAP BETWEEN THE NOZZLE AND THE FILAMENT, NOTE THAT AS THE GRAVITY IS PERPENDICULAR TO THE PLANE, THE FLOW WOULD RISE UPWARDS WHEN IT COMES CLOSE TO THE HOTTER NOZZLE AND GO DOWNWARDS AS IT APPROACHES THE COLDER FILAMENT. ----- | 189 |
| FIGURE 6.21:PRINT SPEED DEPENDENCE OF FILAMENT TEMPERATURE WHEN PEEK EXITS. 191 | |
| FIGURE 6.22:PRINT SPEED DEPENDENCE OF LOCATION WHERE PEEK FILAMENT TEMPERATURE STARTS TO EXCEED THE MELTING TEMPERATURE; TAPERED SECTION IN NOZZLE IS MARKED BY THE SPACE BETWEEN THE TWO DASHED HORIZONTAL LINES. ----- | 193 |
| FIGURE 6.23: RATE OF THERMAL ENERGY ABSORBED BY THE PEEK FILAMENT FOR DIFFERENT PRINT SPEEDS.----- | 194 |
| FIGURE 6.24:TEMPERATURE VARIATION OF THE PEEK FILAMENT IN THE NOZZLE (WITH DIAMETER $0.4mm$) FOR THE REASONABLY ANTICIPATED CASE.----- | 194 |
| FIGURE 6.25:TRANSIENT PEEK FILAMENT HEATING CURVE FOR A CROSS SECTION GOING THROUGH THE NOZZLE. ----- | 195 |
| FIGURE 6.26:MAXIMUM ACHIEVABLE CF/PEEK FILAMENT TEMPERATURE PLOTTED AS A FUNCTION OF THE PRINTING TEMPERATURE.----- | 196 |

| | |
|--|-----|
| FIGURE 6.27: RATE OF THERMAL ENERGY TRANSFERRED INTO THE CF/PEEK FILAMENT FOR DIFFERENT PRINTING SPEEDS. ----- | 197 |
| FIGURE 6.28: TEMPERATURE VARIATION OF CF/PEEK FILAMENT IN THE NOZZLE FOR A LOW HEAT TRANSFER RATE IN THE NOZZLE. ----- | 198 |
| FIGURE 6.29: TRANSIENT HEATING CURVE OF CF/PEEK FILAMENT FOR A LOW HEAT TRANSFER RATE IN THE NOZZLE. ----- | 198 |
| FIGURE 6.30: TEMPERATURE VARIATION OF CF/PEEK FILAMENT IN THE NOZZLE FOR A HIGH HEAT TRANSFER RATE IN THE NOZZLE. ----- | 199 |
| FIGURE 6.31: TRANSIENT HEATING CURVE OF CF/PEEK FILAMENT FOR A HIGH HEAT TRANSFER RATE IN THE NOZZLE. ----- | 200 |
| FIGURE 6.32: (A) E_{prep} AND (B) E_{par} PREDICTED BY THE MODEL (LINES) COMPARED TO THE DMA MEASUREMENTS (POINTS) FOR THE PRESCRIBED PRINTING CONDITIONS. ----- | 204 |

List of Tables

| | |
|--|-----|
| TABLE 2.1:AM PROCESSES AND EQUIPMENT MANUFACTURERS [24] ----- | 21 |
| TABLE 2.2:PROCESSING TEMPERATURE OF COMMON FFF FILAMENT MATERIAL [25]----- | 29 |
| TABLE 2.3: MAJOR FACTORS AFFECTING TGA RESULTS [196] ----- | 54 |
| TABLE 2.4: COMPARISON OF DIFFERENT ELECTRON SOURCES AT 20KV [202] ----- | 57 |
| TABLE 3.1: VICTREX PEEK 450G [219] AND 150G [220] SPECIFICATION. ----- | 65 |
| TABLE 3.2: PEEK NORMALISED ENTHALPY AT THE PHASE TRANSITION OF DSC RESULTS. ---- | 76 |
| TABLE 3.3: CF/PEEK NORMALISED ENTHALPY AT THE PHASE TRANSITION OF DSC RESULTS- | 77 |
| TABLE 4.1: LIST OF KEY FEATURES AND CORRESPONDING EQUATIONS: SOURCE, REF. [240]. | 86 |
| TABLE 4.2: THE MATERIALS FROM WHICH THE INDIVIDUAL COMPONENTS IN THE HOTEND ASSEMBLY IN THE JEREZ-MESA ET AL. [100] ARE MADE. ----- | 99 |
| TABLE 4.3:DIAMETERS FOR EACH PART IN THE JEREZ-MESA ET AL [100]. ----- | 99 |
| TABLE 4.4: THE BUILD-UP MATERIALS OF THE HOTEND IN EACH PART. ----- | 100 |
| TABLE 5.1: PROCESSING CONDITIONS INVESTIGATED.----- | 137 |
| TABLE 6.1: MICROSCOPY OF THE PEEK SAMPLE SURFACE. ----- | 172 |
| TABLE 6.2:VARIATION IN MATERIAL PROPERTIES NEAT PEEK FILAMENT. ----- | 190 |
| TABLE 6.3:VARIATION IN MATERIAL PROPERTIES CF/PEEK FILAMENT.----- | 190 |

Symbols

Latin Symbols

| | | |
|--------------------|--|-------------------|
| A | Geometry of particles in particulate filled composites | [-] |
| A_{cf} | Carbon fibre area in the CF/PEEK filament 2D unit cell | [m ²] |
| A_{cross} | Cross sectional area of the filament | [m ²] |
| A_{uc} | Area in the CF/PEEK filament unit cell | [m ²] |
| A_{wetted} | Wetted area in the die | [m ²] |
| D | Consolidation diameter of commingled CF/PEEK | [m] |
| E | Young's modulus | [GPa] |
| E' | Storage modulus | [GPa] |
| E_{perp} | Perpendicular to print direction DMA measured storage modulus specimen | [GPa] |
| E_{par} | Parallel to the print direction DMA measured storage modulus specimen | [GPa] |
| F | Force | [N] |
| $F_{friction}$ | Friction force | [N] |
| $F_{friction,dry}$ | Dry friction force (Coulomb Friction) | [N] |
| $F_{friction,wet}$ | Viscous friction force | [N] |
| $F_{pulling}$ | The total pulling force | [N] |
| L | Length | [m] |
| L_{die} | Length of the die | [m] |
| L_{i+1} | Top layer filament being actively printed | [-] |
| L_i | Adjacent sub-layer below actively printed layer | [-] |
| M | Bending moment | [Nm] |
| P | Perimeter | [m] |
| P_{rot} | Rotational power shaft | [W] |

| | | |
|-----------------|---|------------------------|
| P_{trans} | Power required for the system under going linear motion holds | [W] |
| R (Chapter 6) | Radius | [m] |
| $R_{t,HB I}$ | Heatbreak thermal resistance region I | [°C/W] |
| $R_{t,HB II}$ | Heatbreak thermal resistance region II | [°C/W] |
| $R_{t,HB III}$ | Heatbreak thermal resistance region III | [°C/W] |
| $R_{t,HB}$ | Total value of heatbreak thermal resistance | [°C/W] |
| $R_{t,cond,R}$ | Thermal resistance of a slice of the cylindrical inner core of the HeatSink | [°C/W] |
| $R_{t,fin}$ | Thermal resistance of each fin | [°C/W] |
| $R_{t,base}$ | Thermal resistance of each base | [°C/W] |
| T | Torque | [Nm] |
| $T_{a,i}$ | Bulk temperature of the ingoing mass flow | [°C] |
| T_c | Crystallisation Peak temperature | [°C] |
| $T_a(z)$ | Local average temperature of the cross section | [°C] |
| T_g | Glass transition temperature | [°C] |
| T_m | Melting temperature | [°C] |
| T_N | Set nozzle temperature | [°C] |
| T_o | Centreline temperature | [°C] |
| T_{total} | The total torque to be overcome by the pulling wheel | [Nm] |
| d_{die} | Die diameter | [m] |
| d_m | Measured mean value filament diameter side view | [m] |
| d_{shaft} | (Minimum) shaft diameter | [m] |
| e_c | Filament voids content | [GPa] |
| g | Gravitational constant | [m/s ²] |
| \bar{h} | Average convection coefficient | [W/m ² · K] |
| I | The second moment of area | [m ⁴] |
| k | The conduction coefficient | [W/m · K] |
| k_{air} | Thermal conductivity of the air | [W/m · K] |

| | | |
|----------------------|---|----------------------|
| $k_{CF/PEEK}$ | Thermal conductivity of CF/PEEK | [W/m · K] |
| k_f | Thermal conductivity of the fibre | [W/m · K] |
| k_m | Thermal conductivity of the matrix | [W/m · K] |
| k_{PEEK} | Thermal conductivity of PEEK | |
| V_i | The filament theoretical volume | [m ³] |
| V_r | The filament real volume | [m ³] |
| ΔV | The filament volume difference | [m ³] |
| W_i | The filament weld line between top and the adjacent filaments | [-] |
| l_r | Filament real length | [m] |
| \dot{m} | Amount of mass flow | [kg/s] |
| m_i | Filament theoretical mass | [kg] |
| m_r | Filament real mass | [kg] |
| q_r | The conduction heat | [W/m ²] |
| r (Chapter 4) | Radius | [m] |
| s | Inter fibre distance | [m] |
| u | The linear velocity | [m/s] |
| z | z-coordinate | [m] |
| Greek Symbols | | |
| δ | The phase angle | [rad] |
| μ_{PEEK} | The PEEK melting viscosity | [Pa · s] |
| μ_{dry} | The dry friction coefficient | [Pa · s] |
| ρ | The density | [kg/m ³] |
| ρ_{CF} | The density of carbon fibre | [kg/m ³] |
| ρ_{comb} | The density of CF/PEEK filament | [kg/m ³] |
| $\rho_{CF/PEEK}$ | The density of commingled CF/PEEK | [kg/m ³] |
| ρ_i | The ideal filament density | [kg/m ³] |
| ρ_r | Real filament density | [kg/m ³] |
| ρ_{PEEK} | Density of PEEK | [kg/m ³] |
| τ | The shear stress | [N/m ²] |

| | | |
|-------------------|---|---------------------|
| τ_{max} | The maximum shear stress between torque and shear stress holds of the shaft | [N/m ²] |
| \emptyset | Carbon fibre fraction | [-] |
| \emptyset_{max} | Maximum packing fraction | [-] |
| ω | Rotational velocity | [rad/s] |

Acronyms

| | |
|--------------------|--|
| 3D | Three Dimensional |
| 150CA30 CF/PEEK | 150PF PEEK with 30% weight percent Carbon Fibre |
| ABS | Acrylonitrile Butadiene Styrene |
| AM | Additive Manufacturing |
| BAAM | Big Area Additive Manufacturing |
| CF/PEEK | Carbon Fibre with PEEK |
| CFLF | Continuous Fibre Lattice Fabrication |
| CFRP | Carbon Fibre Reinforced Thermoplastic |
| Commingled CF/PEEK | Carbon PEEK Commingled Fibres |
| DED | Directed Energy Deposition |
| DMA | Dynamic Mechanical Analysis |
| DMLM | Direct Metal Laser Melting |
| DSC | Differential Scanning Calorimetry |
| FEA | Finite Element Analysis |
| FEM | Finite Element Method |
| FFF | Fused Filament Fabrication |
| FRP | Fibre-Reinforced Plastic |
| FTIR | Fourier Transform Intra-red Spectrometry |
| IR | Infrared |
| LSAM | Large Scale Additive Manufacturing |
| MASNMR | Magic Angle Spinning Nuclear Magnetic Resonance Spectroscopy |
| MCC | Microscale Combustion Calorimeter |
| MJM | MultiJet Modelling |
| OBC | Oxygen Bomb Calorimetry |
| ORNL | Oak Ridge National Laboratory |
| PB | Polymer-Based |
| PC | Polycarbonates |

| | |
|-----------|--|
| PEEK | Polyether Ether Ketone |
| PEEK-CA30 | PEEK with carbon fibre volume fraction of 30% |
| PEEK-GL30 | PEEK with glass fibre volume fraction of 30% |
| PEI | Polyetherimide |
| PLA | Polylactic Acid |
| PP | Polpropylene |
| PPS | polyphenylene sulphide |
| RD | Filament Relative Density |
| SEM | Scanning Electron Microscope |
| SI | Secondary Ion |
| SLA | Stereolithography |
| SLM | Selective Leaser Melting |
| SLS | Selective Laser Sintering |
| TA | Thermal Analysis |
| TGA | Thermogravimetric Analysis |
| TG/MS | Thermogravimetric/Mass Spectrometry |
| ToF-SIMS | Time-of-Flight Secondary Ion Mass Spectrometry |
| TRL | Technology Readiness Level |
| pyGC/MS | pyrolysis Gas Chromatography/Mass Spectrometry |
| UC | Unit Cell |

Publications

- Pu, J., McIlroy, C., Jones, A., & Ashcroft, I. (2021). Understanding mechanical properties in fused filament fabrication of polyether ether ketone. *Additive Manufacturing*, 37, 101673.
- Pu, J., Saleh, E., Ashcroft, I., & Jones, A. (2019). Technique for Processing of Continuous Carbon Fibre Reinforced PEEK for Fused Filament Fabrication. In SFF2019 Symposium, Texas, USA.
- Zhuo, P., Li, S., Ashcroft, I., Jones, A., & Pu, J. (2017). 3D printing of continuous fibre reinforced thermoplastic composites. In 21st International Conference on Composite Materials (pp. 20-25).
- Pu, J., Zhuo, P., Jones, A., Li, S., Ashcroft, I., Yang, T., & Ponggorn, K. (2017, August). Temperature control of continuous carbon fibre reinforced thermoplastic composites by 3D printing. In Proc. Int. Conf. on Composite Materials, Xi'an, China.

CHAPTER 1

Introduction

1.1 Background

Additive Manufacturing (AM), also known as 3D printing, is increasingly becoming a process of choice for many applications as it meets many of today's manufacturing needs, such as: customisation, fast response to customer demands, fast time-to-market and short development time. However, these advantages are currently offset by a number of disadvantages, such as a poor materials palette and poor understanding of the properties of materials processed by 3D printing. In this project, an attempt is made to impact both the functionality of materials available for 3D printing and an understanding of how such materials differ from those processed by traditional means. Continuous carbon fibre reinforced PEEK composites were selected as the feedstock material, since firstly, this composite is highly desirable for applications requiring good structural and thermal properties. PEEK is a polymer with outstanding thermal insulation (due to its low thermal conductivity) and mechanical properties at elevated temperature, and is also chemically inert with good corrosion resistance [2].

Fused Filament Fabrication (FFF) is an AM process that uses a continuous filament of thermoplastic material. For this reason, in theory, FFF is the ideal 3D printing process for continuous fibre reinforced material. From an academic point of view, fundamental research on the 3D printing of fibre composites has recently received a good amount of attention, but as an industrially applied technology, it is still immature [3]. According to the Scopus database, there are approximately 150 publications in the period 1980-2019 containing the keywords "continuous fibre composites" and "3D printing".

Chapter 1 Introduction

From an industrial perspective, the development of applications for this technology can be broadly divided into two categories. On the one hand there are applications of FFF of composites in the automotive, aerospace and construction sectors, which focus on large-scale printing. On the other hand, there are sectors, such as sports and healthcare which focus more on smaller applications requiring higher precision and accuracy. Although FFF technology-based manufacturing has made inroads into industry, fibre printing has not been applied widely to support large-scale and precise manufacturing [3]. The ultimate goal for developing the 3D printing technology of continuous carbon fibre reinforced PEEK matrix is to apply this technology to the manufacturing of high-strength components, thus expanding the potential applications of FFF from significantly those amenable to unreinforced polymer filaments. These components can then be applied in demanding industrial areas, such as bone implants or aerospace components. This project aims to achieve printing filament with a high fibre volume fraction in order to meet typical industrial standards. A survey of the current state-of-the-art in carbon fibre 3D printing, reveals that the fibre volume fraction is typically limited to around 30% to 40%, whereas, for instance, in the aerospace industry, engineers typically design applications with fibre volume fractions up to 60% [4].

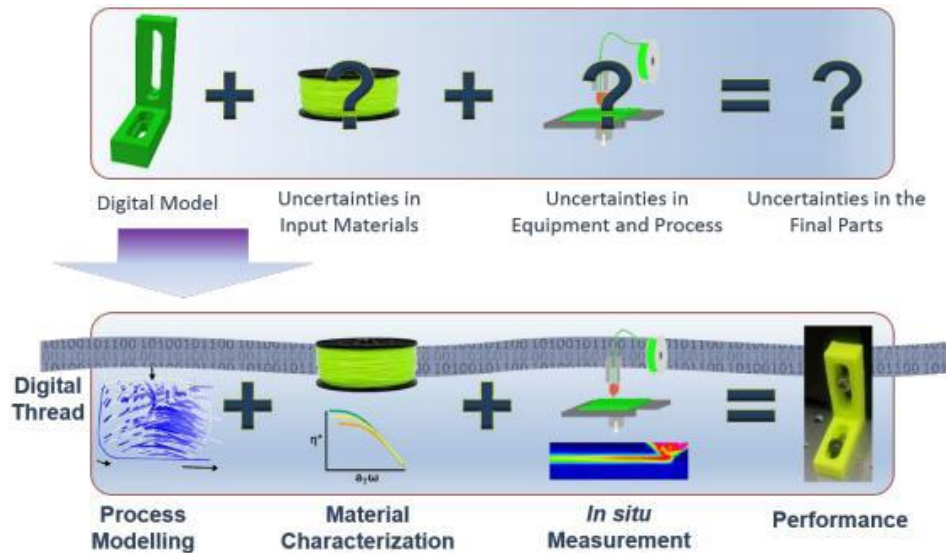


Figure 1.1: Current status and future vision for polymer based (PB) Additive Manufacturing [5]

Figure 1.1 shows that the main difficulties in achieving a production process with the required quality are perceived to lie with the process and quality control. The requirements for industrial application of this technology include high reliability and repeatability, high product lifetime, little post-processing, and the ability to produce more complicated parts than those achievable with current manufacturing methods. More specifically, the challenges include [6]:

- The printed parts quality is still low compared to conventional manufactured parts. Quality problems include voids in printed parts, poor fibre-matrix bonding and low achievable fibre volume fractions.
- Real time control during the printing process requires fast in-process monitoring and control solutions. It is therefore a challenge to apply computationally intensive approaches such as machine learning or big data analytical methods together with in-situ measurement and process monitoring.
- It is not easy to select appropriate measurement to enable optimisation of process parameters. Process parameters are inputs to the process, such as the initial process settings, and can be distinguished from process variables, which are outputs from the process [7]. Process parameters for FFF include

Chapter 1 Introduction

nozzle temperature, chamber temperature, extrusion speed, process time etc. The process variables include surface quality, mechanical properties and density. It is impossible to find a unique method for the in-process measurement of relevant process variables for all AM processes. Also, it can be challenge to obtain accurate results from these measurements.

- Another challenge arises from the requirement for a high level of process and system integration. This requirement includes taking into account the performance of the produced parts, printer technology, processing and post-processing into one platform. All these facets consideration of the additive manufacturing process and their integration can be a set of research projects on its own.
- PEEK is a semi-crystalline polymer, where molten, fusion and mechanical properties are temperature and time dependent. When processing the material, temperature control is of paramount importance since the properties of thermoplastics change when exposed to a high temperature. Moreover, this temperature and time dependent relationship is non-linear.
- The FFF process is generally applied to the processing of polymers with a low melting point, such as acrylonitrile butadiene styrene (ABS), polylactic acid (PLA) and nylon. PEEK on the other hand, with its high melting temperature and comparatively smaller processing window, has not found such wide spread application.

Starting with these considerations, and in order to strive towards the commercial application of continuous carbon fibre reinforced PEEK printing, this project first aims to prove the technology concept in a laboratory setting. The challenges focused on in this thesis are in the low range of technology readiness levels (TRLs): 1 to 3. In particular, this project considers porosity, bonding, feedstock production and establishment of a processing window. Taking into account that there is currently neither any 3D printer capable of printing continuous CF/PEEK with a high fibre volume fraction, nor the feedstock material currently on the market, the aim and objectives for the development of the printing process are described in Section 1.2.

In this project, the CreatBot F430 (Henan Suwei Electronic Technology Co., Ltd, Henan, China) [8] was utilised for the printing. The printer is equipped with two printheads each with a nozzle that can be heated up to a temperature of 420°C. The chamber and print-bed of this printer can both be heated in order to keep the environment at the required temperature, up to a maximum achievable temperature of 90°C.

Due to the equipment limitations for the experiments, some of the test methods in this thesis may not be the conventional methods for establishing material properties, part properties etc. as usually applied in scientific institutes and industry or specified in standards. Detailed justifications are given in the thesis, which defend and explain these choices as the best choice given the equipment available.

1.2 Aim and Objectives

The overall research challenge of this thesis is to develop a method for successfully demonstrating the printability of high volume fraction carbon fibre reinforced PEEK by the FFF process. The definition of the printability is stated in Section 1.3.

This challenge can be divided into two main aims:

- Develop a process to manufacture high volume fraction continuous fraction carbon fibre PEEK (CF/PEEK) feedstock material for FFF printing.
- Develop a method to successfully FFF print high volume fraction continuous carbon fibre reinforced with PEEK.

By investigation of the microstructure of the polymer during processing, this work is mostly focussed on the fundamental study and analysis of the material processing, utilising experimentation and analytical modelling. Subsequently, experiments were designed, to verify and empirically refine the modelling. Using a model-based process design, the processing parameters, such as heating rate, cooling rate controlled by different printing speed, nozzle

temperature and ambient temperature, feed rate can be optimised. Therefore, the final structure of the printed parts, can also be optimised.

The following objectives were identified to achieve the overall aims of the research:

- Design and build pultrusion apparatus for the production of continuous CF/PEEK filaments with a high fibre volume fraction (defined here as between 55 and 60 weight %).
- Establish the optimal process parameters for feedstock production.
- Characterise the PEEK and CF/PEEK materials, before, after and during processing, in order to increase understanding and inform the feedstock production process.
- Modify a commercial 3D printer to enable printing of the high volume fraction CF/PEEK feedstock material.
- Develop a FFF printing strategy for the fabricated continuous CF/PEEK filaments, including establishment of suitable printing parameters for the modified printhead.

1.3 Research Methodology

A schematic of the overall research methodology is given in Figure 1.2. Following the research aim, this project comprises the development of a composite feedstock process, and the development of a FFF printing process using that feedstock. In the development of the composite feedstock process, both neat PEEK and a CF/PEEK mixed fibre material were investigated, as it was instructive to first characterise the behaviour of the PEEK on its own. These materials were firstly characterised by thermogravimetric analysis (TGA) to determine the upper boundary of the processing temperature, by differential scanning calorimetry (DSC) to understand the thermal properties, and scanning electron microscopy (SEM) and optical microscopy studies to characterise the commingled CF/PEEK morphology. The next step was to design and build a pultrusion apparatus to produce the CF/PEEK filaments from

commingled CF/PEEK fibres. The pultruded CF/PEEK filaments were then analysed in terms of consolidation quality, and porosity. Research into the PEEK process was split into two separate studies: printing of neat PEEK and printing of the CF/PEEK composite. This is because firstly, the properties of the CF/PEEK filaments required a significant modification of the process and equipment, whereas neat PEEK printing was carried out using a standard extrusion process. Secondly, different processing parameters were required since the nucleation and crystal growth of PEEK changes when it is comingled with carbon fibre [9]. The remainder of the work was focussed on weld formation (i.e. filament fusion) during the FFF printing of PEEK and CF/PEEK. The temperature profile was recorded by infrared (IR) thermography measurement of the processed material in-situ, and the weld time was derived from these results. Empirical crystal growth models and the IR thermography measurements and DMA tension testing were linked in the model. Eventually, the crystal fraction as a function of time was established, and the printing parameters were optimised to maximise the polymer fusion. In this analysis, it was also found that slower printing speeds and higher temperatures produced stronger printed parts. For this aspect of the work, predictive thermal modelling and simulation of the CF/PEEK printing were also carried out, in order to accurately control the printing temperature during the process.

The printability of continuous CF/PEEK is defined in this thesis based on the combination of physical, rheological and mechanical properties that allow the material to be processed via FFF. Specifically, in order to achieve successful printing of the feedstock material, the following conditions must be met:

1. The filament should have sufficient stiffness to enable extrusion into the print head.
2. The filament should be able to withstand the temperature and speed required for printing without degradation of the PEEK or damage to the carbon fibre.

Chapter 1 Introduction

3. The heated filament should be able to be printed with consistent dimensions without damage to the carbon fibre for an appropriate print path.

4. The heated filament should be able to be printed with a viscosity suitable for bonding to other filaments to enable 3D models to be printed with acceptable porosity and dimensional control.

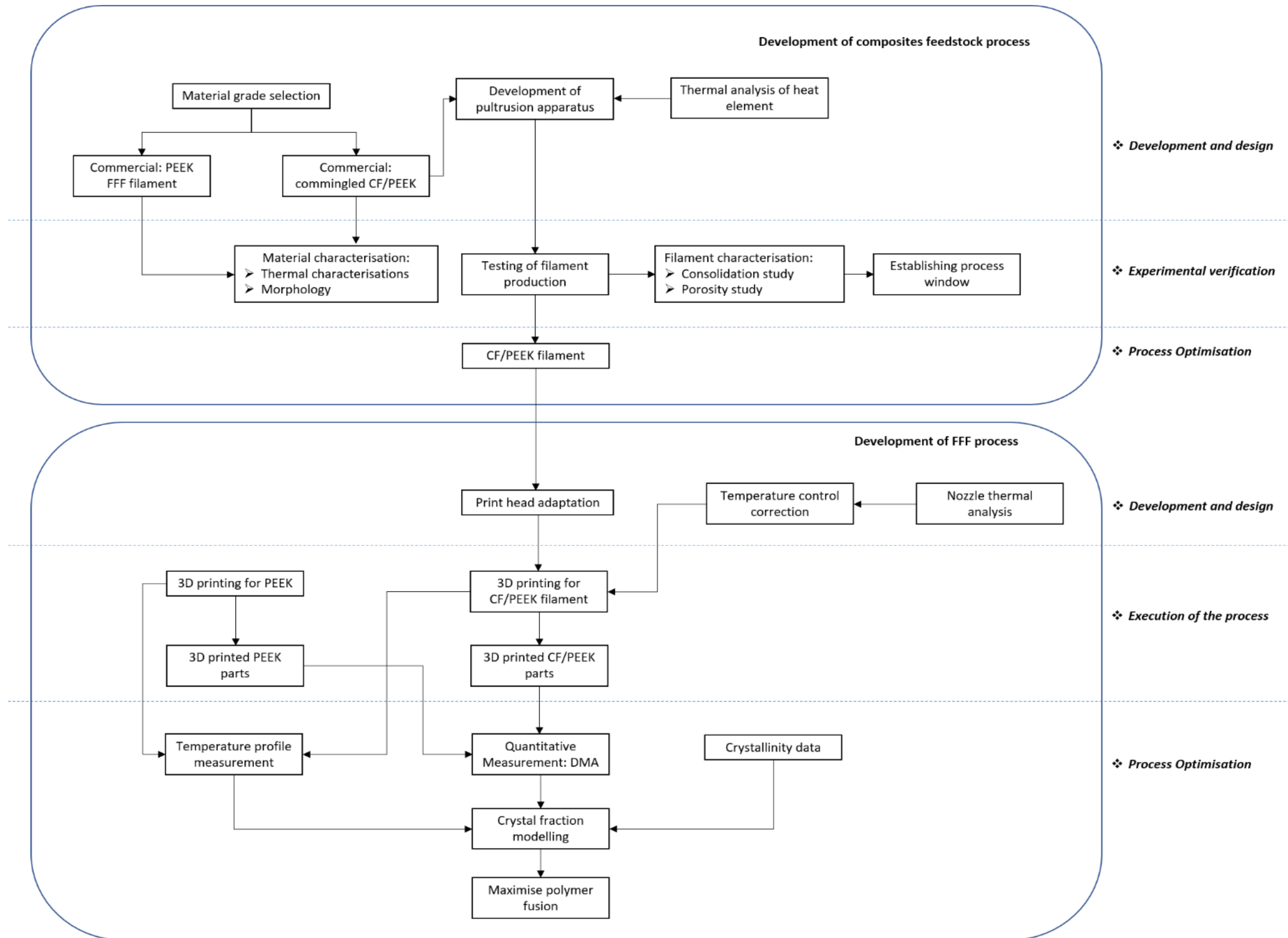


Figure 1.2: Overall research methodology

1.4 Contributions to Knowledge from this Research

Starting with a “conventional” additive manufacturing process to process materials which have not been processed previously, required the processes and equipment to be adapted substantially, in such way that the new materials can be processed in an optimal manner. This adaptation was carried out based on the thermo-physical properties of the materials. The development of this process means an expansion of the FFF processing capabilities in the sense that continuous carbon fibre reinforced PEEK with a high fibre volume fraction can now be printed. Application of CF/PEEK material in additive manufacturing has seen little investigation to date. This work will lead to the following contributions to engineering science:

- Development of a method for high fibre volume fraction feedstock preparation and analysis. As there was no continuous CF/PEEK FFF filament available on the market during this PhD research, and no report of printing with a fibre volume fraction higher than 5% [1], a bespoke process needed to be designed. This work included the material characterisation of continuous CF/PEEK with fibre volume fraction up to 57.4% (the existing reports of CF/PEEK are usually short carbon fibre with fibre volume fractions up to 50%) prior to the feedstock production. Translation of process requirements into the mechanical and thermal design of the feedstock pre-processing apparatus, and an analysis of the filament morphology and porosity after a full factorial study of the production process parameters to optimise the feedstock pre-processing process.
- Analysis of weld formation with a special consideration of the crystal growth. It is reported and well known that the mechanical properties of PEEK and CF/PEEK are highly dependent on the degree of crystallinity in the polymer (matrix) material. The FFF printing process comes with conditions which are significantly different from conventional polymer (composite) processing and a small amount of data is available which can

be used to tune the mathematical models that exist in the field of polymer physics. A predictive model was developed based on the heat transfer in the nozzle and experimental evaluation of the mechanical properties of the printed parts, the nozzle and deposited material temperatures. This led to a method to predict the best printing temperature and will improve the temperature control for the nozzle. Furthermore, this may also improve the thermal control in the feedstock pre-process, and improve the control of heating and cooling down of the material within the printing process. Ultimately, this will lead to improved control of manufacturing process during printing, resulting in parts with better properties and manufactured in a repeatable manner.

- Method for implementation of measurement FFF processing of fibre-reinforced crystalline polymer material. The processing of CF/PEEK requires a carefully calibrated process. The FFF-based process for the printing of CF/PEEK with high fibre volume process had to be fully developed in this work. The setup, use of IR thermography technology and its data correction and associated data processing used for this material under the different processing condition on a standard FFF machine is demonstrated. As a small / medium sized tensile test machine to evaluate the strength of printed parts was not available, it was therefore impossible to obtain the strength of the printed parts as one of the most essential mechanical properties of the bulk material. Instead, alternative DMA tests were set up to relate the stiffness of the printed parts to the printing quality. This will lead to new strategies of quantitative measurements of 3D printing.
- Advancement of mechatronic design strategy for 3D printing system development: the design of a bespoke process for the printing of high fibre volume fraction CF/PEEK material requires a certain degree of automation to accurately control temperature, speeds etc. The selected process to prepare a feedstock material suitable for FFF was pultrusion. To augment the mechanical design, this led to the design and control of a mechatronic device for the production and research of the CF/PEEK feedstock materials.

Chapter 1 Introduction

Normally, the FFF process relies on the melting (liquefying) of its feedstock material. As the carbon fibre component in the composite does not melt, this means that the filament for long and continuous fibre composites remains relatively stiff when it is extruded through the nozzle and deposited on the substrate. Therefore, adaption of the printhead was required to extrude the relatively stiff CF/PEEK filament. This will inform the design of future 3D printer systems in terms of printhead modification.

1.5 Thesis Structure

A brief description of the contents of the remaining chapters is given below:

Chapter 2 Literature Review. This chapter provides a state-of-the-art overview of the relevant research. It starts with a discussion of the general processing technologies used in the field of additive manufacturing, then narrows in on the FFF process with fibre based polymer composites printing. Furthermore, it studies FFF printing equipment, feedstock processing and the physics of the printing process to reveal the relevant process parameters. Subsequently, the influence of PEEK's semi-crystalline nature and the influence of the presence of carbon fibre as reinforcement material on material properties are reported. The material characterisation techniques used for this research are explained with reference to their use within process optimisation.

Chapter 3 Material and Characterisation Prior to the Experiment.

Starting with material selection, this chapter presents the results and analysis of the material characterisation experiments. The results from material characterisation contributed to understanding of the PEEK and CF/PEEK materials. This knowledge was then used in development of the FFF feedstock preparation process and optimisation of the FFF printing parameters.

Chapter 4 Development of Composites Feedstock Process. In this chapter, analysis of the heating element of the pultrusion system is undertaken first to

Chapter 1 Introduction

enable heating element selection. The design and construction of the pultrusion apparatus are then described in detail.

Chapter 5 Characterisation of Composite Filaments. Following the pultrusion-based fabrication, the composite filaments were analysed in terms of their consolidation quality and porosity. ToF-SIMS was utilised to remove ambiguity in material identification in the cross-sectional views of the produced filaments. Automated image processing techniques were applied to analyse the cross-sectional views of the filament, and density measurements were carried out. This study led to the establishment of a suitable processing window for the filament production.

Chapter 6 Development of FFF Printing Process. In this chapter, both PEEK and CF/PEEK printing are described. Infrared thermography was utilised to record the material temperature profile during the printing; quantitative measurement by the DMA tension tests were carried out and the results were analysed. There is also a section on the modification of the 3D printing head for the CF/PEEK printing, with a thermal control analysis for printing CF/PEEK. This allows for a prediction of the real temperature of CF/PEEK filament during the printing in order to achieve an accurate temperature control. Preliminary continuous CF/PEEK printing tests were carried out. Further modelling of PEEK crystal growth during the printing is presented in order to link the printing parameters to the mechanical properties of printed parts.

Chapter 7 Discussion. This chapter presents a discussion that links all the results from the previous chapters.

Chapter 8 Conclusions and Future Works. Conclusions are drawn, and future work which can improve this technology is also identified, based on the limitations of the current work.

CHAPTER 2

Literature Review and Analytical Techniques

2.1 Introduction

“The composites industry has a tendency to get caught off-guard by metals as they make progress into more applications. 3D printing is an area where metals have taken the lead, but a number of developing technologies could put composites back on top.”[10]

There is a trend in the composites field to adapt Additive Manufacturing (AM) technology in the manufacturing of specific parts in very small batches such as the tooling for composites manufacturing, and generic fixturing and tooling components. For composite structures engineers, AM has the potential to expand the freedom to design compared with current composite manufacturing processes. It provides the opportunities to improve the design, whilst not being tied down to a potentially costly redesign of the manufacturing process [11]. 3D printing is a new processing technique for the production of composites. It adds flexible production to achieve rapid customisable components manufacturing with a “batch size of one”, which conventional manufacture cannot do. As illustrated in Figure 2.1, this would be a step change from Fused Filament Fabrication (FFF) printing for prototypes and usher in a new era for truly rapid, flexible and on demand production of composite components.

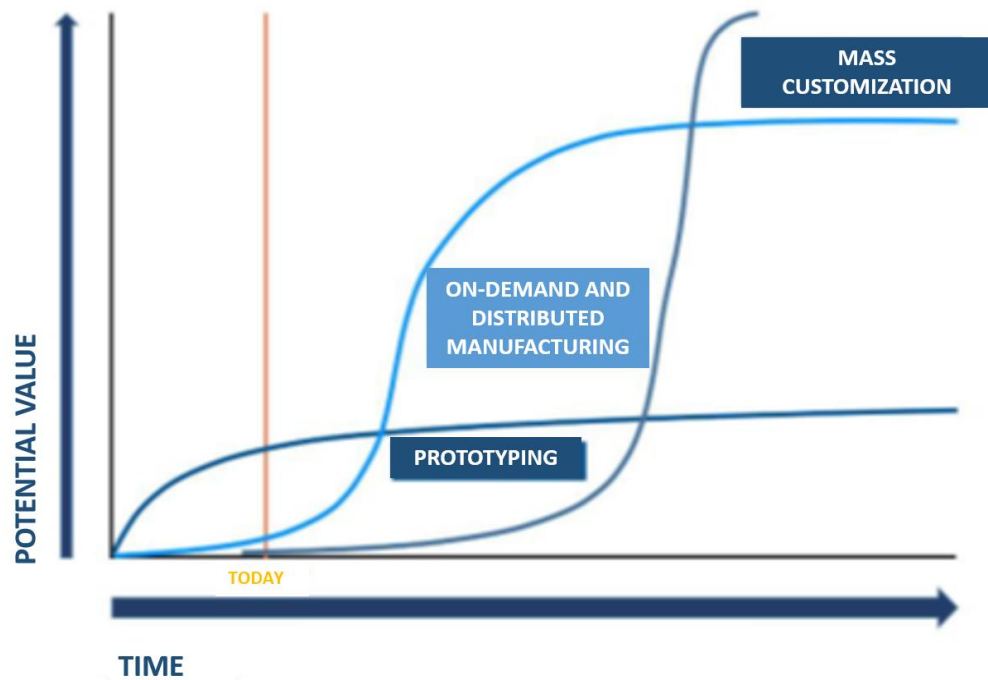


Figure 2.1: The three ages of industrial 3D printing [11]

In this research, the FFF process is selected for the development of CF/PEEK printing. This literature review focusses on the aspects of the 3D printing process which govern its performance. The next section starts with a survey of the general concepts of AM processes including both polymer and metal printing. Their state-of-the-art, future potential, the knowledge gaps and research needs for a selected number of different AM processes are identified. Subsequently, a more in-depth discussion of the FFF process is provided. Finally, the feedstock materials, the PEEK semi-crystalline properties and analytical techniques utilised in this research are reviewed.

2.2 Additive Manufacturing

2.2.1 AM Process in General

Additive Manufacturing (AM), commonly known as 3D printing, represents an increasingly popular class of technologies in the field of advanced manufacturing [12-14]. This technology is used to manufacture objects by adding material layer-by-layer to minimise the need for finishing material

removal operations whilst achieving satisfactory geometric accuracy [15]. One of the advantages of 3D printing compared with traditional manufacturing techniques is that the process does not require templates, moulds or masks. In addition, 3D printing has the unique ability to fabricate complicated forms and shapes such as interlocking geometries, shell structures with embedded features, and multimaterial printing. This technology therefore enables completely new designs and functionalities [16]. The process flow chart of AM is presented in Figure 2.2. All the AM processes share the following operational steps. Firstly, the generation of the 3D model, its subsequent conversion into an STL file, after which it is sliced and converted into G-code [17] before being loaded into the memory of an AM machine. After the uploading of the model, the machine is set up, and the parts are built in the machine, followed by the removal of the parts from the print bed. Some of the processes also require postprocessing to enhance the qualities of the printed parts. To unlock the future potential of AM, *Research and Development of AM Technologies*, managing the acceleration of the former through *an University-Industry based Open Innovation*, and *Education and Training* of future workforces [18] are highlighted as areas for further development of AM.

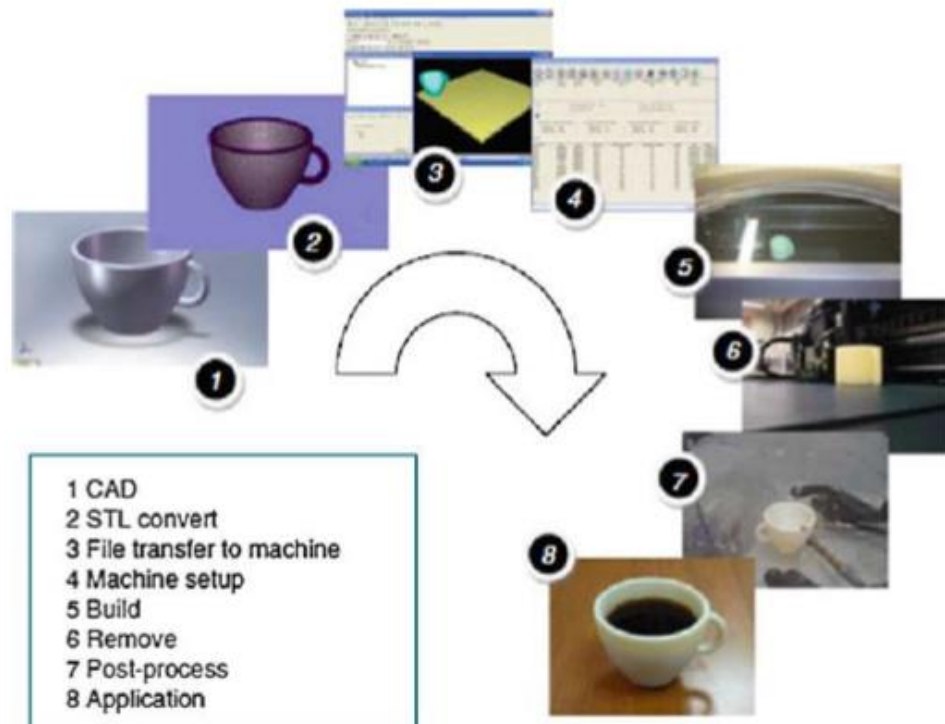


Figure 2.2: Additive manufacturing (AM) process flow chart [16]

The four essential technology elements, and system integration required for the development of 3D printing processes, are shown in Figure 2.3. Currently there are many remaining challenges in each of these elements. Generally, they are [18]:

- **Materials:** there is a limitation in the materials available for use in 3D printing. The 3D printing process requires specially designed and optimised materials for printing. The development of new suitable materials might take a long time.
- **Design:** since 3D printing technology enhances the freedom of designers, there is a call for new design tools that allow easy modelling of product features enabled by 3D printing technologies. These include the development of a variety of AM-oriented design tools; transcendence of the limitations imposed by parameters in current CAD systems for 3D printing; simulation capability development of composite primitive shapes to avoid further deformation during manufacture, and the simulation of materials and material compositions to fit the AM process.

Chapter 2 Literature Review

- Modelling, in-situ sensing, controlling and processing: It is said that the modelling, sensing, controlling and processing of 3D printing are among the highest priority needs for achieving the technology potential [17].
- Characterisation and certification: 3D printing technology is still lacking qualification and certification methodologies. To allow the use of 3D printed parts for applications in e.g. aerospace, and medicine and healthcare, certification is critical to manufacturing processes in order to proof assurance of the quality and safety of finished parts. Currently, AM processes are not mature enough to have sufficient control over end-products to meet requirements for certification. Depending on the intended function of the designed part and selected printing processes, 3D printed parts often fail to meet design requirements as their mechanical properties and dimensional accuracy are insufficient [19]. Therefore, 3D printing processes currently cannot meet the requirements of some specific applications. Gibson *et al.* [16] state that, due to a lack of consensus in industry for standardised conditions and procedures, material data reported by various companies is not comparable. Even where the same AM process or equipment is used, the process parameters favoured by companies differs greatly so that repeatability of results is low between different systems suppliers and service bureaus. There are few standard specifications that end users of equipment can refer on. Overall, this makes it difficult to ensure that a product will be built to design specifications.

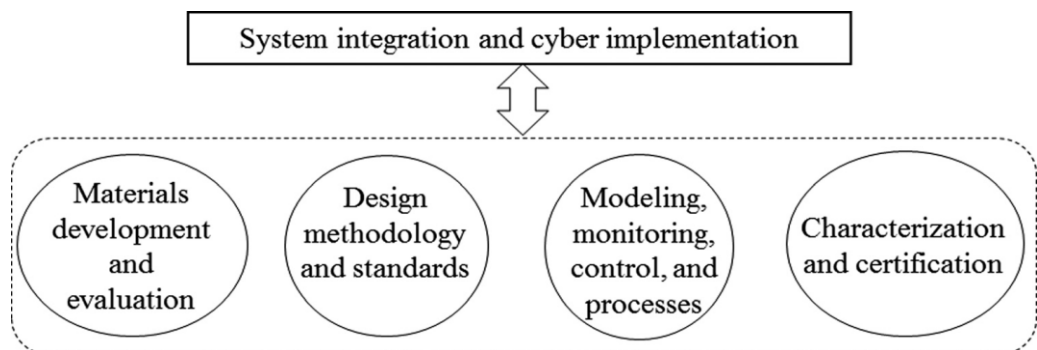


Figure 2.3: Manufacturing system integration of the four key processing technology areas to enable viable AM [18]

Hence, at this current stage, further investigations are carried out in order to mitigate the risks and address these challenges.

2.2.2 Different Types of AM Processes

Since the mid-1980s, AM has been developed through several evolutionary steps. Figure 2.4 presents the timeline of this evolutionary process. This has enabled 3D printing to transform from an application for rapid prototyping to a viable technology for manufacturing, and it leads the AM market towards fast growth. The 2013 Wohlers Report states that [20] “the compound annual growth rate of worldwide revenues of all types of AM products and services over the past 25 years was 25.4%. The rate of growth was 27.4% over the 3-year period from 2010 to 2012, reaching \$2.2 billion in 2012. The unit sales of industrial AM systems (unit price >\$5,000) increased by 19.3% to 7771 units in 2012, while the unit sales of 3D personal printers (unit price ≤ \$5,000) increased by 46.3% to 35,508 units in the same year”. According to the 2016 Wohlers Report, the AM industry grew 25.9% to \$5.165 billion in 2015 [21]. While the 2019 Wohlers Report updates that “there are listing of 107 early-stage investments valued at nearly \$1.3 billion.” [22] These reports show that the demand for 3D printing has increased dramatically in recent years. Filling the gaps and needs for AM process knowledge models, as mentioned in Section 2.2.1, will enable AM to become the driving force behind the so-called “fourth industrial revolution” and unlock its potential for fully agile production.

Chapter 2 Literature Review

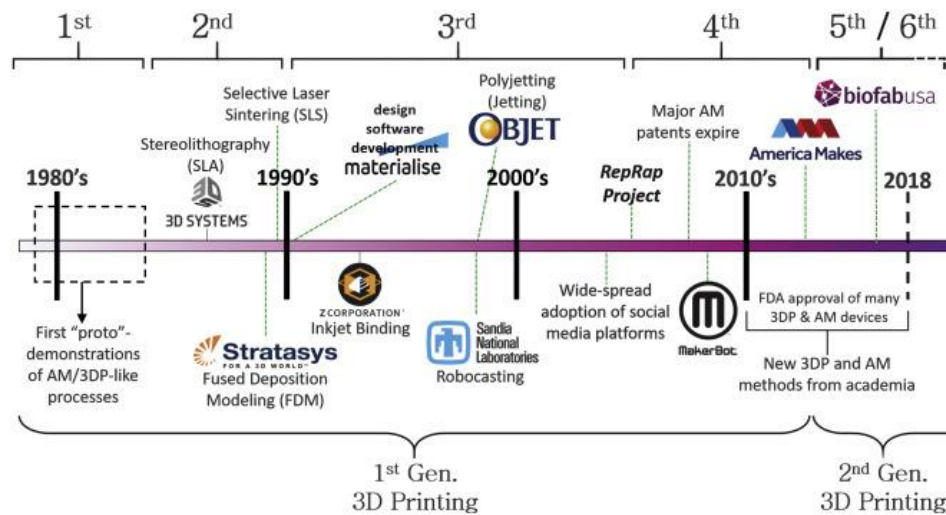


Figure 2.4: The evolution of 3D printing techniques: resolutions and compatible materials [23]

The ASTM F42 committee classified the AM processes into seven categories [24], which are listed in Table 2.1. These seven processes are distinguished based on the deposition strategies. Table 2.1 also provides a list of feedstock materials for each process, the commercial manufacturers and machine.

Table 2.1: AM processes and equipment manufacturers [24]

| Process category | Process/technology ^a | Material | Manufacturer | Machine |
|-------------------------|---------------------------------|--------------------|---------------------------------|-----------------------------------|
| Vat photopolymerization | SLA | UV curable resins | Asiga | Freeform Pico |
| | | | 3D Systems | iPro |
| | | | 3D Systems | Projet6000/7000 |
| | | | EnvisionTEC | Perfactory |
| | | | Rapidshape | S Series |
| | | | DWS | DigitalWax |
| | | | Lithoz | CeraFab 7500 |
| Material jetting | MJM (multijet modelling) | UV curable resins | 3D Systems | Project 3500 HD/3510/5000/5500 |
| | | | Stratasys | Objet |
| | | | Solidscap | 3Z |
| Binder jetting | 3DP (3D printing) | Composites | 3D Systems | Z Printer |
| | | Polymers, ceramics | Voxeljet | VX Series |
| | | Metals | ExOne | M-Flex |
| Material extrusion | FDM | Thermoplastics | Stratasys | Dimension |
| | | | | Fortus |
| | | | | Mojo |
| | | | | uPrint |
| | | | MakerBot | Replicator |
| | | | RepRap | RepRap |
| | | | Bits from Bytes | 3D Touch |
| | | | Fabbster | Fabbster Kit |
| | | | Delta Micro Factory Corporation | UP |
| | | | Beijing TierTime | Inspire A450 |
| Waxes | Choc Edge | Choc Creator V1 | | |
| | Essential Dynamics | Imagine | | |

Chapter 2 Literature Review

| | | | | |
|----------------------------|-----------------------------|----------------|-------------------|-------------|
| | | | Falx@Home | Model |
| Powder bed fusion | SLS | Thermoplastics | EOS | EOSP |
| | | | Blueprinter | SHS |
| | | | 3D Systems | ProX |
| | | | Realizer | SLM |
| | | | Renishaw | AM250 |
| | EBM (electron beam melting) | Metals | Arcam | Acram A2 |
| | | | Sciaky | DM |
| Sheet lamination | LOM | Paper | Mcro Technologies | Matrix 300+ |
| | | Metals | Fabrisonic | SonicLayer |
| | | Thermoplastics | Solido | SD300Pro |
| Directed energy deposition | LMD/LENS | Metals | Optomec | LENS 450 |
| | | | DM3D | DMD |
| | | | Irepa Laser | EasyCLAD |
| | EBAM (electron beam AM) | Metals | Sciaky | VX-110 |

^a Group in this column indicates trademarked terms

Stereolithography (SLA): SLA is a 3D printing technology using photochemical processes by which light causes chemical monomers and oligomers to cross-link to form polymers [25]. Then these polymers can make up the three-dimensional solid body.

MultiJet Modelling (MJM): MJM or PolyJet Modelling (PJM) is a 3D printing process that deposits layers of liquid acrylic polymer onto a build platform with multiple nozzles. The resulting parts can then be cured by exposure to UV. The UV lamps are located on the printhead so it can cure the plastic as soon as it is printed. The intensity of the UV light is adjustable so that the upper most layer does not cure completely to aid fusion of layers. However, since the entire component has received several doses of UV light exposure, it can be completely cured by the end of the printing process.

Binder Jetting: This is a 3D printing process also known as “powder bed and inkjet”, or “drop-on-powder” printing. In this process, the inkjet printhead moves across the print bed, which is covered with powder, and selectively deposits a liquid binding material. Then another thin layer of powder is spread across the completed section and the process will repeat to finish the complete part.

Fused Filament Fabrication (FFF) or Material Extrusion: In this 3D printing process, plastic is usually used as the material, though in some cases the process can be used for metals and ceramics. In these cases, the process is as follows. The filament combines metal or ceramic powder and polymeric binders to print the parts. After the initial print is done, a catalytic debinding and sintering processes will be applied to remove the binder so that the final parts can be achieved [26, 27]. In this process, the material is heated and extruded by an extruder fixed on the printhead. The printhead then moves simultaneously and builds up the parts layer by layer. More recently, attempts have been made to improve the material properties of the extruded thermoplastic polymers by adding short or long fibres to the material. Several approaches are reported to prepare the feedstock material [1, 28-44]. This

process, which is selected for the development of CF/PEEK printing, is an extrusion-based process, and its relevant aspects will be discussed in more detail in Section 2.3.1.

Powder Bed Fusion: This category covers a range of techniques where a laser or electron beam melts or sinters localised powder bed material in a layer-by-layer fashion. The common processes are selective laser sintering (SLS) and selective laser melting (SLM), the latter sometimes also referred to as direct metal laser melting (DMLM). It is a technique that uses a high power density laser to melt and fuse metallic powders together. The difference between SLS and SLM is that for SLM process the metal powder is locally, fully melted to form a solid three-dimensional part. Whereas for SLS the powder is heated below the melting point, it forms solid by fusion.

Sheet Lamination: This is a process that involves stacking and laminating thin sheets of materials layer by layer. Lamination methods used in this 3D printing process include bonding, ultrasonic welding and brazing. Before the actual bonding process takes place, the sheets may be cut to near net-shape with laser cutting. The 3D printer first prints the near net-shaped parts, and the final shape will be achieved by post-processing with a CNC machine tool.

Directed Energy Deposition (DED): In these processes a focused energy source directly fuses material as it is being deposited. The materials used in this technology are mostly blown metal powder or wire source materials. This 3D printing process potentially can print very large parts, as DED has a rapid deposition speed and a multi-axis robot arm can be deployed to hold and move the printhead during the printing process. The use of a robotic arm allows for the printing of parts with complex geometries.

Overall, the range of AM processes provides a huge potential for commercial application. However, the manufacturing readiness level for each of the processes is still low and needs to be improved before it can compete with conventional manufacture processes. The next section focuses on the FFF process, which is the AM process used and adapted in this research.

2.3 Fused Filament Fabrication (FFF) Process in Additive Manufacturing

2.3.1 Introduction to Fused Filament Fabrication (FFF) Process

The 3D printing technique deployed in this research is the extrusion-based Fused Filament Fabrication (FFF) process, since theoretically [28] the technique is capable of processing continuous fibre combined with thermoplastic matrix material. The FFF process is one of the most popular AM methods because of its low cost and high production rates [45]. FFF is a filament-based technology where a temperature-controlled head can extrude a thermoplastic material onto a substrate layer-by-layer (see Figure 2.5). It uses the following method to extrude the thermoplastic filament: the filament is heated into a semi-liquid in the nozzle and when softened, extruded onto the substrate layer-by-layer where layers are fused together and become the final parts after solidification [46]. The printability of FFF filaments depends on their melt viscosity and shear rate [47], two important variables in study of the flow of melted polymers and soft material. Therefore, the rheological properties of the polymer (matrix) are important factors determining the size of the processing window. Consequently, the strength of the FFF printed parts depends on rheology and heat transfer during the printing [48].

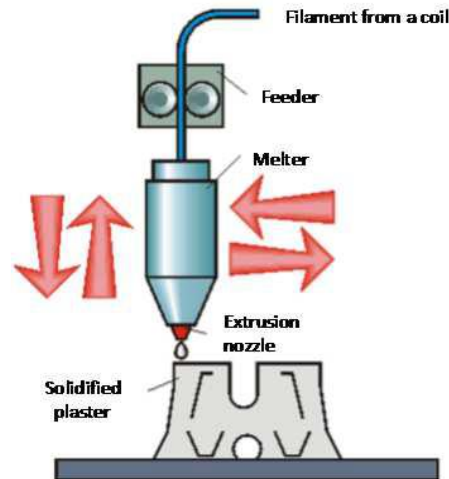


Figure 2.5:Fused Filament Fabrication. From [12]

The FFF process itself has several advantages such as low cost, fast printing speed and operating simplicity; it potentially allows diverse materials to be deposited simultaneously by means of setting up the FFF printer with multiple extrusion nozzles fed with different materials. This means the printed parts can be designed to have a multi-functional composition. On another hand, the disadvantages associated with FFF printing restrict its current applications [46]: First of all, the limited range of the feedstocks available form a limitation. The printing material has to be formed into a filament in order to be extruded, hence, when printing composites, it is difficult to disperse reinforcements homogeneously and remove the voids formed inside the composites filament during the fabrication. Secondly, the choice of potential types of thermoplastic polymer for use as the matrix material is limited by the need for their molten viscosities to lie within a feasible range. The viscosity of the molten material should be high enough to resist deformation due to gravitational forces while also being low enough to enable extrusion. And thirdly, it can be very difficult to remove the support structure used during printing. Other disadvantages include the limitations of the 3D printed parts themselves. Currently, rather than being used as functional components, most of the 3D printed polymer products are used as conceptual prototypes. For instance, the neat polymer parts built by 3D printing fall short of the requirements for predicted strength

and process repeatability. The process outcome cannot achieve reliable load-bearing parts. Such drawbacks currently also restrict these FFF printed polymers for application in industry [46].

The temperature of the printhead's nozzle is one of the most important process parameters for this printing process. The print temperature should be set at a point sufficiently close to the material melting temperature (T_m) point to enable controlled deposition. The temperature is used to control the viscosity of the material to ensure the material can be extruded without just flow out of the nozzle. So the polymer being extruded should turn soft but not melted into liquid.

Several process parameters influence the printed part's quality. Sood *et al.* [49] discussed the effect of processing parameters on FFF printing. The five important process parameters in their discussion comprise layer thickness, orientation, raster angle which is the angle of the raster tool path with respect to the x-axis of the build plate when material is deposited [50], raster width and layer height. These parameters determine the tensile, flexural and impact strength of the test specimen. Research on AM chiefly focuses on improving the mechanical properties of printed components, but sometimes also on thermal properties by optimising the above-mentioned input parameters. The above parameters can interact with each other and results in the printed material having a range of possible properties. This interaction interdependence increases the complexity when optimising the process. The parameters identified here, along with others, will be discussed in further detail in the following sections.

2.3.2 Printing of PEEK

There are several reports of using AM for the production of PEEK parts. Selective laser sintering (SLS) is the most popular AM technology for fabricating PEEK [51, 52], but, due to the lower costs, easier use and higher production rate, FFF printing of PEEK and PEEK composites parts has enjoyed increased popularity in recent years [53]. In 2013, PEEK was first reported to be FFF

printed by Valentan *et al* [54]. PEEK is a difficult polymer to print due to its high melting temperature and high viscosity compared with other easier polymers such as polypropylene (PP) and acrylonitrile butadiene styrene (ABS) [54-56]. Reports [51, 53] have shown that FFF PEEK printing could cause excessive thermal stress and cracks compare with polymers which are easier to process with FFF printing, such as PLA which has a lower melting temperature, and ABS, which does not have semi-crystalline properties. Yang *et al.* [57] and Wu *et al.* [58] compared the mechanical properties of FFF PEEK printed parts and parts manufactured traditionally using injection moulding, and found a lower mechanical strength for FFF printed parts. This proved to be limited by the processing conditions. Several investigations [55, 59, 60] have shown that when the printer chamber is above 150°C , the warping and layer delamination of the 3D printed PEEK parts are reduced by the thermal stresses resulted by high printing temperature. These indicate that by setting up the chamber temperature above the glass transition temperatures (T_g) of 143°C can lead to high performance PEEK printing, although the numbers of these high temperature printers are still limited and are considerably more expensive than the standard FFF printer [61]. These issues form significant challenges for the adaption of the FFF printing of PEEK on a large scale. The details of PEEK material properties will be reviewed in Section 2.4.2.

2.3.3 Printing of Fibre Reinforced Polymers

2.3.3.1 Setting the Rationale

For the printing of polymer composites, FFF based 3D printers are most commonly used [45]. Much of the earlier academic research has been focussed on the printing of short-fibre composites, since these are significantly easier to print than long and continuous fibre composites. Since fibres are the primary material to carry the load in the composites, the mechanical properties of composites can be improved significantly by maintaining fibre continuity in the structural design and the manufacturing process. Similar to the printing of unreinforced polymers, when 3D printing technology is applied in the production

Chapter 2 Literature Review

of composites parts, the advantages of utilising these materials includes their high effective production, low cost and ease of complex geometry customisation, augmented by the high performance of the composite material [1]. The majority of the publications on FFF with composite materials focus on comparison of the fibre reinforced polymers with unreinforced polymer material printed parts. In terms of papers on FFF printing using fibre reinforcement material, there are publications on polymers reinforced with short fibres [62-78], fibrils [79, 80], nanofibres [81, 82] and continuous fibres [29-33, 83-88]. Usually, the matrices are Nylon, polylactic acid (PLA), ABS, polyphenylene sulphide (PPS) and polyetherimide (PEI), though some publications report on epoxy resin matrices [70, 74, 78]. These matrix materials have low melting temperatures or glass transition temperatures. Table 2.2 lists the processing temperatures of common FFF filament.

Table 2.2: Processing temperature of common FFF filament material [25]

| Filament | Melting Temperature (°C) | Glass Transition Temperature (°C) | Print Temperature (°C) | Bed Temperature (°C) |
|-------------------|---------------------------------|--|-------------------------------|-----------------------------|
| ABS | (-) | 105 | 210-250 | 50-100 |
| ASA | 136 | 100 | 240-260 | 100-120 |
| FEP | 260 | 80 | 205-250 | 75 |
| Glow-In-The-Dark | 111.57 | (-) | 215 | No heated bed needed |
| HIPS | 180 | 100 | 210-250 | 50-100 |
| Lignin (bioFila) | (-) | 50-100 | 190-225 | 55 |
| nGen | (-) | 85 | 210-240 | 60 |
| Nylon | 220 | 47-70 | 220-260 | 50-100 |
| PC-ABS | 240-280 | 147 | 260-280 | 120 |
| PEEK | 343 | 143 | 400 | 150 |
| PEI | 354-399 | 217 | 340-380 | 180-200 |
| PET (CEP) | 260 | 67-81 | 220-250 | No heated bed needed |
| PETG (XT, N-Vent) | (-) | 80 | 220-235 | No heated be needed |
| PETT (T-Glase) | (-) | 81 | 235-240 | No heated bed needed |
| Polycarbonate | 155 | 147 | 270-310 | 90-105 |

Chapter 2 Literature Review

| | | | | |
|----------------------|---------|-------|---------|----------------------|
| PLA | 130-180 | 60-65 | 180-230 | No heated bed needed |
| PLA Metal | 130-180 | 60-65 | 195-220 | No heated bed needed |
| PLA Carbon Fibre | 130-180 | 60-65 | 195-220 | No heated bed needed |
| PMMA, Acrylic | 160 | 105 | 235-250 | 100-120 |
| POM, Acetal | 183 | -30 | 210-225 | 130 |
| PP | 173 | -10 | 210-230 | 120-150 |
| PVA | 200 | 80 | 180-230 | No heated bed needed |
| Sandstone (LAYBRICK) | 160 | (-) | 165-210 | No heated bed needed |
| TPU | 190-220 | -44 | 225-235 | No heated be needed |
| Wax (MOLDLAY) | 170 | (-) | 170-180 | No heated bed needed |
| Wood | (-) | 60 | 195-220 | No heated bed needed |

To date, there have been many investigations into the manufacture of 3D printed parts from carbon fibre reinforced polymers, however, there are not many publications on the application of PEEK as the matrix material. Impossible Objects Inc (Illinois, USA) [89] first announced its ability to manufacture high performance carbon fibre reinforced PEEK filaments according to Wang *et al.* [46], and it patented its manufacturing method for carbon fibre reinforced PEEK [87], but this technology is not reported widely in other publications. Stepashkin *et al.* [1] reported the successful 3D printing of continuous carbon fibre reinforced PEEK matrix composites with fibre volume fraction of 5% with the co-extrusion approach. The work presented by Stepashkin *et al.* [1] focussed on the investigation of thermal properties of the printed parts. It proved more difficult to FFF process the neat PEEK compared with other commonly used FFF polymers, since the thermal conductivity is lower than many polymers, the processing window is generally small, and PEEK has a high melting temperature. Processing fibre-reinforced PEEK material is

therefore likely to be even more difficult. All these reasons kept the fibre volume fraction low in the research of Stepashkin *et al.* [1].

2.3.3.2 Short Fibre Printing

In short fibre reinforced polymer composites FFF printing, the polymer material usually takes the material form of pellets, which are mixed with the short fibres in a blender before being delivered to an extruder to be fabricated into the FFF filaments. Subsequently, a second extrusion process will be conducted to ensure a homogeneous fibre distribution [34]. As stated in the beginning of this section, the performance of short fibre reinforced material is significantly lower than that achievable with continuous fibre reinforcement. However, as its mechanical performance is significantly better than unreinforced polymers that are used as the matrix material, it has been used for the development of large-scale 3D printing applications, often in the form of composite tooling, which requires materials with better properties than pure polymers to achieve the required manufacturing quality. In aerospace, large-scale 3D printing can print replacements for tooling as a single part, saving lead and assembly time, and reducing material waste compared to traditional manufacturing methods. Bell Helicopter (Texas, US) [90] 3D printed large blade tooling by Large Scale Additive Manufacturing (LSAM). This technology reduced the tooling manufacture time from months to days [91]. A similar manufacturing technique has been developed and patented by Oak Ridge National Laboratory (ORNL) (Tennessee, US) [92]. Their technique, Big Area Additive Manufacturing (BAAM), has been applied in the construction [93] and automotive [94] sectors. Both BAAM and LSAM rely on the extrusion of thermoplastic beads (with fillers) using a screw extruder and compacting the deposited material with a compaction mechanism [95].

2.3.3.3 Long Fibre Printing

The manufacturing of continuous fibre reinforced polymer (CFRP) under FFF is challenging. Studies show that the process parameters influence the impregnation quality of the printed parts during the manufacturing [96]. The

Chapter 2 Literature Review

FFF process for CFRP composites is a development of the FFF process for fabricating unreinforced plastic materials. After adding fibre reinforcements, it is essential to optimise the process parameters to achieve a good printing performance (quality) in terms of complete bond between layers and fibres. Several investigations have been carried out on continuous fibre reinforced FFF. For instance, Klift *et al* [29] were using a commercially available Mark One printer from Markforged, Inc (Massachusetts, USA) [97] and conducted to evaluate the mechanical properties of CFRC printed parts. The printed part was a sandwich panel consisting of a CFRP core and nylon polymer skins at the top and bottom. Dual printheads were employed to print the CFRP and extrude the nylon independently. Although studies of FFF printing of CFRP have hitherto focussed on optimising the geometries and mechanical properties of the printed parts [1], a recent report on CFRP PEEK printing has also explored their thermal properties [98].

2.3.3.4 Summary

In summary, the matrices used for CFRP printing are usually low melting temperature polymers. There is some published work on the optimisation of FFF printing with a PEEK matrix, however, PEEK is still not commonly used as the matrix because of the difficulties in processing. The forms of the fibres utilised in CFRP printing includes both short fibres and continuous fibres. Research on short fibre printing is usually focussed on large scale printing, while research on continuous fibre printing is mostly focussed on improving the structural and thermal properties of the designed parts. The challenges for short fibre printing therefore mainly lie in improving the printing rate, while for continuous fibre printing increasing the fibre volume fraction and good matrix penetration of the fibres form the main challenges. Although there have been significant technical achievements, there are still many gaps in the fundamental understanding of the physical phenomena that occur in the process, and addressing these gaps could help with achieving improved quality of the printed parts [3].

2.3.4 Description of Elements of Extrusion-based AM Machine

2.3.4.1 Feedstock Production System

Two broad approaches have been employed to create a pre-impregnated feedstock for CFRP printing. These two approaches are co-extrusion and pultrusion. Figure 2.6 shows a schematic of the co-extrusion process. In the co-extrusion device, the thermoplastic polymer filament and the continuous carbon fibre bundle mix in the guide pipe through a heated nozzle at the entrance of an extrusion head. The fibres, impregnated by the molten polymer, and the matrix polymer itself can be printed simultaneously.

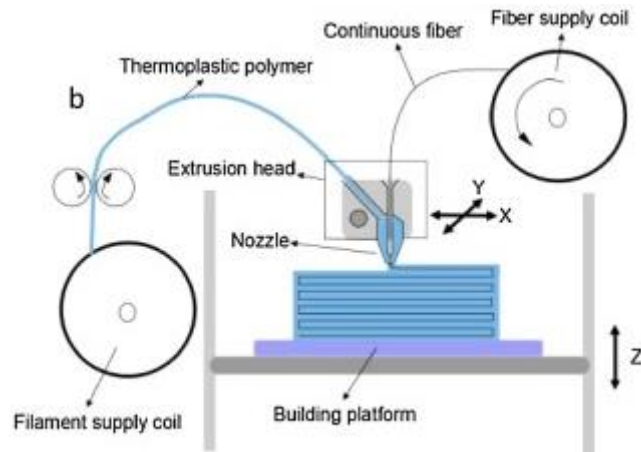


Figure 2.6: The schematic of a designed co-extrusion device to print continuous carbon fibre reinforced polymer [30]

This type of in-situ fibre impregnation was used in the printing of continuous fibre-based polymer composites in a number of studies [28, 31, 32]. In terms of the improvement in mechanical properties of printed CFRP compared with the unreinforced matrix material, Matsuzaki *et al.* [31] reported that for the 3D printed continuous carbon fibre reinforced PLA composites, the tensile modulus was 19.9 (± 2.08) GPa and strength was 185.2 (± 24.6) MPa, which are respectively 599% and 435% of the tensile modulus and strength of the neat PLA specimens. This is a much larger mechanical improvement compared to that achievable with short fibre reinforced PLA composites. However, irregularity and fibre discontinuity was still observed. Moreover, although the

Chapter 2 Literature Review

mechanical properties of composites show considerable improvement compared with those of the neat polymer printed parts, the improvement is still lower than the calculated theoretical value from the rule of mixtures [29, 31].

During the printing of CFRP, Li *et al.* [33] conducted similar experiments to Matsuzaki *et al.* [31]. Li *et al.* found that the increase in flexural strength of the sample was limited to 59 MPa or an increase of 11.3%, which was because of poor adhesion between the PLA and carbon fibres. Based on the report by Yu *et al.* [35] regarding the weak bonding interface between the PLA resin and the carbon fibres, in the second part of their investigation Li *et al.* [33] applied carbon fibre surface modification before the printing to improve the interfacial strength, and achieved a flexural strength improvement of 164%.

Rietema [36] investigated glass fibre reinforced polypropylene material in terms of their suitability for continuous fibre FFF. A feedstock material consisting of a commingled yarn of E-glass and polypropylene filament was investigated. After consolidation, the theoretically realisable compacted diameter was achieved. Building on Rietema's work, Vaneker presented a pultrusion apparatus [37] for pre-processing commingled yarn using a brass die with a central hole of a calculated diameter. This apparatus is shown in Figure 2.7. The heated die, shown top left in Figure 2.8, is shown from another angle in a detailed photograph of the heat die found in Figure 2.8. In the pultrusion mechanism of Figure 2.7, the processed yarn is stored on another, larger spool so it can be used as feedstock for subsequent use in the 3D printer.

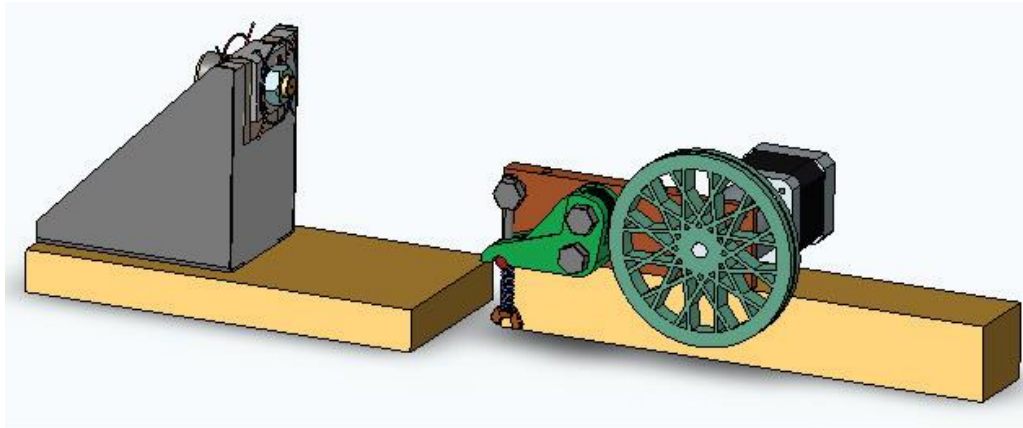


Figure 2.7: Pultrusion mechanism for the commingled yarns of E-glass and polypropylene filaments production, source: [37]

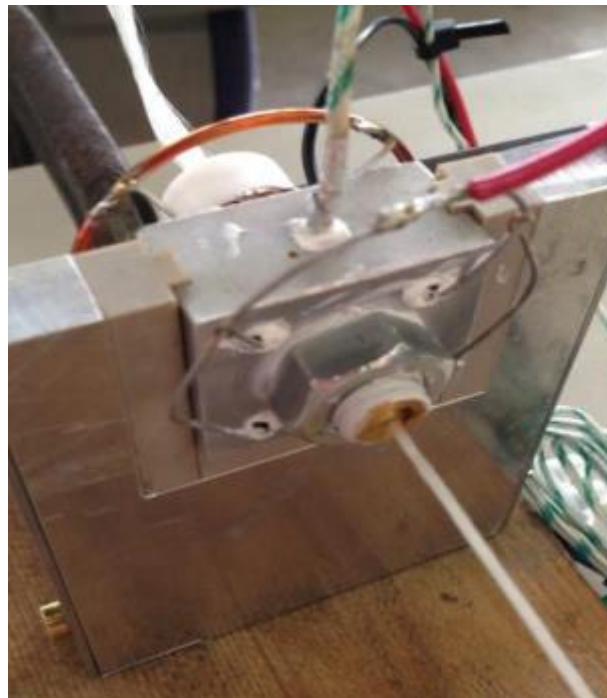


Figure 2.8: Detailed view of the die in the heater with the commingle yarn entering from above and the filament leaving at the bottom for the commingled yarns of E-glass and polypropylene filaments production [37]

Eichenhofer *et al.* [38] presented a process where the 3D printing was combined with customized extrusion. The printhead combined the pultrusion and extrusion processes so that the commingled yarns could be printed directly. The process was named Continuous Fibre Lattice Fabrication (CFLF), and Nylon-12 was utilized as the matrix. The schematic and the prototyping machine are shown in Figure 2.9.

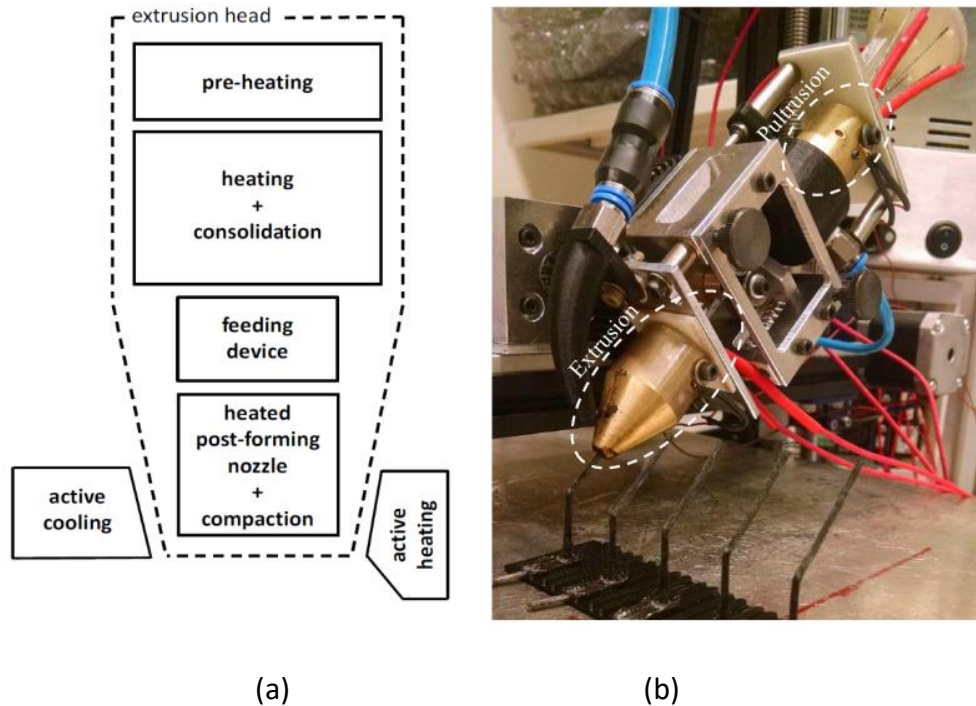


Figure 2.9: (a) Schematic illustration of CFLF processing head, (b) CFLF prototyping machine [38]

Based on preliminary investigations of the thermoplastic commingled yarns [39-44], the speed of the extrusion, outlet die diameter and temperature were found to be the process parameters to have a main influence on the laminate quality. After manufacture, the resulting pultruded material was cut into short rod specimens and analysed with optical microscopy to determine their morphology and the void content. From the analyses of these specimens, an ideal processing window for the CFLF extrusion process of continuous fibre composites material was defined.

2.3.4.2 Liquefier, Printhead and Gantry

In the development of AM-based systems, some attention has been paid to the development of the HotEnd [99] extrusion process. In the extrusion-based AM process, the HotEnd is also known as the liquefier, since it is the device to heat up the thermoplastic feedstock to the target temperature and soften it into an extrudable state [100]. The HotEnd is usually mounted on a motorized gantry, driven by a numerically controlled stepper motor to generate a prescribed speed pattern, as shown schematically in Figure 2.10. Every time a

layer is completed, the HotEnd moves to a controlled height (in some cases, the substrate moves down to that controlled height), and starts to deposit the next layer [100].

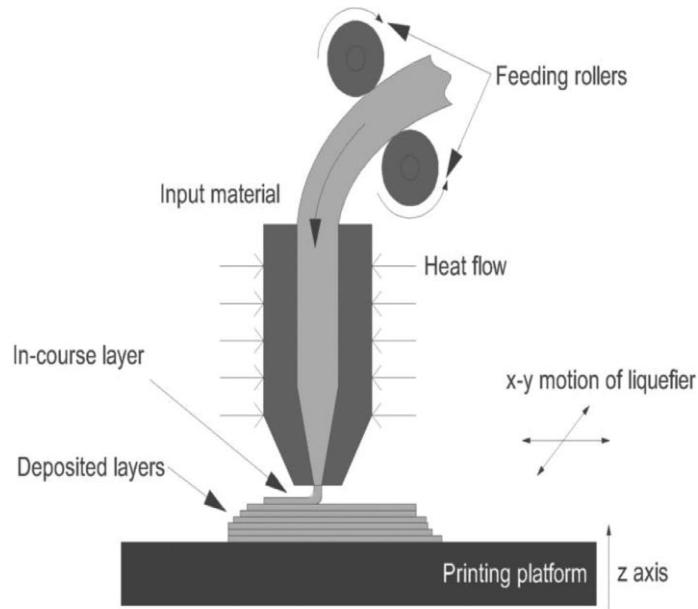


Figure 2.10: Schematic of a liquefier representation in the Fused Filament Fabrication process [100].

Investigating the thermal behaviour of the HotEnd can enhance the accuracy of the temperature control of the material during the printing process [101, 102], and improve the quality of 3D printed parts.

The FFF system's thermal process mostly takes place at the HotEnd. The HotEnd heats the material to attain the desired viscosity, such that the extruder can extrude it onto the print bed. For the design of the HotEnd, its thermal capability must meet two conditions [100]. Firstly, the temperature at the exit of the HotEnd, which is the nozzle, must be kept at a constant temperature to guarantee the material flow whilst preventing nozzle blockages. Secondly, there must be a temperature gradient along the HotEnd axial direction to ensure its entrance temperature is low enough to keep the incoming unsupported feedstock material solid. Based on these two requirements, multiple studies have been conducted to understand the thermal behaviour of the HotEnd [100, 103-105], more details of these analyses can be found in Section 2.3.4.

2.3.4.3 Temperature Control Platform

The temperature control is found to be a critical factor that needs to be considered during the functional design of a HotEnd. The accuracy of the temperature control plays an important role for the FFF printed material. There are mainly two reasons:

- The final mechanical properties of the 3D printed parts are proven to be highly dependent on the bond strength between the deposited filaments. [106-109].
- Warping deformation observed of FFF printed parts was found to be caused by the thermal stresses originating from the hot extrusion of the materials [110-112].

2.3.5 Process Analysis

Bourell *et al.* [113] described how one major factor hindering the future growth of AM in general is the limited understanding of the science of AM extrusion-based process. Figure 2.11 shows a detailed view of the FFF process. The essential modelling of the FFF process includes flow and fibre orientation, bond formation, and solidification behaviour. The following sections will review the modelling of each of these main process elements.

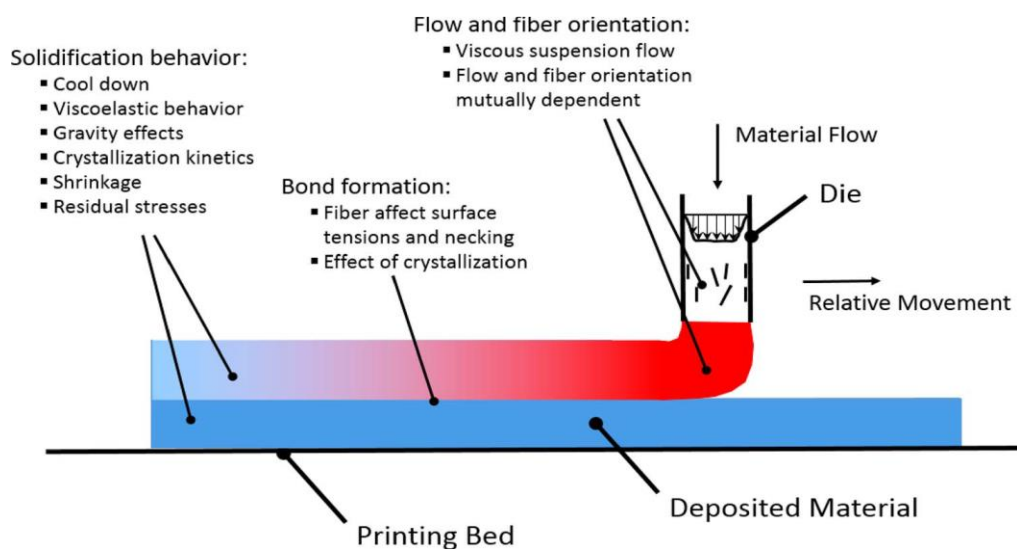


Figure 2.11: FFF process illustration and its related physical phenomena [3].

2.3.5.1 Flow and Fibre Orientation

The modelling of flow and fibre orientation are generally applicable to short fibre composites rather than to continuous fibre composites in FFF printing. Much of the effort on the FFF printing of composites has focused on short fibre composites since they have been proven relatively straightforward to achieve a high deposition rate compared with continuous fibre composites. For continuous carbon fibre FFF printing, there is still an issue that fibres are easily broken due to the shear stress limitation [114]. One of the first publications on this aspect was by Bellini [115], who modelled the pressure drop in the nozzle, and resulting different printed bead shapes before and after deposition on the print bed. Since there is heat transfer from the material during heating, the print speed and temperature of the material during the deposition were taken into account. Ramanath *et al.* [116] modelled the 2D flow of PLA in the liquefier using ANSYS© (Pennsylvania, US) [117], a commercially available Finite Element Analysis (FEA) software package. They compared the mathematical model with the experimental pressure drop and found a reasonable correlation. They also extended this work and investigated how the flow behaviour changes with varying the nozzle diameters and exit inner angles [118]. Another example of modelling using analysis was by Nikzad *et al.* [119]. Iron powder reinforced ABS material was used in this research. The 2D and 3D models of the flow through the HotEnd were established taking variations in the temperature, velocity and the pressure drop at the exit of the nozzle into account. This model optimised the printing parameters to obtain the best quality of the composite parts. In the work described in Ref. [120], three nozzle geometries, convergent, straight and divergent were investigated to see how these affect the fibre orientation for different extrusion rates and fibre volume fractions. Carbon fibre reinforced PEI material was used and the software Moldflow© [121] was utilised. In Folgar *et al.* [122] the Folgar-Tucker equation was implemented to study the fibre orientation. However, this paper only investigated the effect of the nozzle geometries on the fibre orientation, but did include the fibre alignment in more upstream regions. Heller *et al.* [123-

[125] in a series of publications investigated the swelling effects on fibre orientation after the fibre reinforced ABS material exits the nozzle during the FFF process. In their initial publication [123], COMSOL® [126] was utilised to model a Newtonian fluid and velocity field to analyse the flow in the nozzle. These results helped to compute the fibre orientation using the Advani and Tucker orientation tensor approach [124]. From these studies, it was observed that the die swell effect subsequently reduced the high fibre alignment in the region near the exit where materials stayed in the nozzle. Heller *et al* [124] investigated the effect of nozzle geometry on material flow, they also studied how die swell affects mechanical properties based on the fibre orientation changes, and how the geometry of the nozzle affects the fibre orientation. Finally, in their computational study on the deposition flow [125], they used COMSOL® [126] to establish a 2D planar model and considered deposition onto the printing bed. The above researchers all assumed the polymer to be a Newtonian isotropic fluid. The flow models do not account for anisotropic flow properties, this leads to lower fidelity in the prediction of the fibre orientation state. Also, the current modelling approaches require a great amount of detailed inputs, and are computationally expensive. There is a need to simulate the anisotropy in flow of the FFF process and also a need to establish computationally less intensive yet accurate modelling tools.

2.3.5.2 Bond Formation

Inter-filament bond formation, which is also called weld formation in some papers, e.g. [127], deals with the interface properties between filaments during the printing process. Note here that some studies consider that welding is actually the last stage of the bond formation [128]. It has a great influence on the mechanical properties of the final printed parts [129]. Some other publications consider the bond formation to happen between two beads when the material comes out from the nozzle. Thomas and Rodriguez [107] are among the first authors to investigate the fracture strength between two extruded beads. In their research, a 2D heat transfer model was developed to predict the local thermal histories of the weld zone, which in this case, was

taken as the interface between two beads. According to this model, the fracture strength was developed at a high temperature when the polymer is in a molten stage. A decrease of the cooling rate could also increase the bond strength. Sun *et al.* [106] investigated the bond formation between two beads during the FFF process. In Figure 2.12 one can see that when two beads develop a wetted contact region in the molten stage (1), a further connection started to establish. During the stage the “neck” grows (2). Bond formation occurs once the polymer chains diffuse through the interface (3).

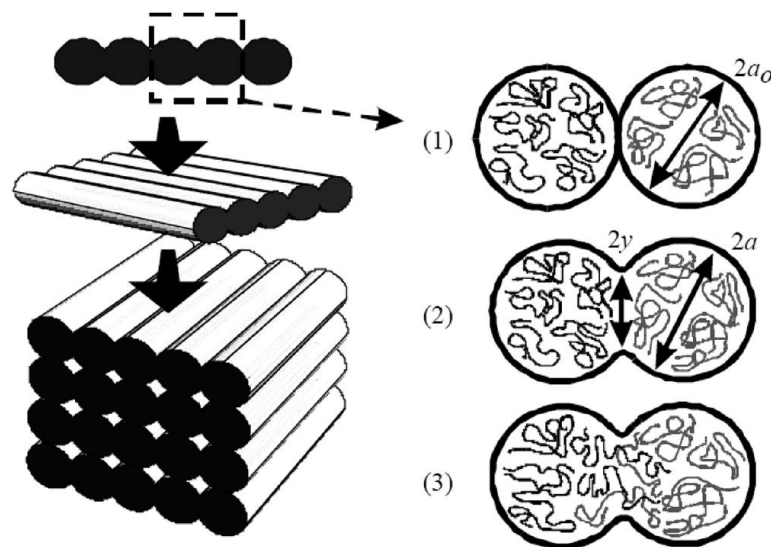


Figure 2.12: Bond formation illustration during process between two adjacent filaments [106].

The majority of studies of bond formation in the FFF process used ABS. In the research by Bellehumeur and co-workers [109, 130, 131], a Newtonian polymer sintering model was first developed [130], then it was applied to model the neck growth in the bond formation of ABS during the FFF process. Later, a lumped capacity heat transfer model [131] was used for temperature prediction when printing. However, the limitation of this sintering model was that it only describes the wetting between beads, and it was only able to predict the fracture strength. The authors found that the necking process between the beads happened above the defined weld temperature. In other words, the bond process took place above the weld temperature; the authors also found there was no complete bond formation due to the fast cooling rate

during the FFF process. In a related work with ABS, Sun [128] investigated the same topics. He predicted the degree of welding using a non-isothermal diffusion model. In this work, the welding process was considered to be the last stage of bond formation. However, it was not easy to predict the bond strength with this model due to the sensitivity of the material to temperature. Later work of Sun *et al.* [106], focused on investigating the effects of changing the extrusion temperature and it was found that there was a strong relationship between temperature history and bond strength. In particular, decreasing the cooling rate could enhance the strength. At this point, the sintering temperature was confirmed to play a critical role. Based on this sintering model, Gurralla and Regalla [132] extended this model with spherical particles to be applied in a cylindrical geometry. With validation from experimental data, the extended model could predict the bond strength based on the computed neck growth.

There are other studies on improving the bond strength focused on the processing. Kishore *et al.* [133], conducted research on ABS filament, using additional heat to re-melt the already laid down material before the deposition of the next bead. In that work, fibre reinforced ABS material was considered, and infrared pre-heating was applied to heat the extruding material. It was found the infrared pre-heating could improve the bond strength, however, at the same time, degradation of the material reduced the strength. Ravi *et al.* [134], investigated in-process laser pre-heating, when printing with ABS. They reported that the bond strength improved by 50% compared with the strength without the laser pre-heating. This demonstrated that an elevated interface temperature could promote fusion between two beads.

Although there are several experimental investigations on bond formation during the FFF process, no modelling work has yet been reported on the effect of the fibres on bond strength for the case of fibre reinforced feedstock. Additionally, since no polymer chains penetrate the fibres during the FFF process, more constraints are created in the modelling since some parts of the polymer will not have the chain interdiffusion. The polymer bond to the fibre still

needs to be understood more. The fibres can also affect the thermal properties of the matrix in the printing material filament, which in turn may change the temperature history. In reports of the thermal conductivity of carbon fibre reinforced polymers, it is shown that the thermal properties are dependent on the carbon fibre direction and the fibre volume fraction [135, 136]. In the case of a semi-crystalline polymer, there will be an initial crystallisation reaction and further neck growth with the interdiffusion. Hence, more details will need to be considered in the modelling than when modelling an amorphous material such as ABS. There are still many needs for fundamental research into the formation of bonds within the FFF process.

2.3.5.3 Solidification Behaviour

Existing research into solidification behaviour has concentrated on the unreinforced polymers. Yardimci and Guceri [101] published some of the earliest research on the solidification behaviour of two beads during the FFF process. They initially built a 1D heat transfer model to estimate the bond of adjacent beads. In their second paper [137], they extended this 1D heat transfer model into a 2D quasi-steady model in order to model a continuous process. The model developed by Rodriguez *et al.* [107], studied bond formation as well as prediction of the bond strength between two beads. In an investigation similar to that of Bellehumeur *et al.* [109], Sun *et al.* [131], who are in the same research team, compared two models established by Bellehumeur *et al.* with experimental results and concluded that the 1D lumped capacity model provides a better fit for the material temperature subsequent to extrusion, while the 2D model has a better match at lower temperatures. However, neither of the models could predict accurately the full heat transfer process in the beads. Going further, Costa *et al.* [138] developed a heat transfer model to predict the thermal histories for actual printed parts. This was a way to establish a full solidification analysis of printed parts. In their paper, Costa and co-workers developed a Matlab® (Massachusetts, US) [139] model to describe the thermal contact between adjacent beads. In subsequent work, they described the implementation and the model structure in more

details. In this work, the authors were able to model the transient 3D temperature histories for parts with simple geometries by applying a 1D solution for each of the bead elements. In the work of Brenken *et al.* [140] COMSOL Multiphysics® (Stockholm, Sweden) [126] was used to implement a 2D heat transfer model coupled with a non-isothermal dual crystallisation model. This model predicted the crystallisation behaviour for a semi-crystalline, fibre reinforced polymer. Zhou *et al.* [141] used 3D analyses to model the behaviour of the printed materials using the thermal analysis platform of ANSYS (Pennsylvania, US) [117]. In this model, the latent heat associated with the phase changes, heat conduction and heat capacity were included. This model could show the temperature profiles for different times during the process. Costa *et al.* [142], using another approach, then presented their work with 3D extruded beads as well. This time, the model was coded in Matlab® (Massachusetts, US) [139]. Based on the results, the authors found that varying thermal resistances and the convection conditions were the most important factors for the heat transfer analysis. In a separate work, Pooladvand and Furlong [143] derived a model to predict the temperature profile for a printed cylindrical geometry. A recent paper by Brenken *et al.* [144] presented a crystallisation kinetics model and a melting model in Abaqus FEA to describe the re-melting phenomena. In summary, this existing solidification modelling, is trying to combine material behaviours with the thermal history analyses. Additionally, the modelling is extended from the 2D to 3D, and typically also includes bond formation modelling.

Residual stresses and part deformation resulting from the printing process are major factors in the part's final mechanical performance and have received considerable focus. Several papers [110, 111, 145-150] have investigated how these issues could be addressed by optimising the part design, machine design and the process parameters. However, the current models do not take into account the physics of semi-crystalline polymers. Even though, their mechanical properties are strongly dependent on the degree of final crystallinity reducing the accuracy of the prediction.

In summary, none of the developed models mentioned above could sufficiently predict the behaviour of bonding and solidification in continuous fibre reinforced semi-crystalline polymers in FFF. Hence, there is a need for fundamental understanding of the FFF process and polymer physics to establish these models.

2.4 Feedstock Material and Properties

2.4.1 FFF Thermoplastic Polymer Filament

Thermoplastic polymer materials such as ABS [151], PLA [152], and Polycarbonates (PC) [153] can be customized for FFF printing due to their low melting temperature. Nowadays, the 3D printing of polymers has been applied to manufacture complex non-load carrying lightweight structures in aerospace industries [154], small size study models in architectural industries [12], art, education [155], and as models to study tissues and organs in the medical field [68]. Due to the limitations of the manufacturing method, the majority of the 3D printing polymer products are still fabricated for prototyping rather than as functional components.

In this project, PEEK has been chosen as the matrix. As a semi-crystalline thermoplastic, PEEK has excellent mechanical and chemical-resistant properties for higher temperature applications than other thermoplastics currently used for FFF. In the aerospace industry, PEEK is considered as one of the best materials for airframe structures. One of the reasons for this is that it can provide significantly higher toughness with long-term resistance to fatigue. Additionally, at the end of its life, it can be recycled more easily compared to many other plastics, which makes the product life cycle more environmentally friendly. Another significant benefit is that PEEK composites show particularly high resistance to hydraulic liquid and fuel induced corrosion. For instance, the H160, a medium duty twin-engine civil helicopter manufactured by Airbus, already has a rotor hub made with PEEK resin matrix composites, because by

using this material, it potentially reduces the maintenance requirements of the main rotor hub in the helicopter. This technology was developed by Porcher Industries (Ecluse-Badinieres France) [156], and according to their report, this carbon fibre PEEK prepreg has already met the quality requirements for safety-critical applications and hence it received the green light for production by Airbus Helicopters [157].

2.4.2 Semi-crystalline Material Characteristics of PEEK

The repeat unit of PEEK (Figure 2.13) was found in the 1980s by Dawson *et al.* [158] with X-Ray technology. The repeat unit later enabled the ability to investigate the crystalline packing of the molecule as PEEK crystallisation occurs.

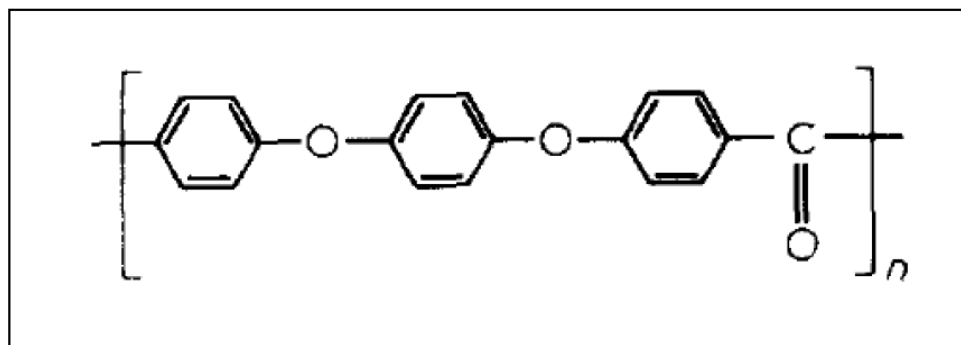


Figure 2.13: Repeat Monomer unit of PEEK [159]

Since PEEK is a semi-crystalline polymer, its stiffness depends strongly on the degree of crystallinity [9, 160]. Studies presented in Refs [161-163] show that in the process of both neat PEEK and CF/PEEK composites, slower cooling rates can increase the degree of crystallinity and therefore increase the tensile strength and modulus. By adjusting the thermal processing parameters [159, 164], it is possible to obtain a wide range of crystallinity fractions in the samples due to the crystallisation kinetics of PEEK. Thus, appropriate design of the processing conditions will allow PEEK parts with the maximum crystal fraction of 50% crystallinity [165].

Chapter 2 Literature Review

As in the literatures of Ref. [166], majority of the continuous fibre reinforced PEEK specimens were manufactured by layup and compaction of heated prepreg material with woven carbon fibre laminates (APC-2, with a CF volume fraction in the range of 59%-61%). Although the 57.4% fibre volume fraction as used for the experimental work of this thesis is close to the standard APC-2 grade, the material used in the experimental work is commingled yarn which is with different physical form of the APC-2. The fibre content used in this thesis is however the highest and closest to the industry standard APC-2 that could be obtained during this PhD project. In the discussion of this thesis, results are compared to the findings in the literature. In addition, the graphs presented Figures 2.14, 2.15 and 2.17 are with 30% CF volume fraction since they are the most detailed analyses available. These materials, according to the literatures, were also manufactured by layup and compaction of heated prepreg with woven fibre laminates. In the study of *Zhang et al.* [167], thermal decomposition of PEEK and PEEK-CA30 (CF/PEEK with fibre volume fraction of 30%) were investigated in both nitrogen and air environments, both of the results showed a two-step decomposition process, as seen in Figure 2.14 for the test under a nitrogen environment. Another study from *Perng et al.* [168] suggests, that, during the first decomposition step, scission of the main chain of the ether and ketone groups of the PEEK was the major pyrolysis mechanism, the ether group scission reaching the maximum value earlier than that of the ketone group. During the second decomposition step, a new structure with higher thermal stability contributes to form pyrolysates. As can be deduced from this, onset decomposition with PEEK occurred at around 575°C, and rapid significant mass loss occurred just below 600°C. Similar results were also found by *Hay et al.* [169]. Their work reported that there is a lower mass loss in the PEEK-CA30 material test. Additionally, in the test carried out in an air environment, PEEK-CA30 exhibited complete decomposition, including the carbon fibres, below 1000°C. The result shown in Figure 2.15 indicates that, in the second combustion step, the carbon oxidation contributes most to the thermal decomposition, since the reaction of PEEK-CA30 happens significantly earlier than PEEK-GL30 and unreinforced PEEK. Within this second step, the

decomposition took place at a slightly lower temperature for PEEK-CA30 than for both neat PEEK and PEEK-GL30 (PEEK with glass fibre volume fraction of 30%). So this means PEEK-CA30 was more readily oxidised than that the other two materials due to the reaction with carbon. In this work, it also pointed out the main products of the PEEK decomposition have been confirmed to be CO and CO₂.

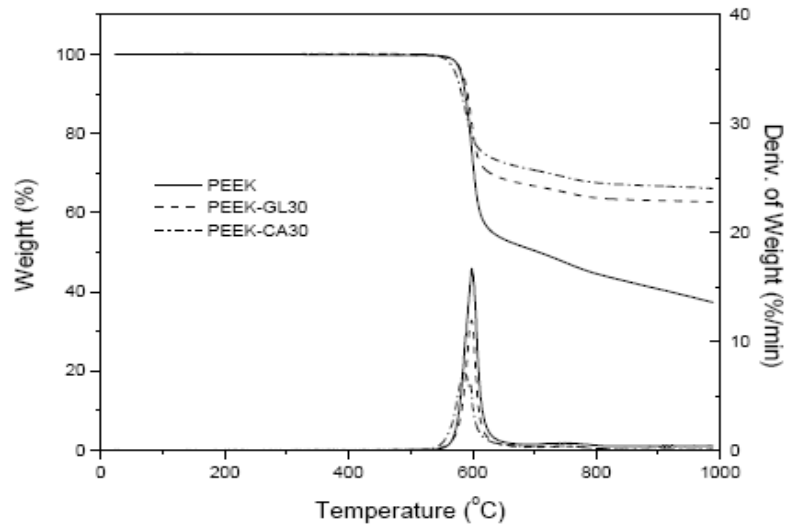


Figure 2.14: Thermal decomposition of PEEK and PEEK-GL30 and carbon-CA30 composites under nitrogen [166]

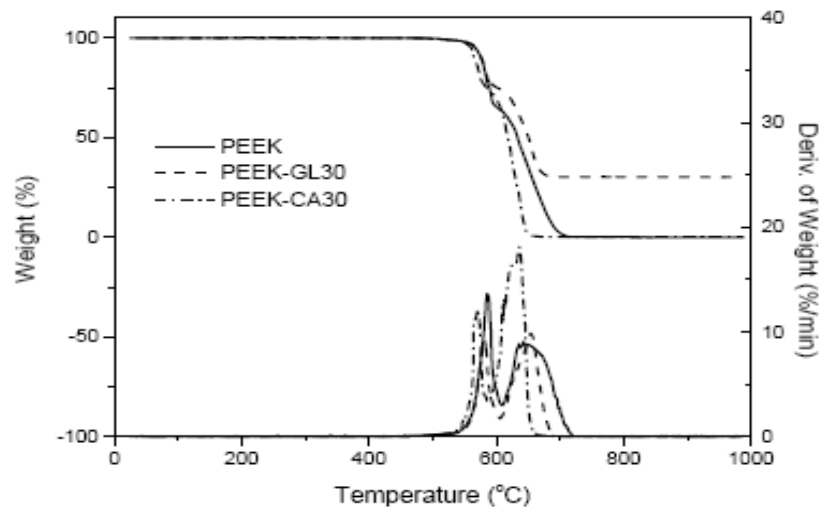


Figure 2.15: Thermal decomposition of PEEK and PEEK-GL30 and PEEK-CA30 composites in air [166].

Chapter 2 Literature Review

In summary, PEEK based material begin to decompose when the temperature is lower than 600°C. Carbon fibre is more thermally stable in nitrogen. However, in the air environment, a higher volume of PEEK can contribute to thermal stability as carbon oxidation causes carbon fibre-based PEEK to decompose at a faster rate in the air environment.

Herrod-Taylor [166] tested neat PEEK finely ground powder (150PF) and pellets reinforced with 30% weight percent short carbon fibre (150CA30) using differential scanning calorimetry (DSC) with the results being shown in Figures 2.16 and 2.17. He stated that the crystallisation of the material only happens between the T_g and T_m . All his materials were dried overnight at 120 °C in a vacuum chamber before the tests in order to minimise the influence of water absorption. In this test, the author varied the temperature and cooling rate and measured the onset temperature of crystallisation for both 150PF PEEK and 150CA30 CF/PEEK. From his results of 150PF PEEK, it was clear that the glass transition occurs at 175°C instead of 143°C, which is the accepted T_g of PEEK. The explanation for this phenomenon can be found in the later publication by Cheng *et al.* [170], namely that the crystalline and rigid amorphous regions constrain the molecular motion in the truly amorphous phase. Cheng *et al.* also found that in the temperature range of 380 °C to 410°C, a 2°C drop in temperature occurred when the crystallisation happened. This means the crystallisation absorbs energy and the degree of crystallisation of the PEEK only changes by a small amount when the temperature is above 380°C. In the non-isothermal crystallisation behaviour of 150CA30, above the melting temperature, the results were similar to those of neat PEEK in terms of crystallinity change, but additional nucleation of PEEK occurred at the fibre surface. Other studies as Peggy *et al.* [163] on the changes of crystallinity in neat PEEK all show similar results indicating that slower cooling rates can increase the degree of crystallinity as well as the tensile strength and modulus. Investigations on the effects of carbon fibre on the crystallisation of PEEK showed that carbon fibre acts an agent for the nucleation of PEEK on carbon fibre. Lee *et al.* [135] found that by increasing the carbon fibre volume fraction,

Chapter 2 Literature Review

the degree of crystallinity occurring during the solidification process decreased. Several studies [172-175] showed there was a high nucleation density of PEEK on the fibres when they are coupled together. In summary, reports show that when PEEK has a higher degree of crystallinity, when combined into carbon fibre composites, there is a significant property improvement [161, 162, 176]. The crystalline morphology, spherulite size, orientation and interface with the carbon fibres also affect the mechanical properties of the resulting composites [177-179].

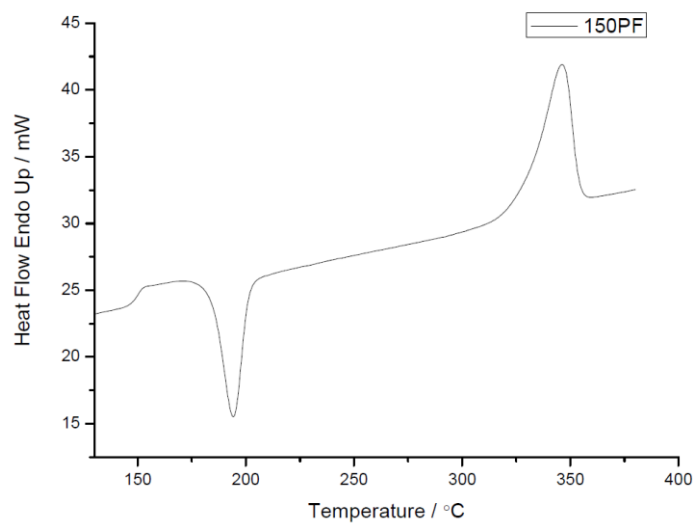


Figure 2.16: DSC heating scan of reprocessed amorphous 150PF PEEK [166].

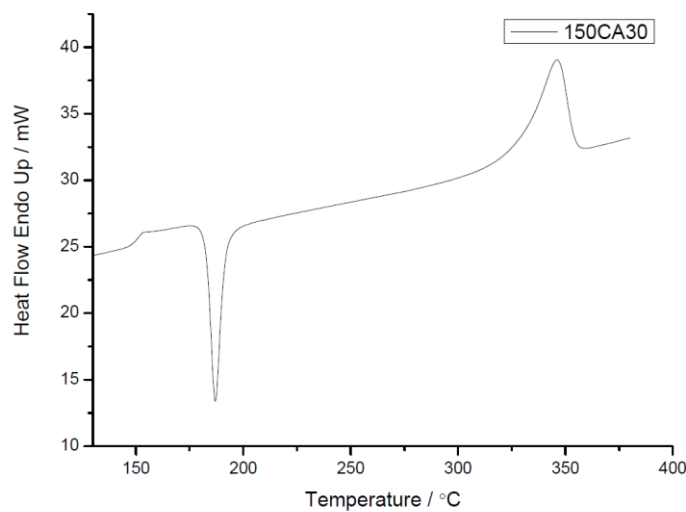


Figure 2.17: DSC heating scan of reprocessed amorphous 150CA30 PEEK [166].

In scanning electron microscopy (SEM) studies, Bassett *et al.* [180] and Blundell *et al.* [181] used SEM for studying the crystalline morphology of PEEK and carbon fibre reinforced PEEK. Blundell *et al.* [181] found that sheaflike crystal structures in the PEEK were formed when the nucleation density was high, and this limited the development of spherulites.

2.4.3 Carbon Fibre Reinforced Polymer Filament

Using the neat polymer as the processing material, FFF components usually lack the strength required for a load-bearing part. However, 3D printing of polymer composites may improve the mechanical properties of printed parts by combining the reinforcements and matrix to enhance the structural or functional properties [182]. There has been considerable scientific research effort focussed on the manufacturing of high-strength products and prototypes with 3D printed carbon composites. Because of the advantageous properties of carbon fibre reinforced PEEK, it is considered as a promising alternative to some metallic materials [183, 184].

However, 3D printing of composites with PEEK matrix and other advanced reinforced polymers is still technically challenging. PEEK, with its high melting temperature, forms a challenge for the FFF process. Arevo Labs (California, USA) [185] state they have solved this problem by optimising polymer formulations with an innovative extrusion technology in order to make it suitable for the FFF printing process [186]. But they have not proven the feasibility of producing carbon fibre with PEEK. Han *et al.* [187] reported using FFF to print carbon fibre reinforced PEEK composites for orthopaedic and dental application. The carbon fibre was formed into particles with a volume fraction of 5%. Their work focused on the improvement of mechanical properties and microstructures of PEEK and carbon fibre reinforced PEEK samples. MarkOne [97], reported as the first commercial carbon fibre 3D printer using continuous fibre, uses carbon fibre with a nylon matrix, however, this technology is not designed to be compatible with PEEK filament [98].

Increasingly, research is being carried out on the 3D printing of carbon fibre reinforced polymer (CFRTP). Various processing techniques have been proposed. These techniques include impregnation [184], mixing and extruding [65], and FFF [66]. The goal of this project is to print with CFRP in order to improve the mechanical properties of the composites parts by maintaining fibre continuity. It is more difficult to achieve 3D printing of CFRP with continuous carbon fibres, but the technology has been proven already for printing with PLA [28]. Prepreg material is chosen as the filament material in this project. This means that the feedstock are pre-impregnated composite fibres with polymer matrix.

In the design of fibre-reinforced plastic (FRP) parts, the fibres are orientated in a particular way as to carry the primary loads by following specially design fibre path. One can find a considerable amount of research work on fibre path design, but this is out of scope for this current project. Carbon fibres have been widely used for many years. They can be obtained by a wide variety of production methods. It has been proven that the carbon fibre has a high modulus of elasticity and a high strength, it has advantages of low weight, and high chemical resistance [188]. Carbon fibres are usually combined with other materials into composites, greatly increasing the mechanical properties, achieving very high strength-to-weight ratios. The aerospace, wind energy and automotive industries are the largest potential markets [157, 189].

2.5 Analytical Equipment

As already mentioned, when processing carbon fibre reinforced PEEK material, the carbon fibre does not undergo any phase changes, which means that only the rheology of the PEEK changes. However, the carbon fibre causes the thermal properties of the composites to differ from neat PEEK. Control of the temperature level and the heating and cooling rates are critical for the process to fit the process window of PEEK, allowing for the repeatable and structurally reliable manufacturing of components [190]. Analytical techniques such as thermogravimetric analysis (TGA) and differential scanning calorimetry (DSC),

both of which are forms of thermal analysis (TA), can help in understanding how the control of temperature at different stages of the process will affect the final quality of the 3D printed part, and aid eventual optimisation of the processing parameters. The scanning electron microscope (SEM) can help study the morphology of the PEEK and CF/PEEK. Other analysis methods, such as time-of-flight secondary ion mass spectrometry (ToF-SIMS) were utilised in this research after the CF/PEEK filaments were produced, to remove ambiguity in material identification in the cross-sectional views of the produced filaments. Thermography was used to record the temperature profile of the material, and indirectly record the temperature profile of the weld zone during the FFF process. Dynamic mechanical analysis (DMA) was used for the mechanical tests of the final printed parts in this research; although it does not provide the information on the strength, it measures the stiffness of the printed parts which can still contribute to the mechanical properties study.

2.5.1 Thermogravimetric Analysis (TGA)

Thermogravimetric Analysis (TGA) or thermogravimetry (TG) is a thermal analysis technique which can measure the amount and rate of change in the weight of a material as a function of temperature and time in a controlled atmosphere [191]. The TGA test can be used to understand the flammability and thermal decomposition properties of PEEK and CF/PEEK [2]. There are many TA techniques which can be used to investigate the combustion behaviour of PEEK based polymers and composites. These include oxygen bomb calorimetry (OBC) [192], microscale combustion calorimeter (MCC) [193], thermogravimetric/mass spectrometry (TG/MS) [168], pyrolysis gas chromatography/mass spectrometry (pyGC/MS) [194], a combination of TG/MS and pyGC/MS [195], and magic angle spinning nuclear magnetic resonance (MASNMR) spectroscopy [196]. However, TGA is the most popular TA techniques for this purpose [197].

According to reference [197], the normal commercial TGA apparatus can reach a chamber temperature up to 1000 °C. Different gases can be inserted, such

as nitrogen, helium, or argon; oxidising gases, for instance, air or oxygen, or reducing such as forming gas (8 – 10% hydrogen in nitrogen). During the TGA test, a polymer generally will show mass loss. Sometimes mass gain is also observed prior to degradation at low heating rates in an oxidising atmosphere. Mass loss may be attributed to various reasons during the TGA tests. A typical TGA instrument consists of a furnace, a thermobalance, a data acquisition device and a computer to analyse the data. The whole thermogravimetric analyser is a thermobalance, and it measures sample mass change as a function of temperature and time. Figure 2.18 is a schematic of TGA. Major factors affecting TGA results are listed in Table 2.3.

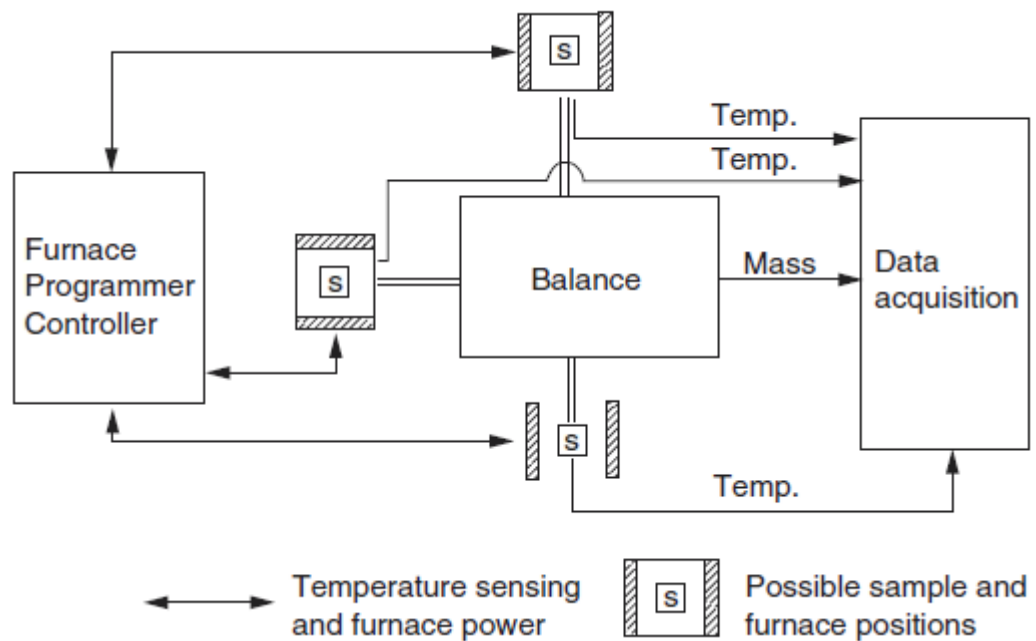


Figure 2.18: General components in a thermobalance [196].

Table 2.3: Major factors affecting TGA results [196]

| | |
|-----------------------------------|-----------------------------------|
| Mass | Temperature |
| Buoyancy and thermal expansion | Heating rate |
| Atmospheric turbulence | Thermal conductivity |
| Condensation and reaction | Enthalpy of the processes |
| Electrostatic and magnetic forces | Sample-furnace-sensor arrangement |
| Electronic drift | Electronic drift |

2.5.2 Differential Scanning Calorimetry (DSC)

Differential scanning calorimetry (DSC) is another popular thermal analysis techniques. It is a thermoanalytical technique that measures the amount of heat required to change the sample temperature. As described in Section 2.4.2, it is important to understand the crystallisation and crystalline state of PEEK in order to optimise the processing parameters, and maximise the mechanical properties of the final printed parts. DSC is one route towards gathering this information.

The DSC technique was developed in 1963 under Perkin-Elmer (Massachusetts, USA) [198]. DSC uses the technique that the difference of the heat amount affects the temperature of the test sample, and a reference is measured as a function of time [196]. Figure 2.19 shows a schematic of the DSC. The important analysis features in DSC include temperature, heat (consisting of heat flow, and latent heat), enthalpy, entropy, Helmholtz and Gibbs free energies, heat capacity, phase transitions, melting point and heat of fusion, crystallisation temperature, and glass transition temperature. The results from a DSC experiment are normally plotted as heat flow vs temperature, where a change in the curve can represent a thermal transition. For a semi-crystalline polymer, a peak in the curve typically represents the crystallisation. A step in the curve normally represents the glass transition or melting temperature. An example of a DSC plot showing a crystallisation peak temperature (T_c), glass transition temperature (T_g) and melting temperature (T_m) can be seen in Figure 2.20.

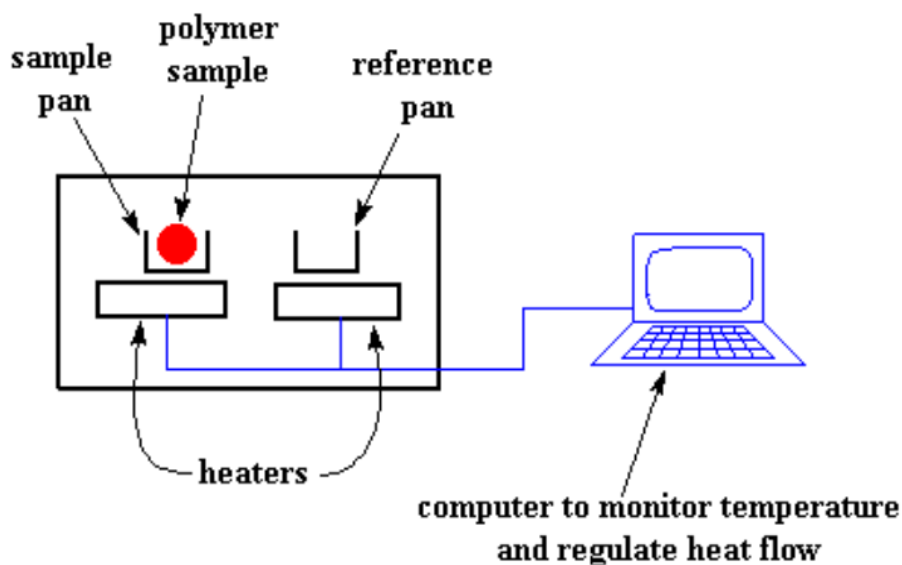


Figure 2.19: Schematic of DSC [199].

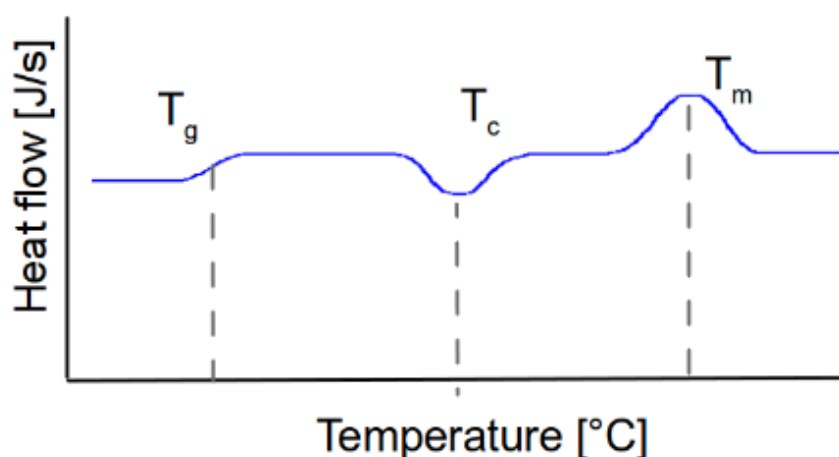


Figure 2.20: Example plot of a heat flow vs. temperature plot for a polymer that undergoes T_g , T_c and T_m . [200].

2.5.3 Scanning Electron Microscope (SEM)

Scanning electron microscopy (SEM) is widely used for studying the microstructures and morphology of materials. In the present research project, SEM was used to examine the morphology of the raw material before the FFF processing. In this thesis, only basic function of SEM will be introduced in this section.

Compared to studying a sample with a normal, optical microscope this technique is not limited by the depth of field and can produce a 3D image of the microstructure, and hence, produce images with more information and better resolution than optical microscopy.

Decrease the lens aberrations or increase the source brightness can improve the resolution in SEM [201]. Table 2.4 shows different electron sources as they were considered to lead the high-resolution SEMs since 1980s [202].

Table 2.4: Comparison of different electron sources at 20kV [202]

| Source | Brightness ($A/cm^2 sr$) | Lifetime (h) | Virtual source size | Energy spread $\Delta E(eV)$ | Beam current stability (%/h) |
|----------------------------|-------------------------------|-----------------|---------------------------|------------------------------------|---------------------------------------|
| Tungsten hairpin | 10^5 | 40-100 | 30-100 μm | 1-3 | 1 |
| LaB ₆ | 10^6 | 200- 1000 | 5-50 μm | 1-2 | 1 |
| Cold field emission | 10^9 | >1000 | <5 nm | 0.3 | 2 |
| Thermal field emission | 10^8 | >1000 | <5 nm | 1 | 2 |
| Schottky field emission | 10^8 | >1000 | 15-30 nm | 0.3-1.0 | ~1 |

2.5.4 Time-of-Flight Secondary Ion Mass Spectrometry (ToF-SIMS)

As the amount and variety of biomaterials dealt with in science has increased, there is increasing demand for better understanding of the materials' components, and hence for more advanced microscopy for the analysis of materials. This triggered the development of the time-of-flight secondary ion

mass spectrometry (ToF-SIMS) [203]. Not all types of material are suitable for ToF-SIMS test, but PEEK is one of them. PEEK has a property that it constitutes a very poor substrate for cell cultivation, and it is extremely reluctant to allow cellular adhesion. This property of PEEK allows a modified PEEK surface to be easily detected by ToF-SIMS for its biological responses [203]. Figure 2.22 shows the schematic of the dual beam ToF-SIMS process and apparatus. A primary ion gun sputters the secondary ions from the sample surface, which is called the “target” in the schematic. The sputtered secondary ion (SI) signals are extracted through the Time-of-Flight tube and the detector obtains the signal outputs information such as mass spectra, ion images, depth profiles and the 3D analysis. The advantages of ToF-SIMS among other surface characterisation techniques is that this method is highly sensitive to the molecular information such as molecular mass, and it is very restricted to the upper-most surface layers (0.1-1 nanometres) [171, 204]. For these reasons, ToF-SIMS is highly suitable for polymer surface analysis [205].

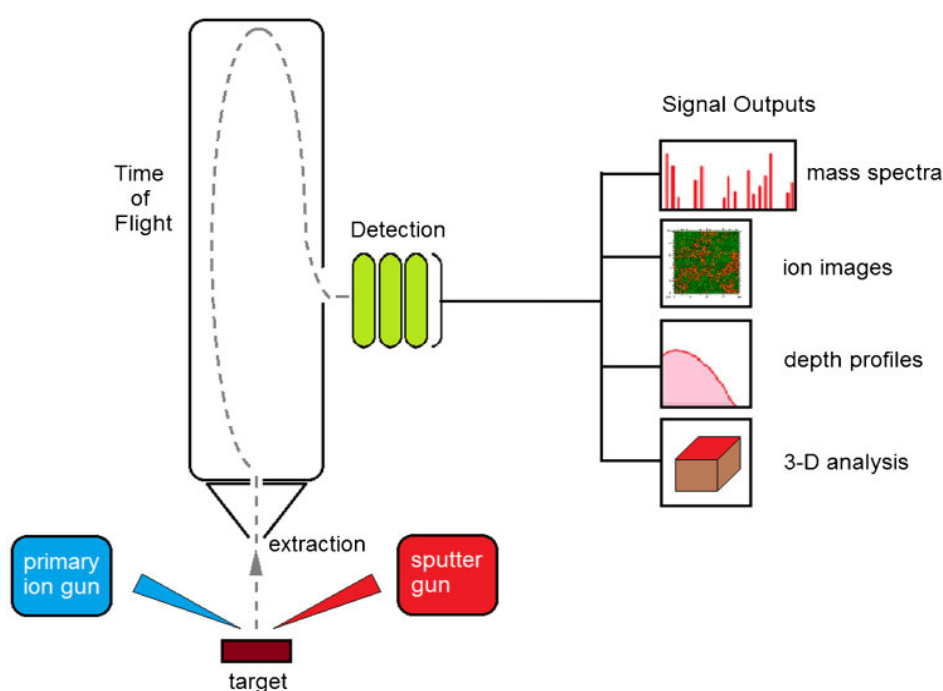


Figure 2.21: Schematic of the components of a dual beam ToF-SIMS instrument [203].

In the research of using this technique to identify PEEK constituents, in several studies PEEK samples were treated with oxygen plasma during the tests [206-

208]. Henneuse-Boxus *et al.* [209] combined X-ray photoelectron spectroscopy (XPS) and ToF-SIMS of chemically modified PEEK films for their tests. These experimental PEEK fragments data results from Henneuse-Boxus *et al.* [209] were used as a PEEK element reference data to the tests described in Chapter 5.

2.5.5 Thermography

Thermography is an in-situ thermal measurement technique that can be used for analysing the weld formation in the FFF process, see e.g. Seppala *et al.* [210]. As also mentioned in Sections 2.3.4 and 2.5.2, it is important to understand the polymer-polymer interface development in the FFF process window. For semi-crystalline material, crystallisation happens between glass transition temperature and crystalline melting temperature. In the AM process, it is unlike traditional polymer manufacturing, where more precise temperature monitoring and controlling are achievable. In the FFF process, the instantaneous temperatures are related to a complex control situation involving nozzle temperature, printing speed, ambient temperature, printing path etc. Hence, in order to establish accurate material temperature control during the FFF process, it is important to first understand how the temperature of the material varies during the printing process, then one can start to correlate the temperature and the material thermal behaviour with the properties such as the bond strength of the final printed parts. For polymer processing, during the heating up phase, the melting temperature holding time affects the viscosity and degradation rate [211], and the cooling rate affects the thermal residual stresses [212-214], which in turn affects the mechanical properties of the printed parts.

Using infrared thermography is one of the best ways to record such material temperature profiles during the printing. Seppala *et al.* [210] identified several reasons to select IR thermography. For instance, it is impossible to place a thermocouple in a flow of molten material with this level of viscosity, and usually FFF polymers have low thermal conductivity which can cause a low accuracy of the temperature measurement. Finally, when a polymer melts, it

can undergo local heating to a higher temperature by the dissipation of mechanical shear energy due to the high viscosity.

However, it is still quite difficult to get an accurate temperature during FFF by thermography. An infrared camera measures the emitted infrared radiation in the form of an image, but it does not measure the temperature directly. The temperature is then calculated as a function of the emissivity. Apart from the emissivity of the object, the measured radiation is also influenced by the reflected apparent temperature, the distance between the object and the camera, the relative humidity of the environment, and the atmosphere temperature [215].

In order to obtain a higher accuracy of temperature recording, instead of using the temperature as calculated by the IR camera software directly, Seppala *et al.* [210] carried out the temperature conversion using Planck's Law. Meanwhile, the reflection correction was applied by moving the heated nozzle without material extrusion, in order to subtract the reflected IR signals from the heated nozzle. This work led to another publication by the same team [127], wherein the weld formation of the material extrusion in additive manufacturing was studied.

2.5.6 Dynamic Mechanical Analysis (DMA)

Dynamic Mechanical Analysis (DMA) is a test that can provide the viscoelastic properties of polymers. It is not common to use DMA as the quantitative measurement for mechanical strength of the 3D printed part, as DMA only provides deformation in the elastic region. However, in this project, DMA was selected since the University of Nottingham does not have a universal testing machine able to deal with small sized samples.

DMA has proved to be a very useful tool for characterising transition temperature and viscoelastic behaviour of polymeric materials. DMA has also been used to test composites to determine their bulk strength properties [213]. Usually for these DMA tests of composites, the samples are heated so the DMA tests can provide not only the polymeric solid mechanical properties,

but can also provide information on the temperature dependent rheological properties. In the DMA test, an oscillatory (sinusoidal) input is applied to a sample, then the material strain and stress responses are measured, and the phase angle δ , which is the phase shift between the input and response, can be obtained [197]. Figure 2.23 shows a schematic of the DMA machine.

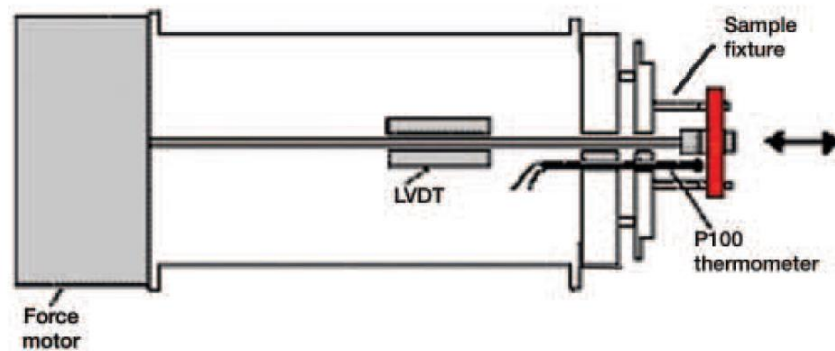


Figure 2.22: Schematic of the DMA 8000 analytic train [216]

The sample fixture is also the rotation analysis head. This rotational design, for instance, in DMA 8000 could permit several configurations for the tests. This fixture design enables 3-point bending, cantilever, compression, shear, and tension tests [217]. In this project, DMA tension test was selected (more details can be found in Chapter 6). Among the results of the DMA tension test, the storage modulus (E') is the modulus which provides the elastic response of the material. These data link in turn to the stiffness of the 3D printed parts.

2.6 Conclusion

In summary, unlike traditional manufacturing, AM provides more freedom to the designers, leads to less material wastage, and reduces the manufacturing processing time. Composite 3D printing, such as that of continuous fibre reinforced PEEK material, has great potential. However, in general, the manufacturing repeatability is still low. In composite FFF printing, there are many phenomena that are still remain poorly understanding. Initial investigations of composite FFF printing have been carried. However, the theoretical understanding of the process is still relatively immature. The

Chapter 2 Literature Review

methodology of combining experiments and modelling is the proposed approach to increase understanding of composite FFF printing to enable the process to be improved. The three main gaps in CFRP printing include:

- Lack of high volume fraction of carbon fibres in prints, especially in CF/PEEK.
- Lack of understanding of PEEK behaviour during FFF, as a semi-crystalline material and its thermal behaviour, especially when PEEK is used as a matrix with carbon fibres. This application of using PEEK as the matrix resulting in poor wetting of the fibres, poor welding quality, and resulting in overall low part quality.
- Lack of good, processable feedstock material for the 3D printing of CF/PEEK.

These all form an obstacle to further certification of the process and industrial exploitation, including upscaling of the process to make large size components. Additionally, the lack of understanding of the microstructural behaviours of the CF/PEEK material during its formation leads to a difficulty in establishing high predictive models that can be used for process control. These gaps form the wider impact of the future work in this field, beyond the achievements that have been made within this PhD project. In this PhD, to address some of these knowledge gaps, both PEEK and CF/PEEK materials were first characterised, then a feedstock manufacturing process was developed, before establishing both PEEK and CF/PEEK printing processes. In terms of the measures of quality of the CF/PEEK feedstock material, the consolidation quality and porosity were explored, while for the printing process, weld formation was a prime focus of the investigation.

CHAPTER 3

Material and Characterisation Prior to the Experiment

3.1 Introduction

Understanding material properties is essential before one is able to set the necessary parameter values for both optimal feedstock manufacturing and 3D printing. When processing carbon fibre to form a PEEK composite material, the carbon fibre does not undergo any phase changes, whereas PEEK will undergo a thermal phase change. However, the addition of carbon fibre influences the thermal properties of the commingled fibre based on the direction and the fibre volume of the carbon fibre. The thermal properties of the material influence its thermal behaviour and therefore its thermal history during processing, which further influences the thermal and mechanical properties of the material, because of the crystallisation of the PEEK polymeric macromolecules. Hence, it is necessary to study how the heating and cooling rates affect the material properties during the processing of both neat PEEK and CF/PEEK composite material. The outcome of these analyses is a process window that is repeatable and yields structurally reliable components. It can also help to optimise the process; for matrix penetration crystallinity for example.

This chapter begins with a study of the morphology of the CF/PEEK composites in order to understand the physical properties of the processing material. Subsequently, the thermal properties of neat PEEK and the selected commingled carbon fibre with PEEK (commingled CF/PEEK) are studied. These studies help in optimising the processing parameters. In the morphology studies, optical microscopy has mainly been used since it is a cheaper and

faster process than SEM: for the latter method, the samples need to be coated and a vacuum needs required in the test environment, while optical microscopy studies can be carried out under ambient conditions without any pre-processing on the sample. SEM was utilised for some samples where the images obtained from the optical microscope did not clearly show the morphology due to the limited depth of field achievable. Characterisation of thermal properties was carried out using thermogravimetric analysis (TGA) and differential scanning calorimetry (DSC). This chapter describes the thermal characterisation of both neat PEEK filament and commingled CF/PEEK materials based on the TGA and DSC results. TGA gives thermal degradation information while DSC provides the crystallisation information and the solidifications during the cooling by showing the thermal transition information of the material during the cooling [200].

3.2 Materials Selection

3.2.1 Polyether Ether Ketone (PEEK)

450G PEEK filament was purchased from iMaker (London, UK) [218]. This is historically the most commonly used molecular grade of PEEK in industry and therefore it is considered to have standard flow properties with a medium melt viscosity. The filament made with this grade is typically used in situations where high strength, stiffness and resistance to aggressive environments are required [219]. A typical material property specification for PEEK 450G can be found in Table 3.1.

Table 3.1: Victrex PEEK 450G [219] and 150G [220] specification.

| Material Properties | | | | | |
|-------------------------------|-------------------|--------------------|--------------|-----------------------------|-----------------------------|
| | Conditions | Test method | Units | Typical Value (450G) | Typical Value (150G) |
| Mechanical data | | | | | |
| Tensile strength | Yield, 23°C | ISO 527 | MPa | 98 | 105 |
| Tensile modulus | 23°C | ISO 527 | GPa | 4.0 | 4.1 |
| Compressive strength | 23°C | ISO 604 | MPa | 125 | 130 |
| Thermal data | | | | | |
| Melting point | | ISO 11357 | °C | 343 | 343 |
| Glass Transition (T_g) | Onset | ISO 11357 | °C | 143 | 143 |
| Flow | | | | | |
| Melting viscosity | 400°C | ISO 11443 | Pa.s | 350 | 130 |
| Miscellaneous | | | | | |
| Water Absorption by immersion | Saturation, 23°C | ISO 62-1 | % | 0.45 | 0.45 |
| | Saturation, 100°C | | | 0.55 | 0.55 |

3.2.2 Commingled Carbon Fibre – Polyether ether Ketone (PEEK) Fibre

A commingled carbon fibre PEEK fibre (commingled CF/PEEK), purchased from Concordia Manufacturing, LLC (Rhode Island, USA) [221], was used as the raw material for fabricating FFF filament. It consists of 57.4 % volume percent of Hexcel AS4C 3K carbon fibres [222] and 42.6 % volume percent of Victrex 150G PEEK fibres [220]. The form of the commingled CF/PEEK is as shown in Figure 3.1.

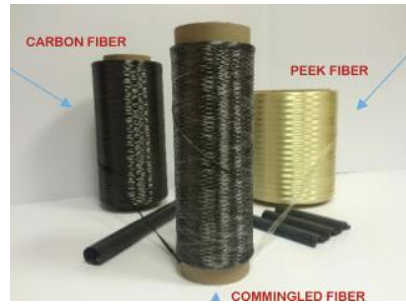


Figure 3.1: Carbon Fibre/PEEK commingled fibres (Hexcel AS4C 3K/Victrex 150G) [223].

As illustrated in Figure 3.1, the PEEK is melt spun into a fibre yarn and mixed with carbon fibre, hence it is called commingled fibres. From the material datasheet [221], the commingled CF/PEEK used contains 0.5 % – 1.5 % of sizing material (sizing agent) [224] as an additive material which could aid the interfacial properties between fibre surface and matrix [225]. 150G type PEEK has an easier flow at 400 °C compared to 450G due to its lower melt viscosity of 130 Pa·s, compared with 450G's melt viscosity of 350 Pa·s at 400°C [220], hence 150G PEEK is usually used when there are infills. 150G has slightly stronger mechanical strength in terms of tensile strength, tensile modulus, and compressive strength tested at 23 °C. Apart from this, the other properties of 150G PEEK, including density and water absorption by immersion are the same as for 450G. Water absorption at saturation is known to be 0.45 % at a temperature of 23 °C and 0.55 % at a temperature of 100 °C [220, 221]. A typical material property specification for PEEK 150G can be referred back to Table 3.1.

The processing of commingled CF/PEEK, as reported in Chapters 4 and 5, was with matrix material grade 150G. When the neat PEEK printing was studied, as reported in Chapter 6, the commercially available PEEK 450G grade filament was used. Hence, two slightly different data sets, for 150G and 450G PEEK were used for the corresponding modelling of these different processes. More details on the processes and the material data can be found in Chapters 4 to 6.

3.3. Material Characterisation

3.3.1 SEM and Optical Microscopy Experiment, Research and Discussion

Images were taken of the side view of a single sample of commingled CF/PEEK using an optical microscope to analyse the structure of the commingled fibres and investigate the fibre direction, inter-fibre distance and size of carbon fibres and PEEK fibres. Optical studies were carried out with a Nikon Eclipse Lv100ND microscope from Nikon UK Ltd (Surbiton UK) [226]. Digital images were analysed by the associated Nikon image processing software called NIS Elements [227]. Figure 3.2 shows microscopy images of the commingled CF/PEEK.

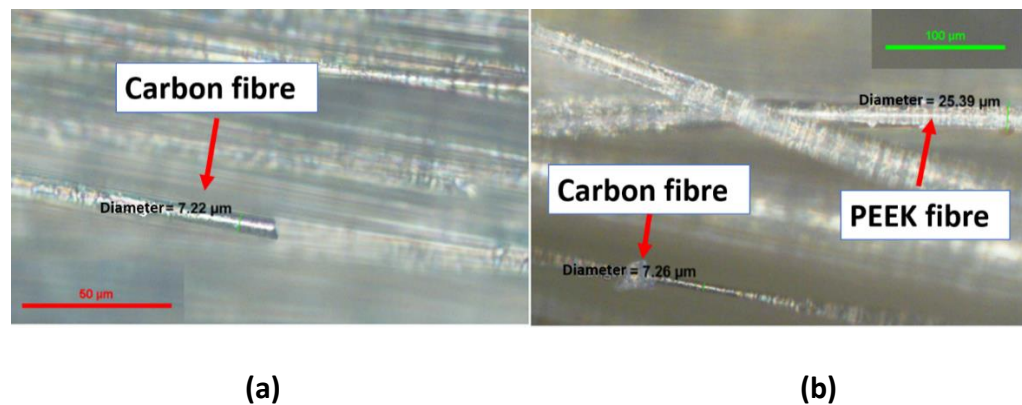


Figure 3.2: Microscopy images of commingled CF/PEEK (a) under magnification factor of 50, (b) under magnification factor of 20.

The relative diameters of carbon fibre and PEEK fibre are shown in Figure 3.2. Due to the depth of field limitations inherent in an optical microscope, the images taken are focused on individual fibres. In order to understand the morphology of the commingled CF/PEEK, SEM images of a single sample were also taken. The SEM images were captured using a Hitachi Ltd (Ibaraki, Japan) [228]. TM3030 SEM with its associated software [229].

Figure 3.3 illustrates an image of the side view commingled CF/PEEK taken under a magnification factor of 600. The sample was coated with gold using an

Agar Sputter Coater (model of MTM-10) [230] in order to maintain high electrical conductivity of the tested sample and hence to obtain a clear image.

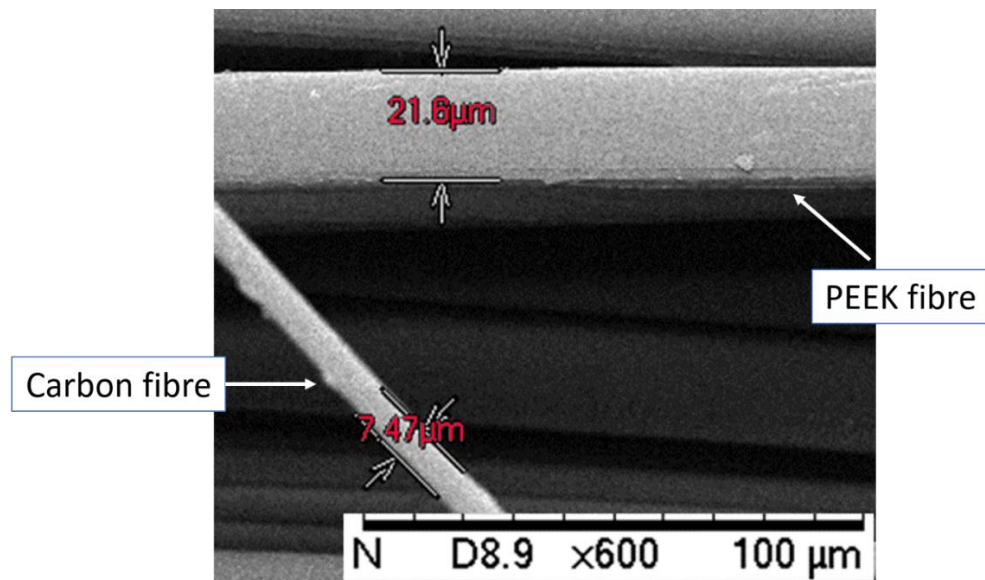


Figure 3.3: SEM image of commingled CF/PEEK indicating relate fibre diameters.

As can be observed in Figure 3.3, the diameter of the PEEK fibres is between 21 and 22 μm , and the diameter of the carbon fibres is between 7 and 8 μm . The carbon and PEEK fibres are loosely mingled in the form of a tow while remaining largely parallel. Further investigation was carried out, and it was found from the cross-sectional views of microscopy images that the fibre distributions were not homogeneous (as seen in Figure. 3.4). These commingled CF/PEEK samples were all taken from the same bundle. The bundle was cut into several pieces to observe the commingled CF/PEEK cross section at various points. Details of how these cross-sectional samples were made are described in Chapter 5.

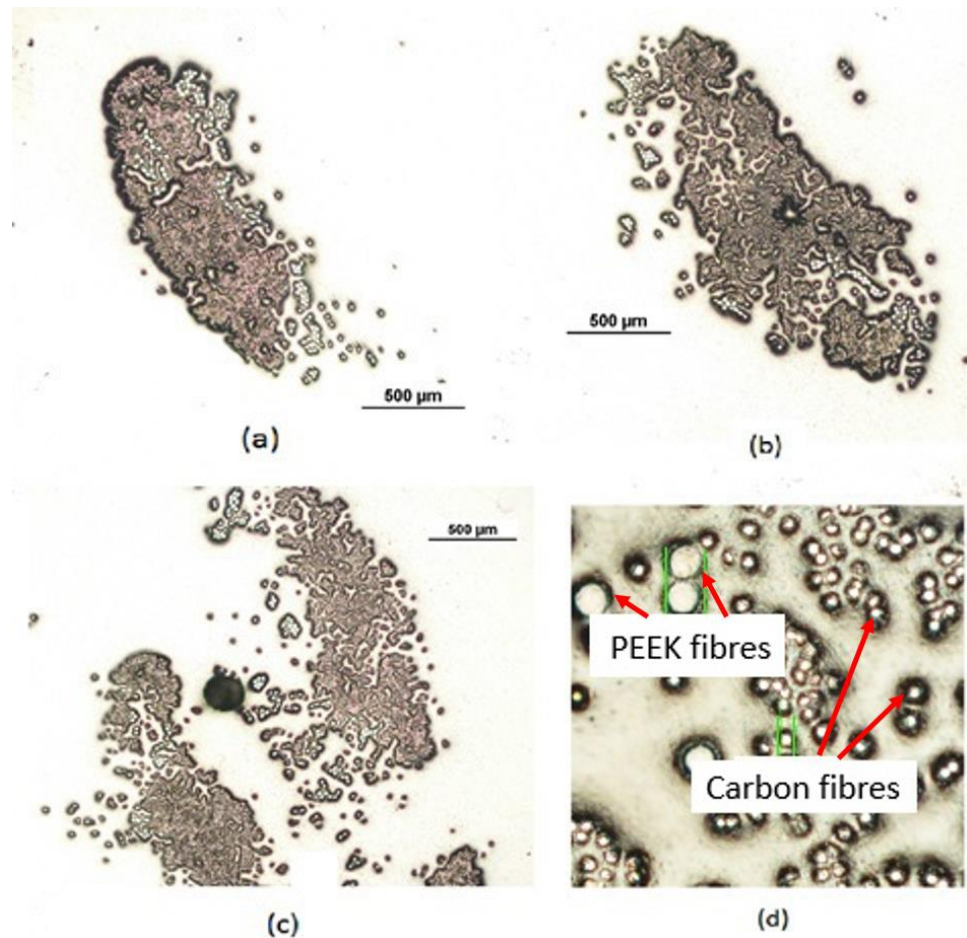


Figure 3.4: Cross-sectional views of the commingled CF/PEEK in the same bundle: (a), (b) and (c) illustrations of the non-homogeneous distribution of PEEK and carbon fibres in cross-sectional views of the commingled CF/PEEK, with the PEEK fibres clearly visible as the larger white “dots”. (d) close up of a smaller region in a cross-section shows how carbon and PEEK fibres can be readily distinguished based on their radial sizes.

3.3.2 TGA Experiment, Results and Discussion

In this research, TGA was used to understand the flammability and thermal decomposition properties of PEEK and commingled CF/PEEK [2]. The objectives of this study were (i) to prevent combustion during processing PEEK and CF/PEEK composites material, (ii) to establish the upper temperature boundary of the processing window, and (iii) to investigate the thermal degradation behaviour.

The TA Instrument Q600 SDT [231] was utilised for the TGA test. The software used to analyse the TGA data was *Universal Analysis 2000* [232]. During these

Chapter 3 Material and Characterisation Prior to the Experiment

tests, two pans were placed in a furnace, one of which held the sample, and the other was empty and used as a reference. The furnace was heated at a known and controlled rate and cooled with an uncontrolled cooling rate during the experiment while the mass of the sample was simultaneously monitored during the experiment. Only the heating stage in the analyses was used to provide information on phase changes and thermal degradation.

In the TGA tests the temperature was increased from 20°C to 800°C at a rate of 20°C/min. The chosen testing environment was air at atmospheric pressure, in order to have a similar environment to the intended 3D printing process. The TGA test was repeated each time with a new material sample until the results showed a clear cluster of measured heatflow-temperature curves. Subsequently, one of the curves that was at centre of the cluster was selected as representative result and is discussed in this thesis. In the test, the PEEK sample weight was 13.39 mg, that of the commingled CF/PEEK sample was 1.413 mg due to the nature of loose commingled CF/PEEK fibres which causes difficulties in preparing the sample and covering the sample pan. Note that the recommended ideal sample weight should be around 10 mg. The TGA test result for PEEK is shown in Figure 3.5, and that for the commingled CF/PEEK is shown in Figure 3.6.

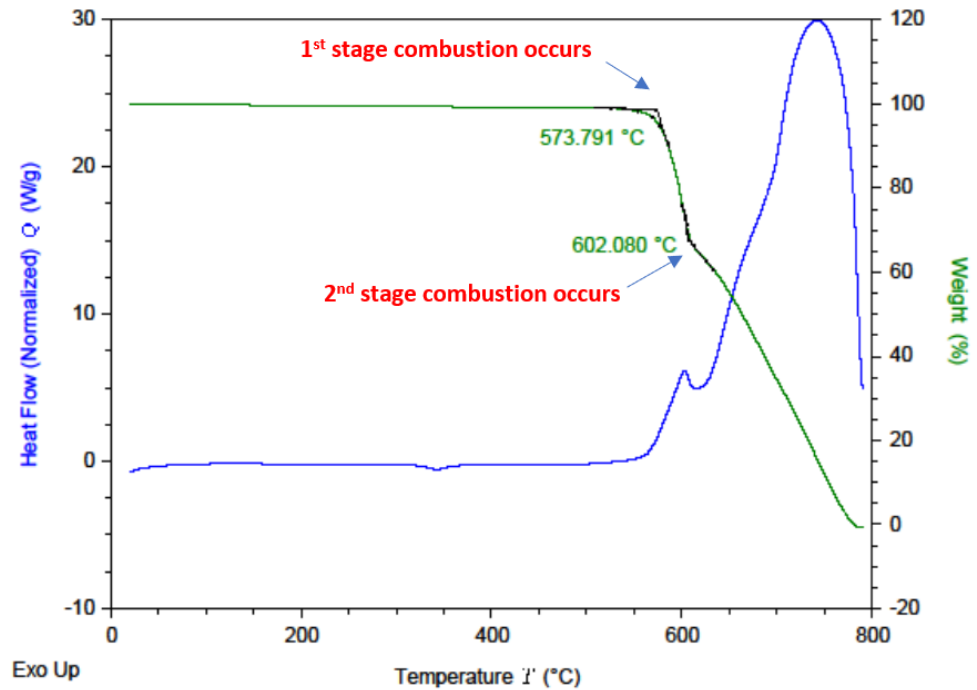


Figure 3.5: The TGA result for PEEK.

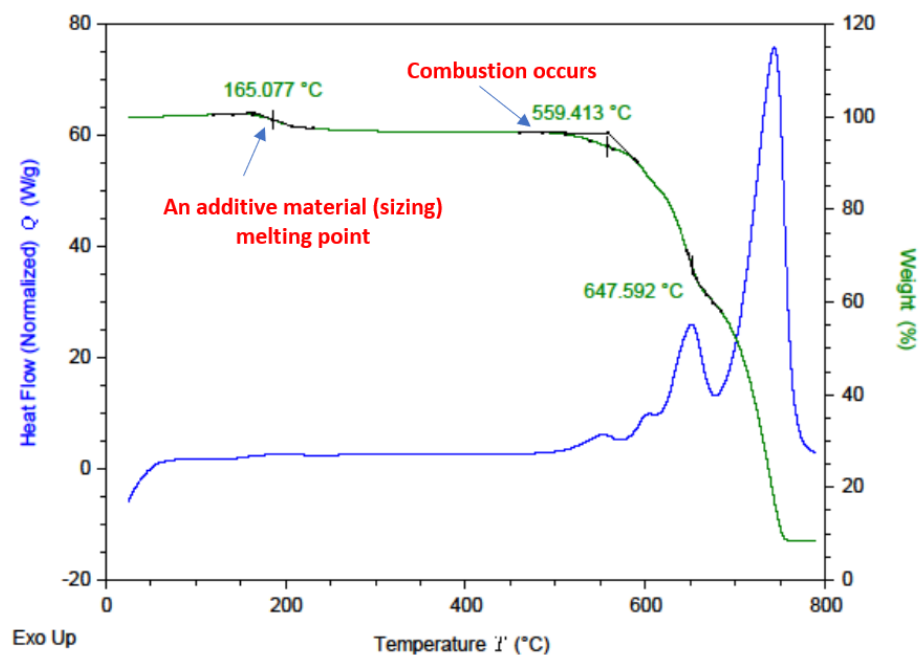


Figure 3.6: The TGA result for commingled CF/PEEK.

The results show that commingled CF/PEEK and PEEK have similar thermal behaviours. This can be seen by the observation that PEEK alone presents two thermal degradation events, at 574 °C and 602 °C whereas commingled

CF/PEEK presents two major thermal degradation events at 559 °C and 648 °C, with a further degradation point at 165 °C not seen in PEEK. Similar results for 450G PEEK were observed in Ref. [2]. This is explained by Ref [124] that random chain scission of the bonds in the chain is the main mechanism during the first thermal degradation. A second thermal decomposition stage occurs at 648 °C where autoignition occurs as shown in Figure 3.6. Further substantive and conclusive proof that the autoignition temperature is reached at this temperature is given in Ref. [2]. The first stage of thermal decomposition of the commingled CF/PEEK (Figure 3.6), occurs at a temperature lower than for neat PEEK. According to Ref. [233] this is because the presence of carbon fibre increases the oxidation in the material, leading to greater combustibility. Although the TGA of PEEK clearly shows two stages of the combustion, the addition of carbon fibre to form the commingled CF/PEEK increased the complexity of the combustion as shown in the additional stages of combustion observed. The nature of these combustion stages was considered beyond the scope of this work and not explored further, however, according to Zhang *et al.* [9] a possible explanation for this could be that the temperature range, and hence crystal growth rate of PEEK varies when adjacent to carbon fibre, thus modifying combustion. When the temperature reaches around 165 °C, it was observed there was a material weight loss. A similar observation was made in the DSC test in the first cycle (see Figure 3.8 (a)) with a heating rate of 5 °C/min. This indicates there is an additional material in the commingled CF/PEEK, which matches the statement of the manufacturer regarding the presence of the sizing agent in the commingled CF/PEEK [221].

The TGA results of PEEK and commingled CF/PEEK show no significant heat related weight change at 100 °C, this is the temperature corresponding to the evaporating temperature of water at atmospheric pressure. Thus, it can be inferred that the water content of the PEEK and CF/PEEK filament is relatively small.

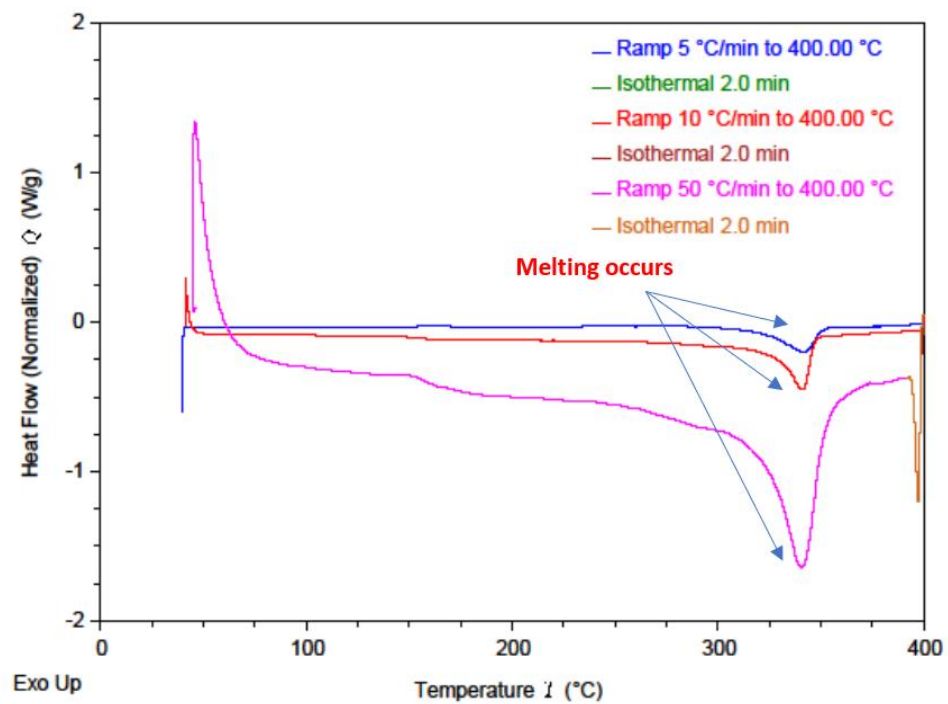
Critically, the TGA results show that the commingled CF/PEEK will be safe to process in an atmospheric air environment at temperatures below 500°C. Furthermore, this confirms that the recommended 400 °C processing temperature will be safe to work at and that the material is safe to analyse in the DSC at 400 °C.

3.3.3 DSC Experiment, Results and Discussion

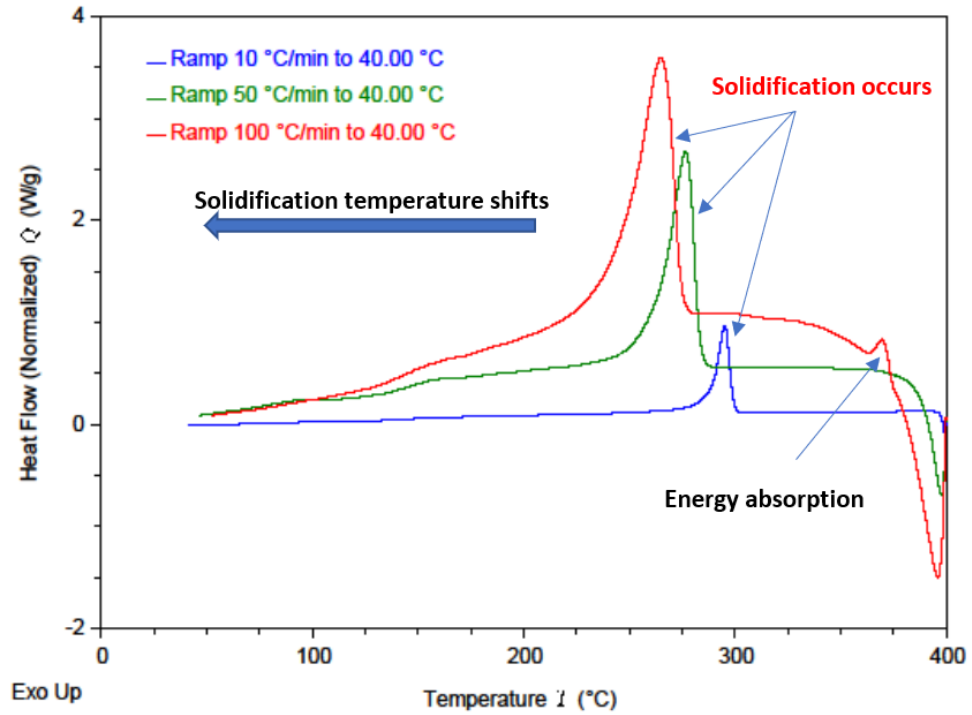
DSC is used to determine the heat of fusion, crystallisation points, melting point and glass transition characteristics of a material [166]. The heat of fusion study can determine the amount of energy a sample absorbs while melting and releases during crystallising. This can help to determine appropriate processing temperatures for a material. For semi-crystalline polymers, crystallisation points reveal the temperatures at which the polymer crystallises upon cooling. By identifying these points, one can optimise the mechanical properties of the final printed parts, as the cooling rate of the material through these points affects the ratio of crystalline to amorphous material in the final part [9, 160, 234]. The glass transition and melting temperatures indicate at which temperature range a crystalline polymer transitions into an amorphous polymer, resulting in the polymer going from a hard brittle state to a soft rubbery state. Furthermore, it shows the temperature at which the polymer will melt or recrystallise. Since PEEK is semi-crystalline material, these data provide a route to understanding when material phase changes take place during the process.

In this test, the Discovery DSC 2500 machine [235] was used for the DSC test and the results were analysed using *TA Instruments TRIOS* [236]. One sample were tested in each of PEEK and CF/PEEK under the same testing conditions. In the DSC characterisation, three cycles were set for each sample to check out the stability and the repeatability of the neat PEEK and commingled CF/PEEK. The temperatures ranged from 40°C to 400°C. For the initial cycle the heating rate was set to 5°C/min and increased 10°C/min and 50°C/min respectively in the subsequent cycles (Figure 3.7 (a) for PEEK and Figure 3.8 (a) for

commingled CF/PEEK) in order to observe how different heating rates affect the materials thermal behaviour. The cooling rate was set to 10°C/min and increased to 50°C/min and 100°C/min in subsequent cycles (Figure 3.7 (b) for PEEK and 3.8 (b) for commingled CF/PEEK) to study how different cooling rates affect the thermal behaviour of the materials. The setup of the heating and cooling rates were adopted from the study carried out in Ref. [166]. The tests were conducted in nitrogen. Encapsulated aluminium pans were used to contain the samples during the tests. Sample weights were 5.7 mg of PEEK, and 4.9 mg of the commingled CF/PEEK in the DSC tests. The DSC tests of PEEK are shown in Figure 3.7, and the commingled CF/PEEK are shown in Figure 3.8.

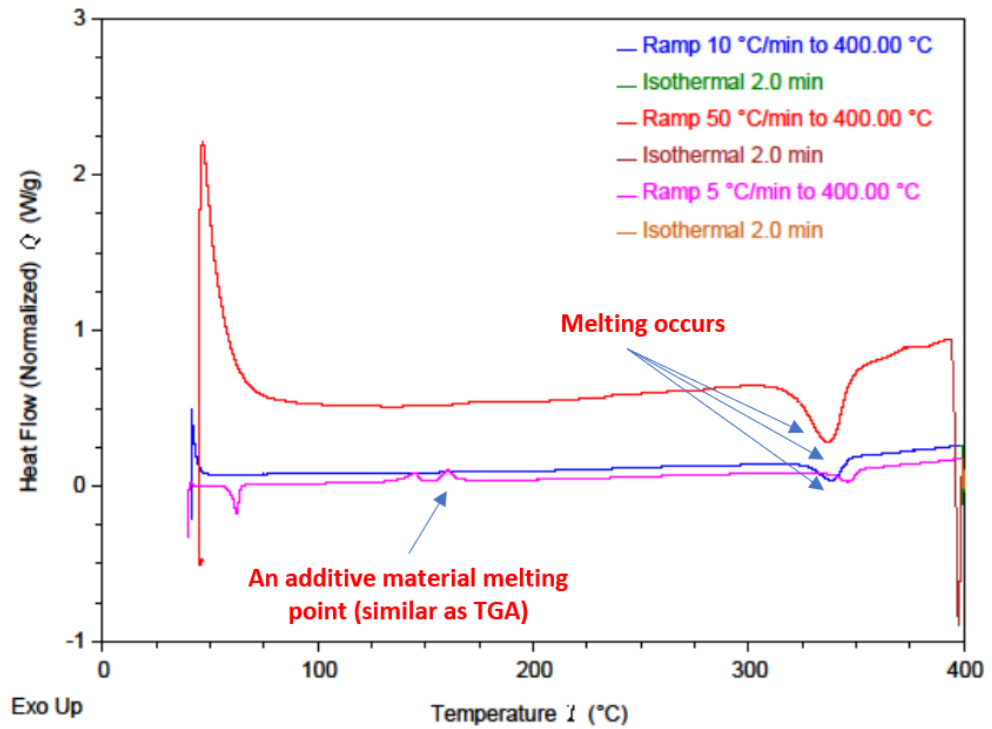


(a)

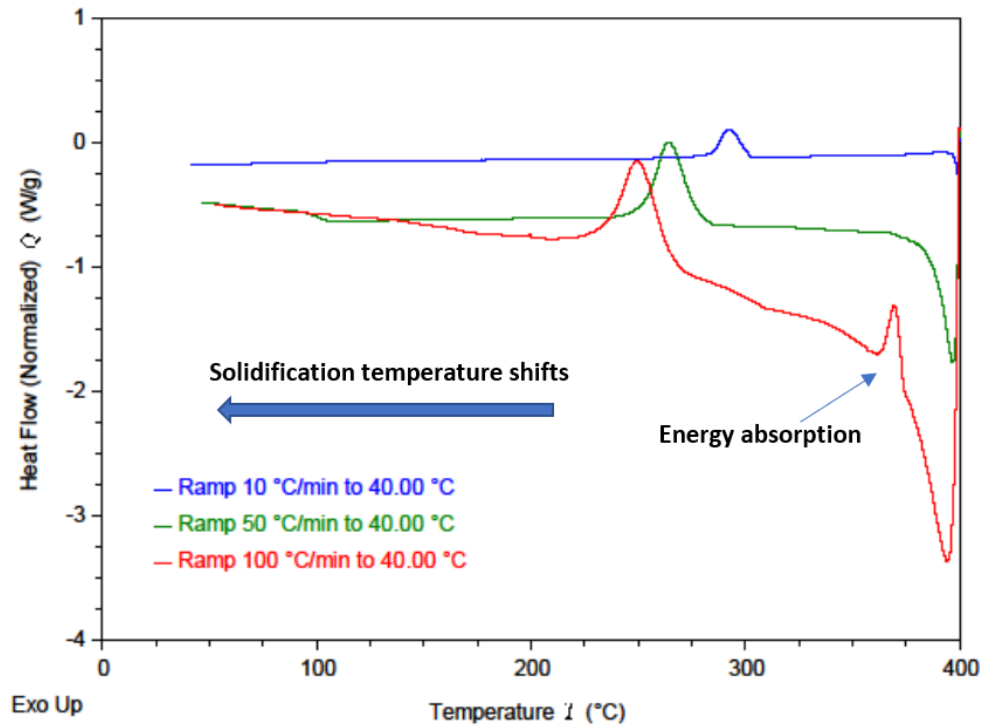


(b)

Figure 3.7: (a) The DSC results for the PEEK with heating rates of 5 °C/min, 10 °C/min, and 50 °C/min in three cycles with the same sample. (b) The DSC result for the PEEK with cooling rates of 10 °C/min, 50 °C/min, and 100 °C/min in three cycles with the same sample.



(a)



(b)

Figure 3.8: (a) The DSC results of the commingled CF/PEEK with heating rates of 5°C/min, 10°C/min, and 50°C/min in three cycles with the same sample. (b) The DSC result of the commingled CF/PEEK with cooling rates of 10°C/min, 50°C/min, and 100°C/min in three cycles with the same sample

Table 3.2: PEEK normalised enthalpy at the phase transition of DSC results.

| Ramp type | Rate (°C/min) | Peak temperature (°C) | Normalized enthalpy (J/g) |
|-----------|---------------|-----------------------|---------------------------|
| Heating | 5 | 342 | 28.84 |
| Heating | 10 | 341 | 23.27 |
| Heating | 50 | 341 | 29.26 |
| Cooling | 10 | 295 | 41.19 |
| Cooling | 50 | 276 | 39.34 |
| Cooling | 100 | 265 | 39.78 |

Table 3.3: CF/PEEK normalised enthalpy at the phase transition of DSC results

| Ramp type | Rate (°C/min) | Peak temperature (°C) | Normalized enthalpy (J/g) |
|-----------|---------------|-----------------------|---------------------------|
| Heating | 5 | 347 | 10.6 |
| Heating | 10 | 339 | 9.77 |
| Heating | 50 | 337 | 10.13 |
| Cooling | 10 | 292 | 13.85 |
| Cooling | 50 | 264 | 13.04 |
| Cooling | 100 | 250 | 13.85 |

In Figure 3.7, the DSC test results of PEEK show how different heating and cooling rates affect the crystallisation peak and occurrence of melting. Changes to either heating or cooling rates do not substantially change the latent heat energy absorbed per unit or released during the melting or solidification (Table 3.2). The phase change involves around 50% more enthalpy during the solidification than the melting process. An increased cooling rate was observed to shift the solidification temperature to a lower temperature (Figure 3.7 (b)) 295°C at 10°C/min, 276°C at 50°C/min and 265°C at 100°C/min cooling rate; whilst the melting temperatures stayed stable for varying heating rates (Figure 3.7(a)). All melting temperatures were around 342°C, which agrees very closely with the melting temperature of 343°C given in the manufacturer's specification. This indicates that the cooling rate is the critical factor affecting the final crystallisation fraction of PEEK and will lead to different mechanical properties of fabricated parts. This can be explained that by accelerating the cooling rate the temperature peak will shift, as long as the DSC system does not modify the material during the testing process [225]. For the commingled CF/PEEK DSC, the results follow the same trend (Figure 3.8). However, the melting and recrystallisation enthalpies are much lower than the results for neat PEEK. This lower quantity of phase change enthalpy for CF/PEEK when compared with neat PEEK is believed to be due to the comparatively smaller amount of PEEK per unit volume, the added carbon fibre

can be assumed as thermally stable below temperatures of 400°C. When comparing the normalised system enthalpies in Figures 3.7 and 3.8, the normalised system enthalpy of CF/PEEK is consistently about a third of that of the neat PEEK. This indicates a non-proportional effect of the fibre volume fraction on the enthalpy, as the volume fraction of PEEK is 42.6 %. This can be explained by the changes in the thermal capacity of the material due to the introduction of carbon fibre into the PEEK. Similarly, the results of the commingled CF/PEEK (Figure 3.8 (b)) show how increasing the cooling rate lowers the solidification temperature. The desorption normalised enthalpy as observed in Figure 3.8 (a) is quite similar for different cooling rates Figure 3.8 (b) and is only on average about 2 Joule per gram higher than the absorption normalised enthalpy. The data can be seen in Table 3.3. The energies released from CF/PEEK do not form a proportional match compared to the energy release in neat PEEK as the CF volume fraction is 57.4 %. Due to the technical limitations of the available equipment, no further analyses could be made to obtain a more precise understanding of this behaviour.

In the cooling process at the third cycle for the PEEK with a rate of 100°C/min, there is a heat flow change around a temperature of 370°C with normalised enthalpy of 0.87 J/g (Figure 3.7 (b)). Similar results were observed with commingled CF/PEEK result (Figure 3.8 (b)), at a temperature around 370 °C, however, the normalised enthalpy is 2.34 J/g, which it is much higher than that of the neat PEEK. This shows that a high cooling rate (100 °C/min) leads to additional energy absorption around 370 °C both for neat PEEK, and for CF/PEEK. From the observation, the infill of carbon fibre leads a greater enthalpy change in the third cycle cooling process around 370 °C. This can be explained as due to the additional crystal growth of PEEK on carbon fibre, according to Zhang *et al.* [9].

Finally, during the processing of the PEEK and the commingled CF/PEEK, humidity absorption is a relatively minor issue. This can also be seen in the findings of both the DSC tests, as there is no significant heat flow and weight change around 100 °C, the evaporating temperature of water. Additionally, in

the heating process of the first cycle, a heat flow fluctuation happens at 160 °C. This result is in agreement with the observation made from Figure 3.6, which indicates a possible melting point for the sizing agent, which is an additive in the commingled CF/PEEK.

3.4 Summary

This chapter focusses on characterising the material to be used in the core experimental research, with experimental test conditions representative of the conditions present in the initial material processing experiments. Contrary to what might have been expected, carbon fibre has a significant effect on the thermal behaviour of PEEK when used with FFF printing, as it affects the thermal properties of the neat PEEK.

Among these results, the initial morphology studies show that PEEK fibres have a larger diameter, around 3 times that of the carbon fibres in the commingled CF/PEEK. Furthermore, it was found that the carbon fibre was not distributed homogeneously in the same bundle of the commingled CF/PEEK. As the PEEK fibre volume fraction is less than 50 %, a larger PEEK fibre diameter may create an even less homogeneous carbon fibre distribution in the later process, if the heating time and the geometry of the die (see Chapter 4 and 5) cannot sufficiently guide the compaction process.

The results from the TGA and DSC both for the PEEK and for the commingled CF/PEEK are generally in good agreement with the data from the literature. However, when looking at the details of the commingled CF/PEEK TGA and DSC results, contrary to what might have been expected, carbon fibre has a significant effect on the thermal behaviour of PEEK when used with FFF printing, as it affects thermal properties of the PEEK in thermal conductivity and latent heat, and possibly crystal growth. This will be explored further in Chapter 6. This also shows that from the TGA result, that under air, carbon fibres introduce a lower resistance to oxidation when commingled CF/PEEK is compared to PEEK since the material degradation occurs at a lower

Chapter 3 Material and Characterisation Prior to the Experiment

temperature. Another particular observation from both the CF/PEEK and PEEK DSC analyses is, that when the cooling rate is higher than $100^{\circ}\text{C}/\text{min}$, an additional energy absorption occurs around 370°C . This can refer to the later research on both filament feedstock production (in Chapter 5) and the 3D printing process (In Chapter 6). As there is no heating chamber in the feedstock manufacturing, the cooling rates of CF/PEEK filament when it comes out from the feedstock die is higher than $1000^{\circ}\text{C}/\text{min}$. This is suggested by the IR measurements in Chapter 6. Likewise, as the chamber of the 3D printer used in this PhD project cannot reach a higher temperature than 100°C (detail description is in Chapter 6), cooling rates of the CF/PEEK and the PEEK in the printing is evaluated more than $1000^{\circ}\text{C}/\text{min}$. This might have impacted the production window for both of the feedstock manufacturing and 3D printing process. More testing around this temperature will be performed in Chapter 5.

CHAPTER 4

Development of a CF/PEEK FFF Feedstock Production Process

4.1 Introduction

This chapter describes the design and development of the feedstock manufacturing process, including analysis of the HotEnd as the heating element of the pultrusion system, the design of the pultrusion apparatus, the electronics and controller setup and the processing of the comingled CF/PEEK using this pultrusion apparatus.

The selected CF/PEEK material for this investigation is a strand of very fine fibres with a low bending stiffness which is impossible to extrude directly through a 3D printer nozzle, as the strand will buckle and jam the supply tube when it is pushed into the HotEnd by an extruder. Therefore, a pre-processing stage for the feedstock has been developed to convert the tow of comingled fibres into a FFF 3D printing filament. This pre-processing stage transforms the comingled fibres into a single consolidated strand of semi-stiff material, which will be easier to print than the strand consisting of many fibres. For this purpose, an inverted extruding process, known as pultrusion, was utilised.

4.2 Selection of the HotEnd

4.2.1 Introduction

A schematic illustration of the E3D (Oxfordshire, UK) HotEnd [99] is shown in Figure 4.1. From the definition of RepRap Wiki [237], a HotEnd is the term for a subsystem of the print device that contains the heating method for the plastic filament, and the print nozzle of the printer. An all-metal HotEnd usually

includes a heater block (heatblock) to hold the thermocouple and a nozzle. A heatbreak is made from a high thermal resistant material to avoid too much heat going from the heatblock to the upper side of the HotEnd. A heatsink joined with a cooling fan can be used to prevent excessive heat at the entrance of the HotEnd, in order to stop the filament melting before it reaches the heatblock.

The purpose of the analysis of the HotEnd in this work was to determine an appropriate heating system to process the PEEK and CF/PEEK materials used in this investigation based on the thermal analyses of the previous chapter. An all-metal HotEnd with a fan cooled heatsink was selected for the commingled CF/PEEK processing. After the thermal analysis, this HotEnd was confirmed as suitable for use in the pultrusion process. The thermal analysis of the HotEnd forms the first stage of the pultrusion apparatus development, and a further study on mechanical design is presented in Section 4.3.

In the thermal analysis of the HotEnd, the energy input and the material properties of the HotEnd are established as the dominant parameters. The framework of this model is then built up by establishing a thermal resistance ladder network model based on electrical circuit analysis methods [238]. This model could be utilised as a universal method for the thermal analysis of all-metal HotEnd-heatbreak-heatsink assemblies (i.e. E3D V6). During the analysis, the heatblock and nozzle are considered to have reached a steady state temperature equal to the desired operating temperature, and the heat flow conducts through the heatbreak to the heatsink. The model is benchmarked and validated against the paper by Jerez-Mesa *et al.* [100], and a similar result was obtained compared with the output of their finite element analysis (FEA). This model was used to predict the performance of the HotEnd which was selected, and gave confidence the PEEK would not melt at the inlet.

Figure 4.1. is a scale sectioned view of the HotEnd which illustrates the heat flow with the red arrows. Since the initial selection of the HotEnd is E3D V6, the illustration scale uses the selected HotEnd as the example.

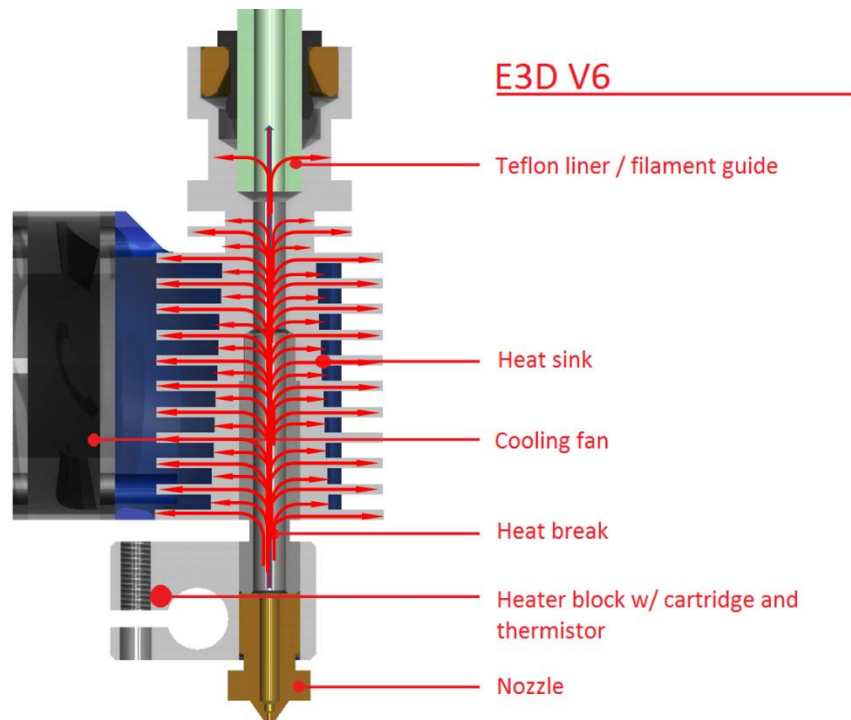


Figure 4.1: A scaled sectioned view of the HotEnd heat flow using example of E3D, modified from Ref. [239].

The thermal resistance of this HotEnd behaves as an adjustable resistance to the environment as the fan speed governs the heat transfer coefficient. The fan velocity of the heatsink can be adjusted as to ensure that:

- the nozzle can be heated up to the designed high temperature;
- the upper part of the HotEnd can remain at a temperature below the PEEK melting point. In this case the material will not melt when it comes in contact with the heatsink where it enters the HotEnd through the inlet at the top of heatsink.

As can be seen in Figure 4.1, the HotEnd system includes a heatblock (to hold the heat cartridge for heating up the nozzle), nozzle, heatbreak (a thermal “break” in the circuit that connects the heatblock and heatsink), and a heatsink with a fan. The model is established based on the various materials and dimensions of the constituent components of the HotEnd used in the pultrusion rig. The heatblock is considered as a heat source. Since the heatsink geometry is axisymmetric, it can straightforwardly be dissected into smaller elements based on the geometric features which are known to have an

analytical solution for the heat flux analysis. Based on the electrical analogue of heat transfer, the thermal resistances can be derived. When the thermal resistances of the individual features are subsequently combined into a single system, modelling of the HotEnd with the thermal network approach can be achieved.

4.2.2 Ladder Network Model – Universal Model

The HotEnd system used in this work is an all-metal HotEnd of a general geometry. It includes a heatblock (for heating up the nozzle), nozzle, heatbreak (thermal break), and a heatsink with a fan.

A thermal network model was built for the HotEnd after calculating the thermal resistances of the heatsink and the other system components.

The main heat flow is assumed to be from the heatblock, through the heatbreak, as shown in Figure 4.2, and subsequently to the heatsink where the heat is transferred into the surrounding air and dissipated, as depicted in Figure 4.3. Since the regions with free and forced heat convection, the thermal model of heatsink needs to be divided into two parts. The Part i is the heatbreak and heatsink conjunction where free air convection occurs. And the Part ii is the heatsink region where forced air convection occurs. Table 4.1 lists the key features and corresponding equations for calculating the heat flow in each of these parts. The thermal resistance in all the features are calculated based on the classical heat transfer functions [240].

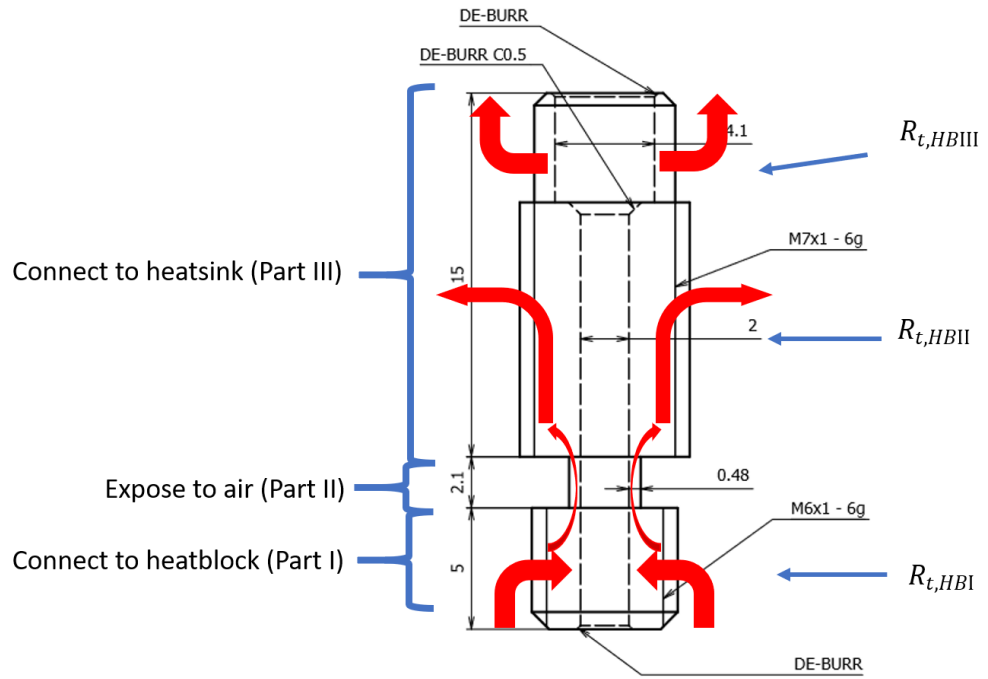


Figure 4.2: Heat flow path of heatbreak: source, Ref [99].

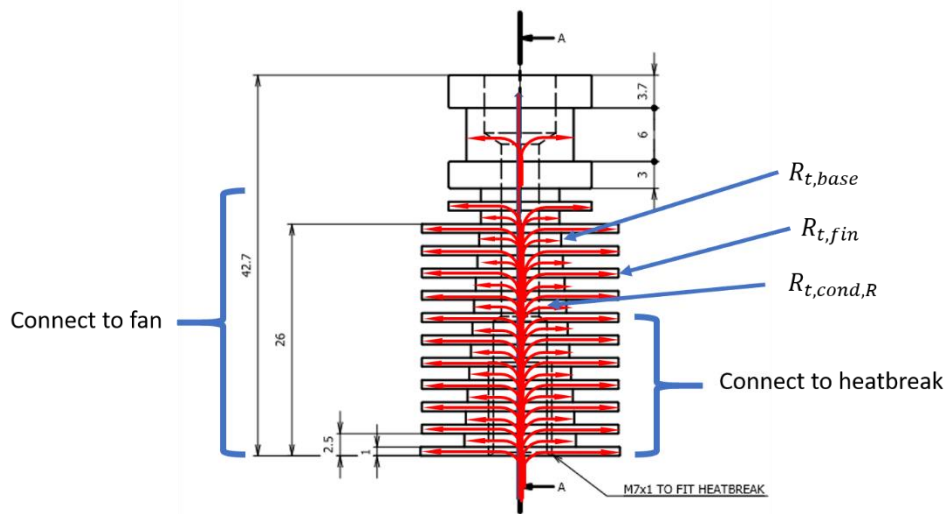


Figure 4.3: Heat flow path of the heatsink: source, Ref. [99].

Table 4.1: List of key features and corresponding equations: source, Ref. [240].

| Feature description | Equation | Symbol description |
|---|--|--|
| Heatbreak: thermal resistance | | |
| Part I and Part III | $R_{t,HB} = \frac{\ln \frac{r_2}{r_1}}{2\pi Lk}$ | $R_{t,HB I}$ and $R_{t,HB III}$ are obtained as the cylindrical wall of the conduction thermal resistance. |
| Part II | $R_{t,HB II} = \frac{L}{kA}$ | $R_{t,HB II}$, it is obtained as thermal resistance for conduction in a 2D plan. |
| The total value | $R_{t,HB} = R_{t,HB I} + R_{t,HB II} + R_{t,HB III}$ | $R_{t,HB}$ includes three parts of the calculation. |
| Heatsink: thermal resistance: | | |
| Thermal resistance of a slice of the cylindrical inner core of the Heatsink | $R_{t,cond,R} = \frac{\ln \frac{r_2}{r_1}}{2\pi Lk}$ | $R_{t,cond,R}$ is obtained as the cylindrical wall of the conduction thermal resistance. |
| Thermal resistance of each fin | $R_{t,fin} = \frac{1}{hA_f\eta_f}$ | $R_{t,fin}$ is obtained by the classical annular fin analytical convection model |
| Thermal resistance of each base | $R_{t,base} = \frac{1}{hA_b}$ | $R_{t,base}$ is obtained by the classical cylindrical pin |

| | | |
|---------------------------|--|---|
| | | analytical convection model |
| The total effective value | | Obtained by assembling the ladder network |

The heatbreak can be divided into three regions: Part I is where the heatbreak is mounted onto the heatblock; Part II is non-connector part where expose to the air; Part III is where the heatbreak is mounted onto the heatsink, as can be seen from Figure 4.4. The reasoning underpinning this assumption is as follows: Assume that the heatblock is at a set, constant temperature, T_s , then the edge of the heatbreak connecting with the heatblock is at the same temperature as the heatblock, T_s . The heating cartridge which is the source of the heat is approximately located below the heatbreak. The heatbreak is used as a thermal barrier, to hinder heat going to the supply entry hole, where the plastic supply tube is attached to the all-metal HotEnd system. For this reason, the heatbreak is usually made of stainless steel, which has a low thermal conductivity and can be considered working as a thermal isolator material to a certain degree. The portion of heat coming from the heat cartridge that flows to the heatsink will mostly take the path with lowest resistance and flow around the heatbreak. It will then take the “shortest path” through the heatbreak to the heatsink as it provides the lowest thermal resistance. Similarly for the heat flowing out, most of the heat will take the “shortest path” through the heatbreak into the heatsink which is usually made of aluminium, as a better conductor than stainless steel. Therefore it can be deduced that the contribution of the two ends of the heatbreak is negligible and the total resistance of the heatbreak is determined and can be calculated by the thermal resistance of Part II and the parts of the two mounting stubs which are positionally close to Part II.

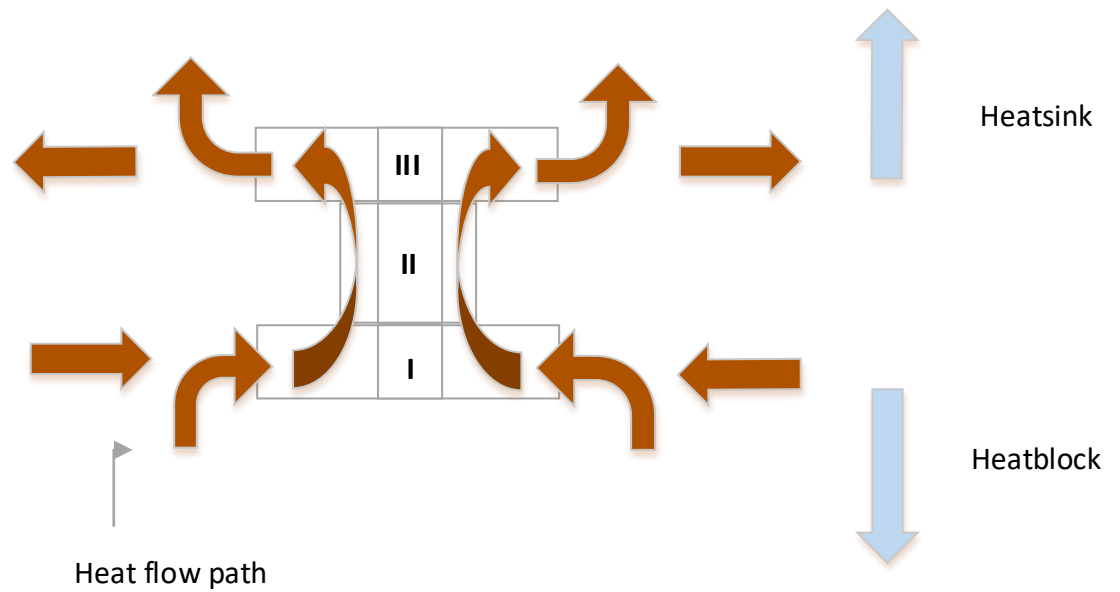


Figure 4.4: Heat flow path of heatbreak.

Hence, the thermal resistance of the heatbreak equation is obtained as below:

$$R_{t,HB} = R_{t,HB I} + R_{t,HB II} + R_{t,HB III} \quad (4.1)$$

From the heat flow path, $R_{t,HB I}$ and $R_{t,HB III}$ are obtained as the cylindrical wall of the conduction thermal resistance [240]. The equation is as below:

$$R_{t,HB} = \frac{\ln \frac{r_2}{r_1}}{2\pi Lk}$$

For the $R_{t,HB II}$, it is obtained as thermal resistance for conduction in a 2D plane.

$$R_{t,HB II} = \frac{L}{kA} \quad (4.2)$$

The heatsink can be divided into two parts, Part I is where forced air convection occurs (with fins and covered with a fan); Part II is the part where there is free air convection (without fins) on the top of the heatsink. Some heatsinks may only have part I and operate under only a forced convection regime. The assumption of the heat flow path for the heatsink is, when heat goes up from the heatbreak, it goes to the first fin and first base directly from the heatbreak. Figure A.5 shows one side of the heatsink with the heat flow path.

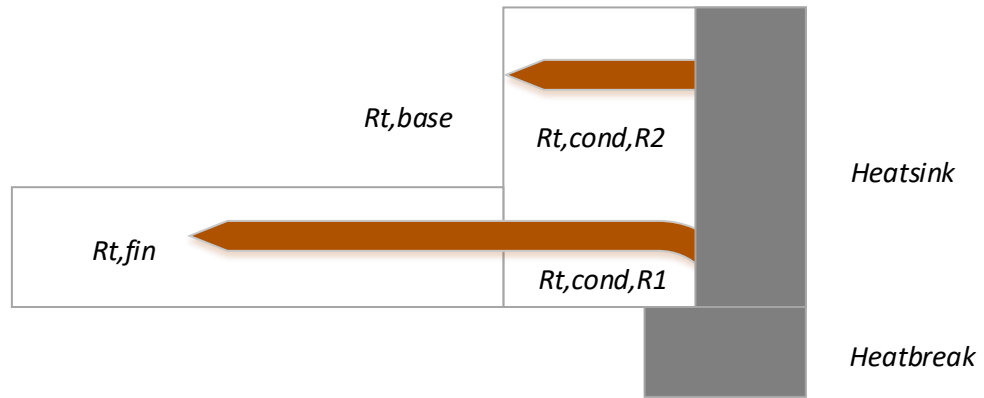


Figure 4.5: Heat flow path of the heatbreak and heatsink conjunction.

Hence, the heat flow is not going up, instead it is going to the side. The thermal resistances of $R_{t,cond,R1}$ and $R_{t,cond,R2}$ are obtained as:

$$R_{t,cond,R} = \frac{\ln \frac{r_2}{r_1}}{2\pi Lk} \quad (4.3)$$

Where r_1 and r_2 are decided by the radius of the bottom of the heatsink.

Above the bottom of the heatsink and heatbreak conjunction, the heat goes up first, then turns in the direction of each fin and base. In this case, the heat flow path of $R_{t,cond,A1}$ and $R_{t,cond,A2}$ are going in a different direction than $R_{t,cond,R1}$ and $R_{t,cond,R2}$. Figure 4.6 shows part I of the heatsink with a qualitative sketch of the heat flow path of one side.

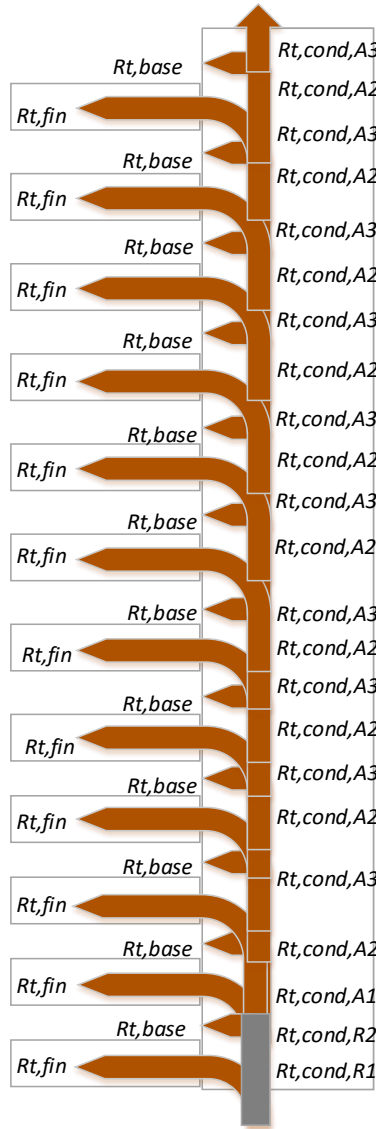


Figure 4.6: Heat flow path of the heatsink region where forced air convection occurs.

In this model, $R_{t,cond,A1}$, $R_{t,cond,A2}$ and $R_{t,cond,A3}$, are used to model the conduction resistance as seen by the heat flow when it is moving to the tip of the heatsink where the entry hole for the filament supply is. These resistances are the thermal resistances of a slice of the core of the heatsink, each with the thicknesses of the fin and the exposed “base” (core) respectively. Hence these are obtained with the following equations to account for these different vertical lengths of fin and base:

$$R_{t,cond,Ai} = \frac{L_i}{kA} \quad (4.4)$$

For the $R_{t,fin}$ and $R_{t,base}$, they are treated as if they only have convection resistance. Thus, for each fin, the fin resistance is calculated as:

$$R_{t,fin} = \frac{1}{hA_f\eta_f} \quad (4.5)$$

Where the efficiency of annular fins of rectangular cross section η_f can be established based on the fin size, heat transfer coefficient and the thermal conductivity (the efficiency takes the thermal conductivity of the fin material into account).

For all the $R_{t,base}$, they are calculated as:

$$R_{t,base} = \frac{1}{hA_b} \quad (4.6)$$

Using these assumptions, this heat path flow can now be modelled by a standard thermal network model in order to allow for an analytical calculation of the temperature distribution on the HotEnd. Following this, the thermal resistance circuit diagram of heatbreak and heatsink part I obtained is given in Figure 4.7:

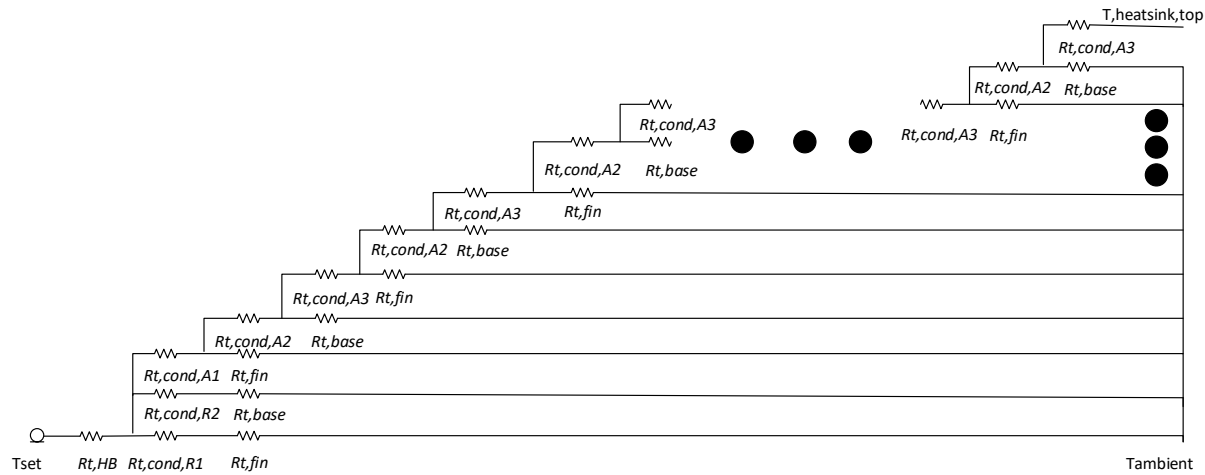


Figure 4.7: Heatblock and heatsink part I thermal resistance circuit diagram.

This thermal resistance circuit diagram, is equivalent to the more familiar ladder network model which is given in Figure 4.8.

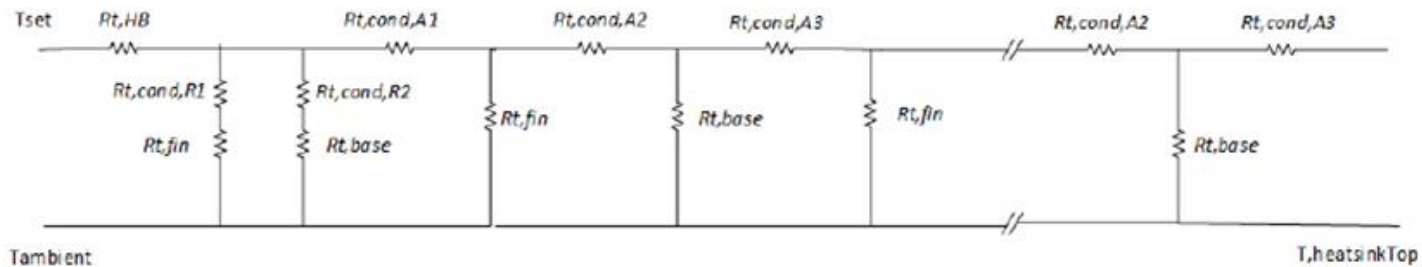


Figure 4.8: Heatbreak and heatsink part I thermal resistance circuit ladder network model version.

The heatsink part II, is modelled as a pin. Therefore, the final thermal resistance circuit of the HotEnd can be described as shown in Figure 4.9:

Chapter 4 Development of a CF/PEEK FFF Feedstock Production Process

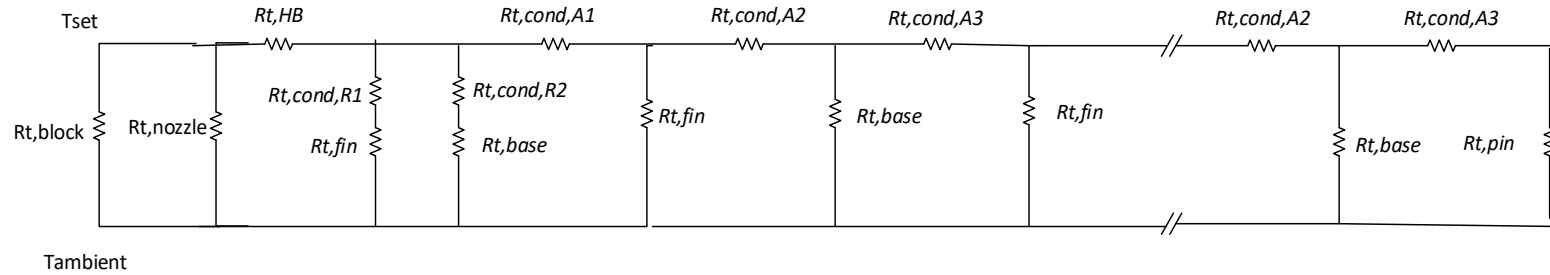


Figure 4.9: Thermal resistance circuit of the HotEnd.

The last step is to apply a mesh analysis for the thermal circuit, shown in Figure 4.10.

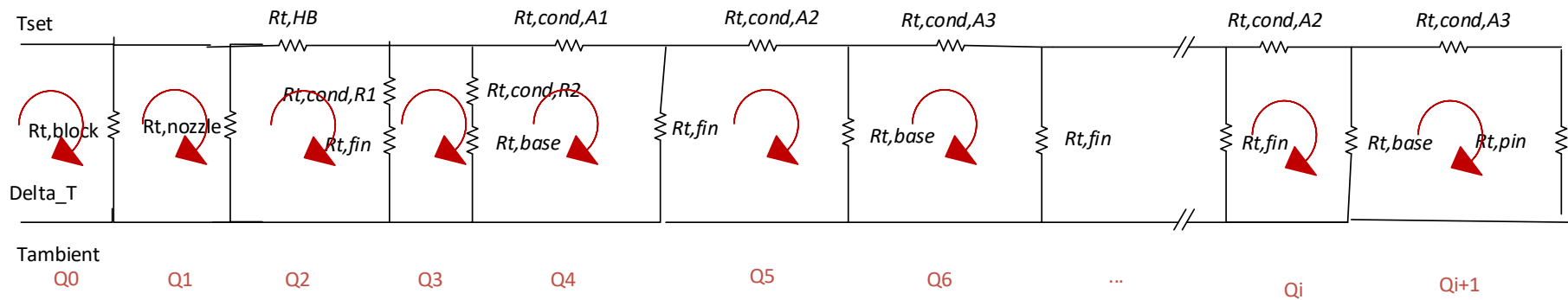


Figure 4.10: Circuit as mesh currents of the thermal resistance.

Setting up the equations:

$$\text{Mesh 1: } \Delta T = Q_0 \times R_{t,block} - Q_1 \times R_{t,block}$$

$$\text{Mesh 2: } 0 = -Q_0 \times R_{t,block} + Q_1 \times R_{t,nozzle}$$

Chapter 4 Development of a CF/PEEK FFF Feedstock Production Process

$$\text{Mesh 3: } 0 = -Q1 \times R_{t, \text{nozzle}} + Q2 \times (R_{t, \text{nozzle}} + R_{t, \text{HB}} + R_{t, \text{cond}, R1} + R_{t, \text{fin}}) - Q3 \times (R_{t, \text{cond}, R1} + R_{t, \text{fin}})$$

$$\text{Mesh 4: } 0 = -Q2 \times (R_{t, \text{cond}, R1} + R_{t, \text{fin}}) + Q3 \times (R_{t, \text{cond}, R1} + R_{t, \text{fin}} + R_{t, \text{cond}, R2} + R_{t, \text{base}}) - Q4 \times (R_{t, \text{cond}, R2} + R_{t, \text{base}})$$

$$\text{Mesh 5: } 0 = -Q3 \times (R_{t, \text{cond}, R2} + R_{t, \text{base}}) + Q4 \times (R_{t, \text{cond}, R2} + R_{t, \text{base}} + R_{t, \text{cond}, A1} + R_{t, \text{fin}}) - Q5 \times R_{t, \text{fin}}$$

$$\text{Mesh 6: } 0 = -Q4 \times R_{t, \text{fin}} + Q5 \times (R_{t, \text{fin}} + R_{t, \text{cond}, A2} + R_{t, \text{base}}) - Q6 \times R_{t, \text{base}}$$

$$\text{Mesh 7: } 0 = -Q5 \times R_{t, \text{base}} + Q6 \times (R_{t, \text{base}} + R_{t, \text{cond}, A3} + R_{t, \text{fin}}) - Q7 \times R_{t, \text{fin}}$$

...

$$\text{Mesh } i+1: 0 = -Q_{i-1} \times R_{t, \text{fin}} + Q_i \times (R_{t, \text{fin}} + R_{t, \text{cond}, A2} + R_{t, \text{base}}) - Q_{i+1} \times R_{t, \text{base}}$$

$$\text{Mesh } i+2: 0 = -Q_i \times R_{t, \text{base}} + Q_{i+1} \times (R_{t, \text{base}} + R_{t, \text{cond}, A3} + R_{t, \text{pin}}) \tag{4.7}$$

Hence, the mesh analysis matrix of the thermal resistance circuit of the HotEnd can be established as below:

Chapter 4 Development of a CF/PEEK FFF Feedstock Production Process

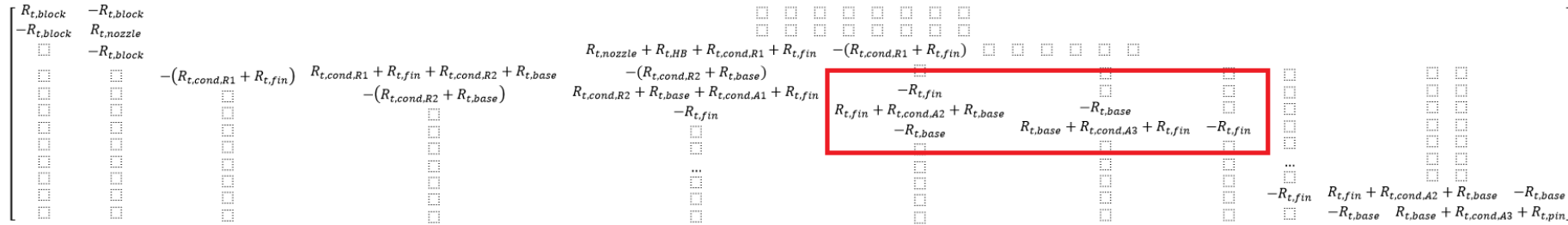


Figure 4.11: Repeating part of the mesh analysis matrix.

Then vector Q can be obtained by solving the $T = \mathbf{R}Q$. After obtaining the solution for the Q vector, the individual heat flow vector q can be obtained. And finally the value of ΔT as a potential drop over each individual thermal resistance of the HotEnd can be obtained.

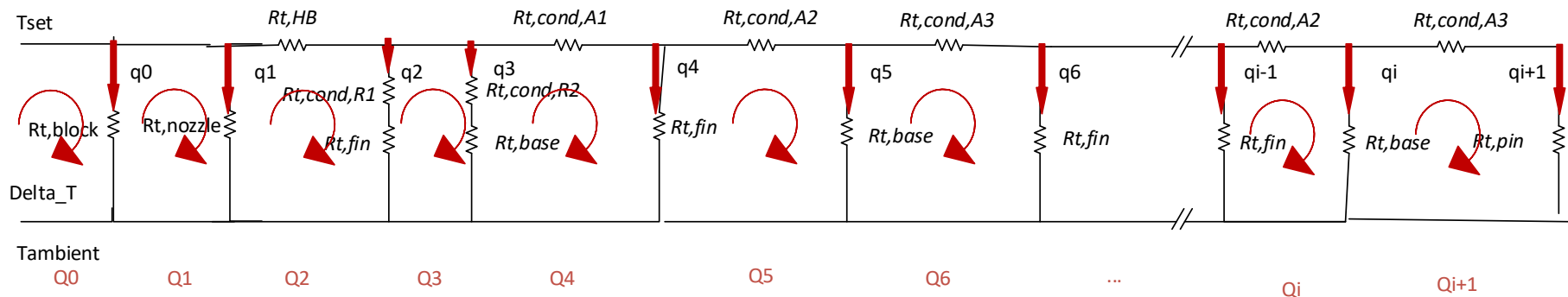


Figure 4.12: Circuit as mesh currents of the thermal resistance.

As shown in Figure 4.10, the equations to calculate q and ΔT are obtained:

$$\begin{aligned}
 &1. q_0 = Q_0 - Q_1; \Delta t_0 = q_0 \times R_{t,block} \\
 &2. q_1 = Q_1 - Q_2; \Delta t_1 = q_1 \times R_{t,nozzle} \\
 &\dots \\
 &i. q_i = Q_i - Q_{i-1}; \Delta t_i = q_i \times R_{t,base} \\
 &i+1. q_{i+1} = Q_{i+1}; \Delta t_{i+1} = q_{i+1} \times R_{t,pin} \tag{4.9}
 \end{aligned}$$

The benefit of this model is its generality. Using the building blocks derived for this model, the working of any type of annular finned HotEnd heatsink can be described, not just the E3D HotEnd. This is because the parameters in the model, such as the part dimension, HotEnd materials (e.g. some of the heatblock models for all-metal HotEnds are made by aluminium, while others are made of copper, etc.), the number of the fins and fan flow velocity of the heatsink can easily be adapted in order to accurately describe the HotEnd design.

4.2.3 Model Verification

As mentioned in Section 4.2.1, this model has been verified against the 3D numerical study by Jerez-Mesa *et al.* [100]. In their paper, Jerez Mesa *et al.* used the Finite Element Method (FEM) to model the temperature distribution in an all-metal HotEnd of a BCNozzle liquefier and compared this with experimental results. They used thermocouples attached onto a number of discrete points on the heated HotEnd while the fan was turned on and a steady-state temperature distribution was attained. The experimentally obtained temperatures for these points on the HotEnd were subsequently compared to the temperatures for these locations as predicted by the FE model. The obtained experimental were found to be similar to those predicted using the FEM modelling. Their modelling and experimental results are shown in Figure 4.13.

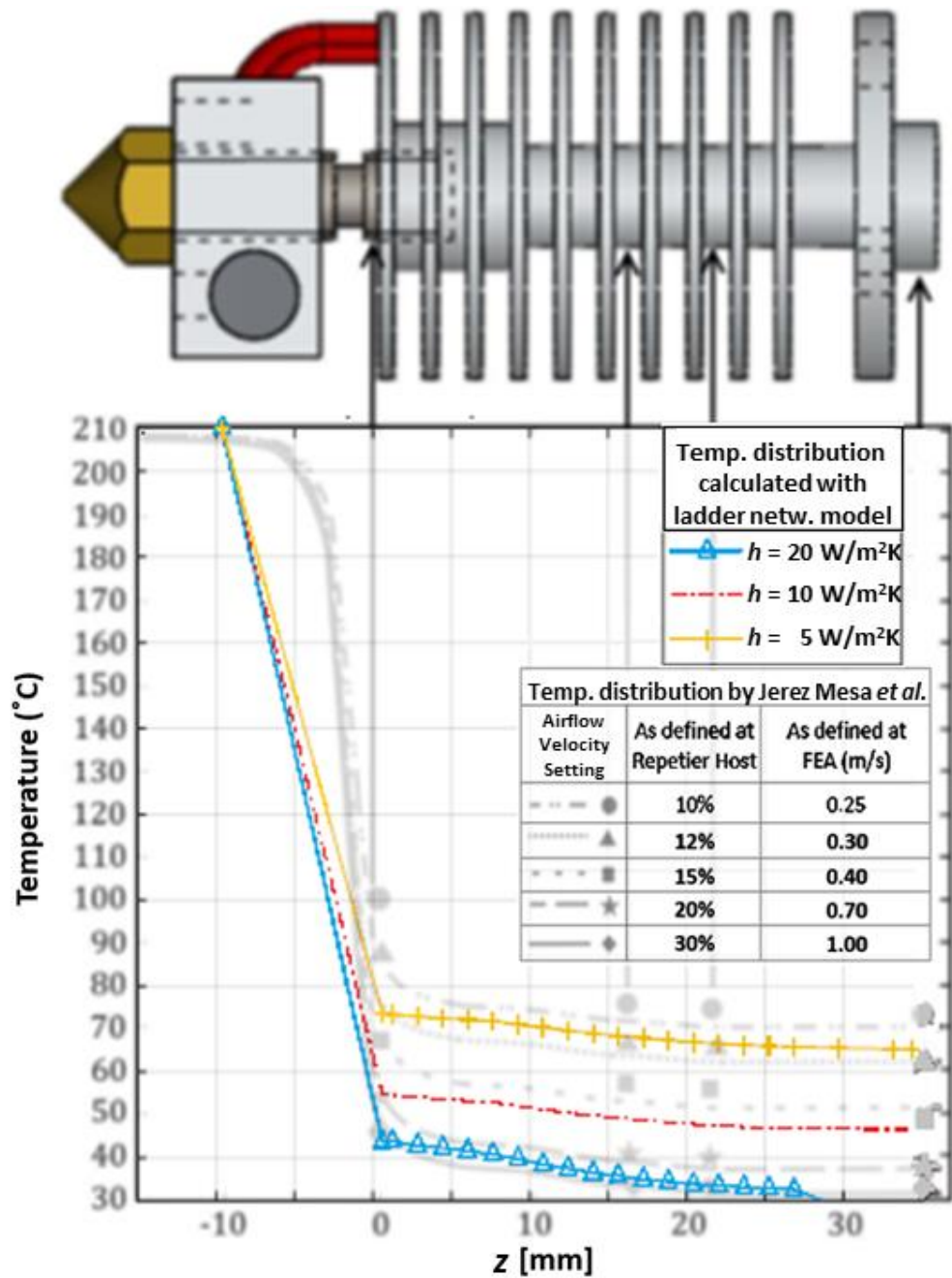


Figure 4.13: Comparison of temperature distributions along the nozzle for different fan velocities ladder network model calculated (coloured lines) with the experimental results (grey markers) and RDA results (grey lines) by Jerez Mesa *et al.* [100].

Table 4.2 shows the materials of each of the components in the HotEnd assembly in the Jerez-Mesa *et al.* paper [100].

Table 4.2: The materials from which the individual components in the HotEnd assembly in the Jerez-Mesa et al. [100] are made.

| Part description | Material |
|------------------|------------------------|
| Heatsink | Aluminium AW-3003-H18 |
| HeatBreak | Stainless steel 1.4306 |
| Heatblock | Aluminium AW-3003-H18 |
| Nozzle | Brass EN CW614N |

The CAD drawings of their components can be found on the GitHub page for the manufacturer of BCN3D[241]. The diameters of each of the components are given in Table 4.3.

Table 4.3: Diameters for each part in the Jerez-Mesa et al [100].

| Part description | Size (mm) |
|--------------------------------------|-----------|
| HeatBreak, Part I, r_{out} | 2.6 |
| HeatBreak, Part I, r_{in} | 1.7 |
| HeatBreak, Part II, III, length | 3.2 |
| HeatBreak, Part II, length | 0.95 |
| HeatBreak, pin II, r_{out} (side) | 2 |
| Heatsink, pin I, length | 3.1 |
| Heatsink, pin I, d_{out} | 5.4 |
| Heatsink, pin II, r_{out} | 4.7 |
| Heatsink, pin II, r_{in} | 1.7 |
| Heatsink, pin III, length | 1.9 |
| Heatsink, pin III, d_{out} | 5 |
| Heatsink, fin, total d_{out} | 23.8 |
| Heatsink, fin, bottom base d_{out} | 9.4 |
| Heatsink, fin, top base d_{out} | 6.2 |
| Heatsink, fin, d_{in} | 5.2 |
| Heatsink, fin, thick | 1.3 |
| Heatsink, base, short length | 1.9 |
| Heatsink, base, long length | 4.4 |

The next step is to obtain the value of each of the thermal resistances and build the thermal resistance circuit and the corresponding thermal resistance matrix. This assembled matrix is found to be a diagonal matrix as can be found in Section 4.2.2, Figure 4.11. Subsequently, the heat flow matrix Q can be obtained by $Q = R^{-1} \cdot \Delta T$ after which the temperature distribution of the HotEnd can be obtained by calculating heat flux q through each thermal

resistance. In Figure 4.13 in colour lines, a plot of the temperature distribution of the BCNozzle HotEnd based on the ladder network model can be found. This temperature distribution is from where the heatbreak is attached to the heatblock up to the top of the heatsink where the filament enters the HotEnd. The scale uses the same horizontal scale as Jerez-Mesa *et al.* in Figure 4.2 (with grey lines). This plot shows the temperature distribution for different values of heat transfer coefficient h , since h is largely dependent on the ambient air velocity. The results for $h = 5$ to $20 \text{ W/m}^2\text{K}$, are very similar to the results from the finite element analysis presented by Jerez-Mesa *et al.* [100, 242] at the airflow velocities defined in their numerical analysis; where 0.25 m/s corresponds to $h = 5 \text{ W/m}^2\text{K}$, 0.40 m/s to $h = 10 \text{ W/m}^2\text{K}$ and 1.00 m/s to $h = 20 \text{ W/m}^2\text{K}$. However, it is not straightforward to relate the h with the fan speed. Ideally, there should be future experiments to correlate the fan speeds with the air forced convection coefficient h . However, this is out of scope for this work.

4.2.4 Ladder Network Model on E3D All-metal HotEnd

Now take E3D V6 all-metal HotEnd [99] as an example to verify this model. Table 4.4 is the materials set up for each part of the HotEnd:

Table 4.4: The build-up materials of the HotEnd in each part.

| Part description | Material |
|------------------|---------------------|
| Heatsink | Aluminium 6061 |
| Heatbreak | Stainless steel 303 |
| Heatblock | Copper |
| Nozzle | Brass |

The assumptions are as follows:

- The system is under steady-state conditions;
- The heatblock with the nozzle has a constant thermal property;
- The system has a negligible radiation exchange with surroundings;
- The heatsink has a uniform convection coefficient over outer surface (with or without fins).

Based on the ladder network model established for the HotEnd in Section 4.2.2, with the equations that describe the thermal resistances given in Table 4.1, the numerical values of these thermal resistances of each part are calculated below:

1. Calculation of the heatbreak ($k=16.2$ (W/mK)):

$$R_{t,HB1} = \frac{\ln \frac{r_2}{r_1}}{2\pi Lk} = 5.6278(K/W) \quad (4.10)$$

Where $r_2 = 2.725$ mm, which is half way of the M6 thread, $r_1 = 1$ mm, $L = 1.75$ mm.

$$R_{t,HBII} = \frac{L}{kA} = 35.0983(K/W) \quad (4.11)$$

Where $L = 2.1$ mm, $A = \frac{\pi}{4}(d_2^2 - d_1^2)$, $d_2 = 2.95$ mm, $d_1 = 2$ mm.

$$R_{t,HBIII} = \frac{\ln \frac{r_2}{r_1}}{2\pi Lk} = 4.4777(K/W) \quad (4.12)$$

Where $r_2 = 3.125$ mm, $r_1 = 1$ mm, $L = 2.5$ mm.

Hence,

$$R_{t,HB} = R_{t,HB1} + R_{t,HBII} + R_{t,HBIII} = 5.6278 + 35.0983 + 4.4777 = 45.2038 (K/W) \quad (4.13)$$

2. Calculation of the heatsink ($k = 167$ (W/mK), $h = 200$ (W/m²k),)

$$R_{t,cond,R1} = \frac{\ln \frac{r_2}{r_1}}{2\pi Lk} = 0.5388(K/W) \quad (4.14)$$

Where $r_2 = 5.5$ mm, $r_1 = 3.125$ mm, $L = 1$ mm.

$$R_{t,cond,R2} = \frac{\ln \frac{r_2}{r_1}}{2\pi Lk} = 0.3592(K/W) \quad (4.15)$$

Where $r_2 = 5.5$ mm, $r_1 = 3.125$ mm, $L = 1.5$ mm.

$$R_{t,cond,A1} = \frac{L_1}{kA} = 0.0448(K/W) \quad (4.16)$$

Where $L_1 = 0.5\text{mm}$, $A = \frac{\pi}{4}(d_2^2 - d_1^2)$, $d_2 = 11\text{mm}$, $d_1 = 6\text{mm}$.

$$R_{t,cond,A2} = \frac{L_2}{kA} = 0.0738(\text{K/W}) \quad (4.17)$$

Where $L_2 = 1\text{mm}$, $A = \frac{\pi}{4}(d_2^2 - d_1^2)$, $d_2 = 11\text{mm}$, $d_1 = 4.2\text{mm}$.

$$R_{t,cond,A3} = \frac{L_3}{kA} = 0.1106(\text{K/W}) \quad (4.18)$$

Where $L_3 = 1.5\text{mm}$. $A = \frac{\pi}{4}(d_2^2 - d_1^2)$, $d_2 = 11\text{mm}$, $d_1 = 4.2\text{mm}$.

$$R_{t,fin} = \frac{1}{hA_f\eta_f} = 8.7029(\text{K/W}) \quad (4.19)$$

Where $A_f = 2\pi(r_{2c}^2 - r_1^2) = 0.00060476(\text{m}^2)$, since $r_{2c} = r_2 + (t/2) = 0.0115(\text{m})$, $h = 200(\text{W/m}^2\text{k})$, $L_c = L + \frac{t}{2} = 0.0055(\text{m})$, then obtain $A_p = L_c \times t = 0.0000055(\text{m}^2)$, hence, $L_c^{3/2}(h/kA_p)^{1/2} = 0.1903$. Hence, from Figure 3.19 of *Introduction to Heat Transfer* [243], the fin efficiency is $\eta_f \approx 0.95$.

$$R_{t,base} = \frac{1}{hA_b} = 96.4575(\text{K/W}) \quad (4.20)$$

Where $A_b = \pi dL = 0.000051836\text{m}^2$.

3. Calculation of heatsink ($h = 5(\text{W/m}^2\text{k})$),

$$R_{t,pin} = \frac{1}{hA_f\eta_f} = 610.9991(\text{K/W}) \quad (4.21)$$

Where $L_c = L + \left(\frac{D}{4}\right)$, $A_f = \pi D L_c = \pi D \left(\frac{D}{4} + L\right) = 7.389 \times 10^{-4}(\text{m}^2)$, $\eta_f = \frac{\tanh mL_c}{mL_c} = 0.443$

4. Calculation of heatblock

Since it is assumed that the temperature of heatblock and nozzle are constantly the same, and there is no temperature distribution of these parts, hence in the calculation, only convection thermal resistance is considered, and the heatblock and nozzle can be considered as the unique one part.

$$R_{t,heatblock} = \frac{1}{hA} = 117.6471(\text{K/W}) \quad (4.22)$$

4.2.5 Experimental Verification of the Thermal Network Modelling with the Selected HotEnd

The next stage was to conduct experiments in order to obtain results against which to assess the accuracy of the results from the ladder network model. An additional purpose of the experiment was to optimise the speed of the heatsink fan to obtain a target heatsink temperature distribution, since this greatly affects the heat dissipation. In this analysis the E3D V6 HotEnd was studied as this was the most likely candidate for the designed pultrusion rig's heating element, and also to verify the calculations in Section 4.2.5 .

Comparison of the analytical, ladder network model results against experiment results allowed the model to be refined. The experimental comparison was made against the temperature distribution predicted by the model, since the distribution is calculated in addition to the heat flow. In order to measure the temperature distributions experimentally, a FLIR T400-series infrared camera [244] was utilised. The experimental set up is shown in Figure 4.3.

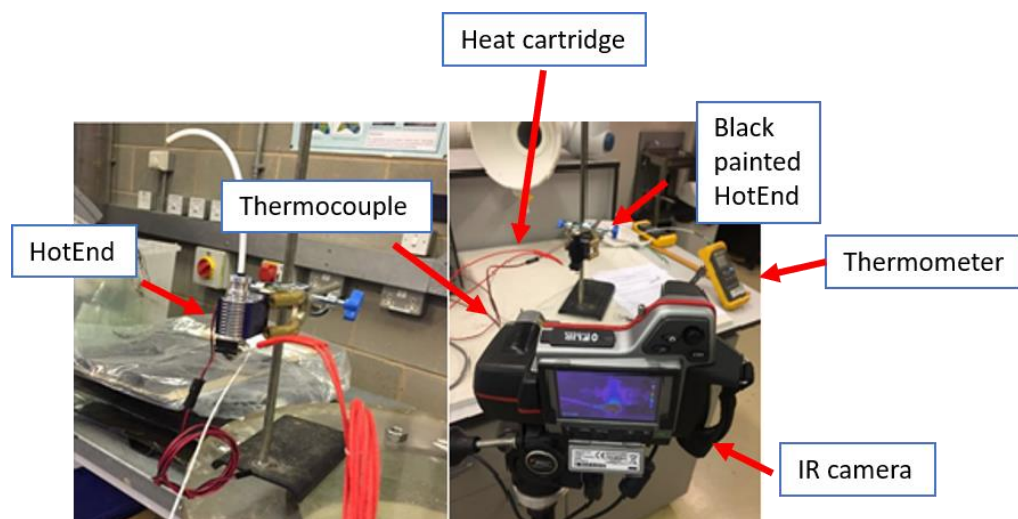
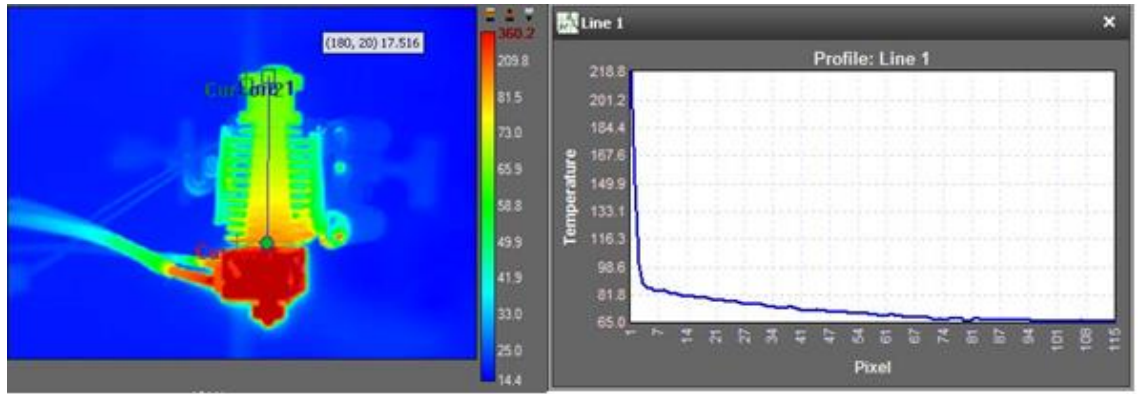


Figure 4.14: HotEnd IR measurement experimental set-up.

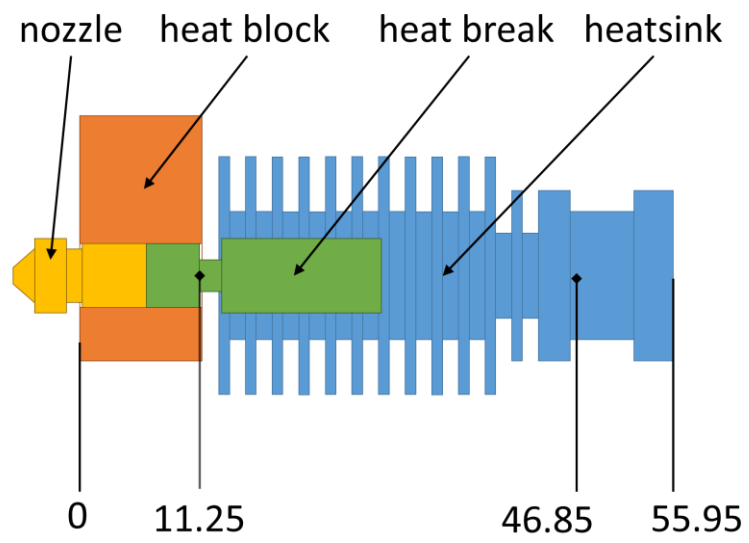
In the experiment, the HotEnd was painted black in order to come as close as possible to an ideal blackbody surface. When an object is painted black, the

amount of reflection from the object and the reflection signal captured by the IR camera are significantly reduced and the spectrum of the emitted infrared radiation depends almost solely on the temperature of the object, as described by Planck's law [245], and not on its shape or composition. Painting an object black with the standard lab paint used resulted in an object emissivity of 0.86, so accordingly the standard setup procedure of the IR camera to read the HotEnd temperature was used, as outlined in Ref. [12]. The distance of measurement was 0.3 m. The measurement was taken after the HotEnd reached a stable target temperature as indicated by the connected thermocouple, so that a steady-state temperature was measured without the filament loaded. The experimentally found temperature distribution at the nozzle with a set temperature of 420°C is shown in Figure 4.15 (a). The temperatures calculated with the ladder network model for this setup and set temperature is given in Figure 4.15 (c) and 4.16 (note that in 4.15 (c) the x -axis is converted from length to pixel in order to compare the result with Figure 4.15 (a)). The IR captured temperature distribution is illustrated with the thick purple line in Figure 4.15 (c)). In the modelling, the temperature distribution starts at the upper edge of the heatblock, and ends at the lower edge of the heatsink top pin, whereas the placement of cursors during IR analyses shows small variation due to the accuracy with which this could be achieved with this experimental set up. However, the model can still be validated by the similar trends from the experimental results. Note that in Figure 4.15 (b), 11.25 mm and 46.85 mm mark the beginning and the end of the modelled range in the results and these two points are overlaid with the two points in the experimental results to obtain the pixel numbers from the experimental results in the plot. The associated HotEnd model can be found in Section 4.2.4.

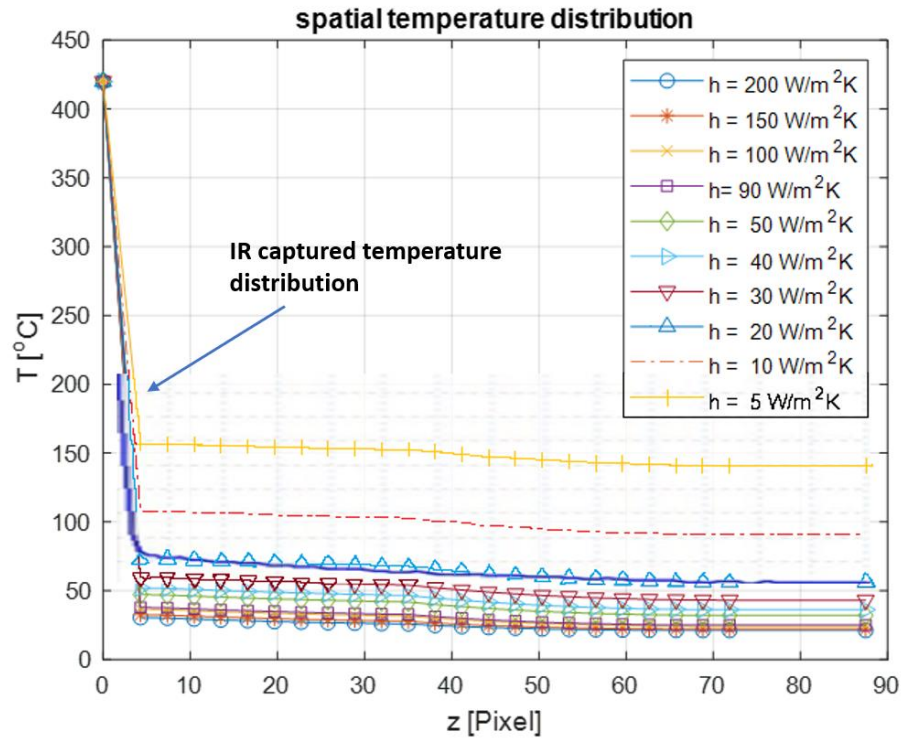
Using $q = \frac{\Delta T}{R_{HB}}$, the thermal power loss is calculated as 8.85 W.



(a)



(b)



(c)

Figure 4.15: (a) Infrared capture and temperature distribution of heatsink at nozzle 420°C. (b) modelling domain of the HotEnd, starting with the heatblock on the left to the heatsink on the right, all lengths in mm. (c) Ladder network model result at nozzle high temperature to compare with the IR measurement result (in thick purple line).

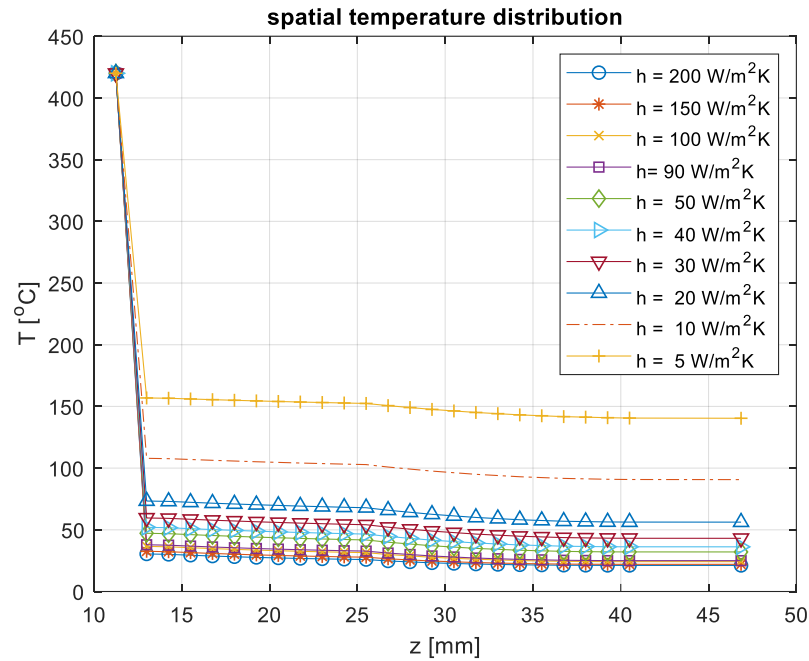
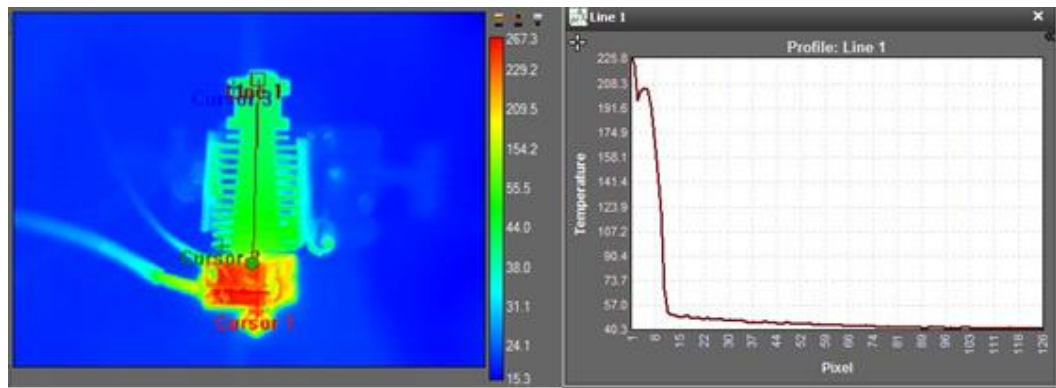
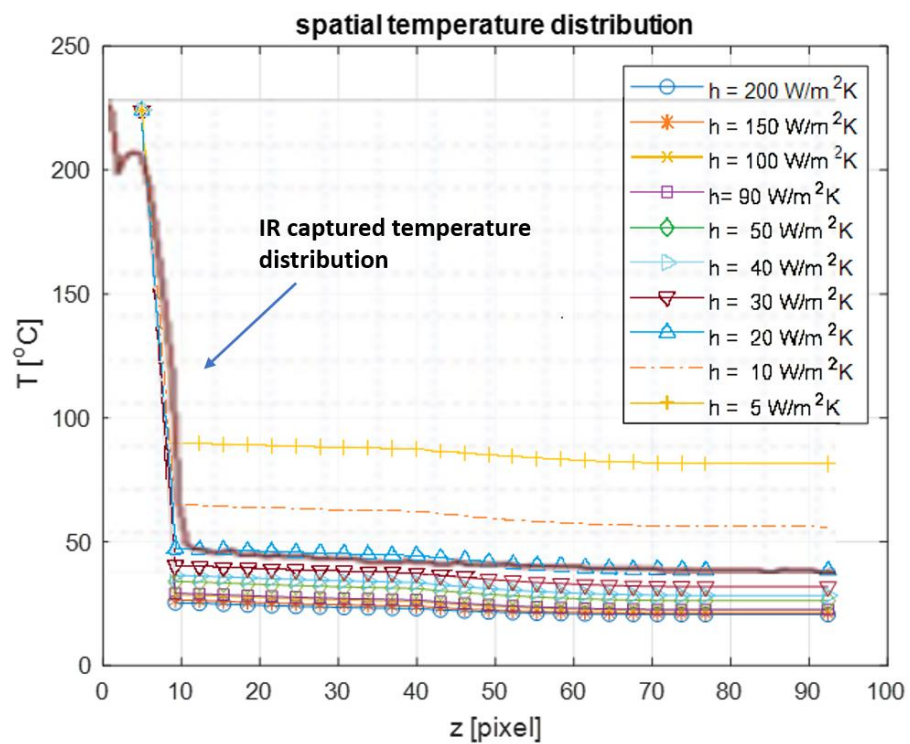


Figure 4.16: Ladder network model result at nozzle high temperature.

The experimental result for the case when the nozzle is heated up to a temperature of 224°C is shown in Figure 4.17 (a). The result calculated by the ladder network model of this intermediate temperature imposed on the nozzle is shown in Figure 4.17 (b) and 4.18 (note that 4.17 (b) the x-axis is converted from length to pixel in order to compare the result of Figure 4.17 (a) using the same length scale of 4.17 (b)). The IR captured temperature distribution is illustrated with the thick red line in Figure 4.17 (b)). Using $q = \frac{\Delta T}{R_{HB}}$, the thermal power loss is calculated as 4.42 W.



(a)



(b)

Figure 4.17: (a) Infrared capture and temperature distribution of heatsink at nozzle 224°C. (b) Ladder network model result at nozzle low temperature to compare with the IR measurement result (in thick red line).

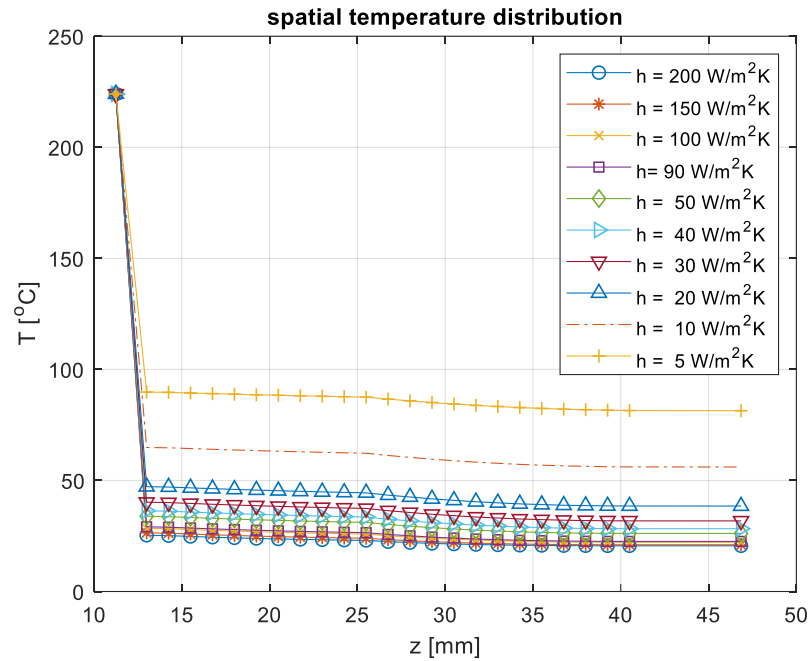


Figure 4.18: Ladder network model result at nozzle low temperature.

4.2.6 Conclusions

The main findings of this analytical and experimental study are:

- The experimental data are found to be a good fit to the calculated results assuming a value of forced air convection heat transfer coefficient of $20 W/m^2K$. This is a reasonable and realistic value for h , which can be compared to Ref [240].
- These experiments validated the calculated result with the ladder network method. This is especially clear in the trends of the temperature distribution with a large temperature drop (and gradient) over the heatbreak. The physical explanation for this is that the thermal resistance of the heatbreak is very large and therefore only a small amount of heat is flowing through the heatbreak and is almost directly dissipated into the surrounding air.
- Experimental and analytical studies confirmed the suitability of this E3D HotEnd for the heating system for pultrusion apparatus, since the temperature drop over the heatbreak is good enough to have (nearly) the whole heatsink region operating at a lower temperature than $65^\circ C$,

which is sufficiently low for the PEEK to be fed into the HotEnd without melting.

- As can be seen in Figure 4.15 (c) and Figure 4.17 (b), the IR measurement closely matches the calculated distribution for $h = 20 \text{ W/m}^2\text{K}$ with approximately 10% error for the 24 – 43 mm range of the z coordinate. The analytical model developed to analyse the HotEnd is a useful tool, since this tool is simpler, and computationally faster than the FEA HotEnd evaluation of Jerez-Mesa *et al* [100], and it obtains the similar results. This tool can quickly evaluate the suitability of a HotEnd for a particular application and/or to design a HotEnd and select a suitable operating temperature.

4.3 Design of the Pultrusion Apparatus

As mentioned previously, since the selected feedstock material has very little flexural stiffness, it is difficult to extrude this material directly to the 3D printer nozzle as it will buckle when it is pushed into the HotEnd by the extruder. This is the reason a process has been developed in order to convert the commingled CF/PEEK into a filament suitable for FFF 3D printing. This pre-processing will convert the commingled fibres into a consolidated semi-stiff material; which will be easier to print using the FFF process. An inverted extrusion process is used which involves pulling the material through a die, known as pultrusion [37]. In the following subsections, the design of the pultruder is presented. Firstly, based on the functional analysis of the pultrusion process, the system architecture is established. Subsequently, the conceptual design is worked out and its components are sized. Thereafter, the control design is explained, and finally, the steps taken to get the process running are discussed.

4.3.1 Functional Analysis and System Architecture

The architecture of the pultrusion system includes four subsystems: the support to hold the supply of commingled fibres; a heating system with the

dies to consolidate the commingled fibres, a traction system to pull the filament, and the final spool to store the filament and transfer it to a high temperature 3D printer. Figure 4.19 shows each of these subsystems required to execute the pultrusion process. In the diagram the thick arrows symbolise the material flow and the thin arrows the function of each of the modules.

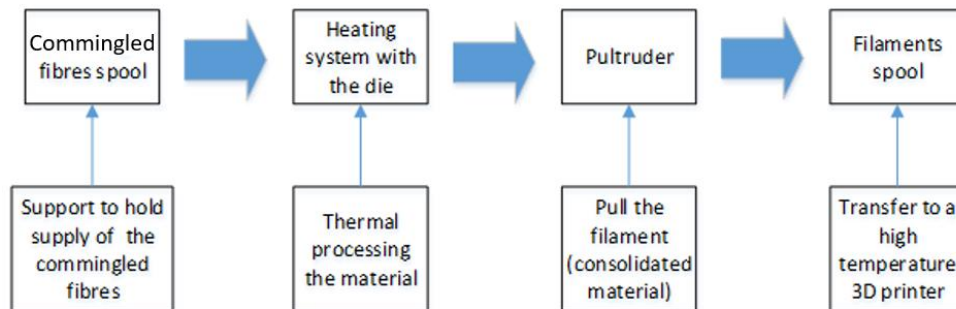


Figure 4.19: Pultrusion system diagram.

The support of each of the modules is designed to keep the filament horizontally aligned during the process. After the thermal analysis of the HotEnd described in the previous section, it was found that the E3D high temperature HotEnd may be utilised without alterations to its thermal design as the heating system for the die. The standard thread and diameter of the nozzle mounting hole also allows for the mounting of a specially designed die. This die has a stepwise tapered entry followed by a 0.5 mm diameter section where the PEEK matrix material can melt. As shown in Section 4.3.3, Figure 4.21, the final diameter determines the final consolidated diameter. Different controllers were used to control the temperature and stepper motors in order to have fully independent control of the variables during the experiments.

4.3.2 Conceptual Design and Its Evolution

Once the functional requirements for the designed pultrusion apparatus had been established, the next step in the design cycle was the conceptual design and its iterations. The pultruder-bracket assembly design went through several iterations. The pultruder includes a pulling wheel controlled directly by the stepper motor, and a pushing wheel which is in contact with the pulling wheel and can be rotated by it. A Stratesys OBJET printer [246] was used to print both

wheels on a single build platform with a one-step process. OBJET technology is capable of multimaterial jetting, enabling functionally graded materials. Wheels were printed with a tough material in the centre and a flexible rubber ring on the outside. On the radial centre line of the pulling wheel's running surface, a groove was designed to work as a guide to keep the consolidated filament in the centre.

The second design iteration slightly improved the push head of the pultruder, however, it was not effective enough. For the third version, and final, version, spacers were introduced on each side of the wheels to achieve better wheel alignment. This version also introduced a spring on the top in order to push the pushing wheel into contact with the pulling wheel. The first version of the pultruder assembly is shown in Figure 4.20 (a) and the final version is shown in Figure 4.20 (b).

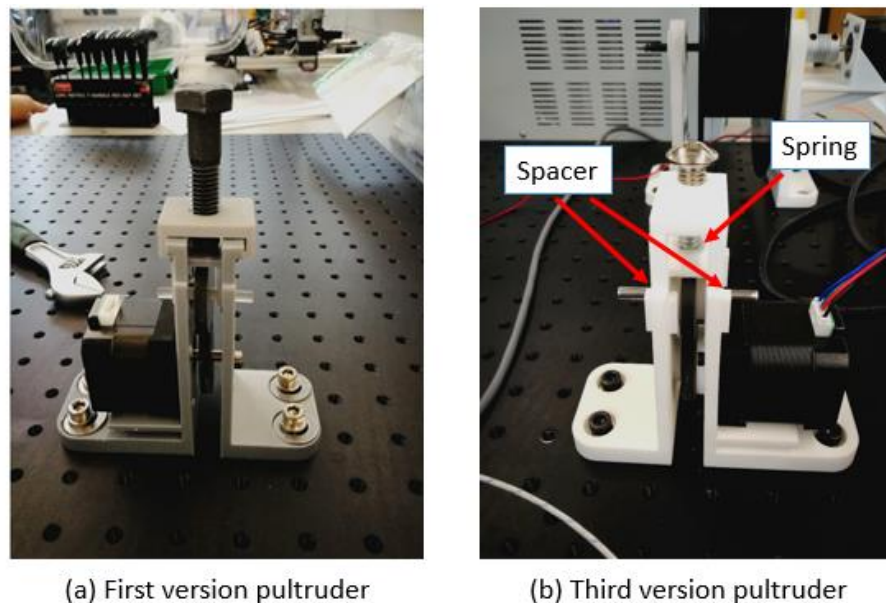


Figure 4.20: Pultruder Prototypes.

4.3.3 Calculation of the Pultrusion Die Diameter for Full Consolidation of the Filament

The diameter of the die is calculated based on the assumption of preservation of mass and density throughout the process. This ideal of mass preservation however, does not exist in reality as small amounts of PEEK leak out from the

die. Additionally, there is some degree of die-swell, also known as extrudate swell or Barus effect, caused by the elastic springback of the polymeric macromolecules undergoing a reorientation when passing through a narrow orifice, such as a pultrusion die [124]. This effect increases the outgoing diameter of the filament and creates porosity.

The consolidation diameter is calculated with the following relation [36]:

$$D = 2 \sqrt{\frac{TEX}{\rho_{comb}\pi}} \quad (4.22)$$

Where D is the diameter of the consolidated filaments. TEX is the linear mass of the commingled fibre, 307.7 TEX (g/km), and ρ_{comb} is the density of the CF/PEEK commingled fibres. The densities of carbon fibre and neat PEEK are $\rho_{CF} = 1780 \text{ kg/m}^3$, $\rho_{PEEK} = 1300 \text{ kg/m}^3$ respectively; with a volume fraction of carbon fibre of 57.4%, the combined density of the commingled fibres is then $\rho_{CF/PEEK} = 1575.5 \text{ kg/m}^3$. This yields a diameter of the consolidated filament of 0.4987 mm of $0.5 \pm 0.0013 \text{ mm}$.

Initial work to create a start point on the unconsolidated strand revealed that a gradual reduction of the diameter is required for smooth entry of the commingled strand. Therefore, a die with a stepwise, gradual reduction was designed and manufactured within the university, as acquisition of a smoothly tapered die which is designed and manufactured specially by an external supplier would be expensive and time consuming. This die design with a stepwise gradual reduction of the diameter, however, can conveniently be made by machining a standard sized bolt (M6). The material selected to make the pultrusion die out of a bolt was stainless steel as its hardness prevents excessive wear of the die, to keep the diameter stable. Since the surface of the nozzle, which is exposed to the air, did not have any additional cooling, the stainless steel nozzle could still reach the designed temperature when in the steady-state status. A cross section of the die nozzle is given in Figure 4.21. The final 0.5 mm diameter hole in the die, seen at the right hand side of the figure,

protrudes a further 5 mm, meaning there is a further 5 mm fully wetted inner diameter in this die.

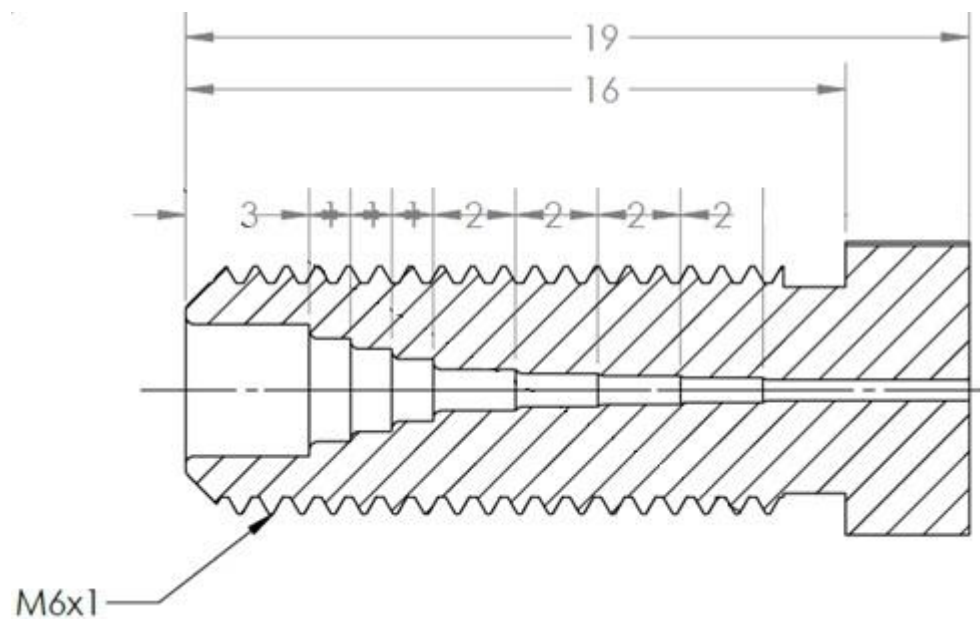


Figure 4.21: Cross section of pultrusion die (unit: mm).

4.3.4 Mechanical Design and Component Sizing

Before the mechanism design could be designed, a theoretical torque required to pull the commingled fibres was calculated, making the following assumptions:

- Irrespective whether a pultruder or just a pulling wheel is used in the pultruder apparatus, the energy required to pull a length of material from the spool of commingled fibres through the pultrusion die is the same.
- As the power required to pull the commingled fibres through the die is independent from the power required to wind up the consolidated filament, these two power requirements can be superimposed onto each other and a bending moment of the filament can be used to estimate the required filament winding torque.

For the mechanical design and sizing of the components, only the shafts are considered here, since the 3D printed support brackets and wheels are already

over-dimensioned in terms of thicknesses. To determine the minimum shaft diameter two failure scenarios were considered due to shear stress. The first considered was the shaft to be in double shear. This double shear happens when the pulling forces on the shaft-reel interface and the reaction forces on the shaft-bearing interface act as a shear force on the shaft. The second scenario considered the shear stress perpendicular to the radius of the shaft, which resulted from the applied torque that twists the shaft. Hence, Section 4.3.4.2 is divided into two subsections to calculate each scenario. However, before investigating these scenarios, the drive torque was first calculated since this is the torque that twists the shaft and it is also proportional to the pulling force that brings the shaft in double shear.

4.3.4.1 Required Torque Calculation

The required torque for the actuation of the winding spool is the torque that is required to overcome the mechanical forces and moments needed for the processing in each of the modules discussed in Section 4.3.1. These are illustrated in Figure 4.22. Firstly, there is the commingled strand wound around the reel in the left hand side of the system. When the commingled strand is unwound, the bending stiffness of the commingled fibre strand was negligible. When the consolidated filament is wound around the reel on the right hand side in the picture, the filament needs to be bent around the reel, requiring another bending moment. For ease of modelling, the commingled fibres can be considered to be a bundle of loose fibres and the consolidated material a solid strand of mixed fibres. In the die there is a region where dry friction occurs due to the weight of the commingled strand. This friction force will be relatively small and will form a negligible contribution to the overall required pulling forces. Where the die diameter approaches the consolidated diameter, it is assumed there is no melt and the increased temperature does not affect the friction coefficient. In this region some “squeezing” of the fibres occurs and the fibres in the strand will be pushed into a new arrangement. This depends on factors which are hard to quantify, as the arrangement and twist of the individual fibres is not known *a priori*. The ‘squeeze’ will increase the

contacting force between the strand and the die and hence increase the friction and also the rearrangement of the fibres will require a certain amount of force, both which are hard to quantify. Because of these unknown behaviours, it is in turn difficult to make quantitative predictions on the size of the 'squeeze' affected region. Additionally, some melting will occur in this region, of unknown size, causing the presence of viscous friction. Although the pulling force in this region will have a more significant contribution on the entire pulling forces in the system, these are very hard to quantify without further tests. It was assumed that the melting of PEEK starts 3 mm ahead of the final stage of the die and this region will be dominated by viscous friction. This is well away from the final stage in the die, as can be seen in Figure 4.21. Finally, there are the viscous friction forces caused by the (almost) pure shear flow (also known as the Couette flow) of the molten PEEK in the outer layers of the strand.

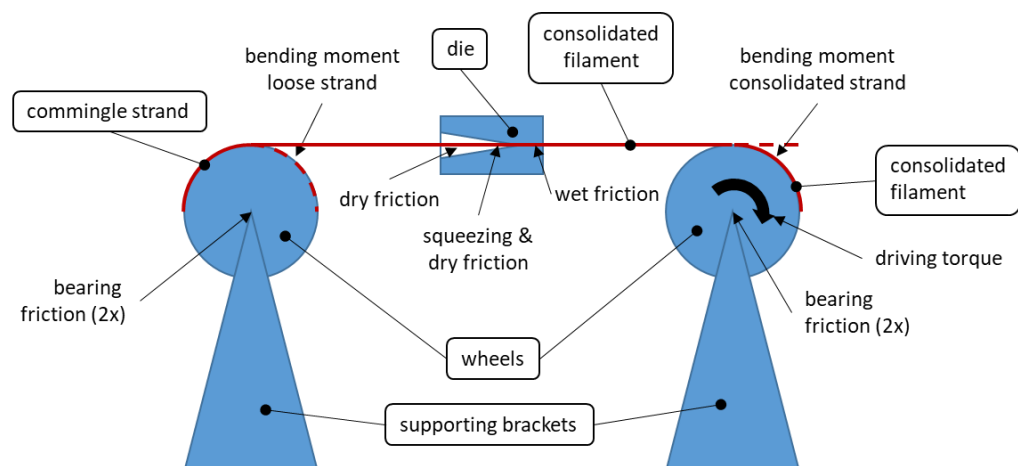


Figure 4.22: Sources of friction to be overcome by the driving torque.

To reduce unnecessary complexity in these calculations the pultruder is assumed to be driven by the pulling spool wheel only. Under steady-state conditions, the power for a rotating shaft is proportional to the torque and the angular velocity:

$$P_{rot} = T\omega \quad (4.23)$$

Furthermore, under steady-state conditions, the power required for a system undergoing linear motion holds that it is proportional to the force and the linear velocity:

$$P_{trans} = Fu \quad (4.24)$$

These equations show that the pulling forces in the die are easily related to the torque required for the motor to drive the pulling wheel.

The sources of friction shown in Figure 4.22, are all seen by the motor driving the pulling wheel as a torque, T_{total} . However, the viscous friction and dry friction are calculated as forces, but the bearing friction and bending moments of the filament for winding and unwinding are calculated directly as torques. Finally, the total pulling force, $F_{pulling}$, is the force that is seen by the pulling wheel and it creates a reaction force on the shaft, that acts as a shearing force, as will be shown later. The remainder of Section 4.3.4.1 is devoted to the calculation of the friction to provide reasonably accurate estimates to calculate the total pulling force and total torque, which in turn allows calculation of the minimum allowable shaft diameter.

4.3.4.1.1 Viscous Friction in the Die

Firstly, the viscous friction in the die is calculated. As mentioned above, the main assumption is that the friction all occurs due to shear flow in the die. Since molten PEEK has a high viscosity, it is assumed here that PEEK residing in between the carbon fibres has no relative velocity with respect to the carbon fibres. For simplicity, it is furthermore assumed that there are no carbon fibres in contact with the die and therefore all fibres are wetted, which is the objective of the pultrusion process in the first place. Consequently, this means that the shear force occurs solely at the outer layer of the strand, which consists of purely molten PEEK. This flow velocity profile is schematically (materials not to scale) in Figure 4.23.

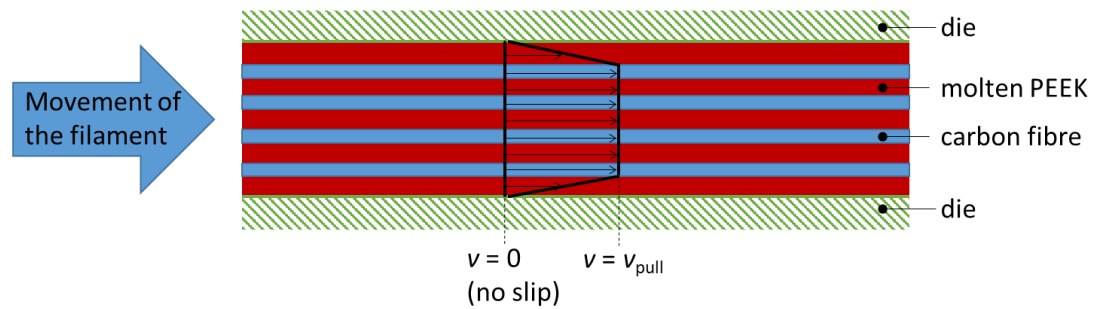


Figure 4.23: Velocity profile of CF/PEEK filament in the pultrusion die (not to scale).

The next step is to make a reasonable assumption about the film thickness where the shear flow occurs. The ideal consolidation would be where the carbon fibres are all wetted equally and distributed evenly after the pultrusion. In reality, the entropy increase in the system, difference in adhesive forces between PEEK and carbon fibre, and the adhesive forces between PEEK and the stainless steel die mean that the fibres will assume a random distribution. It should be noted here that the theoretical maximum fibre fraction is limited to touching fibres in the closest possible packing, namely 90.69 % [247]. The 57.4 % volume fraction is well below that theoretical fraction. In reality, it can be assumed, as also later microscopy tests revealed in Figure 5.4 in Section 5.4.3.1 Chapter 5, there will be regions in the cross section of finally formed filament with a relatively high density of fibres and regions with a lower density. Therefore it is not unrealistic to use a unit cell with a larger average spacing between the fibres, for which reason a representative elementary volume with square fibre arrangement is used to calculate the inter fibre distance. The shear region is assumed to be half of the inter-fibre distance.

In the unit cell (UC) used in these calculations, the space between the carbon fibres in this model is s . Furthermore, it is assumed that all friction in the system is due to the shear between PEEK and the inner side of the nozzle. This assumption requires that all carbon fibres are fully wetted by the PEEK, and the carbon fibre distribution is homogenous. This assumption can be considered reasonable to obtain the upper estimate of the friction forces since the viscous friction is considerable larger than the dry friction, although in

reality there may be areas where dry friction occurs, as can be seen in for instance Figure 5.4. This was also confirmed by the later investigation that established the outside area of the filament consists mostly of PEEK. The schematic drawing of a UC with square arrangement [248] is shown in Figure 4.24. The blue part with radius r represents a quarter carbon fibre and the white colour is PEEK after consolidation from the die.

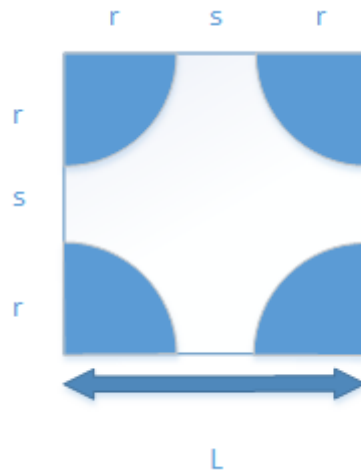


Figure 4.24: Unit cell of consolidated material.

Based on simple geometric relationships shown in the figure, from this unit cell the unknown inter fibre distance s can be worked out as follows. The following equations are from Ref [248]. The length L of the unit cell equals two times radius r and the inter fibre distance s .

$$L = 2r + s \quad (4.25)$$

Since the unit cell is square, its area A_{uc} can be worked out as follows:

$$A_{uc} = L^2 = (2r + s)^2 = 4r^2 + 4rs + s^2 \quad (4.26)$$

The total amount of carbon fibre, A_{cf} in the unit cell covers an area of:

$$A_{cf} = r^2\pi \quad (4.27)$$

Relating this to the carbon fibre fraction Φ one gets: $A_{cf} = \Phi A_{uc}$,

Rearranging gives:

$$\frac{1}{\phi} A_{cf} = A_{uc} \quad (4.28)$$

Substitution of the expression for A_{uc} back into the equation and bringing every component in the equation to one side:

$$s^2 + 4rs + 4r^2 - \frac{r^2\pi}{\phi} = 0 \quad (4.29)$$

Then an expression with known ϕ and r is established and s can be calculated. All the material data used in this section, were taken from the Cocordia Technical Data Sheet [221], and Victrex Data [220] as the material comes from these suppliers. With $r = 3.07 \cdot 10^{-6}$ m and $\phi = 0.574$, $s = 10.40 \cdot 10^{-6}$ m is obtained.

Now that the inter fibre distance is found and therefore the assumed thickness of the shear film is known, the approximate shear stress and the viscous friction force can be calculated. Assuming molten PEEK behaves as a Newtonian fluid, the expression for the shear stress becomes [249]:

$$\tau = -\mu_{PEEK} \frac{du}{dy} = -\mu_{PEEK} \frac{u_{pultrusion}}{\frac{1}{2}s} \quad (4.30)$$

So, when the pulling speed is 5 mm/s, the shear stress $\tau = -1.2495 \times 10^7$ N/m². Now that the shear stress is known, the friction force can be calculated as:

$$F_{friction,wet} = \int \tau dA \quad (4.31)$$

Since τ is constant, this integral reduces to multiplying the shear stress by the wetted area in the die.

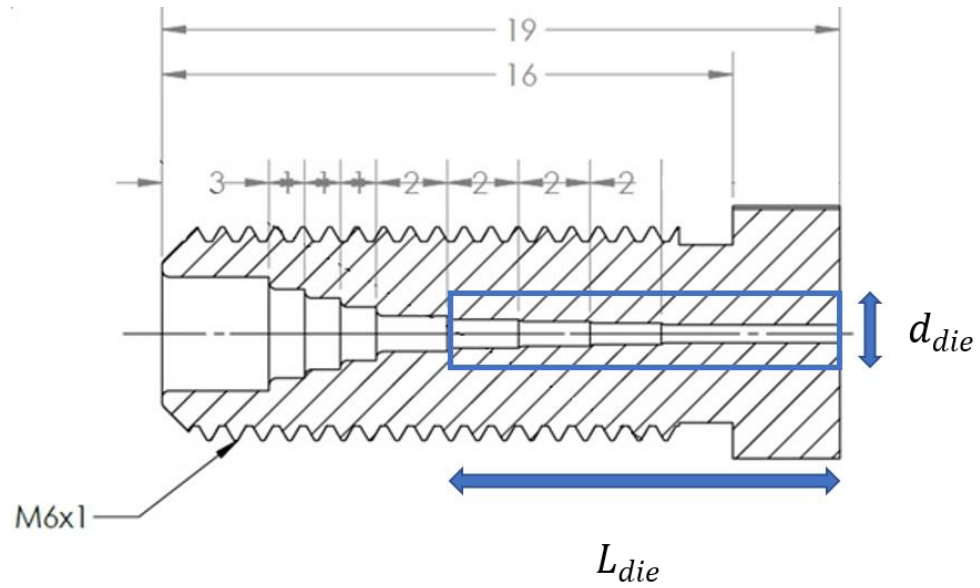


Figure 4.25: Schematic showing the dimension of the consolidation die.

In the assumption, the die is considered to be a cylinder shape. The length of the die is L_{die} , the diameter of the die is d_{die} . The wetted area in the die is then: $A_{wetted} = L_{die} \cdot \pi \cdot d_{die}$. As shown in Figure 4.125. To account for the friction in the ‘squeezing’ region, 8 mm was used as the length of the die. From the datasheet [220], the melt viscosity of PEEK 150G is $\mu_{PEEK} = 130 \text{ Pa} \cdot \text{s}$.

With a die diameter of 0.5 mm, dictated by the theoretically specified consolidation diameter in Section 4.3 and a die length L_{die} of 8 mm, $F_{friction,wet} = -15.7 \text{ N}$.

4.3.4.1.2 Dry Friction in the Die

Taking standard dry friction solely based on the weight of the commingled fibres going through the die, the contribution is almost negligible, as the weight per unit length is low:

$$F_{friction,dry} = \mu_{dry} \frac{L}{2} A_{cross} \rho_{comb} g \quad (4.32)$$

Where μ_{dry} is the dry friction coefficient, which is around 0.2 [250], $L / 2$ is the half the length between the two spools, A_{cross} is the cross sectional area of the filament, ρ_{comb} is the combined density of the filament, see Section 4.3.3, and g is the gravitational constant. The numerically evaluated magnitude of the dry friction $F_{friction,dry} = 3.0 \cdot 10^{-6} \text{ N}$, which is negligible

compared with the viscous friction. The total friction force, the sum of the wet and dry friction can be related to the load as seen by the actuated spool as:

$$F_{friction} = F_{friction,dry} + F_{friction,wet} \approx F_{friction,wet} \quad (4.33)$$

4.3.4.1.3 Bending Moment

Following the usually safe assumption that the linear prediction for the bending moment results in a higher numerical value for the bending moment then applying plasticity and geometrically nonlinearity, a linear calculation for the bending moment represents the worst-case scenario for the estimation of the bending moment. Using the Euler-Bernoulli theory (small rotation assumptions) for beam bending there is the well-established linear relationship between bending moment M and radius of curvature:

$$M = \frac{EI}{\rho} \quad (4.34)$$

Where E is the Young's modulus, also known as the modulus of elasticity, of the material and I is the second moment of area. The value $\rho = 55$ mm, the radius of the spool. The formula to calculate the second moment of area is:

$$I = \frac{\pi d^4}{64} \quad (4.35)$$

For the loose case (module 1 in Figure 4.19), the bending moment is composed of the individual contributions of the individual fibres in the commingled fibres and for the filament it is the combined modulus of elasticity and the consolidated diameter that gives the bending moment.

$$M_{bending,loose} = n_{CF} \frac{E_{CF} I_{CF}}{\rho} + n_{PEEK} \frac{E_{PEEK} I_{PEEK}}{\rho} \quad (4.36)$$

Where $n_{CF} = 3000$ and $n_{PEEK} = 2226$ are the number of carbon fibres from the data sheet and the PEEK fibres based on the volume fraction and the average diameters of both fibres as discussed in Chapter 3 in the commingled fibres respectively. Also, from the data sheet and from Figure 3.3, the average diameter of the carbon fibre is $7.5 \mu\text{m}$ and the estimated average diameter for a PEEK fibre is $22.5 \mu\text{m}$; and $E_{PEEK} = 3.85$ GPa, $E_{CF} = 288$ GPa. For the

bending of the filament (module 4 in Figure 4.19), the following relationship describes the relation between the bending moment, the second moment of area, the combined modulus of elasticity and the radius of curvature:

$$M_{bending,filament} = (\phi E_{CF} + (1 - \phi)E_{PEEK}) \frac{I_{filament}}{\rho} \quad (4.37)$$

Where ϕ is the carbon fibre volume fraction of 57.4 %. For the bending moment at module 1, the bending $M_{bending,loose}$ is obtained as $4.5 \cdot 10^{-6}$ Nm, and in module 4, $M_{bending,filament}$ is 0.0096 Nm. The bending $M_{bending,loose}$ is negligibly small compare with $M_{bending,filament}$ since the $M_{bending,loose}$ less than 0.05% than $M_{bending,filament}$.

4.3.4.1.4 Friction in the Bearings in Modules 1 and 4

There are two bearing pairs used in this pultrusion system. The first pair is utilised to support the spool with the commingled fibres, the other pair is for the pulling wheel. The diagram shown in Figure 4.26 helps in understanding the calculation of bearing friction torque.

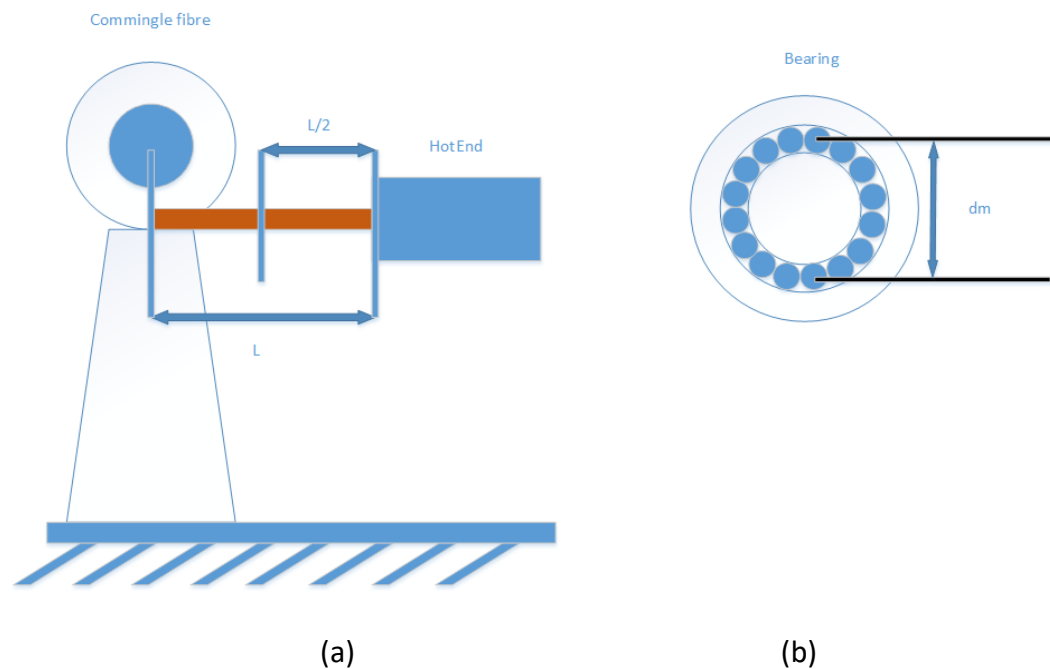


Figure 4.26: Diagram of friction moment for bearing calculation.

For bearing set 1, drawn in the left hand side in Figure 4.26, which include two times two bearings, the calculation of the frictional torque T_{bf} in the bearings is as:

$$T_{bf,1} = m_{spool}g\mu \frac{d_m}{2} \quad (4.38)$$

Where the friction coefficient $\mu = 0.002$ for a standard ball bearing. m_{spool} is half of the material mass and further includes, shaft and wheel, which was assumed to be 0.5 kg, g is the gravitational constant and d_m is the pitch diameter (20 mm) in the bearings, see Figure 4.26 (a). The frictional bearing torque for module 1 is $9.81 \cdot 10^{-5}$ Nm.

The bearings in set 2, at the right hand side in Figure 4.26 (b) are loaded most heavily, since these bearings have to take the horizontal reaction force equal to the pulling load. As the horizontal force is perpendicular to the vertical force cause by the weight of the wheel, with Pythagoras's theorem the frictional torque in the second set of bearings becomes:

$$T_{bf,2} = \sqrt{\left((m_{spool}g)^2 + \left(\frac{T_{friction} + T_{bf,1} + M_{bending,loose}}{r_{spool}} \right)^2 \right)} \mu \frac{d_m}{2} \quad (4.39)$$

Numerical value for the second set of bearings in the right hand side of Figure 4.26 is 0.00033 Nm, still negligibly small.

4.3.4.1.4 Total Force and Torque Requirements for the Pulling Wheel

The total pulling force, i.e. the tension in the filament between the die and the pulling wheel, is:

$$F_{pulling} = \frac{M_{bending,loose} + T_{bf,1}}{r_{spool}} + F_{friction} \quad (4.40)$$

Since contributions to the pulling force from the bending moment and bearing friction are negligibly small, this is equal to the 15.7 N viscous friction force caused by the viscous friction of the molten PEEK in the die

The total torque, which needs to be overcome by the pulling wheel, is the sum of all the torques and moments, and it is calculated:

$$T_{total} = F_{friction} \frac{d_{spool}}{2} + M_{bending,loose} + M_{bending,filament} + \sum_{i=1}^2 T_{bf,i} \quad (4.41)$$

Which, when evaluated numerically, gives a torque of 0.85 Nm. The contribution of the viscous friction is 0.84 Nm, which is 98.8% of the total torque. It is therefore safe to say that within what can be assessed numerically without further, cumbersome, experimental tests on the 'squeezing' effect, the viscous friction is the main contributor to the torques and forces to be overcome by the pulling wheel.

4.3.4.2 Minimum Shaft Diameter

In this section, the minimum shaft diameter is calculated based on failure due to twist. Shear stresses in a shaft can occur due to being subjected to torque and bearing loads.

4.3.4.2.1 Minimum Shaft Diameter for Direct Shear Load

Figure 4.27 shows a schematic of how the spool is attached to the support by the shaft. As the wheel hub is solidly attached to the shaft, the main failure mechanism would be overloading due to the shearing force. From this figure it is clear the shaft is in the so-called double shear condition, and the bearing load V consists of two components: half the weight of the spool and commingled fibres of filaments in y-direction and half of the pulling force in the x-direction. Using Pythagoras's theorem and the standard calculation to find the average shear stress [251]; and equating the average shear stress to the maximum allowable shear stress, bearing load V to the half of the maximum weight of the spool and yarn, then the minimum shaft diameter d_{shaft} can be calculated as follows:

$$d_{shaft} = \sqrt{\frac{4}{\pi} \frac{V}{\tau_{max}}} = \sqrt{\frac{4}{\pi} \frac{\left(\left(\frac{1}{2}m_{spool}g\right)^2 + \left(\frac{1}{2}F_{pulling}\right)^2\right)}{0.5777\sigma_y}} = 0.66231 \text{ mm} \quad (4.42)$$

In the equation above V denotes the shear force and τ_{max} the ultimate shear stress, which the Von Mises yield criterion relates to tensile yield stress σ_y as $0.5777\sigma_y$. Recall that $\frac{1}{2}m_{spool}$ is half of the material mass, $F_{pulling}$ is the total pulling force. The value of σ_y is 340 – 1000 MPa for steel. The worst case is taken by using the yield stress as 340 MPa in the calculations.

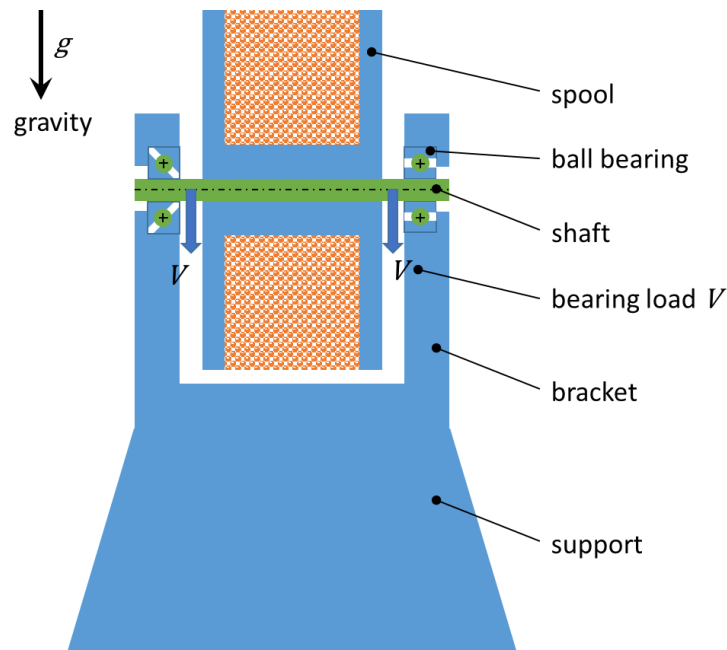


Figure 4.27: Schematic cross section of support and spool.

4.3.2.2 Minimum Shaft Diameter Due to Twist

For shaft selection, a steel shaft was selected. Based on the maximum torque calculated in the preceding section, the minimum shaft diameter based on the shear stress yield criterion can now be calculated. For the maximum shear stress the following relationship between torque and shear stress holds:

$$\tau_{max} = \frac{TR}{J} \quad (4.43)$$

Where R is the outer radius of the shaft and J is the polar moment of inertia, T is the total torque including $T_{friction}$, $M_{bending}$ and T_{bf} . For a solid shaft with circular cross-section the polar second moment of area is defined as:

$$J = \frac{\pi R^4}{2} \quad (4.44)$$

Substituting (4.14) into (4.13) gives:

$$\tau_{max} = \frac{2T}{\pi R^3} \quad (4.45)$$

The maximum occurring shear stress τ_{max} should be lower than the shear stress value for which plasticity occurs. The plasticity mechanism for shear due to twist is different from that of the plasticity occurring under a tensile loading. The yield stress found in tensile tests for a material has been found by Von Mises to be empirically related to the yield shear stress [251]:

$$\tau_{max} = 0.5777 \times \sigma_y \quad (4.46)$$

With the torque calculated in the preceding section, the minimum diameter of the shaft is 2.8 mm. This means that the failure due to shear force V is the dominant mode of failure, which consequently should govern the sizing of the shaft. Doubling the diameter, equating to a safety factor 8, and rounding it off to obtain a standard value for the shaft diameter for ease of assembly, a diameter of 6 mm is adopted in the design.

4.3.4.3 Final Pultrusion System Design and Assembly

The brackets and supports were designed to keep the spool, the loose commingled fibres and filaments levelled horizontally. The 3D CAD drawings of each of the supports are shown in Figures 4.28 (b) and (c).

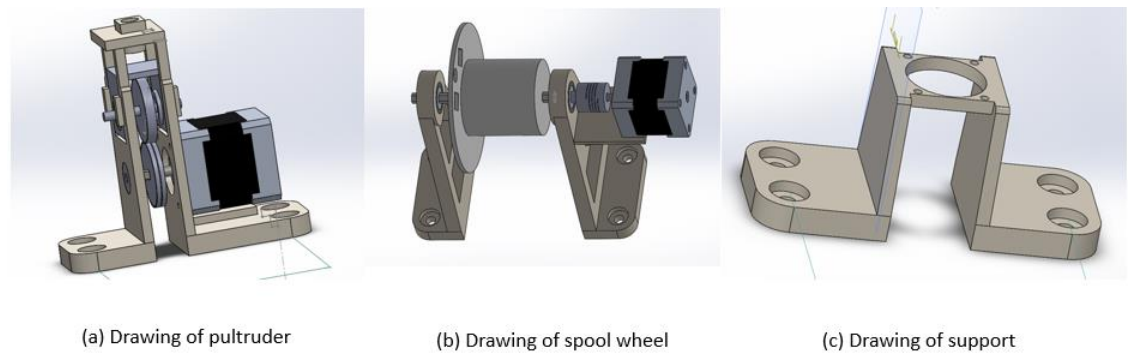


Figure 4.28: Drawing of pultrusion system supports.

All the parts were 3D printed either by the SLS process with nylon, the FFF process with PLA or the jetting process with acrylic. Based on the above design, the pultrusion system setup is shown in Figure 4.29.

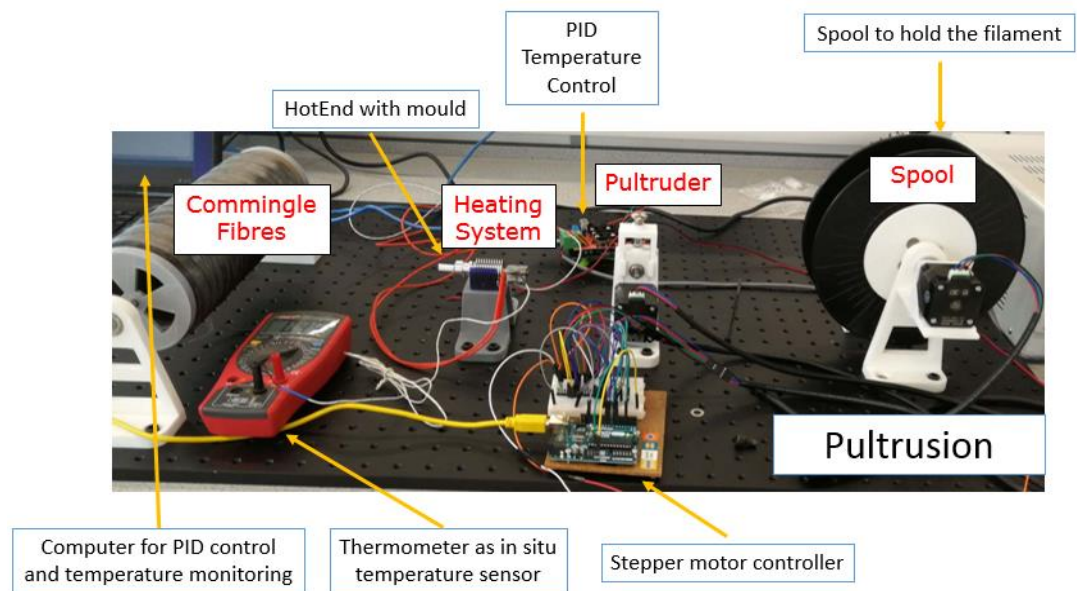


Figure 4.29: Final pultrusion system setup.

The full setup consisted of the two wheels and supporting bracket, the commingled fibre reel, the die, heater and support bracket and a pultruder. Additionally, there were the electronics and the controllers used to drive the stepper motors and control the heating system. The settings of the electronics are described in more detail in Section 4.3.5.

The pultruder in Figures 4.28 (a) and 4.29 was driven by a NEMA17 stepper motor. The pultruder wheel had a diameter of 40 mm. At 5 mm/s pulling speed, the motor was with a rev to $n = 2.4$ RPM. The torque caused by the

pulling by this motor is $15.7 \times 0.02 = 0.314$ Nm, which was sufficiently lower than its holding torque of 0.44 Nm.

4.3.5 Electronics and Controller Setup

For the temperature control, an Arduino Mega 2560 board and RAMPS 1.4 extension board [252] were used. The RAMPS board was used as it has a MOSFET module. PID control was utilised for temperature control. A K-type thermocouple and associated amplifier board were connected via an analogue pin. The heating element was connected with a digital pin as it is driven using pulse width modulation to achieve an approximation to an analogue output. In the temperature control loop, the thermal sensor first detects the temperature, which was subsequently compared with the target temperature, after which it was decided if the heating element needs power input. While the computer could monitor the temperature through the controller board, a thermometer with K-type thermocouple was also used as an in-situ temperature monitor. For the stepper motor control, A4988 stepper drivers were used to drive two NEMA 17 stepper motors, each with a holding torque 0.44 Nm, which was higher than the calculated total torque in Section 4.3.4.1. The drivers are capable of microstepping and were set to 16 pulses per complete step in order to provide a high angular resolution of the stepper motors. When the system was running, the code was called to first heat the die up to the target temperature. When this was achieved, the stepper motors could be started so that they pulled the filament using the pultruder and drive the take-up spool against the opposing torque from the tendency of the stiff filaments to uncoil.

4.3.6 Initial Pultrusion Start-up Steps

Since the loose commingled fibre has a 2.2 mm width and the calculated consolidated diameter is 0.5 ± 0.0013 mm, this poses a challenge to the feedstock processing because of the factor of 4.4 in diameter between the commingled CF/PEEK and consolidated CF/PEEK filament. In order to feed the

commingled fibre into the special designed pultrusion die, the same starting procedure as Rietema *et al.* [36] was applied. Three ready-made standard brass nozzles with size 0.8 mm, 0.6 mm and 0.5 mm were used to consolidate the commingled fibres via the pultrusion process and reduce the diameter of the filament gradually in order to feed the commingled fibre into the specially designed pultrusion die. During the starting process, the die was heated to 400°C, and the commingled fibres were pulled manually. The nozzles used in the starting process are shown in Figure. 4.30.



Figure 4.30: Different types of nozzles for starting process.

After pulling the material through each of the three nozzles, each having a successively smaller diameter, eventually, the material could be fed into the specially designed pultrusion die. Photographs and microscopy pictures of the side view CF/PEEK filaments are shown in Figure 4.31, 4.32, 4.33 and 4.34.

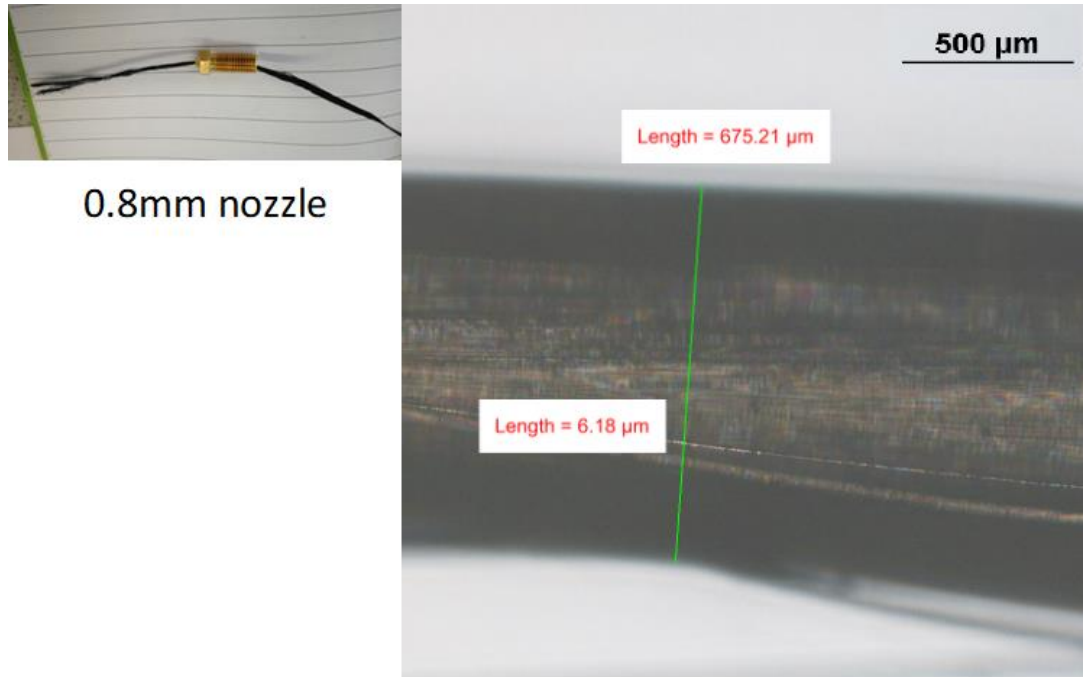


Figure 4.31: 0.8 mm nozzle showing CF/PEEK fibres before and after consolidation, along with micrograph of consolidated CF/PEEK filament.

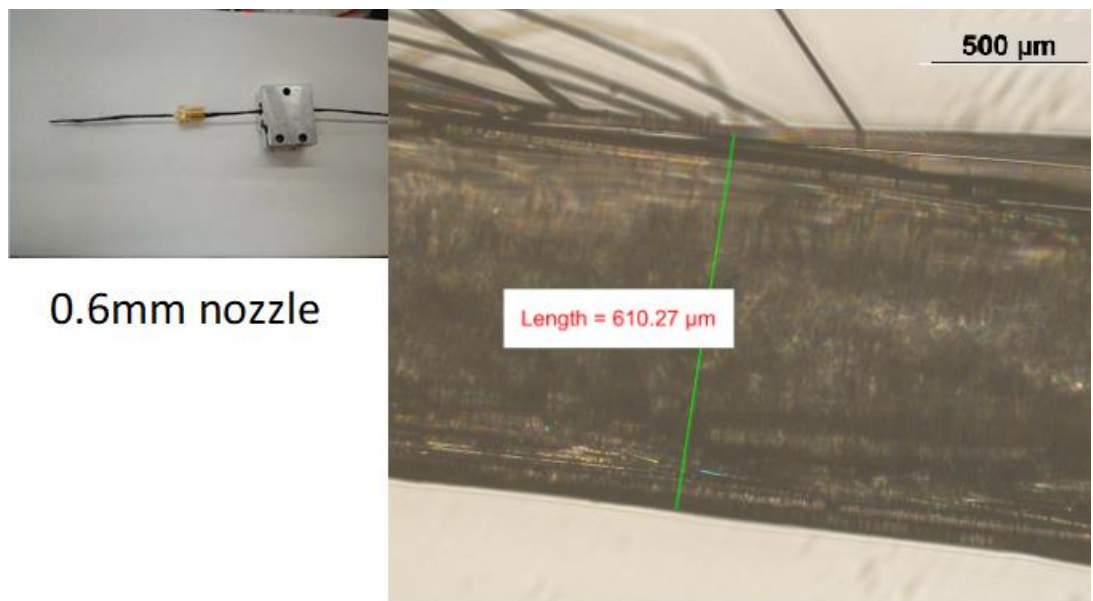


Figure 4.32: 0.6 mm nozzle showing CF/PEEK fibres before and after consolidation, along with micrograph of consolidated CF/PEEK filament.

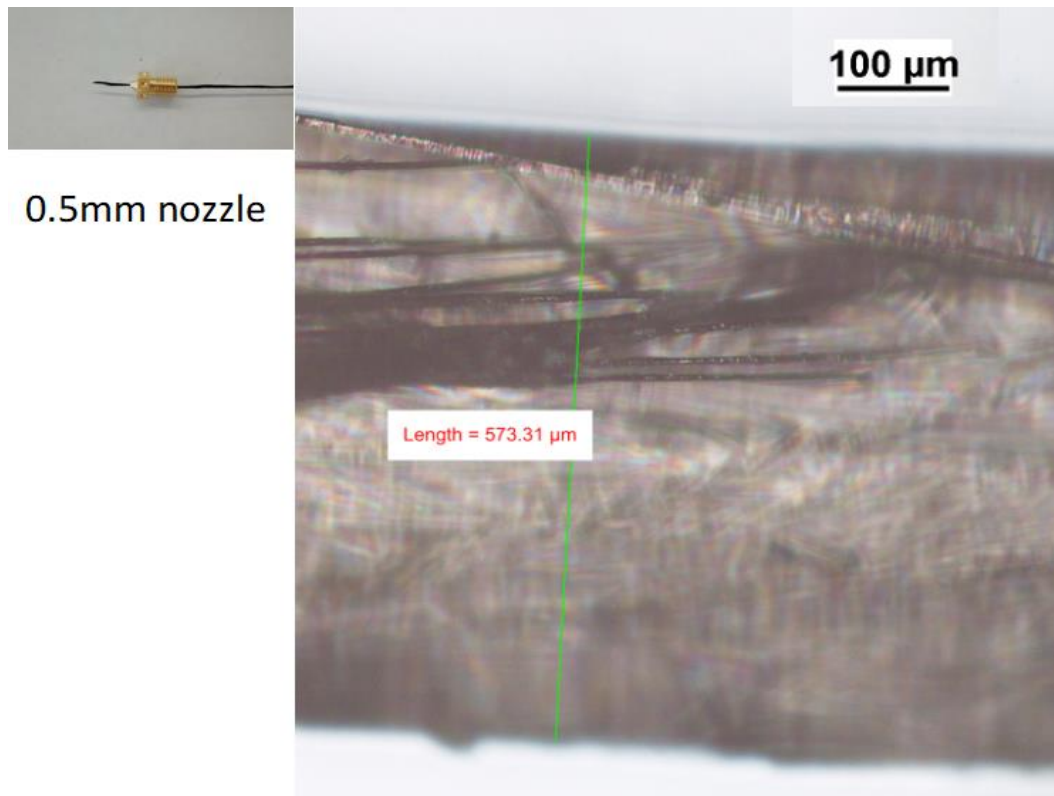


Figure 4.33: 0.5 mm nozzle showing CF/PEEK fibres before and after consolidation, along with micrograph of consolidated CF/PEEK filament.

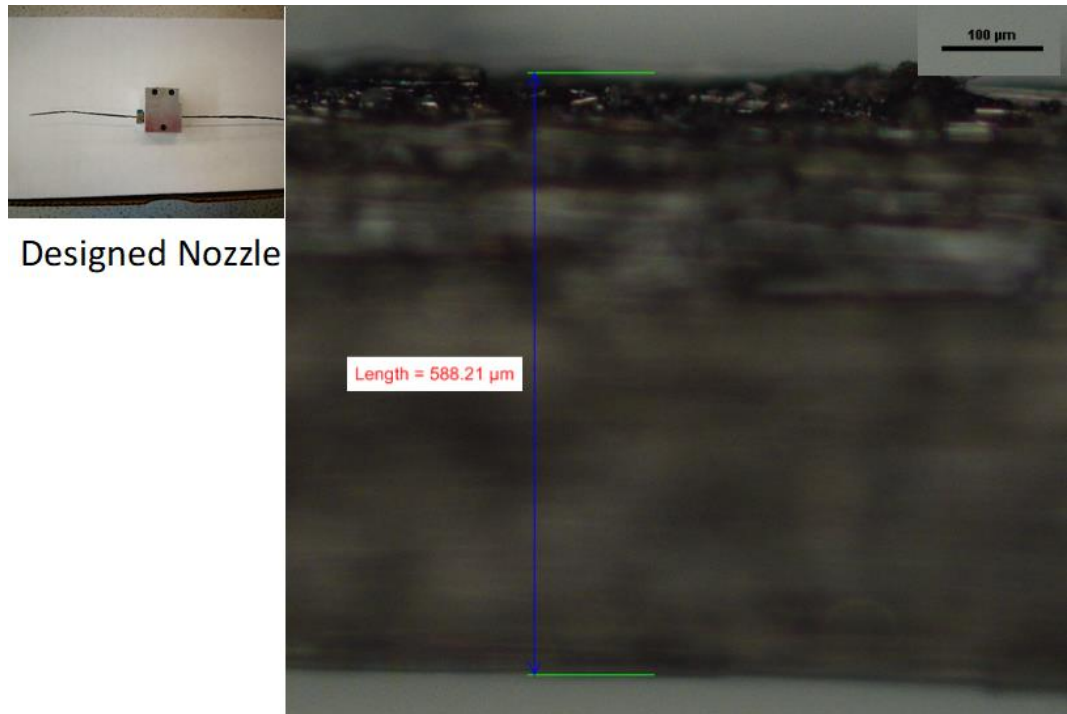


Figure 4.34: Designed pultrusion die showing CF/PEEK fibres before and after consolidation, along with micrograph of consolidated CF/PEEK filament.

After each stage of processing, the diameter of the filament swelled after the material was out of the nozzle. When the commingled CF/PEEK was pulled from the specially designed pultrusion die, a higher pulling force was required than for the 0.5 mm diameter brass nozzle because of the greater length of the 0.5 mm diameter region. The lack of clarity of the images is because the depth of field of the optical microscope is insufficient to contain the radius of the filament. A similar scenario was stated in Chapter 3. However, these images provide sufficient information to obtain measurements of the filament diameter.

Ten diameter measurements were taken for each of the samples. Up to ten samples were investigated for each set of pultrusion conditions. The standard deviation, as a measure of the error, was taken among each set of ten samples with their ten measurements. The error plot of each group of samples are shown in Figure 4.35. When the diameter of the nozzle reduces, the average diameter of the filament reduces and tends to be close to the diameter of the nozzle. The standard deviation reduces when the nozzle diameter reduces. The specially designed nozzle has a longer 0.5 mm constant diameter section than the standard brass nozzle of 0.5 mm diameter. Relative to processing with the standard brass nozzle, the filament diameter error bar becomes smaller when the specially designed die is utilised for processing the commingled CF/PEEK. This indicates that reducing the die size and increasing the die length can improve the consolidation quality. This is due to the higher compaction force during the heating process, giving a better and more stable shape of the filaments. The results show that with increased compaction force and processing time, the filament size can be closer to the consolidation size with a smaller standard deviation.

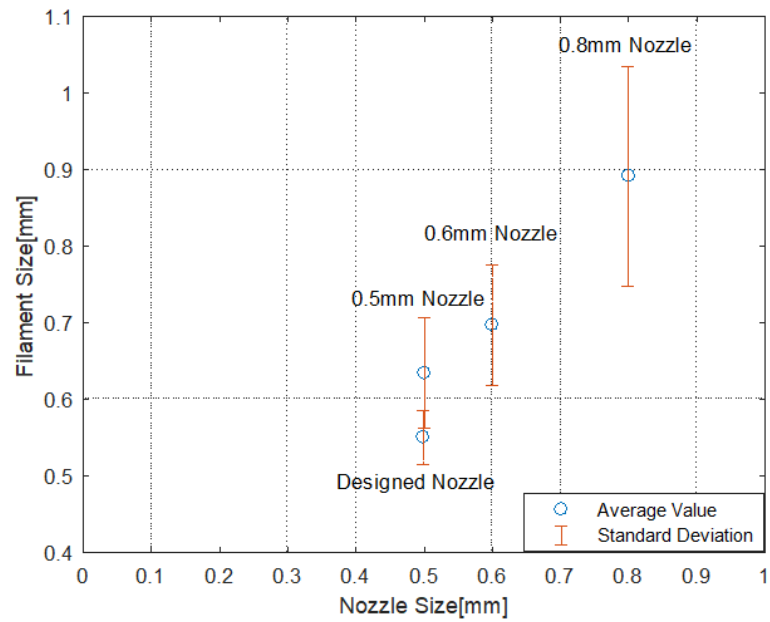


Figure 4.35: Error plot of CF/PEEK size based on different nozzles.

During the priming process, it was found that some material leakage occurred. Microscopy pictures of the inside of the nozzle revealed, that there was some PEEK and carbon fibre remaining in the die. In addition, when the nozzle size reduces, the average pulling force increases since there is more contact with the die and hence higher shear stresses occur in the Couette flow dominated flow of the molten PEEK near the wall of the die. This, however, leads to a better carbon fibre distribution in terms of more straight carbon fibres along the direction of the CF/PEEK filament. The length of the die is also one of the factors which affect the pulling force as it affects the total area where fluid friction due to shear stress occurs in the flow. Figure 4.36 gives a side-by-side comparison of microscopy images taken of filament created with a 0.5 mm standard FFF brass nozzle on the left and the specially designed pultrusion die on the right.

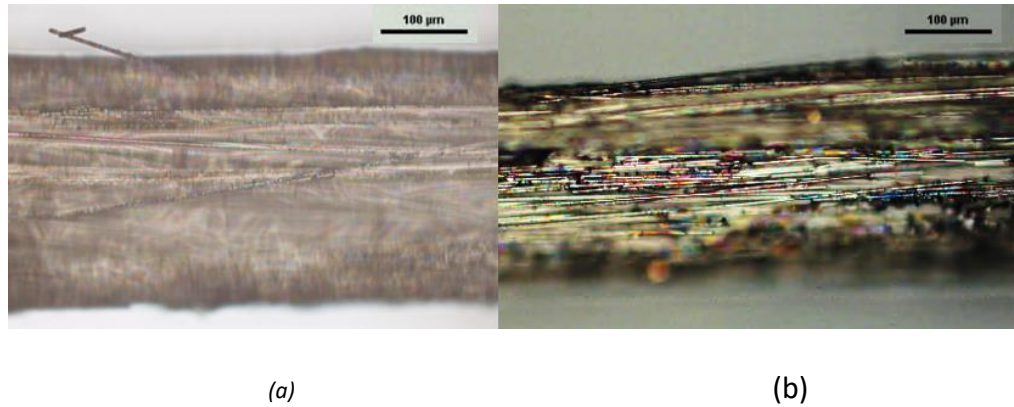


Figure 4.36: Microscopy image of the CF/PEEK filament consolidated by (a) 0.5 mm brass nozzle and (b) specially designed pultrusion die. Both images were taken with a magnification factor 10.

4.4 Conclusions

In this chapter the design and construction of the pultrusion apparatus have been described. The work includes both the thermal analysis of the HotEnd and the mechanical analysis of the apparatus. The initial HotEnd analysis, validated by means of IR measurement, confirmed that the E3D V6 HotEnd was appropriate to be selected as the HotEnd for the pultrusion apparatus. The next stage of mechanical analysis helped to ensure the components were designed and sized properly for the filament fabrication. The initial pultrusion start-up process of reducing the diameter of the commingled yarn in three steps leads to the next stage of the pultrusion process, so that the filament fabrication process could be carried out, as described in Chapter 5. This chapter also describes the die priming and the die-swell after the initial pultrusion start-up process based on observation of the microscopy images. It was found that the diameter of the filament was closer to specification and showed less variation when the 0.5 mm specially designed pultrusion die was used rather than the standard 0.5 mm nozzle. This indicates that the die compaction length is critical to the pultrusion process. With the design and build of the pultrusion apparatus having been completed, the relevant process parameters were investigated in the experimental programme described in Chapter 5, where the filament produced is also characterised.

CHAPTER 5

Characterisation of Composites Filaments

5.1 Introduction

Characterisation of the CF/PEEK filament is a necessary procedure before commencing the 3D printing of the filament. This is because the filament impregnation quality may influence the printed part quality. It is necessary to investigate, firstly, whether any material degradation occurred during the pultrusion process used to fabricate the feedstock, and secondly, whether the compaction of the CF/PEEK filament was good enough to ensure a sufficiently low void content before the 3D printing. Within the framework of this study this is a particular priority since the current 3D printer used does not include a compaction system. Hence, the void content of the 3D printed parts could not be easily reduced after the printing of components. The analysis is to identify the processing window for fabrication of the CF/PEEK filament, and subsequent optimisation of the pultrusion process parameters.

In this programme of experiments, the influence of process parameters were investigated, namely the die temperature and pultrusion speed. Firstly, the filament consolidation quality was studied by analysing the side view of each of the filaments fabricated under the specified variations in process conditions. Subsequently, a filament porosity study was carried out with cross-sectional image analysis and density measurement. After this, the results were compared and summarised, and the pultrusion processing window could finally be established based on further analysis of the results.

5.2 Processing Conditions

A parametric study of temperature and pultrusion speeds was carried out. A full factorial combination of 32 processing conditions was investigated for the production of FFF CF/PEEK filament. Pultrusion speeds were set to 0.5 mm/s, 1 mm/s, 3 mm/s and 5 mm/s. Temperatures were set from 350°C to 420°C in steps of 10°C. Table 5.1 summarises the complete set of processing conditions investigated.

Table 5.1: Processing conditions investigated.

| Pultruding speed | Pultrusion temperature |
|-------------------------|--|
| 0.5 mm/s | 350°C, 360°C, 370°C, 380°C, 390°C, 400°C, 410°C, 420°C |
| 1.0 mm/s | 350°C, 360°C, 370°C, 380°C, 390°C, 400°C, 410°C, 420°C |
| 3.0 mm/s | 350°C, 360°C, 370°C, 380°C, 390°C, 400°C, 410°C, 420°C |
| 5.0 mm/s | 350°C, 360°C, 370°C, 380°C, 390°C, 400°C, 410°C, 420°C |

5.3 Filament Diameter Analysis

Using the method outlined in Chapter 4, Section 4.3.6, ten samples were investigated, with ten measurements being taken on each sample. Figure 5.1 shows the side view mean values of filament diameter (d_m) and the standard deviation as error bars.

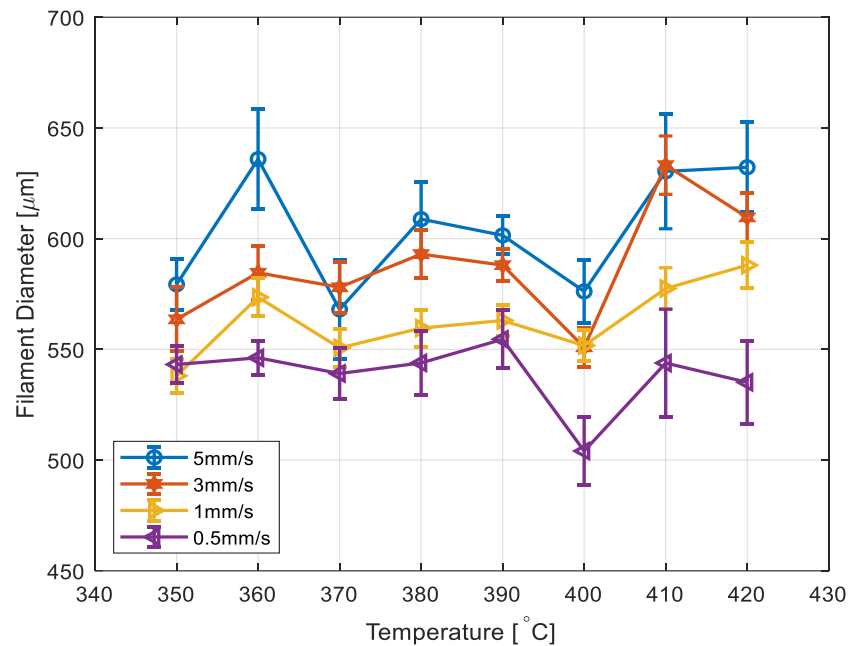


Figure 5.1: Diameters of the CF/PEEK filaments as a function of temperature and pultrusion speed.

It can be seen from Fig 5.1 that the filament mean diameters reduce when the pultrusion speed is lowered. However, varying the temperature between 350 °C to 420 °C does not show a particular trend. Instead, there are two separate temperatures (370°C and 400°C) that appear to be local minima for the filament diameter for all four pultrusion speeds investigated. The values of 0.51 mm at 400°C and 0.5 mm/s are very close to the calculated consolidated diameter of the CF/PEEK filament. Ten measurements were taken of the filament fabricated under each of the specified pultrusion conditions (measurement methods can be found in Chapter 4 Section 4.3.6). The results suggest that there is a dependent relationship between filament diameter and the two investigated filament processing parameters, die temperature and pultrusion speeds. The result shows a trend that when the pultrusion speed is reducing, the mean diameter size reduces. This can be explained as being because increasing residence time in the die allows more time for viscous flow of the polymer molecules, reducing the amount of elastic recovery, also known as springback.

5.4 Filament Porosity Study

Porosity analysis is one of the ways to investigate the quality of the fabricated CF/PEEK filament since it allows for the quality of impregnation of the carbon fibre in the PEEK to be evaluated. The most popular method is by investigating the cross-section of the filaments [36, 37]. The advantage of this method is that it establishes the local void content through the cross-sectional view of the filaments. However, since this is a 2D image analysis, it can only give the information of the filament porosity of that particular cross-section. Density measurement [253], is commonly used in composites porosity studies. The method of measuring density used in this work is described in Section 5.4.2.

5.4.1 Cross Section Analysis

5.4.1.1 Sample Preparation

Up to 7 filaments fabricated under the different investigated process conditions were embedded in resin (EpoFix, Struers, USA [254]) within mounting cups of diameter 30 mm. The samples were ground using silicon carbide paper (Buehler, UK [255]), starting from P240 (coarse) to finish with P1200 (fine) and subsequently polished using a diamond polishing pad (Buehler, UK [255]) from 6 μm to 1 μm in order to obtain an optically smooth cross-sectional area. Using the procedure outlined in Chapter 3, Section 3.3.1, optical studies were carried out with the Nikon Eclipse Lv100ND microscope and analysed using NIS Elements software. All the cross-sectional views were taken with top illumination and an optical magnification factor of 10. Selected images of the cross-sectional views are presented in the following sections and a full set of images for all conditions can be found in Appendix A.

5.4.1.2 Application of ToF-SIMS to differentiate cross-sectional materials

There is a severe limitation to using light microscopy images of the cross sections for investigating the porosity of the cross-sectional samples, since it is not possible to distinguish clearly whether the regions surrounding the carbon

fibres are PEEK or the embedding resin, which may penetrate into air gaps in the filament during sample mounting. Time-of-flight secondary ion mass spectrometry (ToF-SIMS) was employed in order to resolve this ambiguity. The ToF-SIMS images were captured by Dr. Gustavo F. Trindade who is a research fellow at the university. Based on one prepared cross-sectional sample and aided by reference data of the embedding resin, Dr Trindade utilised the ToF-SIMS test to associate the appearance of each region with the material making up that region, so that the same association could be made on the optical images of all the remaining samples to allow their void content to be analysed accurately with confidence.

ToF-SIMS analysis of positively charged secondary ions was carried out using a TOF.SIMSIV system from IONTOF GmbH (Münster, Germany). Each secondary positively charged ion 2D map was acquired using a 25 keV Bi_3^+ primary ion beam operated in the burst alignment mode (high lateral resolution) delivering 0.12 pA and raster scanned cover areas up to $500 \times 500 \mu m^2$. A low-energy (20 eV) electron flood gun was employed to neutralise charge build-up. Prior to analysis, the samples were cleaned in-situ using a pulsed 20 keV Argon gas cluster ion beam delivering 1.5 nA. Cleaning was performed until the maximum mapping contrast of the ToF-SIMS images between carbon fibres and surrounding areas was reached. ToF-SIMS maps were obtained for three cross-sectional samples: unprocessed commingled CF/PEEK; processed filament and pure embedding resin. This provided the identification of characteristic signals coming from each of the three materials of interest and enabled a clear identification of their spatial distribution within the filament cross-section. To achieve such identification, all mapping data as the chemical elements of PEEK and carbon can be potentially derived. These were processed by means of unsupervised machine learning (non-negative matrix factorisation), with its performance improved by a row-wise matrix augmentation of the data matrices using the simsMVA software (www.mvatools.com) [256] multivariate analysis tool of ToF-SIMS datasets. These chemical element to identify PEEK material were referenced and

compared with the data of Henneuse-Boxus *et al* [209]. Carbon fibre was identified by checking for the single element carbon, while rest of the chemical elements were considered as linked to the resin. The method seeks to reduce the dimensionality of a dataset down to a few factors, which enables the interpretation and visualization of the surface chemistry by providing data that can be directly assigned to fingerprint mass-spectra of “pure” compounds and their distribution maps. Details of the data processing methodology can be found in Ref. [257].

Figure 5.2 shows the results of all analysed cross section maps with an overlay of the relative intensity and the characteristic ToF-SIMS signal of each of the individual compounds identified: resin (red), carbon fibre (green) and PEEK (blue).

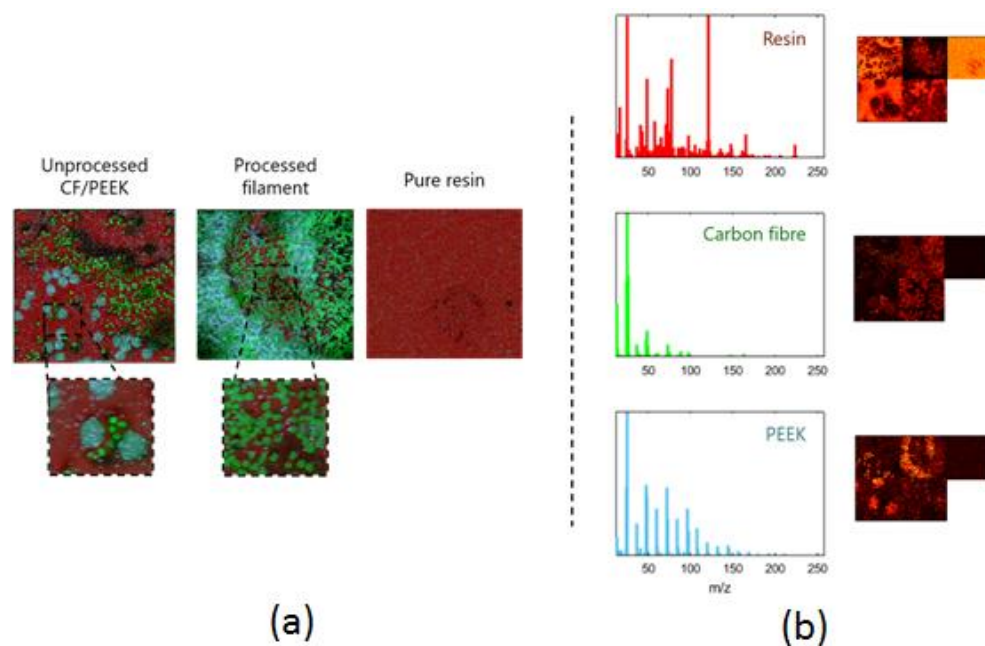


Figure 5.2: ToF-SIMS mapping of filament cross sections before and after processing to unambiguously identify voids in a processed filament. Characteristic signals for each compound (carbon fibre, PEEK and embedding resin) were identified by means of unsupervised machine learning. (a) overlays of maps for unprocessed fibres (left), processed filament (centre) and pure resin (right) with the relative intensities identified for three compounds: resin (red), carbon fibre (green) and PEEK (blue). (b) characteristic mass spectrometry signal identified for each compound (left) and their individual intensity maps (right) used to create the overlay map in (a).

With the confirmation of the spatial distribution for both PEEK and the embedding resin for a cross-sectional view of one of the processed filaments, it was found that the overall void content clearly included the embedding resin and the air void. It was then possible to create a visual correlation between light microscopy images and ToF-SIMS map, as shown in Figure 5.3, and evaluate with high confidence the distribution of filament materials for the various processing parameters, in a high throughput fashion using only contrast observed in light microscopy images. ToF-SIMS analysis also provides a detailed characterisation of the chemical composition in the sample, but this was not investigated further, as it is out of the scope of the work presented in this thesis.

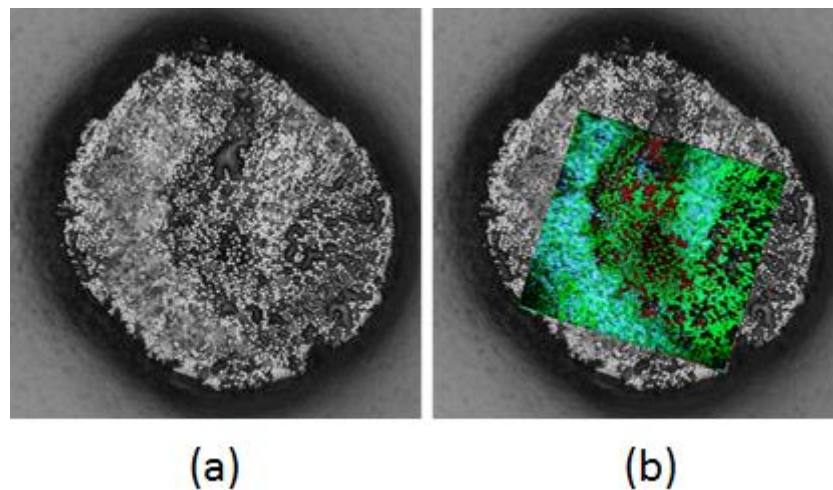


Figure 5.3: (a) Visual correlation between light microscopy images, (b) The ToF-SIMS maps for the identification of distribution of filament materials.

5.4.1.3 Method of Image Processing

The cross-sectional images were analysed statistically for the CF/PEEK filaments prepared under the 32 processing conditions listed in Section 5.2, Table 5.1. As mentioned in Chapter 3, Section 3.3.1, carbon fibre distributions in the commingled CF/PEEK bundle are not homogeneous. This results in non-homogenous carbon fibre distributions of the CF/PEEK filaments after the pultrusion process.

By comparison with the ToF-SIMS images presented in Section 5.4.1.2, the constituents in the cross-sectional views of the CF/PEEK filaments could be

identified, as seen in Figure 5.4 (processing condition, 1 mm/s, 400 °C as an example).

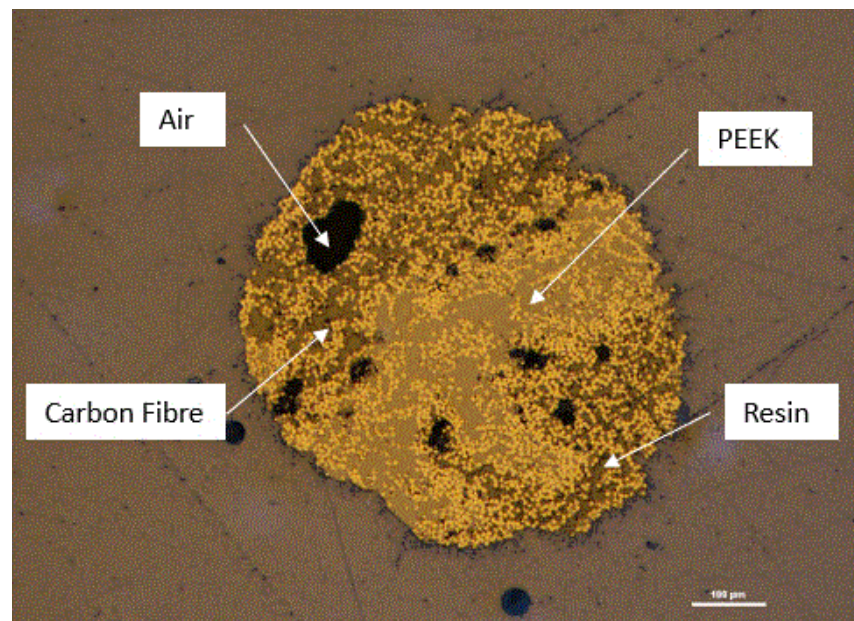


Figure 5.4: Cross-sectional view of filament under processing condition of 1 mm/s pultrusion speed and 400°C operation temperature.

The voids in the filament included both air and resin, the latter originating from penetration by the embedding resin. From observation, the volume of air voids was higher than that of the resin filled voids. Based on the results of the identified areas, imaging analyses were performed to determine the filament properties of circularity, roundness, PEEK area coverage, and overall void content (includes air voids and resin voids). In the tests, up to 7 cross-sectional samples were analysed for each processing condition. ImageJ [258] was used for the initial image editing with a pre-programmed code. The calculation of filament circularity and roundness was carried out with the built-in circularity and roundness function of ImageJ [259]. As certain images contained different grey scales after the automated processing with ImageJ, GIMP [260] was used for further manual editing. Subsequently, the calculation of the area coverage percentage of PEEK, the total void content and the air void content are carried out by extracting the numbers of pixels in GIMP. A list of cross-sectional images of samples obtained from each of the pultrusion conditions can be found in Appendix A.

As the circularity and roundness were analysed by ImageJ, the definition of circularity in ImageJ is [259]:

$$Circ. = 4\pi * area/perimeter^2 \quad (5.1)$$

Where the area is the number of pixels in the shape and the perimeter is the distance between the pixels in boundary of the shape. As defined here, when the *Circ.* has a value 1, the image has a perfect circle circumference. Likewise, if the value approaches 0, it indicates an increasing presence of roughness of outside of the filament. Based on the defined equation, the circularity indicates how smooth outside of the filament is.

The definition of roundness in ImageJ is [259]:

$$Round = 4 * area / (\pi * major_{axis}^2) \quad (5.2)$$

Where the area is the same area as defined above and the major axis is defined by the coordinates of the two endpoints of the longest line that one can draw through the shape. When the *Round* value approaches 1, the cross-sectional area approaches perfect roundness. When the value approaches 0, it indicates an increasingly elongated shape. Therefore, the difference between circularity and roundness is that circularity is more focussed on the smoothness of the circumference, the outer boundary of the filament's cross section, while roundness looks more at how evenly the axes or diameters are distributed.

An example of the image extraction procedure in GIMP outlined above is given in Figure 5.5 below. After setting the thresholds, the image was converted into a 1-bit binary (black and white), used to identify the whole filament area (Figure 5.5 (b)). The PEEK area coverage (Figure 5.5 (c)), the overall void area (Figure 5.5 (d)) and the air void area (Figure 5.5 (e)) were then extracted and quantified by counting the pixels. After image extraction for each of the filament samples, the number of pixels for the PEEK area coverage (Figure 5.5 (c)), and the air void area (Figure 5.5 (d)) were counted, then divided by the number of pixels for the whole filament area (Figure 5.5 (b)). This step was repeated for the other samples (up to 7) for each processing condition, after

which, the mean values for each processing condition were obtained. The accuracy of this technique is limited by the judgement of the operator in setting the threshold between the colours of the filament material, which are limited in contrast. However, the threshold sensitivity is not very high, since by varying the threshold below or above the setup value does not change too much value of the grey scales.

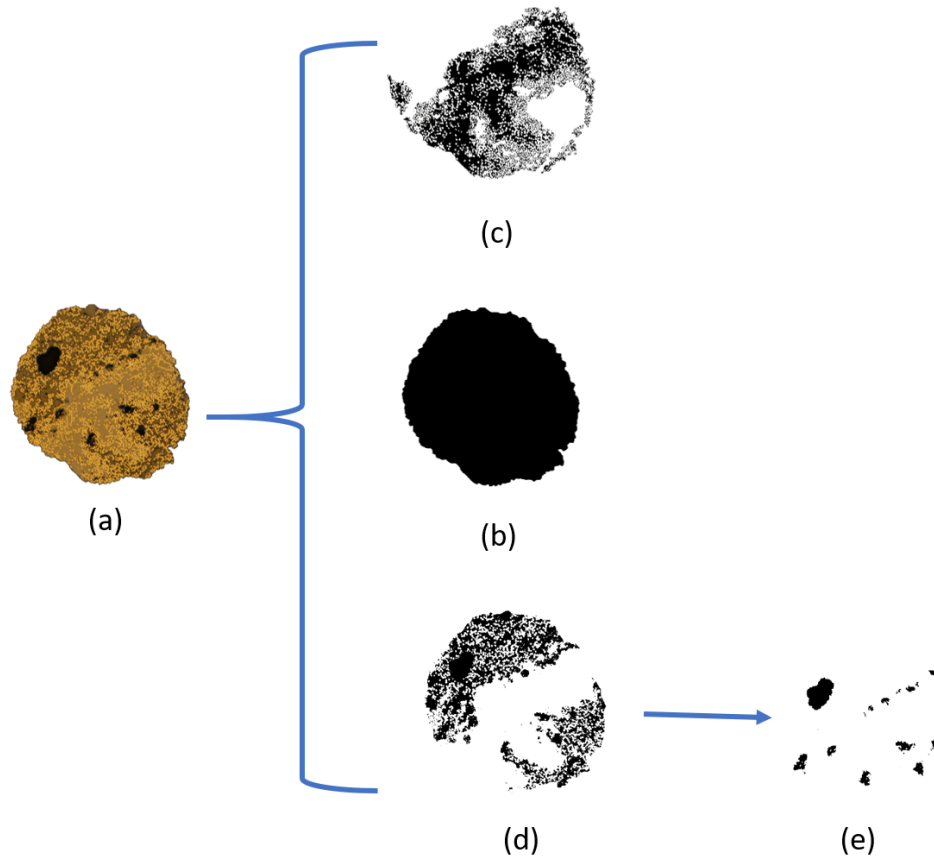


Figure 5.5: (a) Image of filament, (b) the binary black and white of the whole filament area, (c) PEEK area coverage, (d) the whole voids area, (e) the air voids area. This filament is under processing condition of 400°C die temperature at 1mm/s pultrusion speed.

5.4.1.4 Results and Discussion

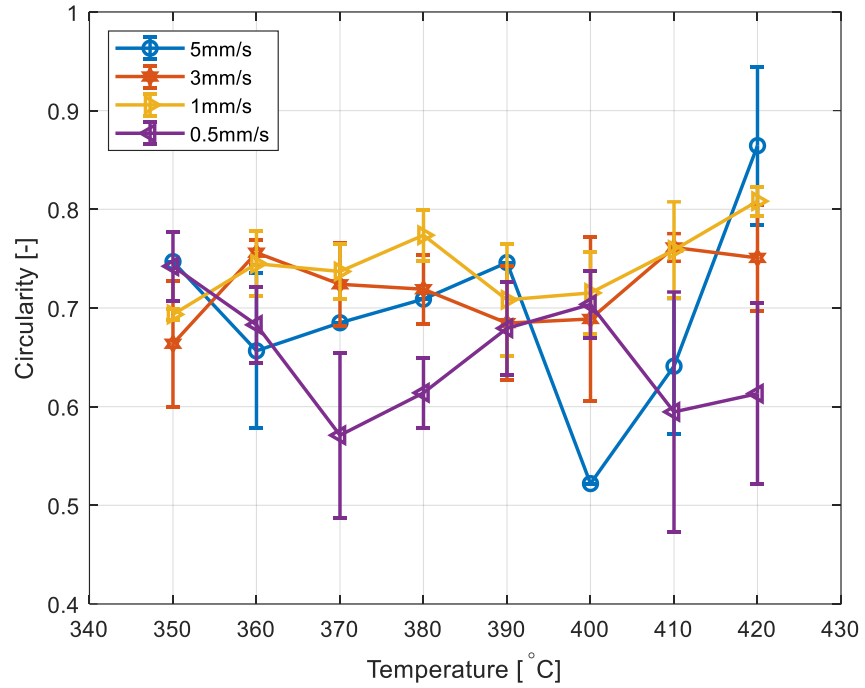


Figure 5.6: Filament circularity.

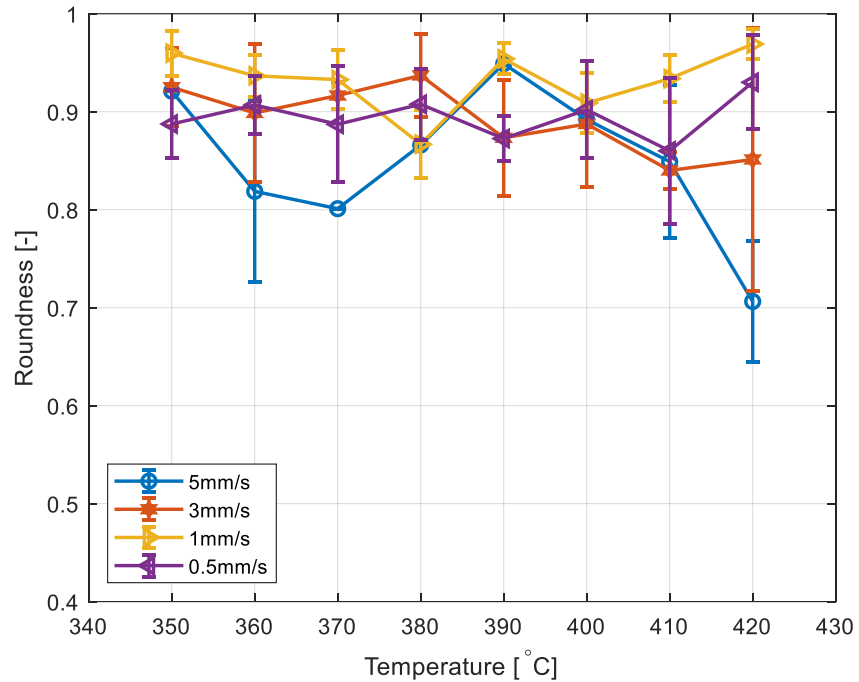


Figure 5.7: Filament roundness.

Note that insufficient data were captured to establish error bars as the standard deviation for the pultrusion at a speed of 5 mm/s under temperature conditions of 350 °C, and 370 °C to 400 °C in Figures 5.6, 5.7, 5.8 and 5.9. The circularity and the roundness of the filaments are shown in Figure

5.6 and Figure 5.7 respectively. The average value of the roundness of the filament samples (0.9) indicates that roundness is quite close to the perfect roundness which is 1.0. However, the filament circularity only lies between 0.6 to 0.8, which indicates that the outside of the filaments is not very smooth. Another observation from these figures is that the pultrusion speed and die temperature have little effect on the achieved circularity. The error bars are set as standard deviations. The error bars are greater for the printing speed of 0.5 mm/s in both circularity and roundness. Results in both Figure 5.6 and Figure 5.7 show that the error bars are the smallest when the pultrusion speed is 1 mm/s. This can be explained by the fact that the slower pultrusion speed leads to a longer exposure time of the PEEK above the melting temperature, and this potentially creates CF/PEEK degradation. However, further investigation should be carried out as future work to confirm this.

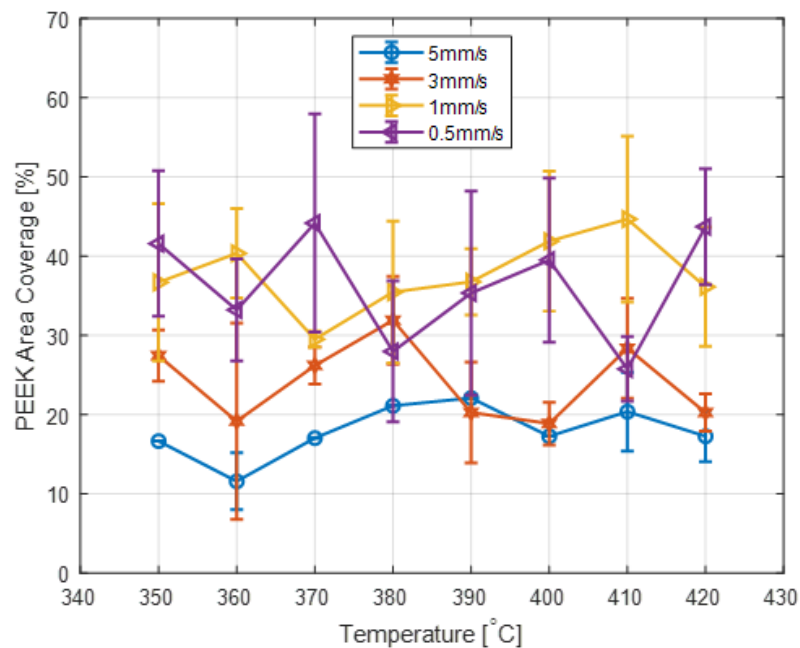


Figure 5.8: The filament PEEK area coverage.

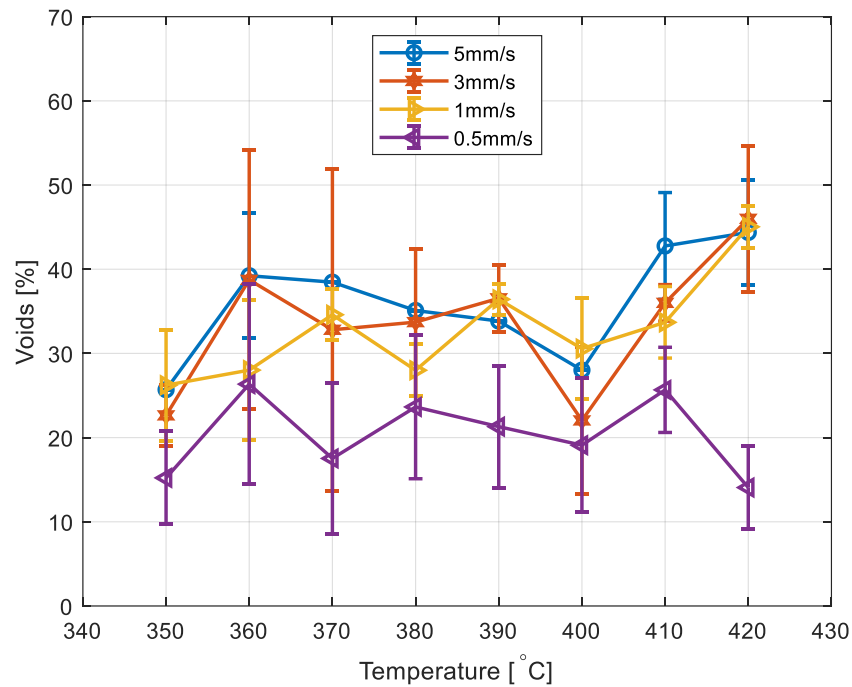


Figure 5.9: The filament overall void content.

As can be seen in Figure 5.8 and Figure 5.9, although there is some overlap of information, overall the PEEK area coverage increases when the pultrusion speed decrease, while the overall percentage area of the voids reduces when the pultrusion speed is lowered. Compared with the result in Figure 5.1, which indicates a larger mean diameter resulting from a higher pultrusion speed, Figure 5.8 shows a higher PEEK area coverage resulting from a lower pultrusion speed. Similarly in Figure 5.9, reducing the pultrusion speed results in a reduction in the overall void content. Based on the results and standard deviations, it can be seen that voids create excess filament diameters even though the pultrusion die has a diameter close to the theoretical consolidation diameter. These voids could lead to a lower structural integrity of the final printed parts if retained after extrusion in the FFF process. In order to minimise the voids, these results show that reducing the pultrusion speed is the most effective appropriate approach, having a more significant impact than increasing the temperature.

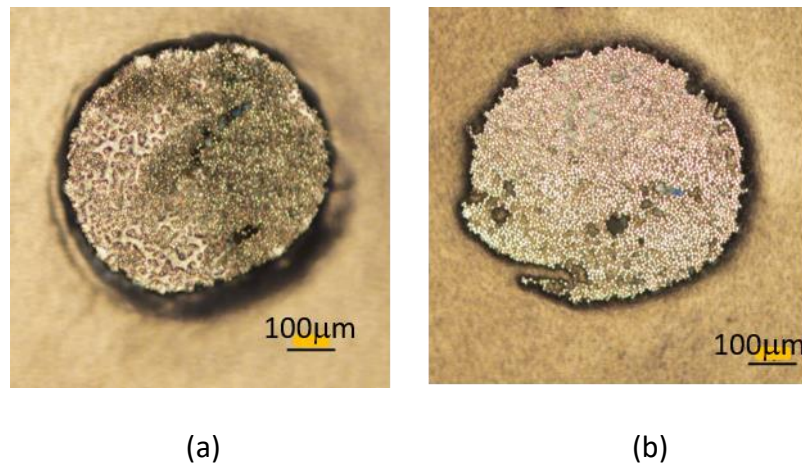


Figure 5.10: Carbon fibre distribution comparison by different PEEK impregnation: (a) is under 0.5 mm/s 360°C temperature, (b) is under 0.5 mm/s 380°C.

As an observation from the images, even though the original carbon and PEEK fibres are not distributed in a homogeneous manner, when the amount of voids reduces, the infusion of the molten PEEK into the carbon fibres improves, and the carbon fibres become more evenly distributed in the PEEK matrix material as can be seen in Figure 5.10. Recall that the circularity and roundness data in Figure 5.6 and Figure 5.7, Figure 5.10 also indicates that the outside smoothness of the filaments is poor. For a pultrusion speed of 0.5 mm/s, a die temperature of 360°C yields a better circularity than setting the die temperature to 380°C. However, the roundness of the filaments shows less variation for the speed range of 0.5 mm/s to 3 mm/s and for temperatures between 350°C to 400°C.

5.4.2 Density Measurement

To mitigate the limitation of only considering a relatively small amount of cross sections that provide very local information, a further density analysis was carried out. A procedure for density measurement was developed in this work that is expected to obtain similar results as standard density measurement method. The density measurement equipment accessible in the author's research institute uses the buoyancy (Archimedes) Method [261]. This method is based on the Archimedes' principle [262] that the object, totally or partially

immersed in a fluid or liquid, is buoyed up by a force equal to the weight of the fluid displaced by the object. Note that some of the voids in the filament may be isolated, i.e. they are not connected to the filament's outer surface, therefore they potentially may not be reached by the liquid, resulting in incomplete wetout by the immersing liquid. The idea of the alternative density measurement pursued in this study is to follow the same principle as the buoyancy method. This gives the void content information based on a comparison of the density established by dividing the sample mass by the measured volume of the specimen assuming it to be a solid, and comparing it with the calculated consolidated CF/PEEK density. Subsequently, this measurement was converted into void content to enable a direct comparison with the results of the cross-sectional analysis. The hypothesis of weight measurement is based on a number of reasonable assumptions for the geometries and other topological values, resulting in a certain error margin in the analysis.

5.4.2.1 Methodology of the Alternative Density Measurement

All sample lengths were around 30 mm. The measurements were carried out on samples fabricated under the 32 processing conditions. For each of the filament fabrication process conditions, up to 5 samples were measured and the standard deviation was calculated as a measure of the error. The DSC sample weighing scale (accuracy ± 0.01 mg) was used for the weight measurement. A digital calliper (accuracy ± 0.05 mm) was used for length measurement. The length of the short filament samples can be measured accurately enough with the digital calliper since they are almost straight.

The filament mean diameter (d_m) was obtained by microscopy measurement. Details of the measurement method are described in Chapter 4, Section 4.3.6. A schematic is shown in Figure 5.12 and measurement, values are shown in Figure 5.1.

The filament real length (l_r) was measured using digital caliper. The following equations were derived by the present author.

Chapter 5 Characterisation of Composites Filament

The filament real volume (V_r) is calculated by d_m and l_r :

$$V_r = l_r \cdot \left(\frac{d_m}{2}\right)^2 \cdot \pi. \quad (5.3)$$

The filament real mass (m_r) is the filament mass measured by the sample weighing scale.

The filament theoretical consolidation diameter (D) refers to the D calculated in Chapter 4, Section 4.3.3 as 0.4987 mm (or 0.5 ± 0.0013 mm). A schematic of this is shown in Figure 5.11.

The filament theoretical volume (V_i) was calculated from l_r and D :

$$V_i = l_r \cdot \left(\frac{D}{2}\right)^2 \cdot \pi. \quad (5.4)$$

The filament theoretical density (ρ_i) refers to the $\rho_{CF/PEEK}$ calculated in Chapter 4, Section 4.3.3 as $\rho_i = 1575.5$ kg/m³.

The filament mean consolidation diameter (d_c) based on the real mass was calculated as:

$$d_c = \sqrt{\frac{4 \cdot m_r}{\pi \cdot l_r \cdot \rho_i}}. \quad (5.5)$$

The filament void content (e_c) (Figure 5.14) based on the mean consolidation diameter (d_m of Figure 5.1) is calculated as:

$$e_c = \frac{d_m^2 - d_c^2}{d_c^2}. \quad (5.6)$$

The filament theoretical mass (m_i) is calculated by as:

$$m_i = V_i \cdot \rho_i. \quad (5.7)$$

The filament volume difference-based on optical imaging mean diameter measurement (ΔV) (Figure 5.13) is calculated as:

$$\Delta V = V_r - V_i. \quad (5.8)$$

Chapter 5 Characterisation of Composites Filament

The filament void percentage based on optical image measurement calculation (e_m) is:

$$e_m = \frac{\Delta V}{V_r - \Delta V} = \frac{\Delta V}{V_i} \quad (5.9)$$

The filament relative density (RD) using the theoretical density as a reference is calculated as:

$$RD = \frac{\rho_r}{\rho_i} \quad (5.10)$$

Where:

$$\rho_r = \frac{m_r}{V_r} \quad (5.11)$$

is the real density of the filaments.

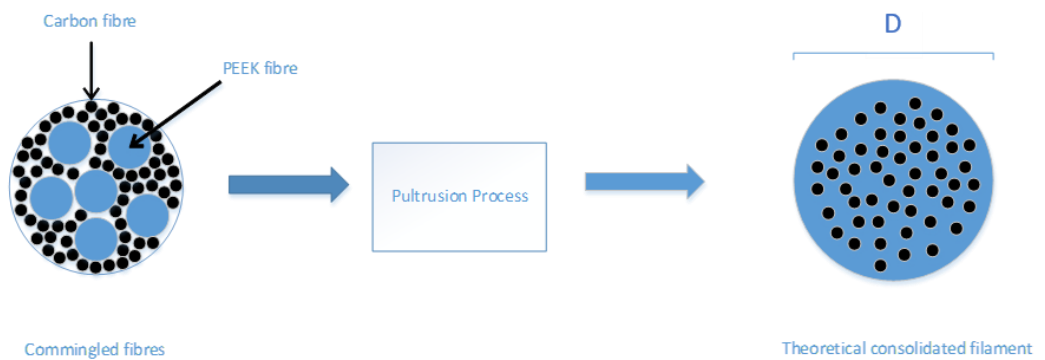


Figure 5.11: Schematic of the pultrusion process. Commingled fibres become consolidated (fully compacted) after the pultrusion process. It leads to a theoretical consolidated diameter D of the filament.

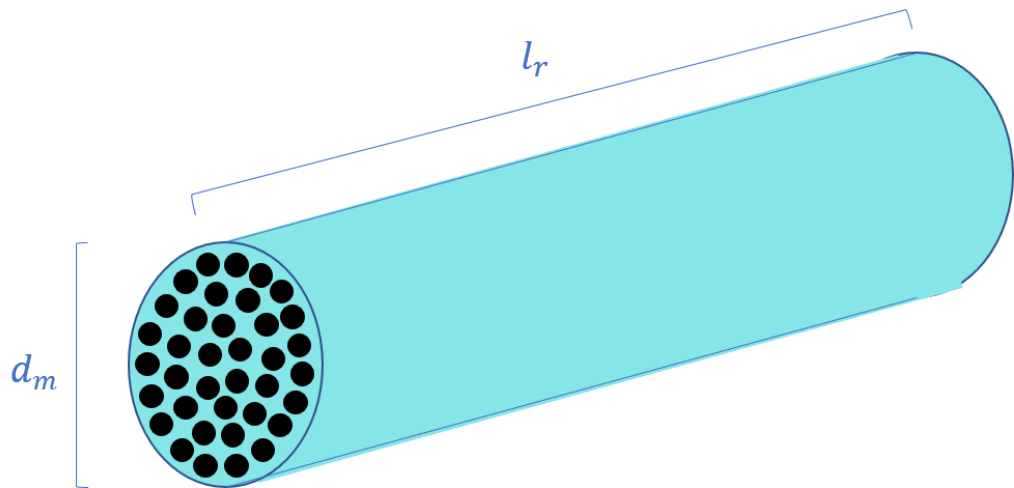


Figure 5.12: Schematic of a filament. The actual cross-section of the produced filaments is closer to an ellipse (oval) shape than a circular shape. The hypothesis of the density analysis assumes the cross-section is circular. The filament mean diameter d_m is obtained by microscopy measurement based on this assumption. The filament real length l_r is the measured length.

ΔV is the light blue volume

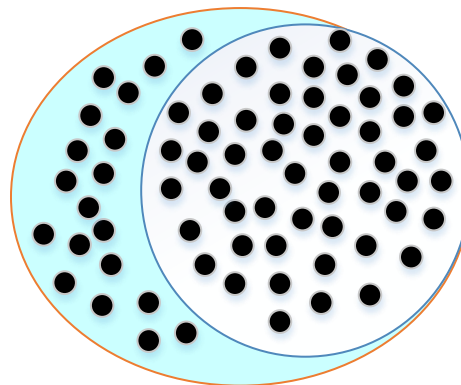


Figure 5.13: Schematic of the filament volume differences. ΔV is calculated by the volume differences of the real filament (light blue) and the theoretical consolidated filament (white).

5.4.2.2 Results and Discussion

The calculated results are shown in Figure 5.14, 5.15, 5.16 and 5.17.

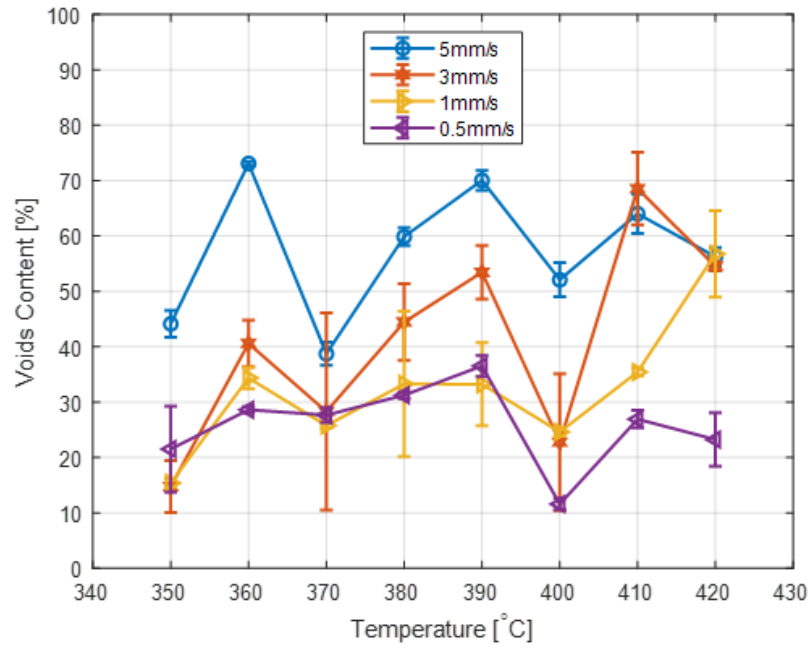


Figure 5.14: The void content e_c (Eq. 5.6) based on the mean consolidation d_c

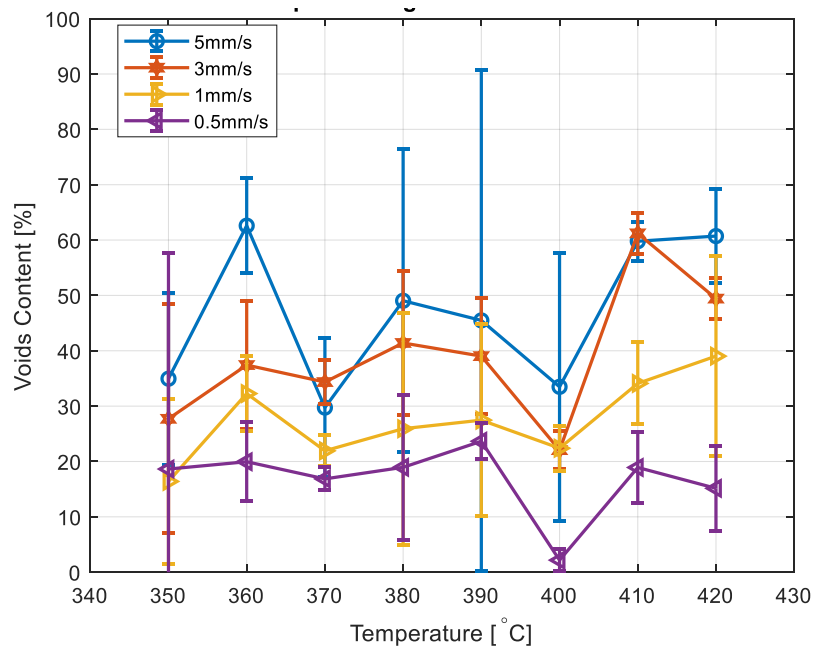


Figure 5.15: Void percentage e_m (Eq. 5.9) based on optical image measured mean diameter in Figure 5.1.

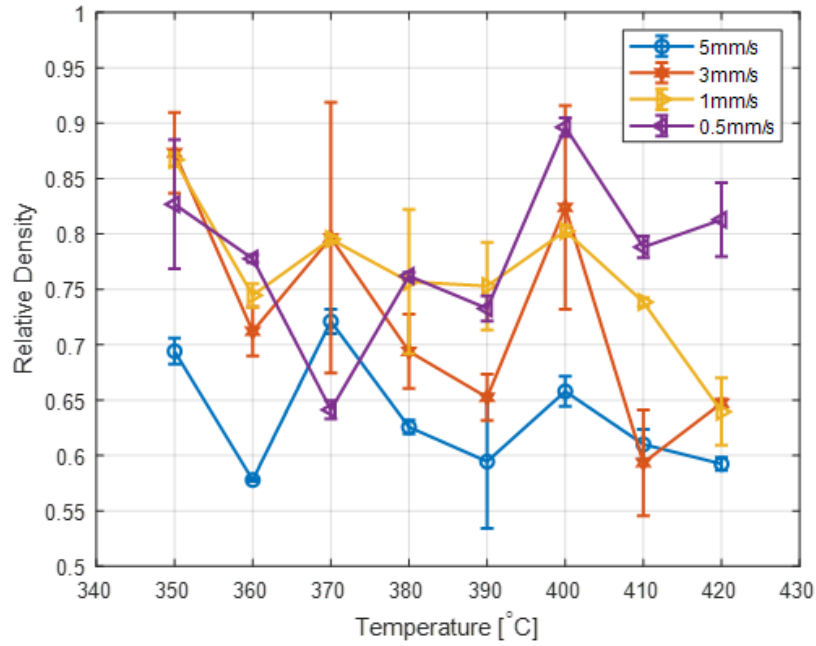


Figure 5.16: The relative density RD (Eq. 5.10) of the filaments.

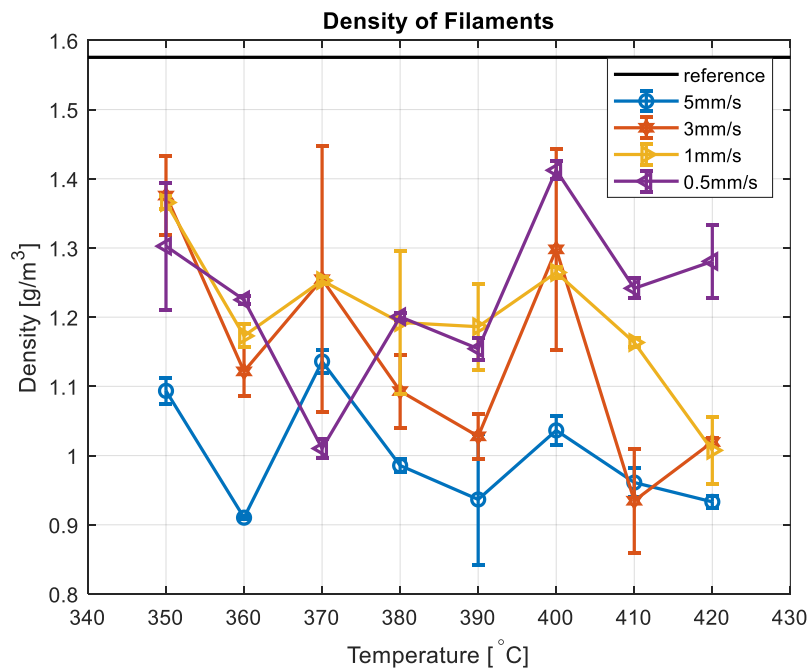


Figure 5.17: The density ρ_r (Eq. 5.11) of the filaments.

The next step is to look at the void content e_c and void percentage e_m . Figure 5.14 shows the void content by calculation based on the mean diameter using the data from the density measurement. Figure 5.15 shows the void percentage calculated based on the mean diameter using the data from Figure 5.1 in Section 5.3. The results obtained from e_c and e_m in both figures show

similar trends. The CF/PEEK filament voids content e_m reflects similar trends to side view mean diameter data. The local optimum die temperatures are 370 °C and 400 °C. Both e_c and e_m are at their local lowest points for a die temperature of 400 °C and a pultrusion speed of 5 mm/s. Although there are some overlaps of data under different sets of parameters, the general trends show that lower pultrusion speed results in smaller e_c and e_m , meaning that the void content over the cross section reduces. In Figure 5.14, the standard deviations are smaller for the temperature range 380 °C to 400 °C, this indicates that the process in this temperature range is more stable than at other temperatures.

The relative density RD and density ρ_r of the filaments can be found in Figure 5.16 and Figure 5.17. The lower the pultrusion speed, the higher the density ρ_r of the filament, and the closer the RD of the filament is to unity. Temperatures of 370 °C and 400 °C are the local optimal points. However, the filament fabricated at 370 °C with 0.5 mm/s shows significantly lower RD and ρ_r than was found for other speeds and processing temperatures.

5.5 Discussion

The measured diameter was compared with the theoretically calculated diameter of the material based on full consolidation of the commingled CF/PEEK. As expected, the void content becomes small and the percentage of cross-sectional area covered by the PEEK increases as the theoretical diameter is approached and compaction approaches its theoretical maximum. It is seen from the results of the investigation that the filament diameter consolidation quality is temperature and time dependent. Moreover, better compaction appears to result in more even distribution of the fibres in the PEEK matrix. The dependence of filament quality upon processing parameters (processing temperature and pultrusion speed) has been demonstrated. There is mainly a monotonic dependence of filament quality upon pultrusion speed, with slower speeds nearly always resulting in lower void content and smaller diameter. However, there is no such unique relationship between filament quality and

temperature, this is believed to be due to multiple trade-offs between improved wetout, ease of relaxation to an uncompact state, and thermal degradation as temperature increases. The local optimal temperatures are seen as 370°C and 400°C in the results. The explanation can be from the DSC results of Chapter 3, Section 3.3.3, which show that there is an additional energy absorption around 370 °C when the cooling rate is high (higher than 100 °C/min). Note that the cooling rate of the pultruded CF/PEEK filament may reasonably be assumed to be higher than 100 °C/min as to the IR-image measurement results of PEEK printing in Chapter 6 captured this order of magnitude for the cooling inside the printing chamber. This indicates there might be an extra thermal reaction related to the melting of crystals happening when the temperature is 370°C, which leads it to be one of the local optimal temperatures. Above 400°C, it is likely that the reduced viscosity of PEEK will result in improved matrix flow. Furthermore, it was found that the CF/PEEK filament diameter never reaches the theoretical consolidation diameter of 0.50 mm. The surface adhesion between PEEK and carbon fibre are different depending on the conditions of processing temperature and time [263]. Note that for the pultrusion process, the speed is inversely proportional to the die residence time. Similar phenomena were also observed by Zhang *et al* [9], who found that the nucleation and crystal growth of PEEK on carbon fibre depend on different combinations of processing temperature and time. This means, that the processing temperature and residence time result in different penetration of PEEK in the distributed carbon fibre, and hence different PEEK coverage. A further explanation is, after the CF/PEEK filament comes out from the die, the CF/PEEK filament diameter does not have a linear relationship with temperature and speed, since PEEK post-process relaxation and recovery does not have a linear relationship with temperature and time. Each of these phenomena mentioned above brings difficulties in predicting the trend of filament diameters with different pultrusion die temperatures and speeds. It was therefore not possible to identify a single unambiguous optimum processing window, though a possible local optimum of 400 °C and 0.5 mm/s

was observed to give a diameter close to the theoretical minimum of 0.5 ± 0.0013 mm. In general, it was found that the apparent optimum temperature of $400\text{ }^{\circ}\text{C}$ presents the best trade-off between ease of compaction (as temperature increase results in a lower viscosity), and the ease with which a molten pultrusion can disintegrate.

When comparing the void content results of cross section analyses in Figure 5.9 with density measurement in Figure 5.14 and Figure 5.15, the latter results show higher void content than the former one. This is because the density measurement takes into account the material leakage, while the cross section analysis does not. If there is no material leakage during the process, from the assumption in the density measurement, d_c equals D , therefore, void content of e_c and e_m should be same. However, results in Figure 5.14 and Figure 5.15 are different. This indicates the occurrence of material leakage during the process. It can also be observed that although the trends shown in Figure 5.9, 5.14 and 5.15 for the filaments produced with a 5 mm/s are similar, the quantitative values for the voids content in Figure 5.9 deviates significantly from Figures 5.14 and 5.15. This is likely to be for the following reason. Figure 5.7 shows that the roundness level of filaments pultruded at 5 mm/s is significantly lower than the filament roundness produced at other pultrusion speeds. This implies that under 5 mm/s pultrusion rate, the major axes of the filament cross sections are larger, which in turn leads a larger measured diameter D . The reason for this is because the second moments of area taking the minor axes as reference axes are larger than the second moment of area about the major axes. As the second moment of area is the bending resistance, bending will occur preferentially in the direction of the minor axis. The slightly curved filament samples will therefore lie on the microscope table with the major axes perpendicular to the table surface. As the filament diameter is measured as it rises from the microscope table, this leads to an overestimation of D and therefore consequently leads to higher calculated voids contents for the results e_m in Figure 5.15 and e_c in Figure 5.14 than the voids content in Figure 5.9. This means that when the filament roundness becomes poor, the

methods that rely on weighing the sample are less reliable and need some alternative ways of measuring the filament diameter, such as results obtained by using the calipers in Figure 5.15.

Moreover, during the pultrusion process, the filament real temperature may not reach the pultrusion die temperature. A more detailed analysis of CF/PEEK filament real temperature during heating can be found in Chapter 6. It should be noted that in all the data of Chapter 5, the temperatures presented relate to the die temperature rather than the filament real temperature.

The trade-off between improved polymer flow and increasing degradation at high temperatures presents a challenge in terms of the narrow processing window for PEEK compared with polymers with lower melting points such as PLA and nylon, requiring accurate control of temperature and pultrusion speed. A further complexity in understanding this trade-off is the influence of carbon fibre as a potential substrate for PEEK crystal nucleation, meaning that the semi-crystalline behaviour of bulk PEEK is not necessarily representative of PEEK's behaviour in the composite material, making theoretical modelling difficult [9]. This led to further investigations into the polymer physics, which are described in Chapter 6.

5.6 Conclusion

Based upon the pultrusion process established in Chapter 4, this chapter describes the validation of the pultrusion based filament fabrication process for use within an FFF printer for the production of continuous fibre composite parts, and to enable subsequent optimisation of fabrication. A parametric study was undertaken to determine the effects of pultrusion speed and temperature on the final filament diameter (measured from transverse views in a microscope), the void content and distribution of fibres and polymer within the pultruded filament product. The major output of this chapter were the optimal pultrusion operating parameters in terms of reducing voids in the filament.

Chapter 5 Characterisation of Composites Filament

Future work will need to take more complete account of the complex semi-crystalline nature of CF/PEEK and the influence of the carbon fibres upon the PEEK's behaviour and gain a better understanding of the trade-off between improved flow and worsening degradation at high temperature. Further approaches that could improve the filament consolidation quality include the treatment of commingled CF/PEEK before the pultrusion process, introduction of an intermediate heating stage with compacting die systems, or by adding solution chemical agent as the treatment of the CF/PEEK to improve the wetout of carbon fibre by PEEK during the process.

CHAPTER 6

Development of FFF Printing Process

6.1 Introduction

As was observed in Chapter 3 where the characterisation of PEEK and CF/PEEK was carried out in order to determine the material properties, the presence of the carbon fibres greatly influences the thermal properties of PEEK during printing. For further discussion on the influence of carbon fibre on the composite's thermal conductivity refer to Reference [248], Chapter 10. In order to investigate the formation of polymer macro-properties, it is therefore necessary to look at the crystal growth, which is in turn dependent on the process parameters of the printed PEEK. In order to obtain a better understanding of PEEK crystallisation for these two different FFF feedstock materials, the printing was divided into the printing of PEEK and CF/PEEK. Based on the observations from the Dynamic Mechanical Analyzer (DMA) experimental results obtained for the printed parts, a hypothesis was proposed to find the relationship between the storage modulus and the layered filament crystal fraction. Part of this work was carried out in collaboration with Dr. Claire McIlroy, who employed a non-isothermal quiescent crystallisation model, informed by the infra-red (IR)-imaging measurements carried out in this research, to better understand the printing process. This helps to establish the relationship between printing parameters and printing quality, and then optimise the printing parameters in order to maximum the polymer fusion in the weld.

The 3D printer used in this work was selected because of its suitability for the printing of PEEK. However, modification of the printer was therefore required for the printing of CF/PEEK. This is described in Section 6.4.1.

DMA testing was used to measure the mechanical performance of a specimen built up from single passes of filament wall. In this way, the disparities between properties in the bulk of the filament and at the weld between the printed filaments could be investigated. In order to understand these properties, a numerical quiescent crystallization mode was employed. As this model requires knowledge of the thermal history, infra-red (IR) thermography was carried out to analyse how cooling varies with print speed and print temperature [127]. Using classical multi-phase composite solid theory [264], it is possible to relate the degree of crystallinity predicted by the model to a storage modulus, and consequently the results of the DMA testing results. This is therefore a method which can relate printing parameters to printed parts mechanical properties, and therefore it is a foundation for optimising crystallisation for mechanical performance. During the printing analysis, the temperature analysis of temperature control for printing CF/PEEK filament has also been done in order to link the real temperature of the CF/PEEK filament when it exits the nozzle with the printing parameters which influence it. This temperature control analysis could help to more accurately temperature control the printing CF/PEEK filament during the process.

The PEEK and CF/PEEK material input information used in this chapter are from the material characterisations of Chapter 3 and data from the literature. Chapter 6 builds on the work presented in Chapter 4 and Chapter 5 by using the feedstock material described in these chapters for 3D print tests.

6.2 Design of the Samples and FFF Printing

Parameters

The FFF printer used in this work is equipped with two printheads. Either nozzle can be heated up to a temperature of 420°C. The chamber and printbed of the printer can be heated up to 90°C.

In order to facilitate thermography measurements using IR-imaging, as in Ref. [128], a rectangular sample that a single filament thick was chosen to be

mechanically tested. The DMA tension test fixture accommodates samples up to 5×10 mm. Thus, to create the test sample, the print path was designed to print a hollow rectangular box, with walls consisting of a single filament, as shown in Figure 6.1 (a). The test samples were then cut by a pair of sharp scissors from the walls of the box, as shown in Figure 6.1 (b). Note that the height of the box in the z -direction was varied according to the test direction; a height of 5 mm (33 layers) was used for the parallel test of longitudinal properties, whereas a height of 15 mm (97 layers) for the perpendicular test of transverse properties. This is shown schematically in Figure 6.1 (c).

The data obtained by the IR-imaging measurements allowed for updated parameters that would lead to a more accurate prediction model than McIlroy *et al.*'s idealised model based on parameters deduced from data in the literature [264]. This is discussed in Section 6.6.5. An illustration of a printed sample can be found in Figure 6.2. During the printing, it was found that only certain combinations of printing parameters could yield printable parts. In practice, this means that two adjacent layers cannot be bonded with either a fast printing speed or a low printing temperature. For this reason, only samples printed in this feasible window were investigated. Samples were printed in the nozzle temperature range between 390°C and 420°C at 10°C intervals and a set of printing speeds of 3 mm/s, 6 mm/s and 18 mm/s in the xy -plane. The printing speed in the x -direction is defined as the speed of movement of the nozzle along the x -axis, V_x . For PEEK printing, within the above print speed range, the width of a deposited filament is consistently 0.5 mm with approximately 2% error. This window for which the road width is independent of print speed has previously been considered in Ref [265]. The machine control data G-code was initially generated using CreateWare 6.4.7 which is software associated with the CreatBot F430 printer. Subsequently the printing path G-code was modified using the Repetier-Host by HotWord GmbH & Co. KG (Willich, Germany) [266]. The G-code was modified to enable printing of the single filament walls shown in Figure 6.1. Note that deposition occurred in the same direction from layer to layer (rather than back and forth) to ensure

consistent cooling profiles in the form of temperature distribution of the x -direction. For the ease and reliability of printing at the start, the printing platform adhesion type was selected as raft in the CreateWare 6.4.7. The primary purpose of a raft is to assist with bed adhesion [267]. Essentially it is a horizontal surface that sits under the printed sample and is removed and disposed when the product is printed and cooled down sufficiently for further handling. The nozzle had a set print temperature (T_N) of 420°C and V_x was set to 6 mm/s to maintain the raft adhesion of the PEEK printed parts to the build plate.

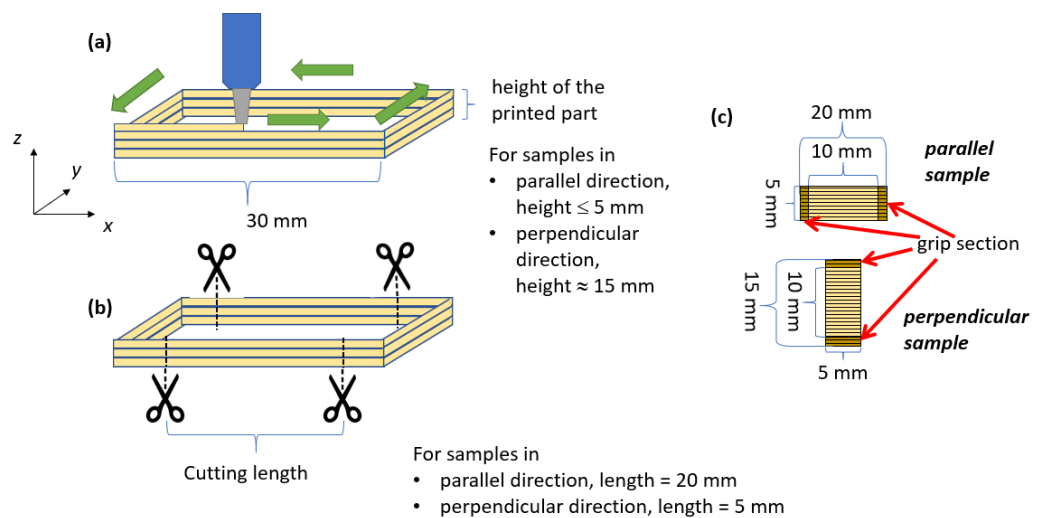


Figure 6.1: Fabrication of DMA test samples from a printed box with walls that are a single filament thick, with (a) the printing direction, (b) cutting lines, and (c) final sample dimensions.

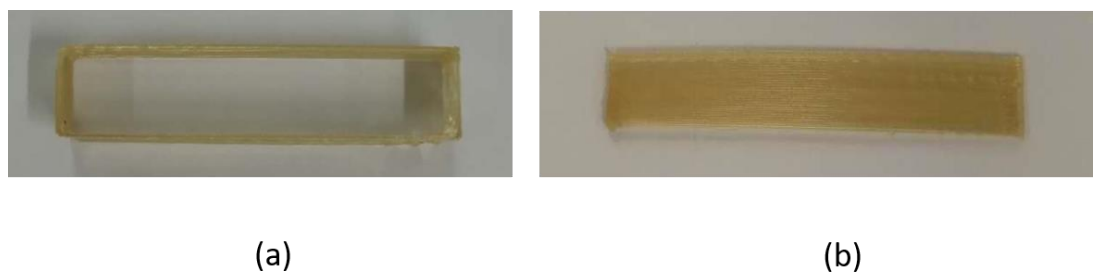


Figure 6.2: An illustration of printed sample in the designed geometry: (a) the top view; (b) the side view.

The printer chamber was closed and the chamber and printbed were heated until a steady-state temperature of 90°C was reached, then the printer front door was opened to allow the IR measurements to be taken.

6.3 Parametric Study of PEEK FFF Printing Process

6.3.1 Infrared Thermography Measurement

Obtaining the temperature history of the printed filament is an important input to understand the PEEK crystal growth. It is also the input for the non-isothermal quiescent crystallization model described in Appendix B. Infrared thermography was used to measure two-dimensional surface temperature profiles for the material in the FFF process. Following the notation of Seppala *et al.* [127], the top filament being actively printed is L_{i+1} , and the adjacent sub-layer is L_i .

The emissivity has been determined using the same method as described in Section 4.2.5. Temperature profiles of these filaments were measured with the FLIR SC7600 IR camera [268] from FLIR Systems (Oregon, U.S.) [269]. The frame rate was set to 100 Hz for the recording. The IR signals were converted into temperature directly using the standard thermographic measurement techniques with the setting of the emissivity of the object, the reflected apparent temperature, the distance between the object and the camera, the relative humidity, and the temperature of the atmosphere [270]. Figure 6.3 shows the IR camera setting in equipment setup window.

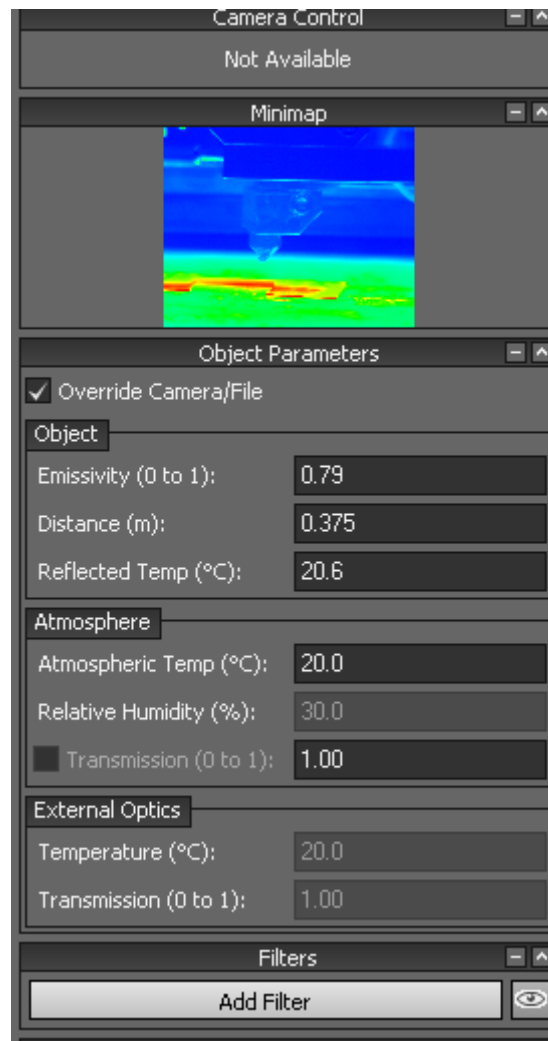


Figure 6.3: IR camera setup.

The region of interest (ROI) is a window of three by three pixels and was placed at the centre of each layer during the printing process. The ROI cursor (shown in Figure 6.4 (a)) was used to take the temperature of the first filament L_{i+1} and was kept at the same position for in all printing conditions. Since crystallisation ceases at the glass transition, the IR measurement was terminated once the temperature decreased below T_g . The reflection IR signals (see Figure 6.4 (b)) were corrected using the same method outlined by Seppala *et al.* [210]. This reflection-correction method requires subtraction of the signal obtained from a pass of just the nozzle without material deposition. In order to make the FFF process work, the amount of heat transferred from the nozzle into the filament should be quite low compared to the power input from the HeatBlock. Therefore, the nozzle temperature can be safely assumed

to be the same in both cases. The heat dissipated by the filament was investigated and quantified in Section 6.4.3.2. The IR measurements were made for both actual printing of the material and for a nozzle without any material being deposited (see Figure. 3.2) to obtain the surface temperature evolution at the filament mid-point. The results can be found in Appendix C.

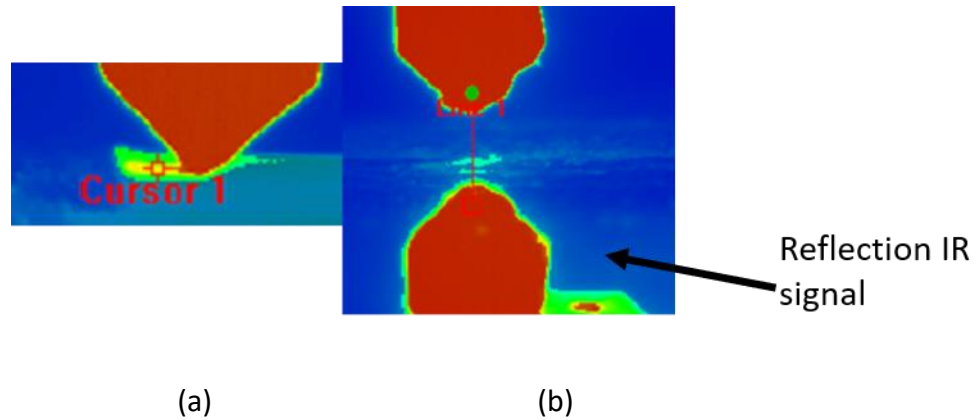


Figure 6.4: IR image of printing (a) printing with loaded nozzle (b) printing without loaded nozzle

The mid-point between adjacent filaments is termed the weld line W_i . Due to the curvature of the filament surfaces, it would not be correct to give the IR-imaging measurement at the weld line directly. Thus, the weld temperature is calculated as the average value of the temperatures of these adjacent filaments as [127]:

$$W_i = \frac{L_{i+1} + L_i}{2} \quad (6.1)$$

A representative result after this correction can be found in Figure 6.5.

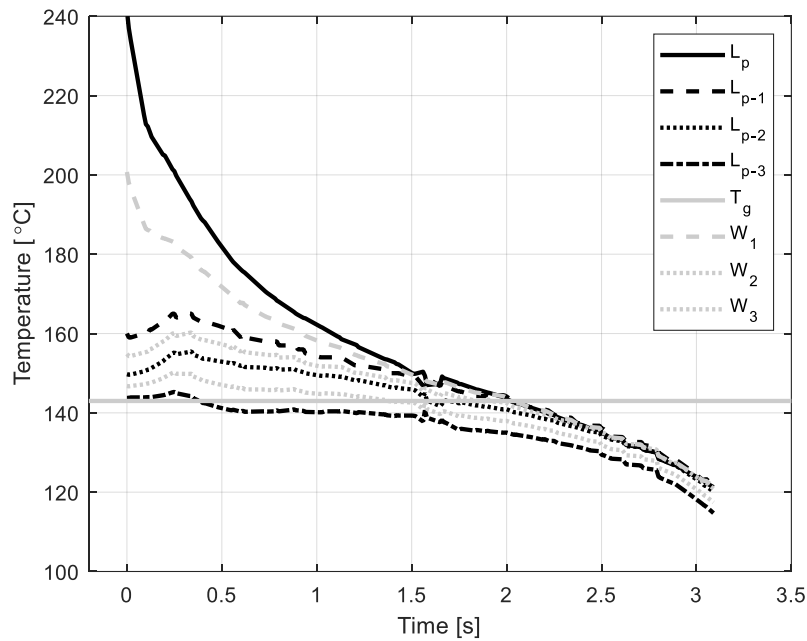


Figure 6.5: Corrected temperature profile of PEEK at 18 mm/s 410°C.

The lines L_p , L_{p-1} and L_{p-2} are the thermal histories of the printed filament measured using IR. Here index p denotes the top layer and the subsequent layers below which are denoted by descending values. W_1 , W_2 and W_3 are the calculated weld temperatures. T_g is the glass transition temperature. The measurement stops at L_{p-2} since the temperature of the next filament drops below T_g . This result shows that with the current print setup, the cooling rate of PEEK filament during printing is quite high due to the fact that the maximum achievable chamber temperature of the printer used was below 90 °C. This will affect the crystal fraction of the final printed parts, which will be further discussed in Section 6.5.

6.3.2 DMA Tension Tests as Quantitative Measurement

6.3.2.1 Sample Preparation and Test Setup

DMA was used to measure the mechanical stiffness of the samples. The PerkinElmer Inc. (Massachusetts, US) [198] DMA 8000 [217] was utilised for this test. A sinusoidal displacement was applied and the strain in the material was measured. The temperature was kept constant at 23°C and the frequency was set at 1 Hz (note that the storage modulus has the same magnitude as the

modulus of elasticity at low frequency [271]). Six samples were tested under each condition, and each of these tests lasted for 5 minutes. The standard deviations of the storage modulus of each of the 6 samples were calculated and used as the errors. The test mode executed was the tension test. The measurements were carried out in two orientations with respect to the print direction, and hence the filament orientation. These are parallel to the print direction (each sample having 33 layers), and perpendicular to the print direction (each sample having 97 layers). By applying the tension force perpendicular to the direction of the printed layers of filament, E_{perp} was measured, whereas applying it parallel to the direction of the printed layers, E_{par} of the sample could be measured, as is illustrated in Figure 6.6. As mentioned in Section 6.2, the samples were cut into a width ≤ 5 mm, and length between 15 mm and 20 mm in order to fit into the DMA fixture.

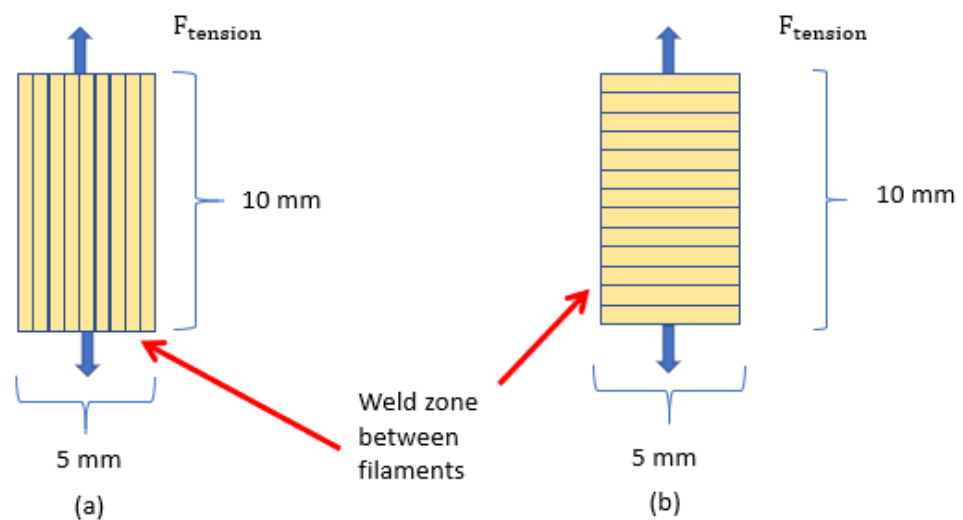


Figure 6.6: Schematic of DMA test samples. The valid test size is less than 5 mm width and 10 mm length. (a) test sample with parallel load direction. (b) test sample with perpendicular load direction.

6.3.2.2 Results and Discussion

Figures 6.7 and 6.8 show the results of the DMA test for the printing conditions listed in Section 6.2; Figure 6.7 shows the storage modulus measured in the perpendicular direction that corresponds to E_{perp} , whereas Figure 6.8 shows the storage modulus measured in the parallel direction that corresponds to

E_{par} . Error bars represent the standard deviation from the time-averaged mean, averaged over the 6 samples.

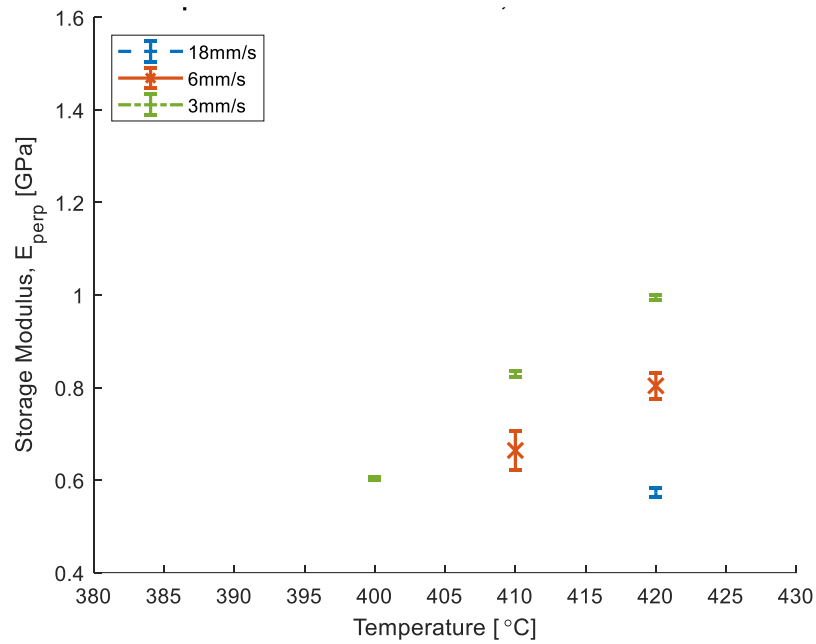


Figure 6.7: Storage modulus for PEEK DMA tested in perpendicular direction. This corresponds to E_{perp} . The printable conditions are: 3 mm/s, 6 mm/s and 18 mm/s at 420°C; 3 mm/s and 6 mm/s at 410°C; 3 mm/s at 400°C.

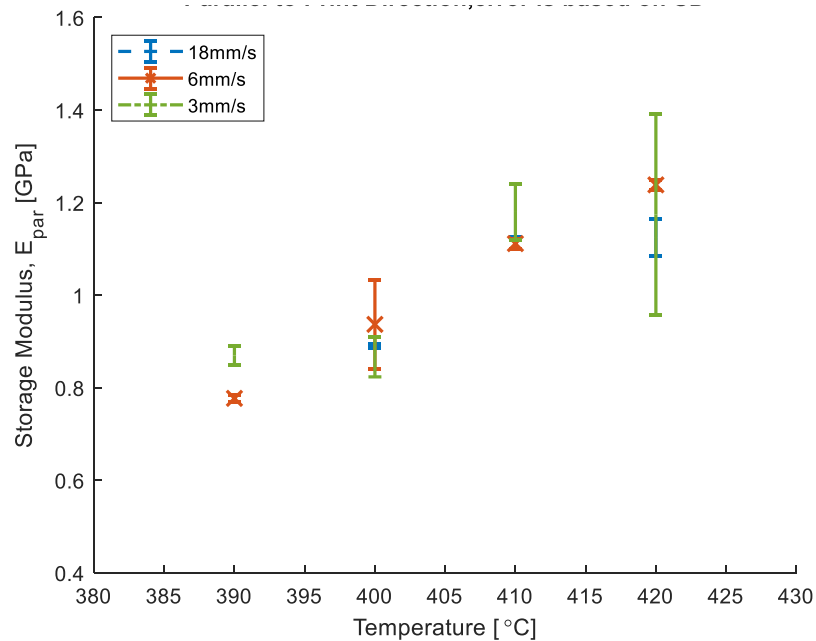


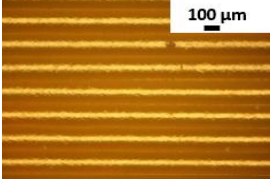
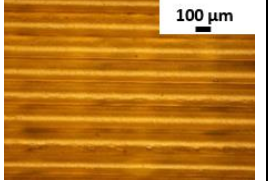
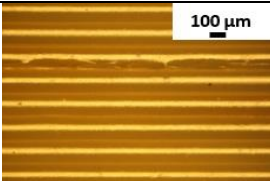
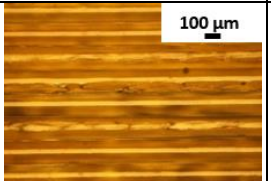
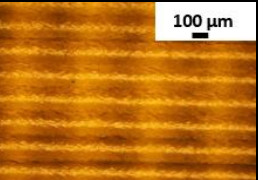
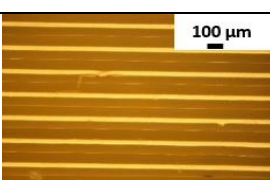
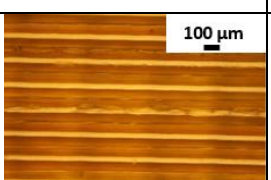
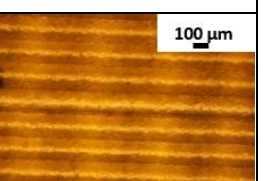
Figure 6.8: Storage modulus for PEEK DMA tested in parallel direction. This corresponds to E_{par} . The printable conditions are: 3 mm/s, 6 mm/s and 18 mm/s at 420°C; 3 mm/s, 6 mm/s and 18 mm/s at 410°C; 3 mm/s, 6 mm/s and 18 mm/s at 400°C; 3 mm/s and 6 mm/s at 390°C.

Firstly, it is noticed that both the perpendicular, E_{perp} , and parallel, E_{par} , storage moduli are greater than the storage modulus of PEEK in its amorphous state ($E_a = 0.07$ GPa [272]). It is also found that E_{par} is, on average, between 24% to 40% greater than E_{perp} . Similar anisotropy has been observed by Capote *et al* [273] for acrylonitrile butadiene. Here tensile, compression and torsion tests were performed to calculate a failure envelop. Considerable interactions were found between the shear stresses applied in directions perpendicular and parallel to the deposited filaments in a typical dog-bone specimen. Secondly, one can see that both E_{par} and E_{perp} depend on the print temperature, with higher print temperatures yielding greater storage moduli. Finally, it is observed that on average there is little dependence on print speed for E_{par} , whereas E_{perp} decreases with increasing print speed.

Since PEEK is a semi-crystalline polymer, it is known that an increase in storage modulus may originate from an increase in crystal fraction [9, 160, 234]. This is found in the results that both E_{par} and E_{perp} are greater than E_a , and a change in transparency was observed during the printing, which indicates that the filament crystallises to some degree during the cooling.

6.3.3 Microscopy of the Sample Surface

Table 6.1: Microscopy of the PEEK sample surface.

| Parameter $s(T_{ext}, V_x)$ | 3 mm/s | 6 mm/s | 18 mm/s |
|--------------------------------|---|--|---|
| 400°C |  |  | |
| 410°C |  |  |  |
| 420°C |  |  |  |

Microscopy images were taken for the side view of the DMA samples before testing. All the pictures were taken on the Nikon Eclipse Lv100ND microscope with a magnification factor 10. For more information on the microscope, refer to its description in Chapter 3. It can be clearly seen in the figure in Table 6.1 that the surface of the printed sample becomes smoother when the print speed reduces and the temperature increases. Surface roughness studies would have been carried out with more laboratory time availability, however, here only a qualitative study of the surface roughness is conducted and further quantitative investigation can be future work of this research.

6.4 Carbon Fibre Reinforced PEEK FFF Printing Process

6.4.1 Adaptation of Traditional 3D Printing Process

The two head printer used in this work was designed for use with PEEK and other polymer filaments and had to be adapted to enable orienting of the CF/PEEK filaments produced by the pultrusion process described in the preceding two chapters. During the printing, an oversized nozzle, 0.8 mm diameter, was used. The filament detection sensor was disabled by putting a small piece of PLA filament in as shown in Figure 6.9. After disabling the filament sensor, the printer was capable of printing the CF/PEEK filament through the oversized nozzle.

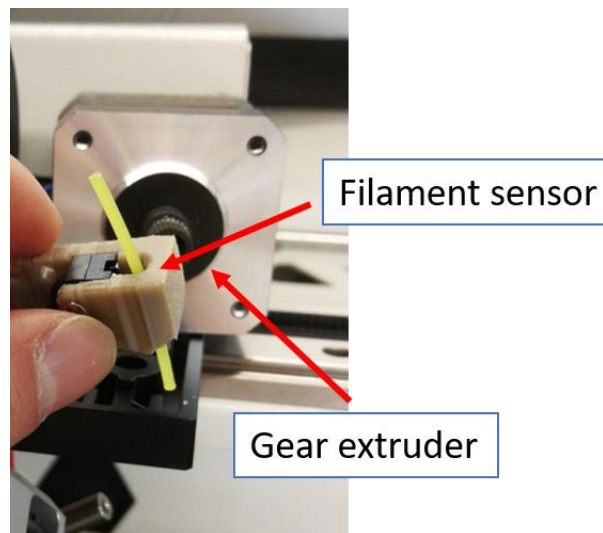


Figure 6.9: Disabled filament detector sensor to ensure the printer work properly with an oversized nozzle.

The CreatBot F430 printer has 2 nozzles. During the printing, Nozzle 1 was assigned to print the raft, the initial layer to assist adhesion, using the same procedure as described in Section 6.2. Nozzle 2 was then used to print the CF/PEEK filament. After the printing, the filament was manually cut. Figure 6.10 shows a final printed CF/PEEK part.

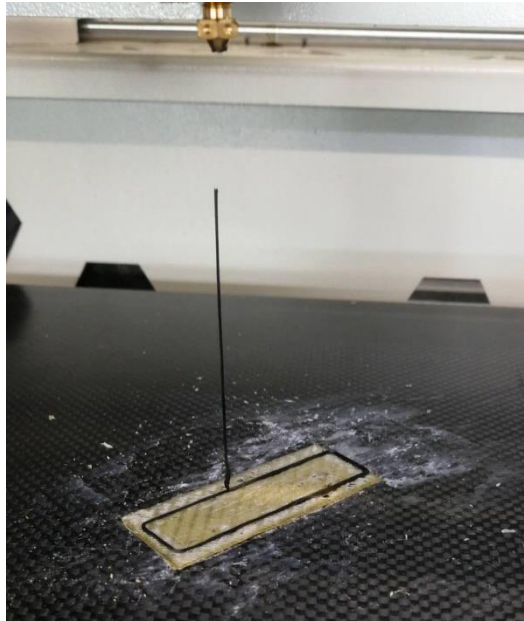


Figure 6.10: Illustration of a printed CF/PEEK part in the final step.

6.4.2 Preliminary CF/PEEK Printing tests

The preliminary trials of the printability of the manufactured CF/PEEK FFF feedstock material using the modified printer described above involved printing conditions of 1 mm/s printing speed and a print temperature of 420°C using CF/PEEK filament fabricated under conditions of 0.5 mm/s pultrusion speed and an operation temperature of 400°C . The ability to print successfully was initially tested experimentally. It was then further confirmed by the predictive model of nozzle performance of CF/PEEK in Section 6.4.3.2. As can be seen in Figure 6.11, these conditions enabled successful printing of the manufactured CF/PEEK filament based on the printability criteria stated in Section 1.3 Chapter 1.

- The feedstock material had sufficient stiffness to be successfully extruded through the modified print head. This fully meets criterion 1.
- The selected printing temperature and speed allowed the filament to be heated above the melting temperature, without reaching temperatures where material degradation occurs. Using the oversized nozzle for better deposition on the print path, the processing forces are relatively low and did not affect the filament and fibre integrity in any

observable manner in subsequent inspection. This fully meets criterion 2.

- The modified nozzle allows for a sufficiently large bending radius to prevent the carbon fibres from cracking, and to enable deposition of fibre tracks with 90 degree angles without failure. A reasonable uniformity in thickness of the printed CF/PEEK was achieved based on visual inspection as the overlaid layers bond reasonably well with a fixed incremental printing layer height. This fully meets criterion 3.
- The printed CF/PEEK adhered to the printed PEEK substrate and the overlaid layers reasonably bond well. The density of the printed track also appeared high from visual inspection with no obvious porosity. However, since the ambient temperature of the chamber was not able to be set sufficiently high, solidification will occur rapidly and the opportunity for bonding between successive layers to occur is relatively short-lived. This results a lower degree of bonding between the polymer regions on the two side of the layer interface. A higher ambient temperature can give a lower temperature gradient of the filament during printing and therefore the welding zone remains for longer at the temperature range where bonding can occur and this would result stronger bonds between layers. Hence, with the current experimental setup, criterion 4 can only be partially met.

Unfortunately, a full characterisation of the printed material and further examination of the effect of printing conditions and performance of printed could not be carried out as access to the laboratory was Covid restricted. The emphasis of the investigation, therefore, switched to a theoretical analysis of printing, as described in the following sections of this chapter. However, further research into the CF/PEEK printability to attain a good printability and ultimately to optimise the printing process should be carried out when possible. This would comprise a consolidation study of the printed material. In this investigation the printed material should be compared with the fabricated filament. Further tests should include finding the maximum number of layers

of a single layer wall that can be printed and the strength of the material with mechanical tests, etc in order to establish the achievable structural integrity.

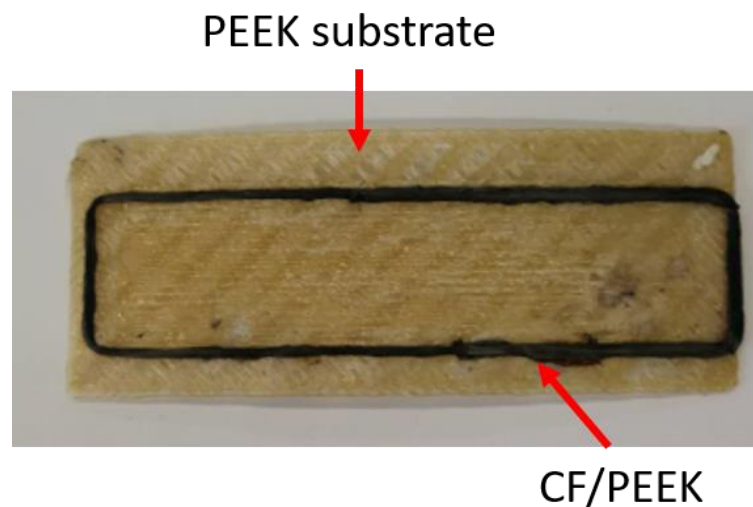


Figure 6.11: FFF CF/PEEK printed part.

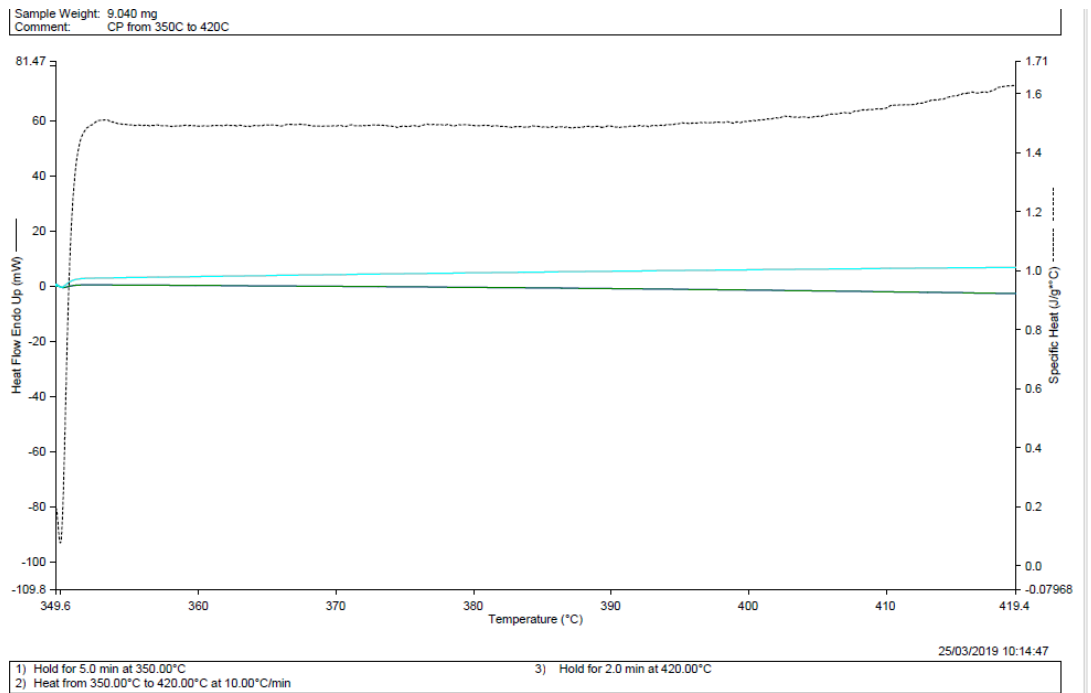
6.4.3 Temperature Control for Printing Carbon Fibre with PEEK Filament

As mentioned above, for the CF/PEEK filament FFF printing, an oversized printing nozzle was used, hence, there was an air gap between the nozzle inner wall and the filament. In order to accurately control the filament temperature during the printing, and then further optimise the printing, a model that can be used to study the steady-state heat and temperature distribution during printing was developed that made it possible to effectively control the CF/PEEK filament temperature during the printing. Concurrently, Dr. Claire McIlroy carried out a calculation based on the 1D heat equation, for completeness this is provided in Appendix D. The equation requires the input of CF/PEEK thermal diffusivity (Section 6.4.3.1), then the non-dimensionalised 1D heat equation can be established as presented in Appendix D. The results contributed by Dr. Claire McIlroy are compared with the predictive nozzle performance modelling in Section 6.4.3.2.

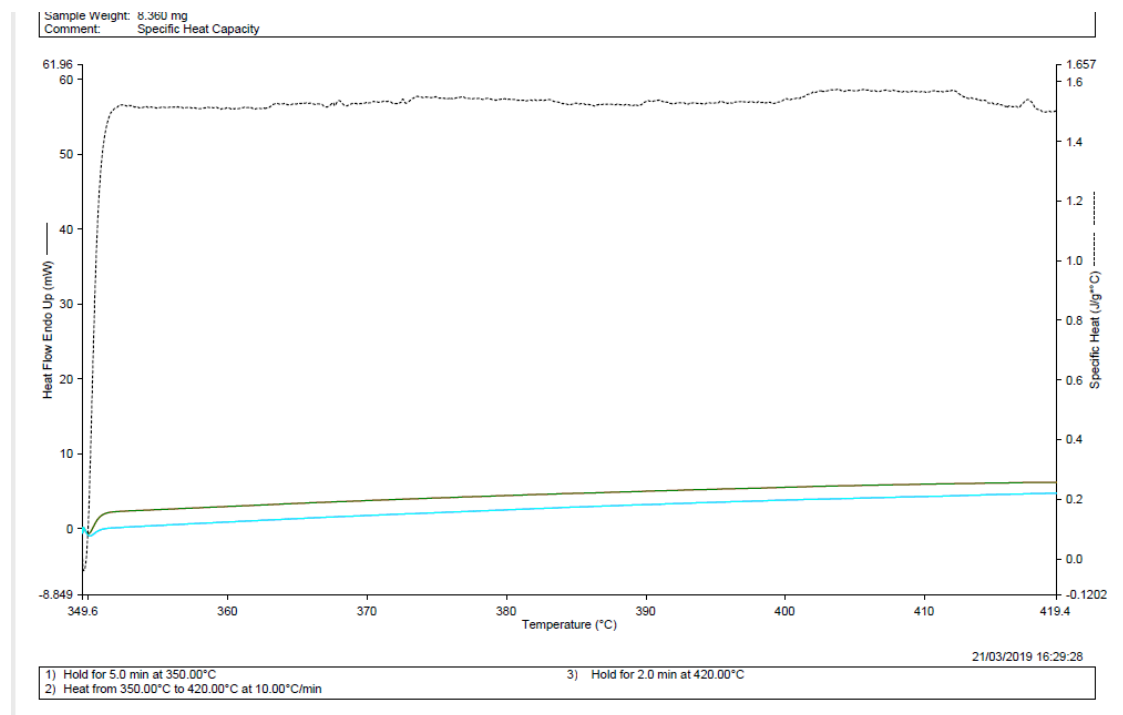
6.4.3.1 Establishing the Thermal Diffusivity of Carbon Fibre with PEEK

The specific heat capacity (c_p) of the CF/PEEK filament was determined by means of the dual furnace DSC 8000 using the traditional 2-Curve method [274]. This is a method to subtract the baseline curve from the sample curve, and further calculate with the sample mass and the heating rate used for the test. With care, specific heat data with around 1.5% absolute error or slightly better accuracy should be obtained. The sample was heated to 350°C first and held for 5 mins. Then the sample was heated from 350°C to 420°C with a heating speed of 10°C/min, and the sample was finally held at 420°C for 2 mins. Five tests were executed, and among these, there were two tests with similar value of c_p results. However, when the test temperature was above 410°C, the calculated specific heat signal provided unreliable c_p information as there was a fluctuation in the c_p value. The unstable heat flow indicates that the CF/PEEK thermal properties are changing. This unstable heat flow is possibly due to degradation of the CF/PEEK since this was previously mentioned in Ref [1]. However, a precise study and understanding of the high temperature degradation behaviour of CF/PEEK was out of scope for this work and therefore will be part of the proposed future work. Figure 6.12 gives two of these results. When the temperature raised above 350 °C, the value of c_p went to plateauing which provides a value of the c_p as 1.5 J/g·K with an error of approximate 6%.

Chapter 6 Development of FFF Printing Process



(a)



(b)

Figure 6.12: DSC results by traditional 2-Curve method, which provides a value of specific heat capacity as 1.5 J/gK .

The transverse thermal conductivity of CF/PEEK is calculated using the Nielsen theory [275], since it is known to give the best predictive results, e.g. Refs [134, 276, 277], where medium length CF/PEEK is investigated. Using the notation by Lee *et al* [135] for two-phase systems, the conductivity k_c of the composite materials as predicted by the Nielsen equation is as follows [275] :

$$\frac{k_c}{k_m} = \frac{1+AB\phi}{1-\phi B\phi} \quad (6.1)$$

Where $B = \frac{k_f/k_m - 1}{k_f/k_m + A}$, and $\phi = 1 + \frac{(1-\phi_{max})\phi}{\phi_{max}^2}$, where, $A = f$ (the geometry of particles), and ϕ_{max} is the maximum packing fraction. Here $k_f = 400$ (W/mK) and $k_m = 0.29$ (W/mK) which is from Ref [136].

Based on [Table I, 275], the values of 0.5, 0.84 and 1 were all applied for constant A, which depends on the shape and orientation of the dispersed filler material. The reason to select these values is the following: $A = 0.5$ is for dispersed aligned fibres. Identical to the commingled yarn utilised in this work, the fibres used in conventional polymer composites are generally yarns made up of many fibres in a bundle, so the proper value of A for aggregated fibres is approximately 0.84 [Table I, 275]. Nielsen [275] also states that, if the fibres are perfectly aligned, the experimental data should be bounded by values of A between 0.5 and 1. Also from Nielsen [275], ϕ_{max} is selected as 0.82 for random packing of aligned fibres. Recall that the commingled CF/PEEK does have a non-homogenous carbon fibre distribution (Chapter 3), this is the reason for the ϕ_{max} to be chosen here. Substituting in the values for ϕ_{max} , A, k_f and k_m into Eq. (6.1) makes it possible to calculate the value of the thermal conductivity for CF/PEEK composite as a function of the fibre volume fraction ϕ as shown in Figure 6.13. Details of the calculation can be found in Appendix E. The results show the volume fraction of carbon fibres versus the value of thermal conductivity. For the case of 50% carbon fibre volume fraction, the thermal conductivity is around 0.82 to 1. These results could also provide the thermal conductivity value with different carbon fibre volume fraction.

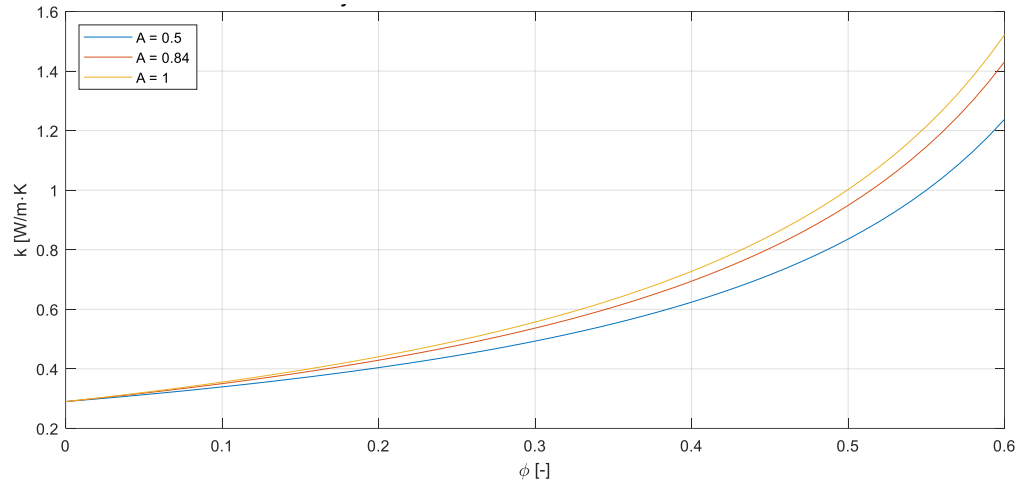


Figure 6.13: Predicted thermal conductivity CF/PEEK in lateral direction as function of fibre volume fraction.

6.4.3.2 Predictive Modelling of Nozzle Performance

One of the important factors that determines the capacity of the printer in terms of print speed is how well the nozzle can transfer the heat generated in the heatblock into the filament.

If the temperature gradients on the nozzle itself can be assumed to be negligible (the power output of the heat cartridges is an order of magnitude larger than the power consumed by the exiting filament heat), then the nozzle can be considered to have a constant surface temperature, and therefore is a heat exchanger with a constant surface temperature heat flux. This type of heat exchanger has a well-established solution in the form of a lumped parameter model [240] to obtain the average or bulk temperature of the mass flow in the pipe based on the surface of the nozzle surface temperature. Note that T_N is the surface temperature of the nozzle pipe. $T_{a,i}$ is the bulk temperature of the ingoing mass flow. P is the perimeter of the pipe. \dot{m} is the amount of mass in the z -coordinate. \bar{h} is the average convection coefficient, and c_p is the heat capacity of the mass flow [240].

$$\frac{T_N - T_a(z)}{T_N - T_{a,i}} = \exp\left(-\frac{Pz}{\dot{m}c_p} \bar{h}\right) \quad (6.2)$$

Rearranging Eq. (6.2) gives:

$$T_a(z) = T_N - (T_N - T_{a,i}) \exp\left(-\frac{Pz}{\dot{m}c_p \bar{h}}\right) \quad (6.3)$$

Which is the well-known exponential distribution, as shown in Figure 6.14.

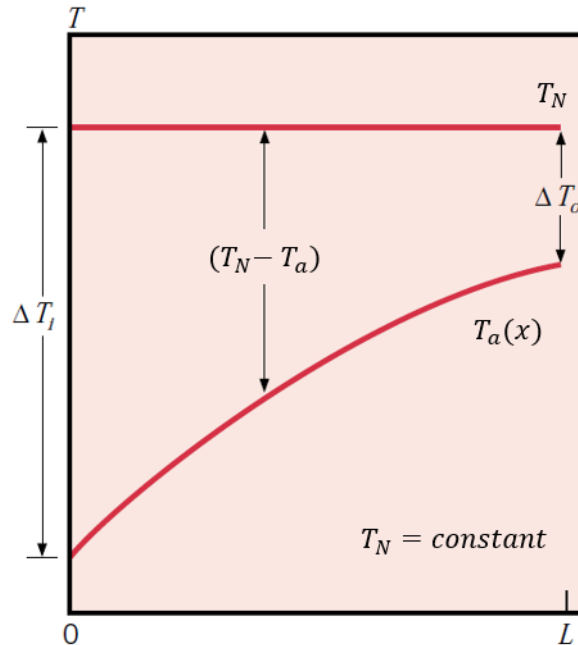


Figure 6.14: Temperature variations in axial direction for heat transfer in a pipe with constant surface temperature. Source Ref. [240], Fig. 8.7 (notations have been adapted).

Eq. (6.2) is the well-known solution for a heat exchanger with a fluid going through a tube. The material going through the nozzle is not a liquid, but a solid filament. Therefore, to model the heat exchange capacity of a nozzle, a value needs to be established for the average convection coefficient \bar{h} . From Dr. McIlroy's numerical model, described in Appendix D, one can see that heat conduction is a significant contribution in the total heat transfer. It is therefore paramount to capture the heat conduction and establish a heat transfer coefficient based on the heat flux due to conduction.

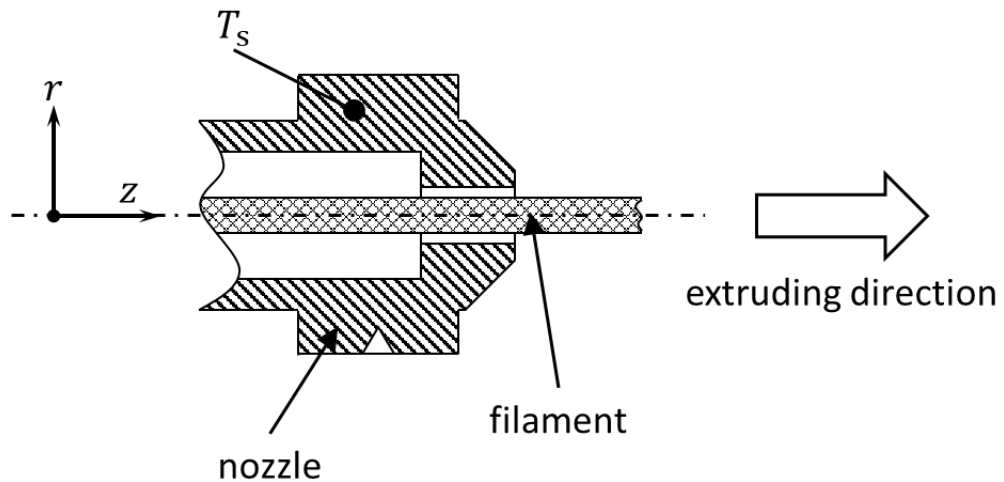


Figure 6.15: Schematic cross sectional view of nozzle and filament, not to scale.

In Figure 6.15 one can see the schematic view of a nozzle shown horizontally rather than in its usual vertical orientation in a 3D printer. The left hand side of the figure shows a cut-off view where the nozzle is fastened by its screw thread into the heatblock. The filament is pushed through the nozzle by the extruder mounted on top of the HotEnd. From the CAD drawing of the nozzle [99], one learns that the filament arrives in the nozzle through a 2 mm diameter entry hole. As mentioned above, the temperature through the nozzle is constant and further denoted as T_N , which is set at 400 °C. The filament exists the nozzle through an orifice, as shown in Figure 6.15. The 60° tapered transition between the 2 mm diameter bore hole and the orifice is not shown in the drawing. This is because for the CF/PEEK filament FFF printing process design, the nozzle is chosen to be oversized and there is no contact between the wall and the filament. However, during printing, the CF/PEEK filament will touch the edge of the nozzle when it just exits from the nozzle. This is a very brief contact and the size of the contact area is difficult to determine or estimate without further complex modelling and or experimentation as the model does not consider any deformation of the filament. Hence, this model does not include this heat source, causing the calculated temperatures for the exiting filament therefore to be lower .

In case of printing the PEEK filament, the filament diameter is 1.75 mm, and melting occurs in the tapered section, hence printheads includes the nozzles are often known as *liquefiers* as mentioned in Chapter 2. As the nozzle orifice has a diameter of 0.4 mm and a length of 0.6 mm, the average diameter in the tapered section is 1.08 mm, which is taken as the average between 1.75 and 0.4 mm. With simple goniometric relations, the length of this tapered section as seen by the filament is 1.17 mm. The print speed in the results is the exit velocity of the extruded filament. The filament velocity in the nozzle sections depends on the squared ratio of the diameters, so the average speed in the tapered section is a factor 0.05 slower, or just over 19 times slower than the print speed.

The consolidated diameter of the CF/PEEK filament is approximately 0.5 mm; for CF/PEEK printing, the nozzle has an oversized 0.8 mm orifice diameter, and an axial length of 1.6 mm. As the orifice has an oversize diameter, there is a small air gap between the wall and the filament. The total length of the nozzle is 12.5 mm, hence the length of the 2mm diameter bore can easily be calculated to be 10.9 mm.

Given that there is a transfer of heat from a fluid and air, the average heat transfer coefficient can be taken as $\bar{h} = 10 - 40 \text{ W/m}^2\text{K}$ [240], with the lower value of 10 taken as the conservative case and 40 as the optimistic case.

When using the geometry to calculate the resistance of the air to conduct heat to the filament, the same method that was applied to establish the heat transfer coefficient for the oversized nozzle in the modelling of CF/PEEK filament, its numerical value becomes $36.6 \text{ W/m}^2\text{K}$, which is very close to the optimistic case of $40 \text{ W/m}^2\text{K}$. Therefore in the results both the most conservative and optimistic cases are studied.

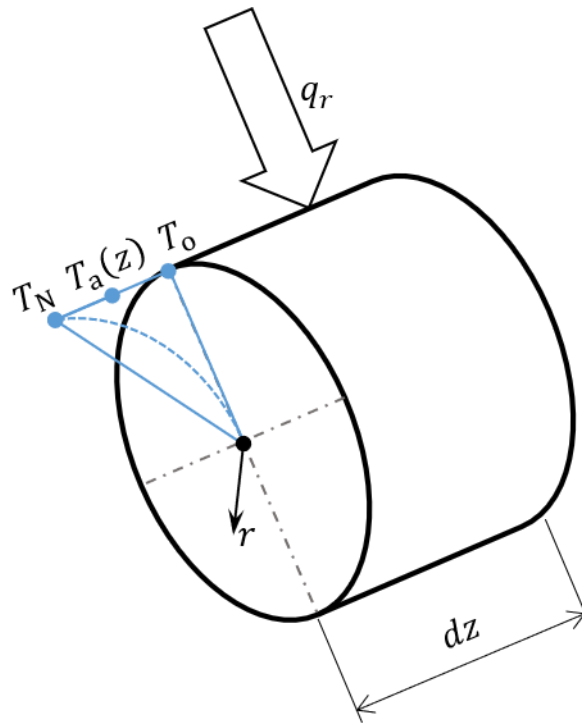


Figure 6.16: Cylindrical control volume of a cylinder with infinitesimal thickness dz in the cylindrical coordinate system, with T_N (as the set temperature as the surface), $T_a(z)$ (the local average temperature of the cross section), and T_o the centreline temperature

For a correct thermal analysis of a heat transfer system, firstly the heat balance must be established. As the filament is being pushed in the axial direction by the extruder, the mass flow is in the same direction. Ignoring the thermal contact resistance at the interface between orifice and filament, for a small control volume as shown in Figure 6.16, one can assume that the heat goes into the control volume is firstly the heat stored in the material that comes as a small slice of the filament moving into the control volume. And secondly, the heat that is conducted from the hot surface into the material, shown as q_r in Figure 6.16. For the normal heat exchanger model where a fully developed laminar flow is assumed, and for a model describing the heat of a moving, continuous solid (the filament), it is reasonable in both cases to assume negligible heat conduction in the axial direction. Using Fourier's law, this conducted heat can be mathematically described as:

$$q_r = -kdA \frac{dT}{dr} = -k2\pi R dz \frac{dT}{dr} \quad (6.4)$$

The energy exiting the control volume is all going out by means of “convection” when the small slice of filament departs the control volume. When following the steps outlined in Section 8.3.1. in Ref. [240], the energy coming into a heat exchanger by convection from the hot surface is:

$$q_r = \bar{h}dA\Delta T = \bar{h}2\pi R dz(T_N - T_a(z)) \quad (6.5)$$

By equating the two expressions Eqs. (6.4) and (6.5) for q_r , a suitable expression for heat transfer coefficient \bar{h} depending on conduction coefficient k can be established. However, firstly a suitable expression for the temperature gradient $\frac{dT}{dr}$ needs to be found. The temperature gradient at the outer surface of a solid cylinder is determined by the solution of the heat equation. If for simplicity the heat dissipated by means of convection (the extruding of the filament) is modelled as a sink term and the system is axisymmetric, then the heat equation given by [240], Eq (2.24):

$$\frac{1}{r} \frac{\partial}{\partial r} \left(kr \frac{\partial T}{\partial r} \right) + \frac{1}{r^2} \frac{\partial}{\partial \phi} \left(k \frac{\partial T}{\partial \phi} \right) + \frac{\partial}{\partial z} \left(k \frac{\partial T}{\partial z} \right) + \dot{q} = \rho c_p \frac{\partial T}{\partial t} \quad (6.6)$$

Reduces to [240], Eq. (3.49):

$$\frac{1}{r} \frac{d}{dr} \left(r \frac{dT}{dr} \right) + \frac{\dot{q}}{k} = 0 \quad (6.7)$$

When the sink term is assumed to be a uniform dissipation and after separating the variables, the expression above can be integrated twice. Applying the boundary conditions as the set surface temperature at $r = r_o, T(r_o) = T_N$ and the axisymmetric condition $\frac{dT}{dr} = 0$ at $r = 0$ the solution for the temperature distribution is found to be *parabolic*, as illustrated in Figure 6.16 with the dashed line, where the minimum temperature is found on the centreline, denoted as T_o . Further details of the solution can be found in Ref. [240], Section 3.5.2.

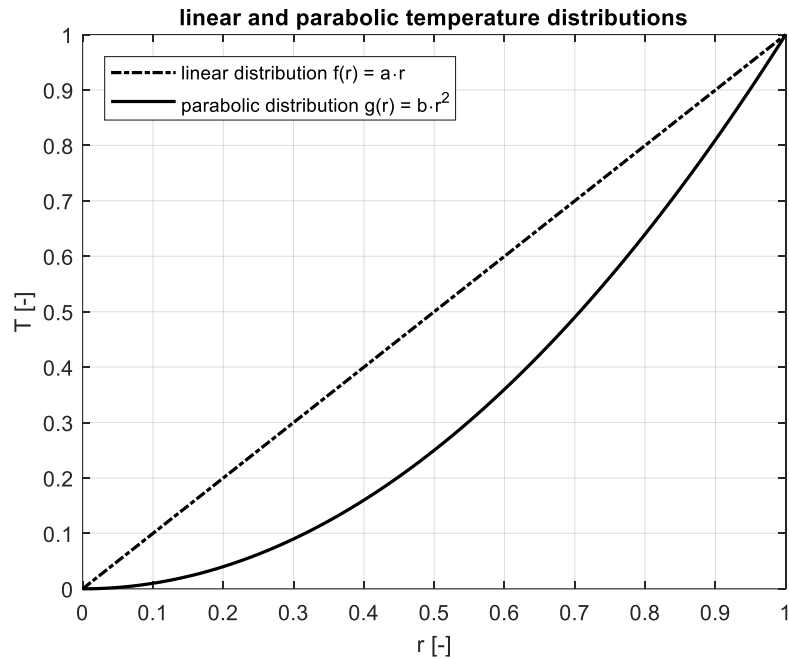


Figure 6.17: Comparison of normalized linear and parabolic temperature distribution.

As the temperature distribution is parabolic rather than linear, it could potentially make it more difficult to find the temperature gradient at the filament surface. The mathematical properties of parabolas give a good starting point. Be $f(r)$ an arbitrary linear function translated such that it crosses the origin: $f(r) = ar$ and be $g(r)$ an arbitrary quadratic function with the origin as the vertex of the parabola: $g(r) = br^2$ and $\{a, b \in \mathbb{R} | a, b > 0\}$, then the coordinates where the two functions intersect each other can be calculated as:

$$ar = br^2 \quad (6.8)$$

Moving the right hand side of the equation to the left hand side:

$$ar - br^2 = 0 \quad (6.9)$$

Factoring of this polynomial allows to find the zeros as follows:

$$r(a - br) = 0 \text{ for } r = 0 \cup r = \frac{a}{b} \quad (6.10)$$

When the gradients of these two functions are considered at the second (non-trivial) intersection point:

$$f'(r) = a|_{r=\frac{a}{b}} = a; \quad g'(r) = 2br|_{r=\frac{a}{b}} = 2a \quad (6.11)$$

Therefore, at the surface of a cylinder, the temperature gradient for a parabolic temperature distribution is always two times larger than for the linear temperature distribution, as schematically illustrated in Figure 6.17.

The calculation of the average temperature in a circular domain, where the temperature distribution is a (3D) paraboloid, is well known. Considering the parabolic distribution shown in Figure 6.18, which is actually the inverse of the inverse of the distribution as calculated from the heat equation, the integral $\int_A T dA = \frac{\pi}{2} TR^2$ [278, 279], which is half of the volume of the cylinder that envelopes the paraboloid. This means that the average temperature T_a is halfway between the maximum temperature occurring in the centre of the cylinder. Now an expression of the heat flux due to conduction can be established.

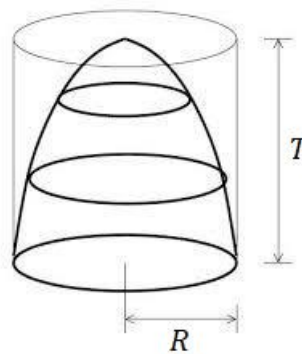
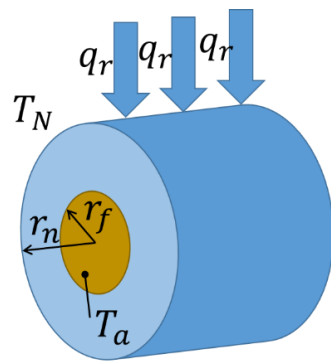


Figure 6.18: Volume of a paraboloid, adapted from [280].

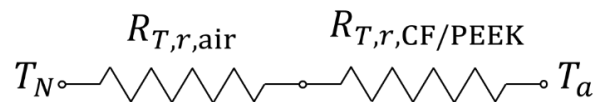
Recall Figure 6.16 shows an assumed linear temperature gradient between the minimum temperature in the cylinder and the surface temperature. The 'real', virtual linear temperature gradient between the minimum temperature and the surface temperature $\frac{(T_N - T_0)}{r_f}$ is twice as a steep as the temperature

gradient between the average temperature and the centreline temperature

$$\frac{(T_a(z) - T_0)}{r_f}$$



(a)



(b)

Figure 6.19: Assumed mode of heat transfer from oversized nozzle to CF/PEEK filament: (a) geometry, (b) equivalent thermal circuit.

Based on the finding that air can still conduct a significant amount of heat in Appendix D, it is also relatively straightforward to establish the heat transfer coefficient in case there is an air gap between the nozzle and the filament. The finding reported by Dr. McIlroy is based on the assumption that *free convective heat transfer* in the air is only a minor contribution in the total heat transfer between two concentric cylinders. An illustration of heat flow between two concentric cylinders is shown in Figure 6.20. The flow pattern will most likely be a rather complex shape, given potential instabilities in the flow, fluid escaping and entering the cylinder at either end of the cylinders. In Figure 6.20, when considering the order of magnitude for the free convection, the Eqs (9.59), (9.60) and (9.23) describe free convection in *horizontal concentric cylinders* in conjunction with the properties for air in Appendix A4 in Ref [240]. Further to assume air behaving as an ideal gas, thus $\beta = 1/T$, where $T = 673 \text{ K}$ is used. Note that as these equations describe empirical correlations for long, horizontal coaxial cylinders will predict incorrect values for the vertical case, as the flow pattern will be different from the horizontal case. However, filling in these equations results in a negligible convective heat transfer coefficient for the air gap. This is inline with Dr. McIlroy's finding in Appendix

D that the amount of heat transferred through conduction transfer is significantly larger than the amount of heat transferred through free convection.

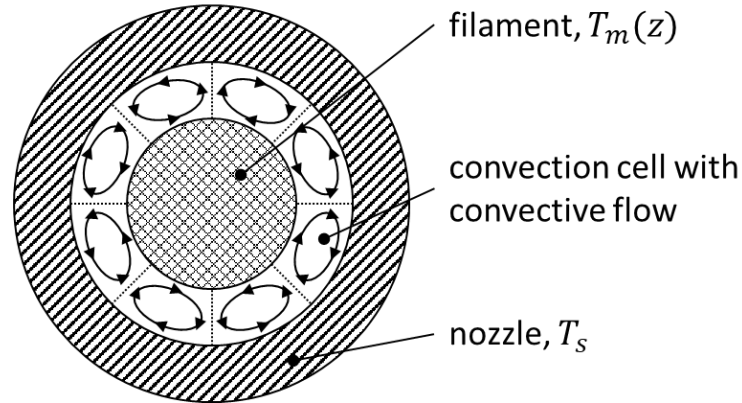


Figure 6.20: Free convection flow pattern in the air gap between the nozzle and the filament, note that as the gravity is perpendicular to the plane, the flow would rise upwards when it comes close to the hotter nozzle and go downwards as it approaches the colder filament.

Following the approach from the previous subsection – ignoring the thermal resistance arising from the nozzle – air layer is given by: $\frac{\ln(r_n/r_f)}{2\pi k_{\text{air}} dz}$ [240]. The total heat flux q_r is given by:

$$q_r = \frac{T_s - T_m(z)}{\frac{\ln(r_n/r_f)}{2\pi k_{\text{air}} dz} + \frac{1}{2\pi r_f dz \frac{4k_{\text{CF/PEEK}}}{r_f}}} \quad (6.12)$$

Equating Eqs. (6.5) and (6.6) allows then to find the expression for the average heat transfer coefficient \bar{h} :

$$\bar{h} = \frac{4k_{\text{air}}k_{\text{CF/PEEK}}}{r_n(4\ln(r_n/r_f)k_{\text{CF/PEEK}} + k_{\text{air}})} \quad (6.13)$$

The material properties utilised in the simulation can be found in Table 6.2 and 6.3.

Table 6.2: Variation in material properties neat PEEK filament.

| Parameter | Lower bound | Reasonable Case | Higher Bound |
|--|-----------------------|-----------------------|-----------------------|
| Heat transfer coefficient nozzle entry \bar{h} , based on free air convection value $h = 10 - 40 \text{ W/m}^2\text{K}$ | 10 W/m ² K | 10 W/m ² K | 40 W/m ² K |
| $k_{\text{PEEK}} = 0.25 - 0.93 \text{ W/mK}$ | 0.25W/mK | 0.59 W/mK | 0.93 W/mK |
| $c_{p,\text{PEEK}} = 1545 \text{ kJ/kg} \cdot \text{K}$ | | | |
| $\rho_{\text{PEEK}} = 1300 \text{ kg/m}^3$ | | | |
| $T_s = 400 \text{ }^\circ\text{C}$ | | | |

Table 6.3: Variation in material properties CF/PEEK filament.

| Parameter | Lower bound | Higher Bound |
|--|-----------------------|-----------------------|
| Heat transfer coefficient nozzle entry \bar{h} , based on free air convection value $h = 10 - 40 \text{ W/m}^2\text{K}$ | 10 W/m ² K | 40 W/m ² K |
| $T_s = 400 \text{ }^\circ\text{C}$ | | |
| Calculated using the Nielsen formula in Chapter 6, Section 6.4.3.1 $k_{\text{CF/PEEK}} = 2.364 \text{ W/mK}$ | | |
| $c_{p,\text{CF/PEEK}} = 1545 \text{ kJ/kg} \cdot \text{K}$ | | |
| $\rho_{\text{CF/PEEK}} = 1780 \text{ kg/m}^3$ | | |

The geometric dimensions are described in the beginning of Section 6.4.3.2. Energy input in terms of enthalpy required for the solid-liquid phase transition

of PEEK is not taken into account in this model. Furthermore, the values entered into the Nielsen formula as found in the fourth row in Table 6.3 are calculated with the average values of the thermal conductivities of carbon fibre and PEEK. For the case of CF/PEEK printing, filament contact with the oversized orifice due to the relative motion between the nozzle and the filament being pulled and the printing bed has not been taken into account. Additionally, the effect of the eccentricity due to the CF/PEEK filament being pulled when printing is assumed to be averaged out.

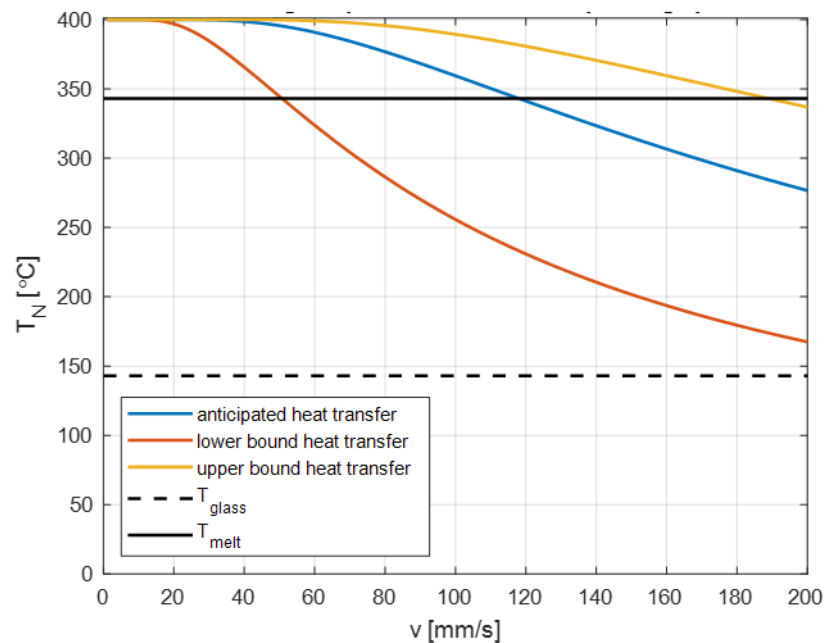


Figure 6.21: Print speed dependence of filament temperature when PEEK exits.

Figure 6.21 shows the filament exiting temperature for the different simulation setting in terms of print speed and heat transfer coefficient. The glass temperature T_g is marked with a dashed, horizontal line and the melt temperature T_m is marked with a black, horizontal line. Once the filament's desired nozzle exiting temperature has been specified, the intersection point of the temperature curve the maximum feasible printing speed is found from the intersection point of the temperature curve with the horizontal line defining the desired temperature. In Figure 6.21, the lower bound or most

conservative case crosses the melting temperature T_m at 50 mm/s printing speed.

This however does not mean that this is an achievable printing speed, as this filament temperature is only achieved at the very end of the nozzle ($z = 12.5$ mm). To find out what the achievable range of print speeds is, one must consider the filament temperature in the tapered section of the nozzle to predict where the melt front is. This is where the filament reduces its diameter from 1.75 mm to 0.4 mm as the nozzle diameter. It is therefore logical to assume that this can only be achieved if the filament is completely molten. Furthermore it is crucial that this melting occurs in the tapered section and not before, otherwise the extrusion forces will generate insufficient pressure and the extruded mass rate will be too low for the relative speed between the nozzle and the printbed. The best location for the melt front will therefore be in the entry of the tapered section. Figure 6.22 shows the print speed dependent location where the filament exceeds the melting temperature. The tapered section is highlighted by the space between the two horizontal, dashed lines. It can readily be seen that in order to reach the T_m early in the tapered section, and have the melt front location there, the printing speed needs to be around 10 mm/s for all cases.

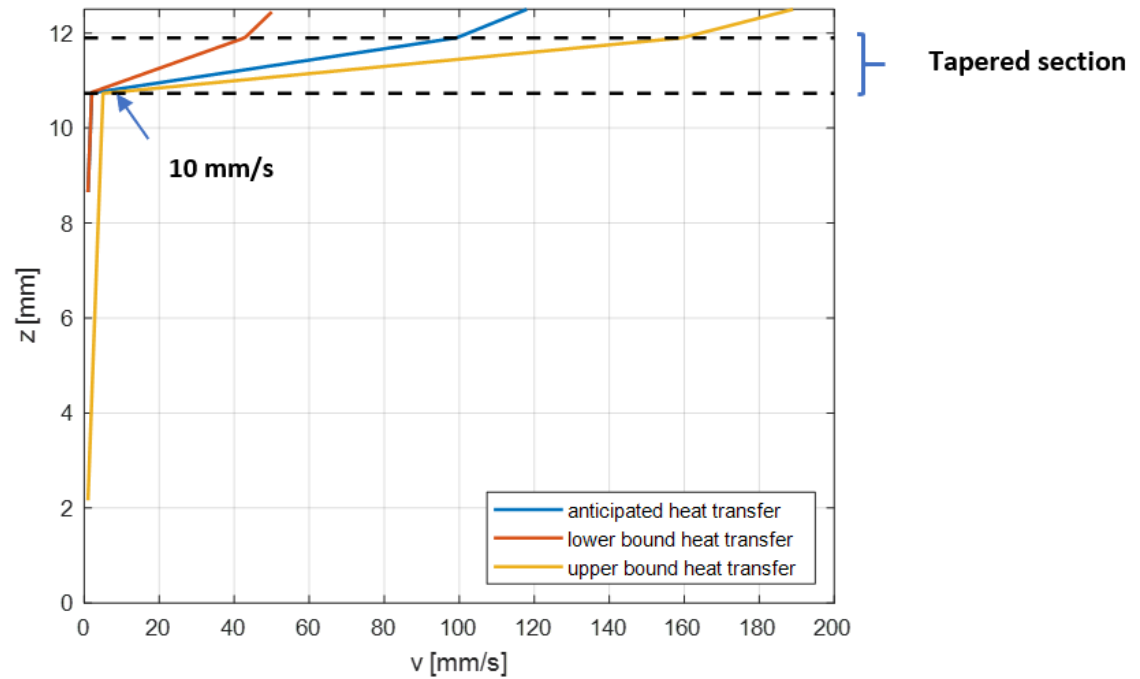


Figure 6.22: Print speed dependence of location where PEEK filament temperature starts to exceed the melting temperature; tapered section in nozzle is marked by the space between the two dashed horizontal lines.

Figure 6.23 shows the thermal power, or heat, absorbed by the filament for certain printing speeds. It can readily be seen that the required thermal power which is required to heat up the filament is quite low. Since the practical printing speed depends on getting the filament temperature to exceed T_m in the tapered section of the nozzle, which is around 10 mm/s, the required power consumed by the filament remains below 2 W. This is an order of magnitude lower than the power output of the heat cartridges in the HotEnd.

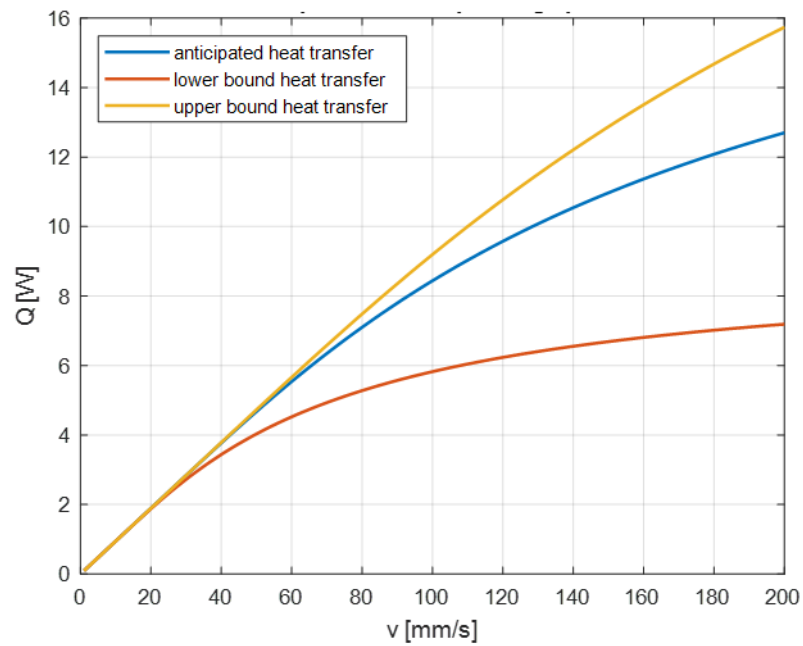


Figure 6.23: Rate of thermal energy absorbed by the PEEK filament for different print speeds.

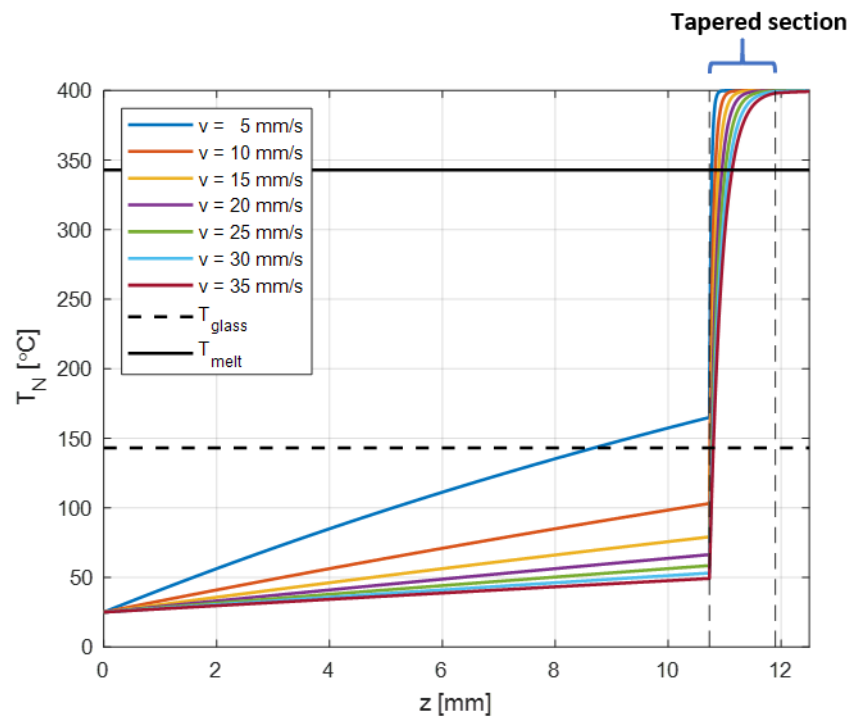


Figure 6.24: Temperature variation of the PEEK filament in the nozzle (with diameter 0.4mm) for the reasonably anticipated case.

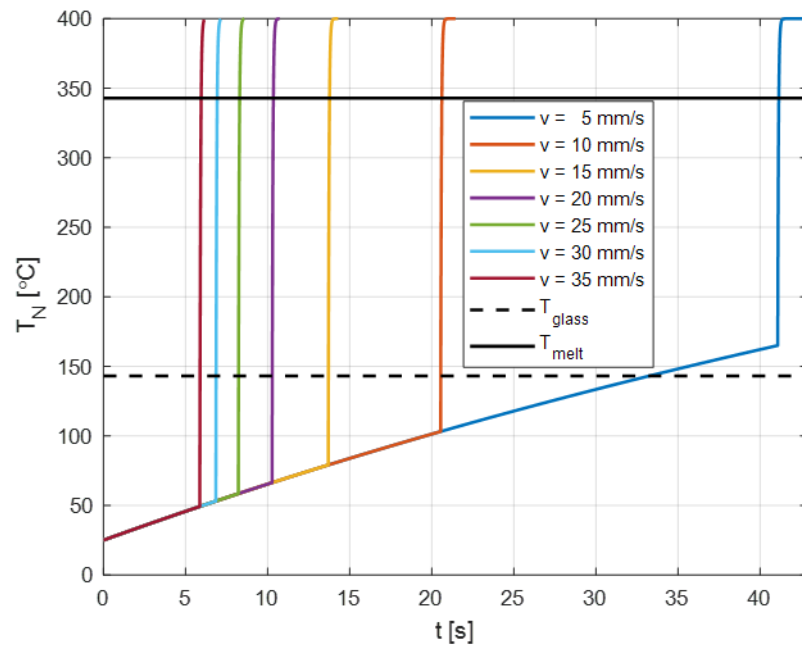


Figure 6.25: Transient PEEK filament heating curve for a cross section going through the nozzle.

The temperature variations over the axial length of the nozzle can be found in Figure 6.24. The schematic diagram of the nozzle can be found in Figure 6.15. As followed from the description of the results found in Figure 6.21, the first conclusion from Figure 6.24 is that when the print speed decreases, the temperature gradient increases. Additionally, it can be seen that most of the heat transfer occurs in the orifice which is the edge of the nozzle exit after tapered section. The length of orifice is 1.6 mm [99]. This is because there is a larger increase in temperature in the tapered section, where the filament is direct contact with the nozzle wall. Figure 6.25 shows nearly the same information as Figure 6.24, but as a temperature variation in time. Furthermore it can be clearly seen that the heat transfer rate is temperature dependent as different print speeds follow the same curve for the same residence time.

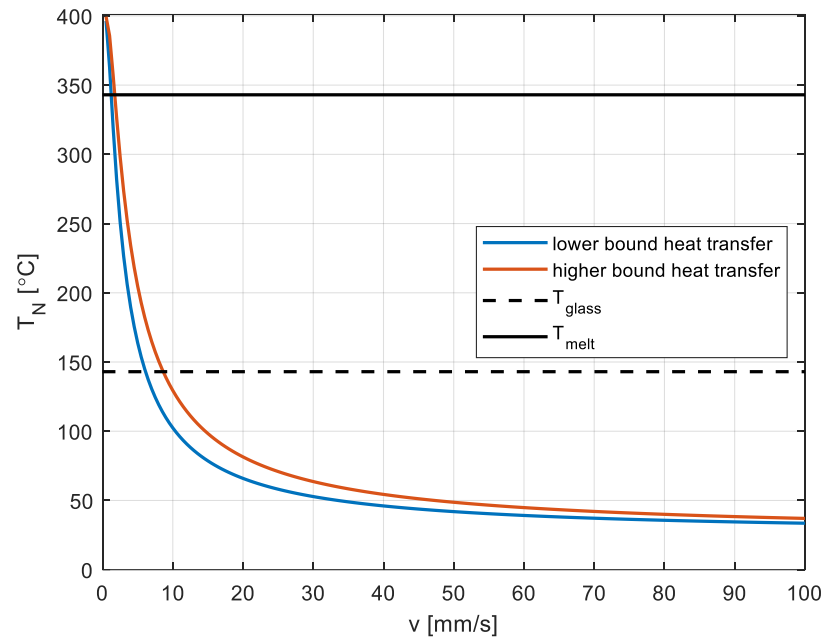


Figure 6.26: Maximum achievable CF/PEEK filament temperature plotted as a function of the printing temperature.

Figure 6.26 shows the final filament temperatures for the CF/PEEK filament with a low and a high convective heat transfer rate in the exit section of the nozzle. The CF/PEEK filament temperature drops faster when the print speed increases. As variation of the conductivity of the CF/PEEK filament is not taken into account, these values are slightly closer to each other than they would have been if the variation of the conductivity had been considered in the simulation. Compared with Figure 6.21 of PEEK results, the trend is quite clear. Since during the CF/PEEK printing process, there is no direct contact between nozzle and CF/PEEK filament the application of the oversized nozzle (0.8 mm diameter) to create an air gap to accommodate the lower mechanical flexibility (compliance) of the CF/PEEK significantly reduces the achievable printing speed.

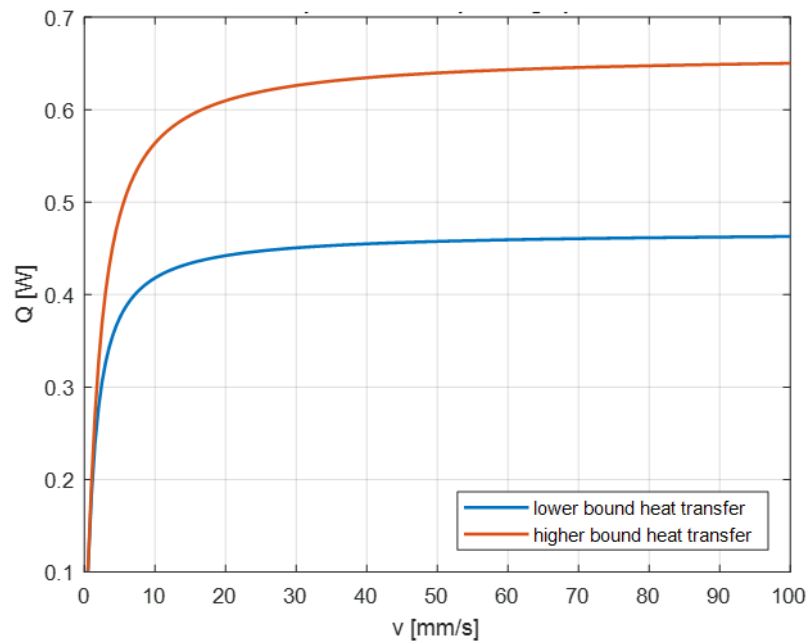


Figure 6.27: Rate of thermal energy transferred into the CF/PEEK filament for different printing speeds.

Figure 6.27 shows the required thermal power to print 0.5 mm diameter CF/PEEK (see the print speed requirement in Figure 6.26) is below 0.3 W. This means, during the printing, the CF/PEEK filament does not take too much energy, so the nozzle temperature can be considered as constantly stable.

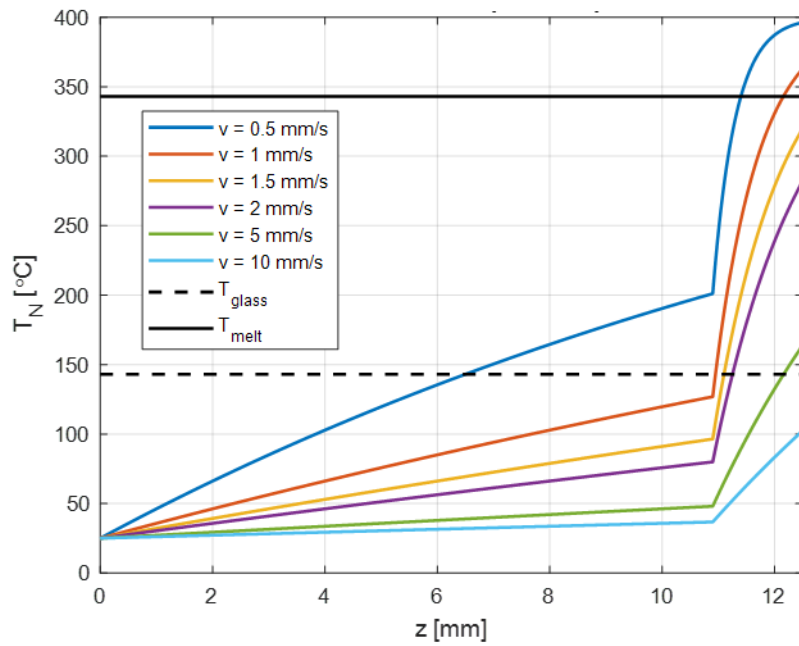


Figure 6.28: Temperature variation of CF/PEEK filament in the nozzle for a low heat transfer rate in the nozzle.

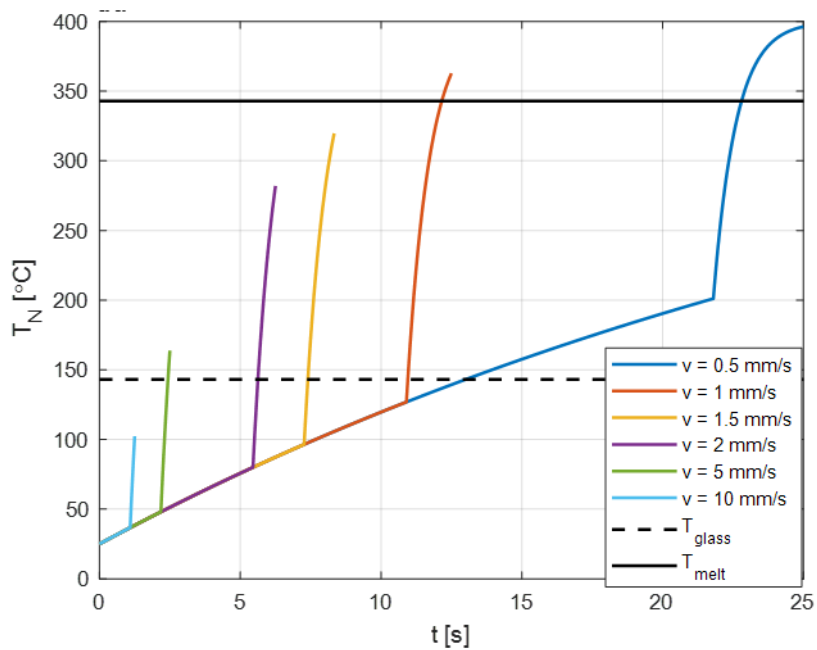


Figure 6.29: Transient heating curve of CF/PEEK filament for a low heat transfer rate in the nozzle.

Figure 6.28 shows the temperature variation in the nozzle with a low heat transfer rate. Figure 6.29 shows temperature variation with the time changes.

As the required residence times take longer than for the PEEK printing because of the air gap created by the oversized nozzle, this causes the temperature variation in the exit section to show a more distinct exponential nature.

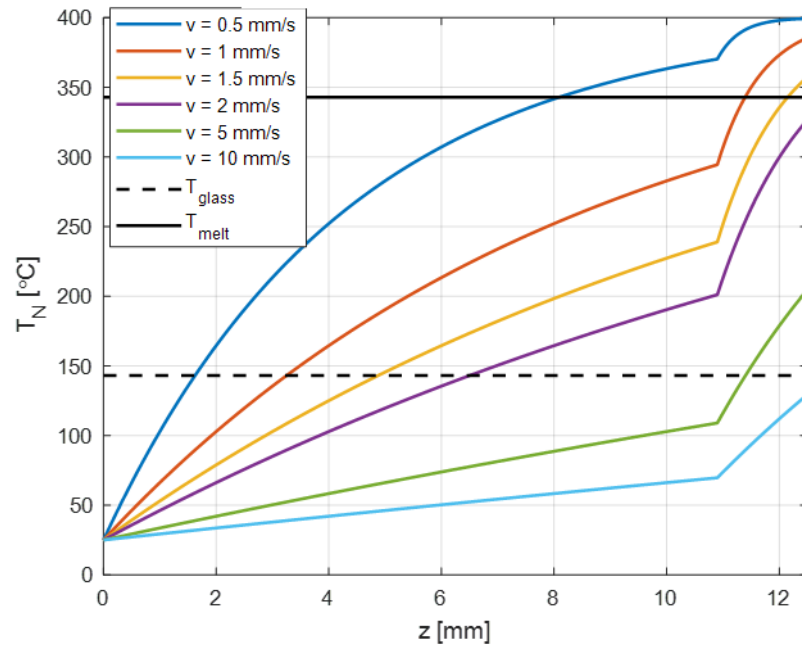


Figure 6.30: Temperature variation of CF/PEEK filament in the nozzle for a high heat transfer rate in the nozzle.

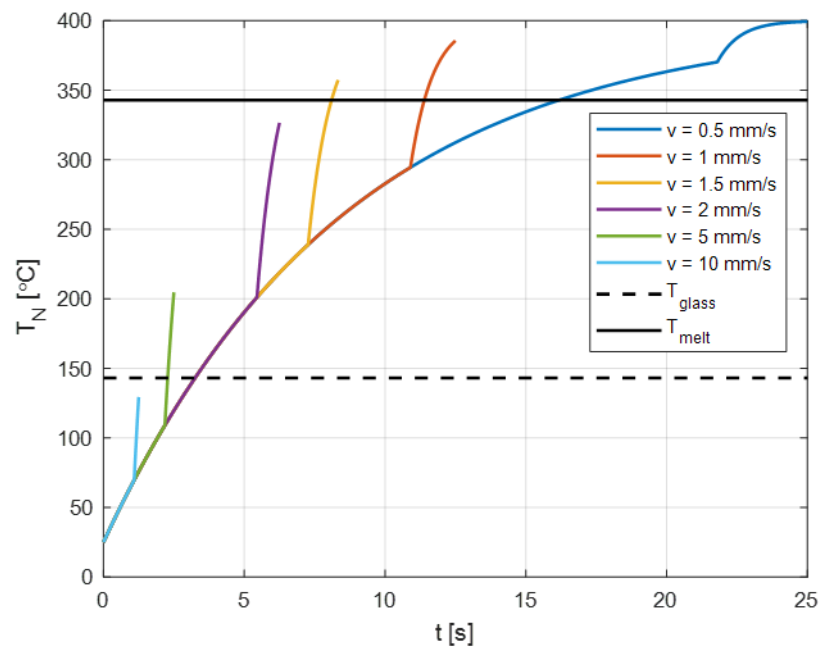


Figure 6.31: Transient heating curve of CF/PEEK filament for a high heat transfer rate in the nozzle.

The same holds for Figures 6.30 and 6.31, where the same variables are plotted, but then for the case with a high convective heat transfer in the exit section.

6.3.2.2 Discussion and Observations

In this section, a simple lumped parameter model for the heat transfer has been established. As it uses an exponential curve to establish the temperature variations in the nozzle, a prediction for the exiting temperature can be made without calculating the temperature in the whole nozzle. This makes the model an easy tool to predict the filament exiting temperature.

In addition, when the filament undergoes a diameter reduction, the temperature in the tapered section of the nozzle also needs to be considered. It is paramount that the filament temperature reaches the melting temperature very early in the tapered section. In this particular case, the 10 mm/s print speed determined from the thermal analysis coincides with the print speed which is advised by the 3D printer manufacture. To achieve lower or higher print speeds, the set temperature T_N needs to be decreased or increased respectively.

The transverse conductivity of the CF/PEEK filament proves to be very important for how quickly the filament can heat up. In order to make the printing of CF/PEEK commercially viable, the higher the output the better. Hence, print speeds as high as possible are desirable. The effect the filament diameter has on the heat penetration rate, and therefore the amount of heat that is actually transferred from the nozzle into the moving filament is not taken into account in this analysis. For a proper analytical calculation of the heat transfer rate for the nozzle-filament system, and the calculation of the rate of change in temperature in the filament requires the Fourier and Biot numbers to be established. The Fourier number signifies a dimensionless time constant related to an object's thermal diffusivity and its dimensions, and the Biot number represents the ratio of the thermal resistances of an object's internal conductive heat flow and convective heat transfer between the object and its surroundings. Both these dimensionless numbers reduce the number of independent variables that exist when solving the transient heat equation analytically [240]. These analyses lead to an optimisation of the process which also requires the combination of materials to be chosen appropriately and the geometrical interfaces in the nozzle to be properly designed.

From Figures 6.21 and 6.26 it can be deduced that for low printing speeds the filament temperature exiting temperature is as high as the set nozzle temperature T_N , and the gradient $\left. \frac{dT_a}{dv} \right|_{z=L} = 0$, however, for a certain printing speed, the maximum filament temperature reduces from T_N , and the gradient $\left. \frac{dT_a}{dv} \right|_{z=L} < 0$. This printing speed is still lower than the maximally achievable print speed, for which the exiting temperature becomes the minimum desirable exiting temperature. Consequently, increasing the nozzle temperature T_N and printing in the speed range where the exiting temperature is lower than T_N will allow for higher print speeds with minimal thermal degradation of the PEEK material.

Another insight from the thermal analysis is that, introducing the air gap to accommodate for the inflexibility of the CF/PEEK filament significantly reduces

the heat transfer. This significant drawback can be overcome by the following design improvements:

- Increase the axial length of the orifice section (bespoke nozzle design).
- Pre-heat the filament in the printhead by means of electromagnetic radiation (laser, IR, microwave), ultrasound or increasing the convection by actively blowing hot air in the printhead.
- Introduce additional degrees of freedom in the printhead motion: *ROTX* and *ROTY*, or roll and pitch. This would also allow for full contact between the filament and the nozzle in the orifice section. The adaptation for the filament deposition angle will achieve positional accurate deposition of the filament for the required geometrically accuracy and structural integrity in the same layer and between layers.

Note that making a bespoke design with a longer orifice section would improve the heat transfer of the nozzle in general and would allow for higher print speeds, but will also affect the friction on the filament, the required extrusion force and likelihood of filament buckling. Clearly a balance needs to be made between these competing requirements.

6.5 Modelling of PEEK Crystal Growth

The modelling of PEEK crystal growth was developed by Dr. Claire McIlroy based on the experimental results of the author of this thesis. The modelling of PEEK crystal growth gives insight into the existence of disparities between weld and bulk mechanical properties in FFF of PEEK, by investigating the differences between the weld and bulk properties in the samples of PEEK constructed using the FFF technique under a range of printing conditions using DMA. The accuracy of the results predicted by the model depends on both the IR measurement data, and the selection of the fitting parameters of the filament thermal diffusivity time scale [281]. Since PEEK is a semi-crystalline polymer, a non-isothermal quiescent crystallisation model was employed, updated using the IR-imaging measurements, to understand the findings. The

working hypothesis was proposed that the increase in E_{par} with print temperature in Figure 6.8 is due to an increase in the degree of crystallinity. Furthermore, since $E_{par} > E_{perp}$, it was proposed that the core of the filaments achieve a greater degree of crystallinity than that of the weld regions during cooling. The non-isothermal quiescent crystallisation model was used to predict the growth of the crystalline matter in PEEK. This is a process that is dependent on the thermal history. When the printing temperature is higher, the printed layers stay above the T_g for a longer time, which allows for more crystal formation. Note that PEEK can undergo a heat treatment process to optimise or maximise crystallinity, this is called annealing. Dr. Claire McIlroy has modelled the temperature decay for steady state printing as a function of time. The IR-imaging thermography results discussed in Section 6.3.1 have been used by Dr. McIlroy to update her thermal model of the printed PEEK. The thermal model is in turn used to establish the thermal history of the printed PEEK, which then can be used in the non-isothermal quiescent crystallization model to predict the amount of crystalline material that has been formed after the PEEK material has been deposited.

The Halpin & Kardos model [160] predicts the modulus of elasticity for the PEEK based on the crystalline and amorphous fractions, and is presented in Appendix F. With known moduli of elasticity for the weld region and for the filament region, the crystal fraction can be determined based on the Halpin equation. This makes it possible to compare the experimentally obtained amount of crystallinity with the amount of crystallinity predicted by the non-isothermal quiescent crystallization model. The predicted crystal fraction is then corrected by the calculated data of bulk storage modulus, which agrees quantitatively with the DMA measurements. The theory of the model and the finding results can be found in Appendix B.

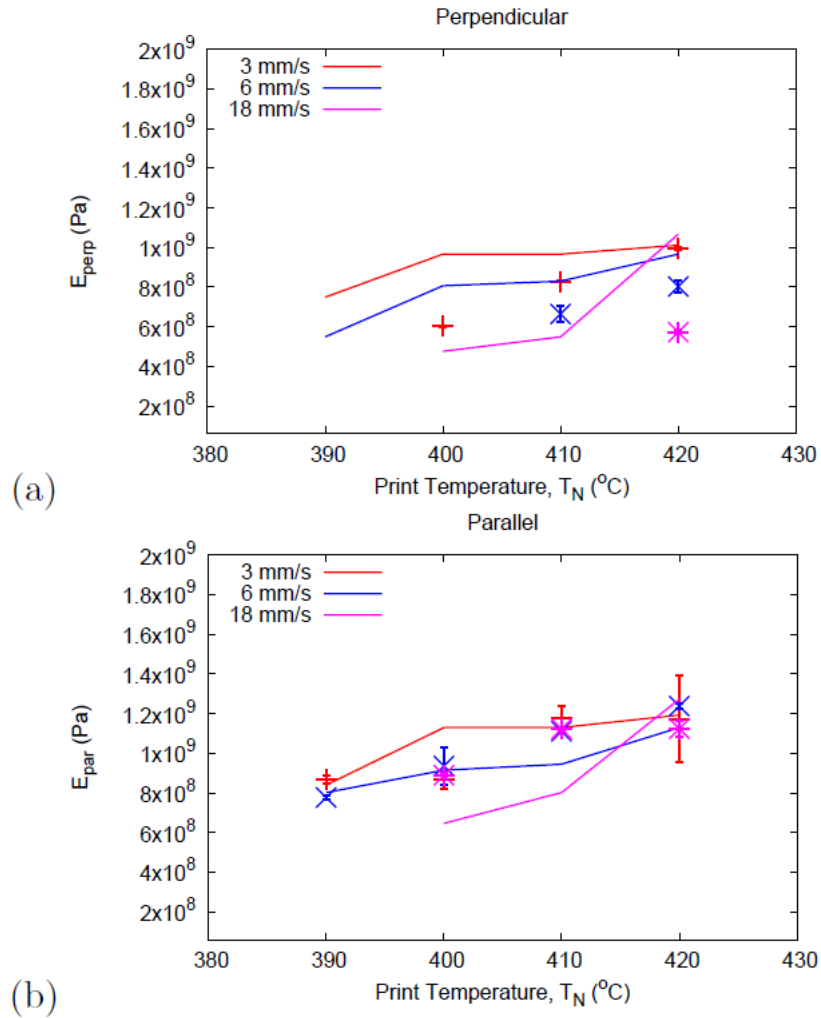


Figure 6.32: (a) E_{prep} and (b) E_{par} predicted by the model (lines) compared to the DMA measurements (points) for the prescribed printing conditions.

Figure 6.32 shows the model predictions using a suitable model fitting parameter for all printing conditions. Recall that not all the printing conditions were successful due to the poor bonding between each layers. Six samples were taken from each printing condition to be DMA tested. The model results are in reasonable agreement with the DMA measurements since the predicted and experimental trends consistently match each other. Specifically, differences between model and experiment are observed which are up to maximum of 20% for the parallel tensile modulus and up to maximum 60% for the perpendicular tensile modulus at certain combinations of processing temperatures and speeds. However, further investigation can be carried out into the choice of model fitting parameter for the filament thermal diffusivity

time scale to improve the accuracy of the modelled predictions. From only a single parallel and perpendicular DMA measurement, it is possible to predict for the perpendicular and parallel storage moduli E_{perp} and E_{par} across a range of printing conditions, thus enabling to optimize the printing conditions for a required mechanical performance.

6.6 Summary

This chapter describes the dynamic thermal analysis of both neat PEEK printing, and CF/PEEK filament printing.

In the study of neat PEEK printing, DMA was used to investigate the mechanical properties of a wall of PEEK printed using FFF with a single filament. The findings are that the storage modulus increases with print temperature, and that there is a difference between the properties measured perpendicular and parallel to the printing direction. Based on the crystalline nature of PEEK, the hypothesis proposed is that these disparities arise due to the differences in the degree of crystallinity achieved under typical FFF conditions. From the experimental investigation, the PEEK processing window is found to be relatively small compared with polymers such as ABS, PLA and nylon. This means that, under the same FFF printing conditions, there is little time above the glass transition temperature for crystals to grow.

In summary, the model presents a framework for understanding the effect of thermal history, and hence crystal formation in FFF printed PEEK. This method relates printing parameters, specially the print temperature and print speed, to mechanical properties of semi-crystalline polymers. Therefore it provides a foundation for optimising crystallisation for the mechanical performance of the FFF printed PEEK.

Unfortunately, the planned research into CF/PEEK printing could not be completed due to limited laboratory access. However, initial trials indicated that the CF/PEEK feedstock material developed in this work could be successfully printed using the adapted printer. The logical next step would be

to characterise the effect of FFF process parameters in the quality of printed parts. The previous crystal modelling of PEEK printing could also be usefully applied to give an initial understanding of the printing of the CF/PEEK and modifications made to the model to account for the effect of the presence of the carbon fibres in the feedstock. These would be very fruitful areas for future research.

CHAPTER 7

Discussion

7.1 Introduction

The motivation for this project is to combine the manufacturing advantages of 3D printing with the high mechanical performance of continuous fibre polymer composites, requiring the development of a novel 3D printing feedstock material with a high fibre volume fraction and high strength polymer matrix. For this reason, carbon fibre reinforced PEEK was selected as the processing material. In this chapter, the identified knowledge gaps, and the applied methodology and workflow of this project are recapitulated. Subsequently, how these knowledge gaps were addressed by this research and the significance of the work done in the context of both existing literature and industrial application is discussed. The limitations to the current work are determined, and this will lead to the formulation of future work. Finally, the most important contributions are summarised.

7.2 Contributions

7.2.1. Identified Knowledge Gaps

This work aimed to develop a method to FFF print CF/PEEK composite material with a high fibre volume fraction. It was found that the challenges that needed to be overcome to develop an AM process in general and the FFF process in particular were:

- Lack of understanding of the behaviour of unreinforced and fibre reinforced polymers (PEEK) in the FFF process.
- Lack of real-time control solutions for the processing parameters.

Chapter 7 Discussion

- Lack of appropriate in-situ measurement during the process.
- Lack of standardisation of the process, which makes it hard to certify for industrial applications.

A review of the current state-of-the art of the FFF processing of PEEK and its carbon fibre reinforced composites revealed the following main knowledge gaps:

- Characterisation and explanation of difficulties of FFF printing carbon fibre reinforced PEEK with high fibre volume fraction. This is related with lack of understanding on how to effectively mix PEEK and high volume fraction carbon fibre before the process.
- Lack of understanding regarding PEEK thermal and mechanical behaviour during printing. This involves how PEEK thermal behaviour influences on the mechanical properties of both PEEK and CF/PEEK FFF printed parts.
- A method to make good quality CF/PEEK filaments for the FFF process. This means there is still limitations to reduce the void contents of CF/PEEK filaments based on the current technology.

7.2.2 Workflow and Methodology

The project comprised firstly the development of a CF/PEEK composites feedstock process, followed by the development of the FFF process. As stated in the overall methodology (Chapter 1, Section 1.3 Figure 1.2), each step included development and design, and subsequent experimental verification and process optimisation. For the development of the composites feedstock process, material characterisation was carried out prior to the design and development of process and apparatus. Filament analyses and optimisation of the feedstock pre-process were carried out posteriori. Finally, the filament was proven to be printable as shown in Chapter 6, Section 6.4.2, Figure. 6.11. The development of the FFF process required analyses of the thermal history of the printed layer, the crystal fractions and establishment of an optimised process window.

The results of this project include the characterisation of the feedstock materials, pultrusion apparatus design, filament analyses, pultrusion process optimisation, printing analysis and printing process optimisation. The remainder of this section is organised along the two main steps in this work, the feedstock pre-processing and the printing process.

7.2.3 Contributions in the Work

The knowledge gap on the ‘characterisation and explanation’ of difficulties of FFF printing carbon fibre reinforced PEEK with high fibre volume fraction has broadly been covered by successfully printing CF/PEEK with a high CF volume fraction. The printing of CF/PEEK as outlined and discussed in this thesis meets the criteria of FFF printability as outlined in Section 1.3 Chapter 1. Successfully printing CF/PEEK with a high CF volume fraction depends on the processing window of both the pultrusion and FFF processes. The CF/PEEK filaments must have low porosity, good consolidation and sufficient stiffness in order not to buckle during processing and to achieve good inter-layer bonding and desirable material properties. Printing with this volume fraction has not been reported previously in the literature. The pultrusion process as an intermediate step to produce filament was selected rather than dual extrusion of the commingled strand. This selected process has overcome the low limit for allowable CF volume fraction of printing observed by Stepashkin *et al* [1], who reported a continuous CF volume fraction of 5% in the printing. Additionally, a lumped parameter model of the heat transfer in the oversized nozzle helped to determine the required print temperature for a selected print speed. The novelty of this model is that it relies on the conduction to estimate the heat flux, rather than assuming hundred percent efficiency in the heat transfer as done by other authors in the engineering field, c.f. [Eq. (10), 282]. The selection of an oversized nozzle is not standard in the FFF printing. An approach similar as Markforged’s CF/nylon printing process was adopted for this fabricated CF/PEEK filament printing. This modelling approach can also be used to predict the melt front in the extrusion section of the nozzle. It also predicted that it was possible to heat up the CF/PEEK filament to the melting

temperature within our current PEEK machine setup. This was proven by the successful printing of the developed CF/PEEK filament. This analysis can predict the real temperature of the CF/PEEK filament, hence it can assist the nozzle temperature control more effectively during the printing. It will contribute to the future work of CF/PEEK printing if this project will continue. This model did give a good prediction for the exiting temperature, which was measured experimentally and the predictions for the achieved print speed were inline with the recommended speed. As this model is a lumped parameter model, it provides an easy and fast tool for practitioners compared to some of the more computationally demanding models reported by Turner *et al* [282].

To address the knowledge gap on lack of understanding regarding PEEK thermal and mechanical behaviour during printing, firstly, the TGA and DSC analyses of the feedstock material showed that the CF/PEEK filament consolidation quality depends on the pultrusion temperature and speed. This implies that the cooling rate of the CF/PEEK is critical to the pultrusion process, and will also have an impact on the printing quality. The obtained results of the TGA and DSC analyses are in line with previous findings reported in the literature, such as Refs [166-179]. These results helped to find the boundary of the CF/PEEK filament manufacturing processing window. Secondly, a crystallisation analysis of PEEK has been carried out. This involved obtaining the thermal history of the deposited material by means of IR thermography, followed by a DMA analysis. The thermal history was fed into a non-isothermal quiescent crystallisation model adapted for FFF PEEK processing by Dr. McIlroy. Using IR-measurement with corresponding correction is a novel method to obtain the thermal history of printing filament. The method was adapted from Seppala *et al* [210]. The predicted crystallisation was linked to the modulus of elasticity. The DMA tests analysed the stiffness of printed samples parallel and perpendicular to the printing direction. This made it possible to find the crystal fractions in the filament's core and in the weld regions. The practical outcome of this study is that PEEK based FFF material has a very narrow processing

window due to its sensitivity to the cooling rate. A high cooling rate means less time for the crystals to form, leading to a lower crystal fraction. This implies by increasing the chamber temperature heating capacities or reducing the print speed capacities can lead to stronger printed PEEK and CF/PEEK FFF printed parts. This approach have not been taken in the literature before. This model can be used in FFF process optimisation on PEEK related printing. With an appropriate fitting parameter, this model can also be used to optimise FFF process with other semi-crystalline materials.

To address the knowledge gap on developing a method to make good quality CF/PEEK filaments for the FFF process, firstly, the quality of the produced filament was judged on the porosity. It was found that the pultrusion speed for the range examined had an influence on the quality, that is a lower speed did have better results, but the temperature proved to have a monotonic influence only between 370°C to 400 °C. Furthermore, the findings of the porosity studies showed that the relatively inexpensive density measurement carried out with standard engineering equipment resulted in almost the same results as the image processing based study of material analyses with optical and ToF-SIMS microscopes. The main drawback of using microscopes is that one analyses a particular cross-section, rather than a whole sample. This means that multiple cross-sections need to be analysed in order to get a reliable result. ToF-SIMS microscopy has one advantage over optical microscopy in that it can unambiguously distinguish between the materials in the sample as it proves hard to distinguish the resin from the PEEK in a sample studied with an optical microscope. The density measurement method used in the thesis is much cheaper, and takes much less time than the conventional image processing method which used to analyse the cross sectional view of the filament. The proposed density measurement method could be used to save research time and expense of would avoid the need for (smaller) manufacturers to invest in expensive equipment for quality control.

Other contributions in the work include firstly, the founding of a thermal analysis that could verify whether the standard heatbreak and heatsink of the

E3D V6 HotEnd could be used in the design. As the heatbreak/heatsink system consists of a series of relatively simple geometries, each of which has a well-known analytical solution the heat transfer, the whole system can be analysed by means of a 1D lumped parameter model. The thermal network in the form of a ladder network model can easily be set up and analysed. This analysis was benchmarked against the FE analysis by Jerez-Mesa *et al* [100] and experimentally verified by an IR measurement. The temperature distribution found in both cases using a forced heat transfer coefficient $h = 20 \text{ W/m}^2\text{K}$ proved to be good match for the fan running on full speed. This means that a relatively simple analysis can be used to study the thermal behaviour of a heatbreak/heatsink system, limiting the need for more time consuming FE analyses in the early stages of design. This ladder network model provides a quick method of evaluating the HotEnd in the pultrusion design, which can easily be converted into a design tool for (small) manufacturers in a MS Excel spreadsheet, GNU Octave or Scilab. Secondly, in the printing process development, it was concluded from the DSC results that the cooling rate is the critical factor affecting the final crystallisation fraction of PEEK. This phenomenon was the motivation for the crystallisation modelling in this project. The final crystallisation fraction of the PEEK leads to different mechanical properties in fabricated parts. This analysis feeds into the further weld formation studies conducted in Chapter 6 where the crystallisation model was built to optimise the printing parameters and the mechanical properties of the printed parts. Based on the thermal history that could be created in the printer, the numerical model that describes the crystallisation of the PEEK material predicts that the mechanical properties at the weld are largely determined by those of PEEK in its amorphous state due to rapid cooling at that location. Conversely, the storage modulus at the filament core is much larger than at the weld due to the slower cooling and greater crystallinity. A typical example is when printing condition is $420 \text{ }^\circ\text{C}$ at 3 mm/s , the storage modulus at the filament core E_f is two orders of magnitude larger than the storage modulus at the weld E_w . This model relates print temperature, ambient temperature in the chamber, and print speed to mechanical

properties of the semi-crystalline polymer processed using FFF. It also shows that PEEK crystallisation process is more sensitive to cooling rate than other semi-crystalline polymers such as PLA and nylon by applying the same cooling conditions. This means that PEEK has a narrow processing window. This work provides a novel method for predicting mechanical properties of FFF-printed PEEK, as well as a new framework to optimise FFF crystallisation for printed parts performance. All the results in the printing process development could help to further design the process to optimise the mechanical properties of the FFF printed PEEK.

7.3 Limitations of Current Work

In the feedstock process development, a pultrusion apparatus was designed to have two adjustable process parameters: the pultrusion temperature and pultrusion speed. Due to the high void content of produced CF/PEEK filament, ideally a further compaction process would be required, however, this will be part of the future work discussed in Chapter 8, Section 8.3.

The 1D lumped parameter model of the heat transfer in the nozzle during the PEEK and CF/PEEK printing does not provide an accurate prediction of the temperature at the material nozzle interface and it does not take melting into account. Incorporating the melt enthalpy into the model or conducting a more accurate 3D FEA study would be required to model the melting process.

In the filament analyses, for each processing speed, the temperature dependency of the voids content revealed there were two local minima found to be 370 °C and 400 °C. 370 °C was linked to the DSC testing results when there was a high cooling rate (around 100 °C), there was additional heat flow fluctuation around 370 °C. However, the reason for the 370 °C corresponding to a local minimum has not been investigated due to the limited time available for this project. Although unlike reports in the literature that there is no material degradation of CF/PEEK when processing temperature is higher than 400 °C, it was actually found in this project that when processing

temperature was higher than 400 °C, the CF/PEEK might undergo very slight material degradation in one of the DSC tests. This was aligned with the results of the DSC analysis conducted to establish the heat specific capacity (C_p) of CF/PEEK in Chapter 6. However, further investigation should be carried out on confirming the lowest temperature at which CF/PEEK starts to degrade in an atmosphere of air.

In the crystallisation modelling, the limitations were related to the experiments conducted during the printing process development. The measurement method of the cooling rate recording has a limited accuracy as the reflection infrared signals introduces noise into the measurement, which is not easy to be filtered out. The heating capacities of chamber and the printbed should be improved so the ambient temperature can reach to an appropriate temperature (ideally higher than T_g) to help the crystallisation process by reducing the cooling rate.

Finally, the use of an oversized nozzle of CF/PEEK filament printing limited the print speed and bound quality, a better designed nozzle is required to increase the print efficiency. Recommendations described in Chapter 8, Section 8.3 as part of the future work. Unfortunately, a comprehensive parameter study of CF/PEEK filament printing could not be accomplished.

7.4 Summary

In summary, the biggest challenge of this project was understanding PEEK and CF/PEEK material properties related to the processing of the materials. In the porosity studies of CF/PEEK filament, it indicated a method of ToF-SIMS has advantage to identify unambiguous materials as for carbon fibre and PEEK. Then it was confirmed that a novel method of a bespoke pultrusion apparatus was built to manufacture the CF/PEEK filament. The first time continuous CF high fraction with 57.4% reinforced PEEK matrix composites was developed. It was also found that the work at the crystallisation of the PEEK and PEEK on carbon fibres greatly influences the process outcome in terms of the printed

parts' final mechanical properties. From the final finding, a reduction of the cooling rate of the deposited material could improve the mechanical properties of the printed parts of both PEEK and CF/PEEK. This can be achieved by increasing the ambient temperature and reducing the printed speed. In this part of the work, DMA was innovatively used to test very small FFF samples. A new analysis combines polymer crystallisation and composite micromechanical theory was used. IR thermography was used to validate non-isothermal analysis. And the model provided a new framework to optimise FFF crystallisation for PEEK FFF printed parts performance. The development of carbon fibre reinforced PEEK printing could potentially contribute to the industrial field of automobile, aerospace, construction where strength design need to be applied, and medical application where functional 3D printing is required.

In this project, due to the limitations of the technical equipment, some of the material properties required as inputs for the process design could not be obtained using the university's facilities. Specifically, the rheology tests could not be carried out due to the limited capabilities of the testing equipment in the lab. The rheology behaviour of the processing material was instead calculated from the data available in the literature. Also, in general, more theoretical studies will need to be carried out to understand the observations made during the experiments.

CHAPTER 8

Conclusions and Future Work

8.1 Introduction

Recall that the aim of this project was to develop a composites feedstock process and FFF process, the aim and objectives of the research, as stated in Chapter 1 Section 1.2, have largely been successfully achieved in terms of: (i) development of a feedstock process to feed the loose commingled CF/PEEK into FFF printer; and (ii) successful printing of CF/PEEK parts and investigation of the relationship between printing parameters and FFF printed PEEK mechanical properties. The conclusions and recommendations for future work are presented below.

8.2 Conclusions

The main conclusions of this research are as follows:

- Compared with previous reports, in this project a significantly higher CF volume fraction CF/PEEK composites has been initially successfully printed. The meaning of the word printed here follows the definition of printability in Section 1.3 Chapter 1. Additionally, a pultrusion process to manufacture the feedstock has been established, and a processing window has been established.
- The effects of process parameters on the CF/PEEK filament quality have been studied. A parameter combination of pultrusion temperature and speed was investigated in this project to establish the above-mentioned processing window.
- A novel method for predicting mechanical properties of PEEK FFF-printed parts has been presented.

Chapter 8 Conclusions and Future Works

The detail technical conclusions include:

- It was shown that the material characterisation carried out initially gave the outcome to predict that the cooling range of the PEEK and CF/PEEK during the process is a critical factor that strongly influence mechanical properties of the final printed parts.
- It was shown that the pultrusion apparatus designed and built as part of this project was capable of manufacturing the CF/PEEK form commingled yarn to form into CF/PEEK filament.
- It was confirmed that the E3D HotEnd is an appropriate choice as the heating element for the pultrusion apparatus. Here a thermal analysis of the HotEnd and a mechanical analysis of the apparatus have been carried out to ensure the pultrusion apparatus works functionally. The HotEnd analysis was validated by IR-imaging measurement.
- It was found the CF/PEEK filament quality is dependent on the temperature and speed of the pultrusion process. Within a pultrusion temperature range, higher pultrusion temperature and slower pultrusion speed lead better filament consolidation.
- It was shown that by adaptation the printhead of a commercial PEEK printer, the manufactured high carbon fibre volume fraction CF/PEEK filament is capable to be printed.
- It was presented that a crystallisation model of PEEK printing is established based on the IR-image measurement and DMA tests results.
- It was shown an established lumped parameter model, which analyse the heat transfer from the nozzle to the filament, helped to establish the actual exiting temperature of the CF/PEEK filament and informed the achievable range of printing speed.

8.3 Recommendations for Future Work

The quality of the produced feedstock was optimised as far as possible within the constraints imposed by the current equipment. However, in the future, it would be beneficial to improve the filament consolidation quality further and to investigate even higher fibre volume fractions. Future approaches could include the treatment of commingled CF/PEEK before the pultrusion process, inserting an intermediate heating stage with compacting die systems, as well as chemistry solutions by adding more additive materials before the pultrusion process to improve the wetout of carbon fibre bundles into the PEEK. These chemistry solutions are similar to the treatment of PLA in Li *et al* [33].

Further investigation is still required to establish a more definite and quantitative model for the CF/PEEK degradation as a function of print temperature and print speed. It was observed that during the DSC tests to obtain the specific heat capacity c_p , when testing temperature was above 410°C, the signal provides an unstable reading for heat flow. This unstable heat flow might be due to a possible degradation of the CF/PEEK material based on the discussion in Ref. [1]. However, a more detailed study in order to understand the influence on the degradation of CF/PEEK of high temperature, in combination with a certain values of processing (or residing) time corresponding to slow printing or pultrusion speed, will be part of the proposed future work. For instance, this can be carried out by Fourier Transform Infra-red Spectrometry (FTIR) [1].

The surface roughness of parts printed with PEEK, when analysed using the optical microscope, had different visual appearances depending on different printing conditions. More investigations of surface roughness of FFF printed PEEK should therefore be carried out to find out how the printing parameters influence the surface roughness of the printed parts, and how the surface roughness can be linked to the mechanical properties of the printed parts. This could potentially be carried out using a profilometer [283].

Chapter 8 Conclusions and Future Works

The crystallisation model of FFF printed PEEK provides a foundation for optimising the crystallisation for the mechanical performance of FFF printed PEEK. Further exploration of the mechanisms of interdiffusion and residual anisotropy when FFF printing PEEK filaments is needed to better understand the amorphous properties in the weld, which will require measurement of a linear viscoelastic properties of the specimens. Additionally, an independent measurement of crystallinity is required, for instance using Raman spectroscopy, to compare to the model predictions and to investigate the possibility of flow-enhanced crystallisation. Furthermore, the correction of IR-imaging measurement by means of a more accurate measurement data of the relationship between crystal fractions with material cooling rates coming from flash DSC will improve the accuracy in-situ crystallinity measurement. Finally, studying the effect of a thermal post-treatment would provide an avenue for achieving higher levels of crystallisation in the weld regions.

Although this work demonstrated that the manufactured high volume fraction CF/PEEK FFF feedstock filament could be successfully printed using the modified printer, there was insufficient laboratory time to optimise the printing process or to characterise the printed material. The next step should be to characterise the printed filaments. Comparison of the fibre distribution and presence of porosity, and their dependence on processing parameters would be an obvious next step. A comparison with the feedstock material would provide an interesting insight into the effect of the printing process, and process parameters, on the filament. Next steps should be to print test parts to enable property measurements. Comprehensive mechanical testing of the CF/PEEK printed specimens will also need to be part of the future work. Based on the established FFF printed PEEK crystal growth model, with the DMA test, E_{perp} and E_{par} will be predicted to investigate the mechanical properties of the anisotropic composites printed parts. The nucleation and crystal growth rates of semi-crystalline PEEK matrix will be explored based on the influence of carbon fibres. The printed part tensile and flexural properties can be established by following the standards regarding printing specimens [284]:

{ISO 527 or ASTM D638 for neat PEEK and ASTM D3039 for CF/PEEK} and {ISO 178, ISO 14125, or ASTM D790 (neat PEEK and CF/PEEK) and ASTM D7264 (CF/PEEK)} respectively.

There can be some expanded work based on this research, includes increasing of the axial length of the orifice section requiring some bespoke nozzle design. This design modification will consist of introducing initial contact between the filament and the nozzle in the orifice, followed by a gradual widening of the orifice section, which allows for the filament to be draped gradually into the deposition direction tangential to the printbed. Pre-heating of the filament in the printhead can be employed to allow for higher deposition rates. This can involve the integration of electromagnetic radiation (laser, IR, microwave), ultrasound or increasing the convection by actively blowing hot air in the printhead. The expanded work can also include introducing additional degrees of freedom into the printhead motion, namely roll and pitch rotations of the printhead about the the x – and y – axes of the machine. This would also allow for full contact between the filament and the nozzle in the orifice section. This development also allows an adaptation of the nozzle for the filament deposition angle to achieve a more accurate positional deposition, which could improve the geometrical accuracy and structural integrity between layers.

In this project, based on the lab research and development proof of printing concept and process development, the knowledge challenges addressed in porosity, bonding, feedstock production, processing window, and crystallization studies to optimise the processing parameters can contribute to the future industrial system enhancement and optimisation on pre-commercial scale. The next routes will be more focus on the high deposition rate of the continuous carbon fibre with PEEK printing. The required development of the nozzle and printhead for higher deposition rates has been discussed above. Another further requirement would be formed by the development of more accurate in-situ measurement in temperature control, surface roughness monitoring, layers bonding monitoring etc. These will improve the manufacturing readiness level, printed parts quality control.

Chapter 8 Conclusions and Future Works

Finally, development of printing strategies that yield a controllable and repeatable thermal history resulting in a consistent and controllable degree of crystallinity would be an important step towards parts certification.

Another interesting follow on work would be to look at the geometrical freedoms and constraints of printing the CF/PEEK filaments, such as tightest radii without filament damage achievable, and then to use this knowledge to design fibre paths to optimize reinforcement for particular applications. This would move the work from a materials and process project to one looking at component design and analysis using the materials and processes enable with this work, with the ultimate aim of demonstrating new and improved methods of manufacturing continuous CF reinforced parts and products.

References

- [1] Stepashkin, A. A., Chukov, D. I., Senatov, F. S., Salimon, A. I., Korsunsky, A. M., & Kaloshkin, S. D. (2018). 3D-printed PEEK-carbon fiber (CF) composites: Structure and thermal properties. *Composites Science and Technology*, 164, 319-326.
- [2] Patel, P. (2011). Investigation of the Fire Behaviour of PEEK-based Polymers and Compounds (Doctoral dissertation, University of Central Lancashire).
- [3] Brenken, B., Barocio, E., Favaloro, A., Kunc, V., & Pipes, R. B. (2018). Fused filament fabrication of fiber-reinforced polymers: A review. *Additive Manufacturing*, 21, 1-16.
- [4] <https://www.engineering.com/3DPrinting/3DPrintingArticles/ArticleID/19608/Anisoprint-Anisotropy-as-Advantage-in-Carbon-Fiber-3D-Printing.aspx>, accessed on 14 Oct. 2019
- [5] Pellegrino, J., Pellegrino, J., Makila, T., McQueen, S., & Taylor, E. (2016). Measurement science roadmap for polymer-based additive manufacturing. US Department of Commerce, National Institute of Standards and Technology. Pellegrino, J., Makila, T., McQueen, S., & Taylor, E. (2016). Roadmap for Polymer-Based Additive Manufacturing.
- [6] <https://nvlpubs.nist.gov/nistpubs/ams/NIST.AMS.100-5.pdf> , accessed on 25, Nov 2019.
- [7] Qi, X., Chen, G., Li, Y., Cheng, X., & Li, C. (2019). Applying neural-network-based machine learning to additive manufacturing: current applications, challenges, and future perspectives. *Engineering*, 5(4), 721-729.
- [8] <https://www.creatbot.com/en/default.html>, accessed on 28 August, 2020.
- [9] Zhang, Z., & Zeng, H. (1993). Nucleation and crystal growth of PEEK on carbon fiber. *Journal of applied polymer science*, 48(11), 1987-1995.

References

- [10] Chapiro, M. (2016). Current achievements and future outlook for composites in 3D printing. *Reinforced Plastics*, 60(6), 372-375.
- [11] <https://markforged.com/blog/3d-printing-assembly-fixtures/>. accessed on 23 April 2019.
- [12] Wong, K. V., & Hernandez, A. (2012). A review of additive manufacturing. *ISRN Mechanical Engineering*, 2012, 208760, 10 pp.
- [13] Huang, S. H., Liu, P., Mokusdar, A., & Hou, L. (2013). Additive manufacturing and its societal impact: a literature review. *The International Journal of Advanced Manufacturing Technology*, 1-13.
- [14] Frazier, W. E. (2014). Metal additive manufacturing: a review. *Journal of Materials Engineering and Performance*, 23(6), 1917-1928.
- [15] Levy, G. N., Schindel, R., & Kruth, J. P. (2003). Rapid manufacturing and rapid tooling with layer manufacturing (LM) technologies, state of the art and future perspectives. *CIRP Annals-Manufacturing Technology*, 52(2), 589-609.
- [16] Gibson, I., Rosen, D., & Stucker, B. (2014). *Additive manufacturing technologies: 3D printing, rapid prototyping, and direct digital manufacturing*. Springer.
- [17] <https://en.wikipedia.org/wiki/G-code>, accessed on 09,04,2020.
- [18] Huang, Y., Leu, M. C., Mazumder, J., & Donmez, A. (2015). Additive manufacturing: current state, future potential, gaps and needs, and recommendations. *Journal of Manufacturing Science and Engineering*, 137(1), 014001.
- [19] Rahim, T. N. A. T., Abdullah, A. M., & Md Akil, H. (2019). Recent developments in fused deposition modeling-based 3D printing of polymers and their composites. *Polymer Reviews*, 59(4), 589-624.
- [20] Wohlers Associates, Inc., 2013, *Wohlers Report Additive Manufacturing and 3D Printing State of the Industry*, Wohlers Associates, Fort Collins, CO.

References

[21] Wohlers Associates, Inc., 2016, Wohlers Report Additive Manufacturing and 3D Printing State of the Industry, Wohlers Associates, Fort Collins, CO.

[22] Wohlers Associates, Inc., 2019, Wohlers Report Additive Manufacturing and 3D Printing State of the Industry, Wohlers Associates, Fort Collins, CO.

[23] Jakus, A. E. (2019). An Introduction to 3D Printing—Past, Present, and Future Promise. In 3D Printing in Orthopaedic Surgery (pp. 1-15). Elsevier.

[24] ASTM, 2009, ASTM International Committee F42 on Additive Manufacturing Technologies, ASTM F2792–10 Standard Terminology for Additive Manufacturing Technologies, ASTM, West Conshohocken, PA.

[25] Hull, C. W. (1984). Apparatus for production of three-dimensional objects by stereolithography. United States Patent, Appl., No. 638905, Filed.

[26] <https://all3dp.com/1/all-you-need-to-know-for-successful-metal-fff-printing/>, accessed on 18 February, 2021.

[27]

https://www.ikts.fraunhofer.de/en/departments/structural_ceramics/processes_and_components/shaping/cr_fused-filament-fabrication.html, accessed on 18 February, 2021.

[28] Namiki, M., Ueda, M., Todoroki, A., Hirano, Y., & Matsuzaki, R. (2014, January). 3D printing of continuous fiber reinforced plastic. In SAMPE Tech Seattle 2014 Conference. Soc. for the Advancement of Material and Process Engineering.

[29] Van der Klift, F., Koga, Y., Todoroki, A., Ueda, M., Hirano, Y., & Matsuzaki, R. (2015). 3D printing of continuous carbon fibre reinforced thermo-plastic (CFRTP) tensile test specimens. Open Journal of Composite Materials, 6(01), 18.

References

- [30] Yang, C., Tian, X., Liu, T., Cao, Y., & Li, D. (2017). 3D printing for continuous fiber reinforced thermoplastic composites: mechanism and performance. *Rapid Prototyping Journal*, 23(1), 209-215.
- [31] Matsuzaki, R., Ueda, M., Namiki, M., Jeong, T. K., Asahara, H., Horiguchi, K., Nakamura, T., Todoroki, A. & Hirano, Y. (2016). Three-dimensional printing of continuous-fiber composites by in-nozzle impregnation. *Scientific reports*, 6, 23058.
- [32] Tian, X., Liu, T., Yang, C., Wang, Q., & Li, D. (2016). Interface and performance of 3D printed continuous carbon fiber reinforced PLA composites. *Composites Part A: Applied Science and Manufacturing*, 88, 198-205.
- [33] Li, N., Li, Y., & Liu, S. (2016). Rapid prototyping of continuous carbon fiber reinforced polylactic acid composites by 3D printing. *Journal of Materials Processing Technology*, 238, 218-225.
- [34] Guo, N., & Leu, M. C. (2013). Additive manufacturing: technology, applications and research needs. *Frontiers of Mechanical Engineering*, 8(3), 215-243.
- [35] Yu, T., Ren, J., Li, S., Yuan, H., & Li, Y. (2010). Effect of fiber surface-treatments on the properties of poly (lactic acid)/ramie composites. *Composites Part A: Applied Science and Manufacturing*, 41(4), 499-505.
- [36] Rietema, M. J. (2015). Design of a prototype machine for 3D printing with continuous fibre reinforcement (Master's thesis, University of Twente).
- [37] Vaneker, T. H. J. (2017). Material extrusion of continuous fiber reinforced plastics using commingled yarn. *Procedia CIRP*, 66, 317-322.
- [38] Eichenhofer, M., Maldonado, J. I., Klunker, F., & Ermanni, P. (2015, July). Analysis of processing conditions for a novel 3D-composite production technique. In *20th International Conference on Composite Materials*.

References

- [39] Bernet, N., Michaud, V., Bourban, P. E., & Manson, J. A. E. (1999). An impregnation model for the consolidation of thermoplastic composites made from commingled yarns. *Journal of Composite Materials*, 33(8), 751-772.
- [40] Kim, D. H., Han, P. G., Jin, G. H., & Lee, W. I. (1997). A model for thermosetting composite pultrusion process. *Journal of composite materials*, 31(20), 2105-2122.
- [41] Kim, D. H., Lee, W. I., & Friedrich, K. (2001). A model for a thermoplastic pultrusion process using commingled yarns. *Composites science and technology*, 61(8), 1065-1077.
- [42] Nair, K. C. M., Kumar, R. P., Thomas, S., Schit, S. C., & Ramamurthy, K. (2000). Rheological behavior of short sisal fiber-reinforced polystyrene composites. *Composites Part A: Applied Science and Manufacturing*, 31(11), 1231-1240.
- [43] Van West, B. P., Pipes, R. B., & Advani, S. G. (1991). The consolidation of commingled thermoplastic fabrics. *Polymer Composites*, 12(6), 417-427.
- [44] Van de Velde, K., & Kiekens, P. (2001). Thermoplastic pultrusion of natural fibre reinforced composites. *Composite structures*, 54(2-3), 355-360.
- [45] <https://www.3dhubs.com/knowledge-base/selecting-right-3d-printing-process>, Website, accessed on 31 may 2019.
- [46] Wang, X., Jiang, M., Zhou, Z., Gou, J., & Hui, D. (2017). 3D printing of polymer matrix composites: A review and prospective. *Composites Part B: Engineering*, 110, 442-458.
- [47] Nguyen, N. A., Bowland, C. C., & Naskar, A. K. (2018). A general method to improve 3D-printability and inter-layer adhesion in lignin-based composites. *Applied Materials Today*, 12, 138-152.
- [48] Phan, D. D., Swain, Z. R., & Mackay, M. E. (2018). Rheological and heat transfer effects in fused filament fabrication. *Journal of Rheology*, 62(5), 1097-1107.

References

- [49] Sood, A. K., Ohdar, R. K., & Mahapatra, S. S. (2010). Parametric appraisal of mechanical property of fused deposition modelling processed parts. *Materials & Design*, 31(1), 287-295.
- [50] Murr, L. E., & Gaytan, S. M. (2014). Advances in additive manufacturing and tooling. *Comprehensive Materials Processing*, 135-161.
- [51] Deng, X., Zeng, Z., Peng, B., Yan, S., & Ke, W. (2018). Mechanical properties optimization of poly-ether-ether-ketone via fused deposition modeling. *Materials*, 11(2), 216.
- [52] Zhao, X., Xiong, D., & Liu, Y. (2018). Improving surface wettability and lubrication of polyetheretherketone (PEEK) by combining with polyvinyl alcohol (PVA) hydrogel. *Journal of the mechanical behavior of biomedical materials*, 82, 27-34.
- [53] Punchak, M., Chung, L. K., Lagman, C., Bui, T. T., Lazareff, J., Rezzadeh, K., ... & Yang, I. (2017). Outcomes following polyetheretherketone (PEEK) cranioplasty: systematic review and meta-analysis. *Journal of Clinical Neuroscience*, 41, 30-35.
- [54] Valentan, B., Kadivnik, Ž., Brajljih, T., Anderson, A., & Drstvenšek, I. (2013). Processing poly (ether etherketone) an a 3D printer for thermoplastic modelling. *Materiali in tehnologije*, 47(6), 715-721.
- [55] Vaezi, M., & Yang, S. (2015). Extrusion-based additive manufacturing of PEEK for biomedical applications. *Virtual and Physical Prototyping*, 10(3), 123-135.
- [56] Arif, M. F., Kumar, S., Varadarajan, K. M., & Cantwell, W. J. (2018). Performance of biocompatible PEEK processed by fused deposition additive manufacturing. *Materials & Design*, 146, 249-259.
- [57] Yang, C., Tian, X., Li, D., Cao, Y., Zhao, F., & Shi, C. (2017). Influence of thermal processing conditions in 3D printing on the crystallinity and

References

mechanical properties of PEEK material. *Journal of Materials Processing Technology*, 248, 1-7.

[58] Wu, W., Geng, P., Li, G., Zhao, D., Zhang, H., & Zhao, J. (2015). Influence of layer thickness and raster angle on the mechanical properties of 3D-printed PEEK and a comparative mechanical study between PEEK and ABS. *Materials*, 8(9), 5834-5846.

[59] Wu, W. Z., Geng, P., Zhao, J., Zhang, Y., Rosen, D. W., & Zhang, H. B. (2014). Manufacture and thermal deformation analysis of semicrystalline polymer polyether ether ketone by 3D printing. *Materials Research Innovations*, 18(sup5), S5-12.

[60] Yang, C., Tian, X., Li, D., Cao, Y., Zhao, F., & Shi, C. (2017). Influence of thermal processing conditions in 3D printing on the crystallinity and mechanical properties of PEEK material. *Journal of Materials Processing Technology*, 248, 1-7.

[61] Harding, M. J., Brady, S., O'Connor, H., Lopez-Rodriguez, R., Edwards, M. D., Tracy, S., ... & Ferguson, S. (2020). 3D printing of PEEK reactors for flow chemistry and continuous chemical processing. *Reaction Chemistry & Engineering*, 5(4), 728-735.

[62] Love, L. J., Kunc, V., Rios, O., Duty, C. E., Elliott, A. M., Post, B. K., ... & Blue, C. A. (2014). The importance of carbon fiber to polymer additive manufacturing. *Journal of Materials Research*, 29(17), 1893-1898.

[63] DeNardo, N. M. (2016). Additive manufacturing of carbon fiber-reinforced thermoplastic composites.

[64] Hassen, A. A., Lindahl, J., Chen, X., Post, B., Love, L., & Kunc, V. (2016, May). Additive manufacturing of composite tooling using high temperature thermoplastic materials. In SAMPE Conference Proceedings, Long Beach, CA, May (pp. 23-26).

References

- [65] Tekinalp, H. L., Kunc, V., Velez-Garcia, G. M., Duty, C. E., Love, L. J., Naskar, A. K., Blue C. A & Ozcan, S. (2014). Highly oriented carbon fiber–polymer composites via additive manufacturing. *Composites Science and Technology*, 105, 144-150.
- [66] Zhong, W., Li, F., Zhang, Z., Song, L., & Li, Z. (2001). Short fiber reinforced composites for fused deposition modeling. *Materials Science and Engineering: A*, 301(2), 125-130.
- [67] Ning, F., Cong, W., Qiu, J., Wei, J., & Wang, S. (2015). Additive manufacturing of carbon fiber reinforced thermoplastic composites using fused deposition modeling. *Composites Part B: Engineering*, 80, 369-378.
- [68] Hill, C., Rowe, K., Bedsole, R., Earle, J., & Kunc, V. (2016, May). Materials and process development for direct digital manufacturing of vehicles. In SAMPE Long Beach 2016 Conference and Exhibition.
- [69] Duty, C. E., Drye, T., & Franc, A. (2015). Material development for tooling applications using big area additive manufacturing (BAAM) (No. ORNL/TM-2015/78). Oak Ridge National Lab.(ORNL), Oak Ridge, TN (United States). Manufacturing Demonstration Facility (MDF).
- [70] Compton, B. G., & Lewis, J. A. (2014). 3D-printing of lightweight cellular composites. *Advanced materials*, 26(34), 5930-5935.
- [71] Kunc, V. (2015, September). Advances and challenges in large scale polymer additive manufacturing. In Proceedings of the 15th SPE Automotive Composites Conference, Novi, MI, USA (Vol. 9).
- [72] Perez, A. R. T., Roberson, D. A., & Wicker, R. B. (2014). Fracture surface analysis of 3D-printed tensile specimens of novel ABS-based materials. *Journal of Failure Analysis and Prevention*, 14(3), 343-353.
- [73] Carneiro, O. S., Silva, A. F., & Gomes, R. (2015). Fused deposition modeling with polypropylene. *Materials & Design*, 83, 768-776.

References

- [74] Mahajan, C., & Cormier, D. (2015). 3D printing of carbon fiber composites with preferentially aligned fibers. In IIE annual conference. Proceedings (p. 2953). Institute of Industrial and Systems Engineers (IISE).
- [75] Duty, C. E., Kunc, V., Compton, B., Post, B., Erdman, D., Smith, R., ... & Love, L. (2017). Structure and mechanical behavior of Big Area Additive Manufacturing (BAAM) materials. *Rapid Prototyping Journal*, 23(1), 181-189.
- [76] Ferreira, R. T. L., Amatte, I. C., Dutra, T. A., & Bürger, D. (2017). Experimental characterization and micrography of 3D printed PLA and PLA reinforced with short carbon fibers. *Composites Part B: Engineering*, 124, 88-100.
- [77] Ning, F., Cong, W., Hu, Y., & Wang, H. (2017). Additive manufacturing of carbon fiber-reinforced plastic composites using fused deposition modeling: Effects of process parameters on tensile properties. *Journal of Composite Materials*, 51(4), 451-462.
- [78] Lewicki, J. P., Rodriguez, J. N., Zhu, C., Worsley, M. A., Wu, A. S., Kanarska, Y., Horn J.D., Duoss E.B., Ortega J.M., Elmer W, Hensleigh, R. Fellini R.A & King, M. J. (2017). 3D-printing of meso-structurally ordered carbon fiber/polymer composites with unprecedented orthotropic physical properties. *Scientific reports*, 7, 43401.
- [79] Gray IV, R. W., Baird, D. G., & Bøhn, J. H. (1998). Thermoplastic composites reinforced with long fiber thermotropic liquid crystalline polymers for fused deposition modeling. *Polymer composites*, 19(4), 383-394.
- [80] Gray IV, R. W., Baird, D. G., & Helge Bøhn, J. (1998). Effects of processing conditions on short TLCP fiber reinforced FDM parts. *Rapid Prototyping Journal*, 4(1), 14-25.
- [81] Shofner, M. L., Lozano, K., Rodríguez-Macías, F. J., & Barrera, E. V. (2003). Nanofiber - reinforced polymers prepared by fused deposition modeling. *Journal of applied polymer science*, 89(11), 3081-3090.

References

- [82] Gardner, J. M., Sauti, G., Kim, J. W., Cano, R. J., Wincheski, R. A., Stelter, C. J., Grimsley, B. W., Working, D. C., & Siochi, E. J. (2016). Additive manufacturing of multifunctional components using high density carbon nanotube yarn filaments.
- [83] Melenka, G. W., Cheung, B. K., Schofield, J. S., Dawson, M. R., & Carey, J. P. (2016). Evaluation and prediction of the tensile properties of continuous fiber-reinforced 3D printed structures. *Composite Structures*, 153, 866-875.
- [84] Koga, Y., Van Der Klift, F., Todoroki, A., Ueda, M., Hirano, Y., & Matsuzaki, R. (2016, January). The printing process of 3D printer for continuous CFRT. In *SAMPE Long Beach 2016 Conference and Exhibition*. Soc. for the Advancement of Material and Process Engineering.
- [85] Tian, X., Liu, T., Wang, Q., Dilmurat, A., Li, D., & Ziegmann, G. (2017). Recycling and remanufacturing of 3D printed continuous carbon fiber reinforced PLA composites. *Journal of cleaner production*, 142, 1609-1618.
- [86] Bettini, P., Alitta, G., Sala, G., & Di Landro, L. (2017). Fused deposition technique for continuous fiber reinforced thermoplastic. *Journal of Materials Engineering and Performance*, 26(2), 843-848.
- [87] Dickson, A. N., Barry, J. N., McDonnell, K. A., & Dowling, D. P. (2017). Fabrication of continuous carbon, glass and Kevlar fibre reinforced polymer composites using additive manufacturing. *Additive Manufacturing*, 16, 146-152.
- [88] Christian, P., Jones, I. A., Rudd, C. D., Campbell, R. I., & Corden, T. J. (2001). Monomer transfer moulding and rapid prototyping methods for fibre reinforced thermoplastics for medical applications. *Composites part A: Applied science and manufacturing*, 32(7), 969-976.
- [89] <https://www.impossible-objects.com/>, accessed on 20 August, 2020.
- [90] <https://www.bellflight.com/>, accessed on 20 August, 2020.

References

- [91] <https://amfg.ai/2019/04/02/thinking-big-4-impressive-applications-of-large-scale-3d-printing/>. Websites, accessed on 24 May 2019.
- [92] <https://www.ornl.gov/>, accessed on 20 August, 2020.
- [93] <https://www.additivemanufacturing.media/articles/3d-printed-tooling-offers-durability-for-precast-concrete>. Website, accessed on 26 May 2019.
- [94] <https://3dprint.com/22534/strati-3d-print-car/>. Website, accessed on 26 May 2019.
- [95] <http://compositesmanufacturingmagazine.com/2018/07/thermwood-installs-worlds-largest-composite-3-d-printer-at-local-motors/>. Website, accessed on 28 May 2019.
- [96] Mitschang, P., Blinzler, M., & Wöginger, A. (2003). Processing technologies for continuous fibre reinforced thermoplastics with novel polymer blends. *Composites Science and Technology*, 63(14), 2099-2110.
- [97] <https://www.markforged.com/>, accessed on 21 August, 2020.
- [98] “3D Printing High-Strength Carbon Composites Using PEEK, PAEK”, <https://www.designnews.com/design-hardware-software/3d-printing-high-strength-carbon-composites-using-peek-paek/143795958032579>. Accessed on 18 Oct. 19.
- [99] <https://e3d-online.com/v6-all-metal-hotend>. Accessed on 12 Nov, 2019.
- [100] Jerez-Mesa, R., Travieso-Rodriguez, J. A., Corbella, X., Busqué, R., & Gomez-Gras, G. (2016). Finite element analysis of the thermal behavior of a RepRap 3D printer liquefier. *Mechatronics*, 36, 119-126.
- [101] Atif Yardimci, M., & Güçeri, S. (1996). Conceptual framework for the thermal process modelling of fused deposition. *Rapid Prototyping Journal*, 2(2), 26-31.
- [102] Domingo-Espin, M., Puigoriol-Forcada, J. M., Garcia-Granada, A. A., Llumà, J., Borros, S., & Reyes, G. (2015). Mechanical property characterization

References

and simulation of fused deposition modeling Polycarbonate parts. *Materials & Design*, 83, 670-677.

[103] Heller, B. P., Smith, D. E., & Jack, D. A. (2016). Effects of extrudate swell and nozzle geometry on fiber orientation in Fused Filament Fabrication nozzle flow. *Additive Manufacturing*, 12, 252-264.

[104] Go, J., & Hart, A. J. (2017). Fast desktop-scale extrusion additive manufacturing. *Additive Manufacturing*, 18, 276-284.

[105] <https://uk.comsol.com/blogs/optimize-3d-printers-by-modeling-the-glass-transition-temperature/>, accessed on 21 August, 2020.

[106] Sun, Q., Rizvi, G. M., Bellehumeur, C. T., & Gu, P. (2008). Effect of processing conditions on the bonding quality of FDM polymer filaments. *Rapid Prototyping Journal*, 14(2), 72-80.

[107] Thomas, J. P., & Rodríguez, J. F. (2000). Modeling the Fracture Strength between Fused-Deposition Extruded Roads 16. In 2000 International Solid Freeform Fabrication Symposium.

[108] Bellini, A., & Güçeri, S. (2003). Mechanical characterization of parts fabricated using fused deposition modeling. *Rapid Prototyping Journal*, 9(4), 252-264.

[109] Bellehumeur, C., Li, L., Sun, Q., & Gu, P. (2004). Modeling of bond formation between polymer filaments in the fused deposition modeling process. *Journal of Manufacturing Processes*, 6(2), 170-178.

[110] Zhang, Y., & Chou, K. (2008). A parametric study of part distortions in fused deposition modelling using three-dimensional finite element analysis. *Proceedings of the Institution of Mechanical Engineers, Part B: Journal of Engineering Manufacture*, 222(8), 959-968.

References

- [111] Wang, T. M., Xi, J. T., & Jin, Y. (2007). A model research for prototype warp deformation in the FDM process. *The International Journal of Advanced Manufacturing Technology*, 33(11-12), 1087-1096.
- [112] Nickel, A. H., Barnett, D. M., & Prinz, F. B. (2001). Thermal stresses and deposition patterns in layered manufacturing. *Materials Science and Engineering: A*, 317(1-2), 59-64.
- [113] Bourell, D. L., Rosen, D. W., & Leu, M. C. (2014). The roadmap for additive manufacturing and its impact. *3D Printing and Additive Manufacturing*, 1(1), 6-9.
- [114] Nedele, M. R., & Wisnom, M. R. (1994). Stress concentration factors around a broken fibre in a unidirectional carbon fibre-reinforced epoxy. *Composites*, 25(7), 549-557.
- [115] Bellini, A. (2002). Fused deposition of ceramics: a comprehensive experimental, analytical and computational study of material behavior, fabrication process and equipment design.
- [116] Ramanath, H. S., Chandrasekaran, M., Chua, C. K., Leong, K. F., & Shah, K. D. (2007). Modelling of extrusion behaviour of biopolymer and composites in fused deposition modelling. In *Key Engineering Materials* (Vol. 334, pp. 1241-1244). Trans Tech Publications.
- [117] <https://www.ansys.com/en-gb>, accessed on 21 August, 2020.
- [118] Ramanath, H. S., Chua, C. K., Leong, K. F., & Shah, K. D. (2008). Melt flow behaviour of poly- ϵ -caprolactone in fused deposition modelling. *Journal of Materials Science: Materials in Medicine*, 19(7), 2541-2550.
- [119] Mostafa, N., Syed, H. M., Igor, S., & Andrew, G. (2009). A study of melt flow analysis of an ABS-Iron composite in fused deposition modelling process. *Tsinghua Science & Technology*, 14, 29-37.

References

- [120] Ramirez, M. A. (2018). In-silico Tensile Testing of Additively Manufactured Short Fiber Composite (Doctoral dissertation, Purdue University).
- [121] <https://www.autodesk.co.uk/products/moldflow/overview>, accessed on 21 August, 2020.
- [122] Folgar, F., & Tucker III, C. L. (1984). Orientation behavior of fibers in concentrated suspensions. *Journal of reinforced plastics and composites*, 3(2), 98-119.
- [123] HELLER, B., SMITH, D. E., & JACK, D. A. (2015, November). The Effects of Extrudate Swell, Nozzle Shape, and the Nozzle Convergence Zone on Fiber Orientation in Fused Deposition Modeling Nozzle Flow. In American Society of Composites-30th Technical Conference.
- [124] Heller, B. P., Smith, D. E., & Jack, D. A. (2016). Effects of extrudate swell and nozzle geometry on fiber orientation in Fused Filament Fabrication nozzle flow. *Additive Manufacturing*, 12, 252-264.
- [125] B.P. Heller, D.E. Smith, D.A. Jack, Computing mechanical properties from orientation tensor for fiber filled polymers in axisymmetric flow and planar deposition flow, SPE ACCE Conf. (2016) 1–13.
- [126] <https://uk.comsol.com/>, accessed on 21 August, 2020.
- [127] Seppala, J. E., Han, S. H., Hillgartner, K. E., Davis, C. S., & Migler, K. B. (2017). Weld formation during material extrusion additive manufacturing. *Soft Matter*, 13(38), 6761-6769.
- [128] Sun, Q. (2005). Bond formation between polymer filaments in fused deposition modeling process (Master's thesis, Calgary).
- [129] Wool, R. P., Yuan, B. L., & McGarel, O. J. (1989). Welding of polymer interfaces. *Polymer Engineering & Science*, 29(19), 1340-1367.

References

- [130] Pokluda, O., Bellehumeur, C. T., & Vlachopoulos, J. (1997). Modification of Frenkel's model for sintering. *AIChE journal*, 43(12), 3253-3256.
- [131] Li, L., Sun, Q., Bellehumeur, C., & Gu, P. (2002). Investigation of bond formation in FDM process. *Solid Freeform Fabrication Proceedings*,(403), 400407.
- [132] Gurralla, P. K., & Regalla, S. P. (2014). Part strength evolution with bonding between filaments in fused deposition modelling: This paper studies how coalescence of filaments contributes to the strength of final FDM part. *Virtual and Physical Prototyping*, 9(3), 141-149.
- [133] Kishore, V., Ajinjeru, C., Duty, C. E., Nycz, A., Post, B. K., Lindahl, J. M., & Kunc, V. (2017). Infrared preheating to enhance interlayer strength of components printed on the big area additive manufacturing (BAAM) system. Oak Ridge National Lab.(ORNL), Oak Ridge, TN (United States). Manufacturing Demonstration Facility (MDF).
- [134] Ravi, A. K., Deshpande, A., & Hsu, K. H. (2016). An in-process laser localized pre-deposition heating approach to inter-layer bond strengthening in extrusion based polymer additive manufacturing. *Journal of Manufacturing Processes*, 24, 179-185.
- [135] Lee, G. W., Park, M., Kim, J., Lee, J. I., & Yoon, H. G. (2006). Enhanced thermal conductivity of polymer composites filled with hybrid filler. *Composites Part A: Applied science and manufacturing*, 37(5), 727-734.
- [136] Kim, S. R., Kim, D. H., Kim, D. J., Kim, M. H., & Park, J. M. (2007). Study on thermal conductivity of polyetheretherketone/thermally conductive filler composites. In *Solid state phenomena* (Vol. 124, pp. 1079-1082). Trans Tech Publications.
- [137] Atif Yardimci, M., Hattori, T., Guceri, S. I., & Danforth, S. C. (1997). Thermal analysis of fused deposition. In *1997 International Solid Freeform Fabrication Symposium*.

References

- [138] Costa, S. F., Duarte, F. M., & Covas, J. A. (2008). Towards modelling of Free Form Extrusion: analytical solution of transient heat transfer. *International Journal of Material Forming*, 1(1), 703-706.
- [139] <https://www.mathworks.com/products/matlab.html>, accessed on 21 August, 2020.
- [140] Brenken, B., Favaloro, A., Barocio, E., DeNardo, N. M., & Pipes, R. B. (2016, May). Development of a model to predict temperature history and crystallization behavior of 3D printed parts made from fiber-reinforced thermoplastic polymers. In SAMPE conference, Long Beach, CA.
- [141] Zhou, Y., Nyberg, T., Xiong, G., & Liu, D. (2016, July). Temperature analysis in the fused deposition modeling process. In 2016 3rd international conference on information science and control engineering (ICISCE) (pp. 678-682). IEEE.
- [142] Costa, S. F., Duarte, F. M., & Covas, J. A. (2015). Thermal conditions affecting heat transfer in FDM/FFE: a contribution towards the numerical modelling of the process: This paper investigates convection, conduction and radiation phenomena in the filament deposition process. *Virtual and Physical Prototyping*, 10(1), 35-46.
- [143] Pooladvand, K., & Furlong, C. (2017). Thermo-mechanical investigation of fused deposition modeling by computational and experimental methods. In *Mechanics of Composite and Multi-functional Materials, Volume 7* (pp. 45-54). Springer, Cham.
- [144] B. Brenken, E. Barocio, A. Favaloro, R.B. Pipes, Simulation of Semi-Crystalline Composites in the Extrusion Deposition Additive Manufacturing Process, in: Proc. Sci. Age Exp. Conf. by Dassault Syst., Chicago, IL, n.d.
- [145] Liu, X., Li, S., Liu, Z., Zheng, X., Chen, X., & Wang, Z. (2015). An investigation on distortion of PLA thin-plate part in the FDM process. The

References

International Journal of Advanced Manufacturing Technology, 79(5-8), 1117-1126.

[146] Zhang, Y., Pan, D., Sun, X., Sun, G., Wang, X., Liu, X., Li, Y., Dai, Y & Li, N. (2006). Production of porcine cloned transgenic embryos expressing green fluorescent protein by somatic cell nuclear transfer. *Science in China Series C*, 49(1), 1-8.

[147] P. Hébert, S. Mathieu, L. Adam, D. Gianotta, C. Basire, Holistic multiscale simulation approach for additive layer manufacturing of plastics, SPE ACCE Conf. (2016) 1–15.

[148] Favaloro, A. J., Brenken, B., Barocio, E., & Pipes, R. B. (2017). Simulation of polymeric composites additive manufacturing using Abaqus. *Science in the Age of Experience*, 103-114.

[149] Brenken, B., Favaloro, A., Barocio, E., & Pipes, R. B. (2017). Simulation of semi-crystalline composite tooling made by extrusion deposition additive manufacturing. In *Int. SAMPE Tech. Conf* (pp. 1758-1770).

[150] Barocio, E., Brenken, B., Favaloro, A., & Pipes, R. B. (2017, May). Extrusion deposition additive manufacturing of composite molds for high-temperature applications. In *Proceedings of the Int. SAMPE Tech. Conf.*, Seattle, WA, USA (pp. 22-25).

[151] Tymrak, B. M., Kreiger, M., & Pearce, J. M. (2014). Mechanical properties of components fabricated with open-source 3-D printers under realistic environmental conditions. *Materials & Design*, 58, 242-246.

[152] Melnikova, R., Ehrmann, A., & Finsterbusch, K. (2014). 3D printing of textile-based structures by Fused Deposition Modelling (FDM) with different polymer materials. In *IOP conference series: materials science and engineering* (Vol. 62, No. 1, p. 012018). IOP publishing.

References

- [153] Garcia, C. R., Correa, J., Espalin, D., Barton, J. H., Rumpf, R. C., Wicker, R., & Gonzalez, V. (2012). 3D printing of anisotropic metamaterials. *Progress In Electromagnetics Research*, 34, 75-82.
- [154] Kroll, E., & Artzi, D. (2011). Enhancing aerospace engineering students' learning with 3D printing wind-tunnel models. *Rapid Prototyping Journal*, 17(5), 393-402.
- [155] Short, D. B. (2015). Use of 3D printing by museums: Educational exhibits, artifact education, and artifact restoration. *3D Printing and Additive Manufacturing*, 2(4), 209-215.
- [156] <https://www.porcher-ind.com/en>, accessed on 21 August, 2020.
- [157] <https://www.insidecomposites.com/porcher-industries-to-showcase-carbonpeek-helicopter-rotor-hub-at-jec-world-2017/>, accessed on 19 Oct. 19
- [158] Dawson, P. C., PC, D., & DJ, B. (1980). X-ray data for poly (aryl ether ketones). *Polymer* – Elsevier.
- [159] Blundell, D. J., & Osborn, B. N. (1983). The morphology of poly (aryl-ether-ether-ketone). *Polymer*, 24(8), 953-958.
- [160] Halpin, J. C., & Kardos, J. L. (1972). Moduli of crystalline polymers employing composite theory. *Journal of Applied Physics*, 43(5), 2235-2241.
- [161] Talbott, M. F., Springer, G. S., & Berglund, L. A. (1987). The effects of crystallinity on the mechanical properties of PEEK polymer and graphite fiber reinforced PEEK. *Journal of Composite Materials*, 21(11), 1056-1081.
- [162] Lee, W. I., Talbott, M. F., Springer, G. S., & Berglund, L. A. (1987). Effects of cooling rate on the crystallinity and mechanical properties of thermoplastic composites. *Journal of Reinforced Plastics and Composites*, 6(1), 2-12.
- [163] Cebe, P., Chung, S. Y., & Hong, S. D. (1987). Effect of thermal history on mechanical properties of polyetheretherketone below the glass transition temperature. *Journal of applied polymer science*, 33(2), 487-503.

References

- [164] Velisaris, C. N., & Seferis, J. C. (1986). Crystallization kinetics of polyetheretherketone (PEEK) matrices. *Polymer Engineering & Science*, 26(22), 1574-1581.
- [165] Chivers, R. A., & Moore, D. R. (1994). The effect of molecular weight and crystallinity on the mechanical properties of injection moulded poly (aryl-ether-ether-ketone) resin. *Polymer*, 35(1), 110-116.
- [166] Herrod-Taylor, A. J. (2011). The crystallisation of Poly (aryl ether etherketone)(PEEK) and its carbon fibre composites (Doctoral dissertation, University of Birmingham).
- [167] Zhang, H. (2004). Fire-safe polymers and polymer composites. Office of Aviation Research, Federal Aviation Administration.
- [168] Perng, L. H., Tsai, C. J., & Ling, Y. C. (1999). Mechanism and kinetic modelling of PEEK pyrolysis by TG/MS. *Polymer*, 40(26), 7321-7329.
- [169] Hay, J. N., & Kemmish, D. J. (1987). Thermal decomposition of poly (aryl ether ketones). *Polymer*, 28(12), 2047-2051.
- [170] Cheng, S. Z., Cao, M. Y., & Wunderlich, B. (1986). Glass transition and melting behavior of poly (oxy-1, 4-phenyleneoxy-1, 4-phenylenecarbonyl-1, 4-phenylene)(PEEK). *Macromolecules*, 19(7), 1868-1876.
- [171] Briggs, D. (1992). Ion and neutral spectroscopy. *Practical surface analysis*, 2.
- [172] Hachmi, B. D., & Vu-Khanh, T. (1997). Crystallization mechanism in PEEK/carbon fiber composites. *Journal of thermoplastic composite materials*, 10(5), 488-501.
- [173] Waddon, A. J., Hill, M. J., Keller, A., & Blundell, D. J. (1987). On the crystal texture of linear polyaryls (PEEK, PEK and PPS). *Journal of Materials Science*, 22(5), 1773-1784.

References

- [174] Zhang, M., Xu, J., Zhang, Z., Zeng, H., & Xiong, X. (1996). Effect of transcrystallinity on tensile behaviour of discontinuous carbon fibre reinforced semicrystalline thermoplastic composites. *Polymer*, 37(23), 5151-5158.
- [175] Jeng, C. C., & Chen, M. (2000). Flexural failure mechanisms in injection-moulded carbon fibre/PEEK composites. *Composites science and technology*, 60(9), 1863-1872.
- [176] Sarasua, J. R., Remiro, P. M., & Pouyet, J. B. (1996). Effects of thermal history on mechanical behavior of PEEK and its short - fiber composites. *Polymer composites*, 17(3), 468-477.
- [177] Lustiger, A., Uralil, F. S., & Newaz, G. M. (1990). Processing and structural optimization of PEEK composites. *Polymer composites*, 11(1), 65-75.
- [178] Jar, P. Y., Mulone, R., Davies, P., & Kausch, H. H. (1993). A study of the effect of forming temperature on the mechanical behaviour of carbon-fibre/peek composites. *Composites science and technology*, 46(1), 7-19.
- [179] Vu-Khanh, T., & Frikha, S. (1999). Influence of processing on morphology, interface, and delamination in PEEK/carbon composites. *Journal of Thermoplastic Composite Materials*, 12(2), 84-95.
- [180] Bassett, D. C., Olley, R. H., & Al Raheil, I. A. M. (1988). On crystallization phenomena in PEEK. *Polymer*, 29(10), 1745-1754.
- [181] Blundell, D. J., Crick, R. A., Fife, B., Peacock, J., Keller, A., & Waddon, A. (1989). Spherulitic morphology of the matrix of thermoplastic PEEK/carbon fibre aromatic polymer composites. *Journal of materials science*, 24(6), 2057-2064.
- [182] Thomas, S., Joseph, K., Malhotra, S. K., Goda, K., & Sreekala, M. S. (Eds.). (2012). *Polymer Composites, Macro-and Microcomposites (Vol. 1)*. John Wiley & Sons.

References

- [183] Devine, D. M., Hahn, J., Richards, R. G., Gruner, H., Wieling, R., & Pearce, S. G. (2013). Coating of carbon fiber - reinforced polyetheretherketone implants with titanium to improve bone apposition. *Journal of Biomedical Materials Research Part B: Applied Biomaterials*, 101(4), 591-598.
- [184] Lu, T., Liu, X., Qian, S., Cao, H., Qiao, Y., Mei, Y., Chu, P. K. & Ding, C. (2014). Multilevel surface engineering of nanostructured TiO₂ on carbon-fiber-reinforced polyetheretherketone. *Biomaterials*, 35(22), 5731-5740.
- [185] <https://arevo.com/>, accessed on 21 August, 2020.
- [186] "Arevo Labs announces Carbon Fiber and Nanotube-reinforced High Performance materials for 3D Printing Process", <https://3dprint.com/1755/arevo-labs-announces-carbon-nanotube-reinforced-3d-printing/>. Accessed on 18 Oct. 19.
- [187] Han, X., Yang, D., Yang, C., Spintzyk, S., Scheideler, L., Li, P., Li, D., Geis-Gerstorfer, J. & Rupp, F. (2019). Carbon Fiber Reinforced PEEK Composites Based on 3D-Printing Technology for Orthopedic and Dental Applications. *Journal of clinical medicine*, 8(2), 240.
- [188] McCool, R., Murphy, A., Wilson, R., Jiang, Z., Price, M., Butterfield, J., & Hornsby, P. (2012). Thermoforming carbon fibre-reinforced thermoplastic composites. *Proceedings of the Institution of Mechanical Engineers, Part L: Journal of Materials: Design and Applications*, 226(2), 91-102.
- [189] Hillermeier, R., Hasson, T., Friedrich, L., & Ball, C. (2013). Advanced thermosetting resin matrix technology for next generation high volume manufacture of automotive composite structures (No. 2013-01-1176). SAE Technical Paper.
- [190] Tierney, J. J., & Gillespie Jr, J. W. (2004). Crystallization kinetics behavior of PEEK based composites exposed to high heating and cooling rates. *Composites Part A: Applied science and manufacturing*, 35(5), 547-558.

References

- [191] Earnest, C. M. (1988). *Compositional analysis by thermogravimetry* (Vol. 997). ASTM International.
- [192] Walters, R. N. (2002). Molar group contributions to the heat of combustion. *Fire and materials*, 26(3), 131-145.
- [193] Walters, R., & Lyon, R. E. (2001). Calculating polymer flammability from molar group contributions (No. DOT/FAA/AR-01/31). FEDERAL AVIATION ADMINISTRATION WASHINGTON DC OFFICE OF AVIATION RESEARCH.
- [194] Tsai, C. J., Perng, L. H., & Ling, Y. C. (1997). A study of thermal degradation of poly (aryl - ether - ether - ketone) using stepwise pyrolysis/gas chromatography/mass spectrometry. *Rapid communications in mass spectrometry*, 11(18), 1987-1995.
- [195] Day, M., Cooney, J. D., & Wiles, D. M. (1990). The thermal degradation of poly (aryl—ether—ether—ketone)(PEEK) as monitored by pyrolysis—GC/MS and TG/MS. *Journal of analytical and applied pyrolysis*, 18(2), 163-173.
- [196] Stevens, M. P., (1999), *Polymer Chemistry: An Introduction*. Third Edition. Oxford University Press, New York, USA.
- [197] Menczel, J. D., & Prime, R. B. (Eds.). (2009). *Thermal analysis of polymers*. John Wiley.
- [198] <https://www.perkinelmer.com/uk/>, accessed on 21 August, 2020.
- [199] <https://www.slideshare.net/MokhtarPashaie/dsc-tga>. Accessed on 25 Oct. 2019.
- [200] <https://polymerscience.physik.hu-berlin.de/docs/manuals/DSC.pdf>, accessed 05/07/2020.
- [201] Bogner, A., Jouneau, P. H., Thollet, G., Basset, D., & Gauthier, C. (2007). A history of scanning electron microscopy developments: Towards “wet-STEM” imaging. *Micron*, 38(4), 390-401.

References

- [202] Goldstein, J. I., Newbury, D. E., Michael, J. R., Ritchie, N. W., Scott, J. H. J., & Joy, D. C. (2017). *Scanning electron microscopy and X-ray microanalysis*. Springer.
- [203] Fearn, S. (2015). Characterisation of biological material with ToF-SIMS: a review. *Materials Science and Technology*, 31(2), 148-161.
- [204] Delcorte, A., Bertrand, P., Arys, X., Jonas, A., Wischerhoff, E., Mayer, B., & Laschewsky, A. (1996). ToF-SIMS study of alternate polyelectrolyte thin films: Chemical surface characterization and molecular secondary ions sampling depth. *Surface science*, 366(1), 149-165.
- [205] Spells, S. J. (Ed.). (1994). *Characterization of solid polymers: new techniques and developments*. Springer Science & Business Media.
- [206] Pawson, D. J., Ameen, A. P., Short, R. D., Denison, P., & Jones, F. R. (1992). An investigation of the surface chemistry of poly (ether etherketone). I. The effect of oxygen plasma treatment on surface structure. *Surface and interface analysis*, 18(1), 13-22.
- [207] Ameen, A. P. (1996). An investigation of the surface chemical homogeneity of plasma oxidised poly (ether etherketone). *Polymer degradation and stability*, 51(2), 179-184.
- [208] Short, R. D., Ameen, A. P., Jackson, S. T., Pawson, D. J., O'toole, L., & Ward, A. J. (1993). 1992 CR Burch prize TOF SIMS in polymer surface studies. *Vacuum*, 44(11-12), 1143-1160.
- [209] Henneuse-Boxus, C., Poleunis, C., De Ro, A., Adriaensen, Y., Bertrand, P., & Marchand - Brynaert, J. (1999). Surface functionalization of PEEK films studied by time - of - flight secondary ion mass spectrometry and x - ray photoelectron spectroscopy. *Surface and Interface Analysis: An International Journal devoted to the development and application of techniques for the analysis of surfaces, interfaces and thin films*, 27(3), 142-152.

References

[210] Seppala, J. E., & Migler, K. D. (2016). Infrared thermography of welding zones produced by polymer extrusion additive manufacturing. *Additive manufacturing*, 12, 71-76.

[211] Fried, J. R. (2014). *Polymer science and technology*. Pearson Education.

[212] Akay, M., & Ozden, S. (1994). Measurement of residual stresses in injection moulded thermoplastics. *Polymer Testing*, 13(4), 323-354.

[213] So, P., & Broutman, L. J. (1976). Residual stresses in polymers and their effect on mechanical behavior. *Polymer Engineering & Science*, 16(12), 785-791.

[214] Thompson, M., & White, J. R. (1984). The effect of a temperature gradient on residual stresses and distortion in injection moldings. *Polymer Engineering & Science*, 24(4), 227-241.

[215] Usamentiaga, R., Venegas, P., Guerediaga, J., Vega, L., Molleda, J., & Bulnes, F. G. (2014). Infrared thermography for temperature measurement and non-destructive testing. *Sensors*, 14(7), 12305-12348.

[216] https://www.perkinelmer.com/labsolutions/resources/docs/GDE_IntroductionToDMA.pdf, accessed on 28 Oct. 2019.

[217] https://www.perkinelmer.com/labsolutions/resources/docs/BRO_DMA8000.pdf, accessed on 28 Oct. 2019.

[218] <https://www.imakr.com/uk/peek-filaments-for-3d-printers> accessed on 03 June, 2020.

[219] https://www.victrex.com/~media/datasheets/victrex_tds_450g.pdf, accessed on 2 Nov 2019.

[220] <https://www.victrex.com/~media/datasheets/victrextds150g-151g.pdf>, accessed on 07 Oct, 2019.

[221] <https://www.concordiafibers.com/fiber-volume-fractions.html>, accessed on 05 Oct. 2019.

References

- [222] https://www.hexcel.com/user_area/content_media/raw/AS4C_Aerospace_HexTow_DataSheet.pdf, accessed on 07 Oct. 2019.
- [223] <https://www.concordiafibers.com/commingled-fibers.html>, accessed on 22 Jan, 2020.
- [224] <http://www.scbe.ntu.edu.sg/Research/Pages/Research-Facilities-and-Equipment4.aspx>, accessed on 22 Jan, 2020.
- [225] <https://netcomposites.com/guide/reinforcements/sizing-chemistry/> accessed on 21 April, 2020.
- [226] https://www.nikon.co.uk/en_GB/, accessed on 22 August, 2020.
- [227] <https://www.well.ox.ac.uk/files-library/niselements-v4-0-manual.pdf/@@download>, accessed on 09 Nov, 2019.
- [228] <https://www.hitachi.com/>, accessed on 22 August, 2020.
- [229] <https://all-guidesbox.com/model/hitachi/tm3030-plus.html>, accessed on 10 Nov, 2019.
- [230] <https://www.agarscientific.com/manual-sputter-coater>, accessed on 11 Nov, 2019.
- [231] <https://www.tainstruments.com/?s=Q600+SDT>, accessed on 07 Oct. 2019.
- [232] <https://www.tainstruments.com › universal-analysis-quickstart-course> ,accessed on 05 Nov, 2019
- [233] Czyżewski, J., Burzyński, P., Gawęł, K., & Meisner, J. (2009). Rapid prototyping of electrically conductive components using 3D printing technology. *Journal of Materials Processing Technology*, 209(12-13), 5281-5285.
- [234] Seo, J., Gohn, A. M., Dubin, O., Takahashi, H., Hasegawa, H., Sato, R., ... & Colby, R. H. (2019). Isothermal crystallization of poly (ether ether ketone)

References

with different molecular weights over a wide temperature range. *Polymer Crystallization*, 2(1), e10055.

[235] <https://www.tainstruments.com/dsc-2500/>, accessed on 10 Nov, 2019.

[236] http://www.tainstruments.com/pdf/NewFeaturesTRIOS_v4.1.pdf, accessed on 11 Nov, 2019.

[237] <https://reprap.org/wiki/RepRap>, accessed on 21 Oct. 2019.

[238] C. M. Ionescu, J. A. T. Machado and R. De Keyser, "Modeling of the Lung Impedance Using a Fractional-Order Ladder Network With Constant Phase Elements," in *IEEE Transactions on Biomedical Circuits and Systems*, vol. 5, no. 1, pp. 83-89, Feb. 2011.

[239] <https://forum.prusaprinters.org/forum/english-forum-general-discussion-announcements-and-releases/scars-on-prints-after-upgrade-to-mk2-5s/>, accessed on 24 Feb 2020.

[240] Incropera, F. P., Lavine, A. S., Bergman, T. L., & DeWitt, D. P. (2007). *Fundamentals of heat and mass transfer*. Wiley.

[241] <https://github.com/BCN3D/BCN3DPlusandR-Manuals>. Accessed on 18, Nov 2019.

[242] Chen, H. T., & Hsu, W. L. (2008). Estimation of heat-transfer characteristics on a vertical annular circular fin of finned-tube heat exchangers in forced convection. *International journal of heat and mass transfer*, 51(7-8), 1920-1932.

[243] Bergman, T. L., Incropera, F. P., Lavine, A. S., & DeWitt, D. P. (2011). *Introduction to heat transfer*. John Wiley & Sons.

[244] https://www.testequipmentdepot.com/flir/pdf/t400-series_manual.pdf. Accessed on 18 Nov 2019.

References

[245] Ianiro, A., & Cardone, G. (2010). Measurement of surface temperature and emissivity with stereo dual-wavelength IR thermography. *Journal of Modern Optics*, 57(18), 1708-1715.

[246] <https://3dprinting.co.uk/polyjet-3d-printers/>, accessed on 12 Nov 2019

[247] Derek, H. (1981). *An introduction to composite materials*. Cambridge University Press.

[248] Clyne, T. W., & Hull, D. (2019). *An introduction to composite materials*. Cambridge university press.

[249] White, F. M. (1999). *Fluid mechanics*. McGraw-hill.

[250] Rzatki, F. D., Barboza, D. V. D., Schroeder, R. M., de Oliveira Barra, G. M., Binder, C., Klein, A. N., & De Mello, J. D. B. (2015). Effect of temperature and atmosphere on the tribological behavior of a polyether ether ketone composite. *Friction*, 3(4), 259-265.

[251] Goodno, B.J., & Gere. J.M., *Mechanics of materials*. 9th Ed., SI / James M. Gere, Barry J. Goodno. ed. Boston, Mass., 2018. Print.

[252] <https://store.arduino.cc/arduino-mega-2560-rev3> , accessed on 20 Nov 2019.

[253] Winistorfer, P. M., Moschler, W. W., Wang, S., DePaula, E., & Bledsoe, B. L. (2007). Fundamentals of vertical density profile formation in wood composites. Part I. In-situ density measurement of the consolidation process. *Wood and fiber science*, 32(2), 209-219.

[254] <https://www.struers.com/en>, accessed on 25 August, 2020.

[255] <https://www.buehler.co.uk/>, accessed on 25 August, 2020.

[256] Trindade, G. F., Abel, M. L., Lowe, C., Tshulu, R., & Watts, J. F. (2018). A Time-of-Flight Secondary Ion Mass Spectrometry/Multivariate Analysis (ToF-SIMS/MVA) Approach To Identify Phase Segregation in Blends of Incompatible but Extremely Similar Resins. *Analytical chemistry*, 90(6), 3936-3941.

References

[257] Trindade, G. F., Abel, M. L., & Watts, J. F. (2018). simsMVA: A tool for multivariate analysis of ToF-SIMS datasets. *Chemometrics and Intelligent Laboratory Systems*, 182, 180-187.

[258] <https://en.wikipedia.org/wiki/ImageJ>, accessed on 29 Nov, 2019.

[259] <https://imagej.nih.gov/ij/docs/menus/analyze.html>, accessed on 3 Dec 2019.

[260] <https://en.wikipedia.org/wiki/GIMP>, accessed on 29 Nov, 2019.

[261] Ghiorse, S. R. (1991). A comparison of void measurement methods for carbon/epoxy composites (No. MTL-TR-91-13). ARMY LAB COMMAND WATERTOWN MA MATERIAL TECHNOLOGY LAB.

[262] https://en.wikipedia.org/wiki/Archimedes%27_principle, accessed on 17 March 2020

[263] Nguyen, H. X., & Ishida, H. (1986). Molecular analysis of the melting behaviour of poly (aryl-ether-ether-ketone). *Polymer*, 27(9), 1400-1405.

[264] McIlroy, C., & Graham, R. S. (2018). Modelling flow-enhanced crystallisation during fused filament fabrication of semi-crystalline polymer melts. *Additive Manufacturing*, 24, 323-340.

[265] Geng, P., Zhao, J., Wu, W., Ye, W., Wang, Y., Wang, S., & Zhang, S. (2019). Effects of extrusion speed and printing speed on the 3D printing stability of extruded PEEK filament. *Journal of Manufacturing Processes*, 37, 266-273.

[266] <https://www.repetier.com/>, accessed on 28 August, 2020.

[267] <https://rigid.ink/blogs/news/3d-printed-raft-brim-skirt>, accessed on 03 March 2020.

[268] <https://www.flir.co.uk/support/products/sc6700#Overview>, accessed on 28 August, 2020.

[269] <https://www.flir.com/>, accessed on 28 August, 2020.

References

- [270] F. Systems, FLIR VideoReport User as manual, FLIR Systems, 2009. URL: <https://www.flir.com>.
- [271] Shaw, M. T., & MacKnight, W. J. (2018). Introduction to polymer viscoelasticity. John Wiley & Sons.
- [272] Martineau, L., Chabert, F., Bernhart, G., & Djilali, T. (2016, June). Mechanical behavior of amorphous PEEK in the rubbery state
- [273] Capote, G. A. M., Rudolph, N. M., Osswald, P. V., & Osswald, T. A. (2019). Failure surface development for ABS fused filament fabrication parts. *Additive Manufacturing*, 28, 169-175.
- [274] https://www.gimitec.com//file/010612_01_app_practical_specific_heat_determination_by_dual_furnace_dsc.pdf. Accessed on 11 Feb 2020.
- [275] Nielsen, L. E. (1974). The thermal and electrical conductivity of two-phase systems. *Industrial & Engineering chemistry fundamentals*, 13(1), 17-20.
- [276] Progelhof, R. C., Throne, J. L., & Ruetsch, R. R. (1976). Methods for predicting the thermal conductivity of composite systems: a review. *Polymer Engineering & Science*, 16(9), 615-625.
- [277] Kim, S. R., Kim, D. H., Kim, D. J., Kim, M. H., & Park, J. M. (2007). Study on thermal conductivity of polyetheretherketone/thermally conductive filler composites. In *Solid state phenomena* (Vol. 124, pp. 1079-1082). Trans Tech Publications Ltd.
- [278] White, F. M. (2010). Fluid mechanics.
- [279] Stewart, J. (2006). Calculus. Thomson Brooks/Cole.
- [280] <https://www.quora.com/What-is-the-volume-of-a-paraboloid>, accessed on 31 March, 2020.
- [281] Pu, J., McIlroy, C., Jones, A., & Ashcroft, I. (2021). Understanding mechanical properties in fused filament fabrication of polyether ether ketone. *Additive Manufacturing*, 37, 101673.

References

[282] Turner, B. N., Strong, R., & Gold, S. A. (2014). A review of melt extrusion additive manufacturing processes: I. Process design and modeling. *Rapid Prototyping Journal*.

[283] <https://www.additivemanufacturing.media/articles/the-link-between-3d-printing-surface-finish-and-mold-tools>, accessed on 12 March 2021.



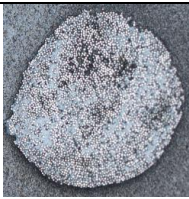


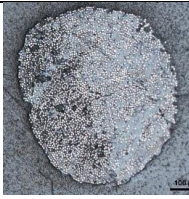
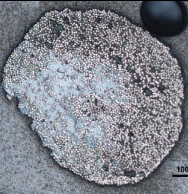



[284] Shanmugam, V., Johnson, D. J., Babu, K., Rajendran, S., Veerasimman, A., Marimuthu, U., Singh, S., Das, O., Neisiany, R., Hedenqvist, M., Berto, F. & Ramakrishna, S. (2020). The mechanical testing and performance analysis of polymer-fibre composites prepared through the additive manufacturing. *Polymer Testing*, 106925.

[285] Kumlutas, D., & Tavman, I. H. (2006). A numerical and experimental study on thermal conductivity of particle filled polymer composites. *Journal of thermoplastic composite materials*, 19(4), 441-455.

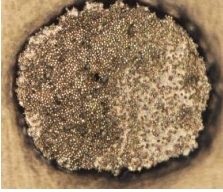
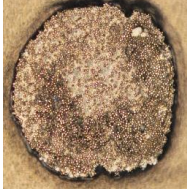
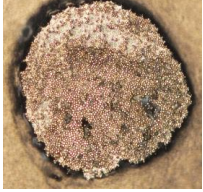



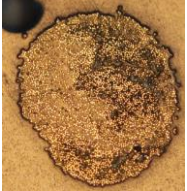

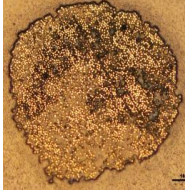
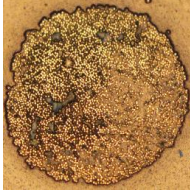

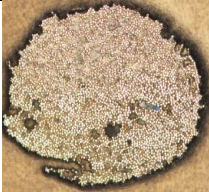


Appendix A

Cross Sectional Images of CF/PEEK Filament

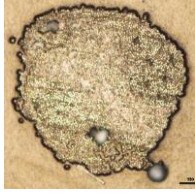


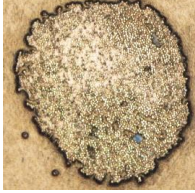
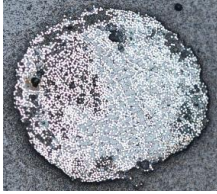


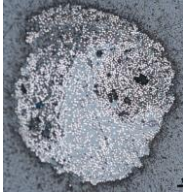
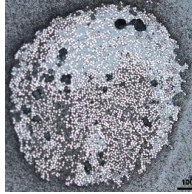
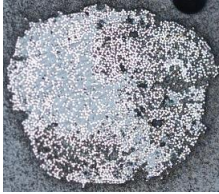
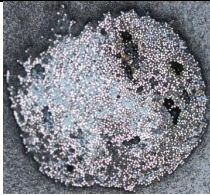
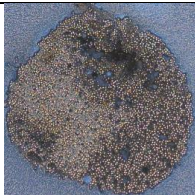
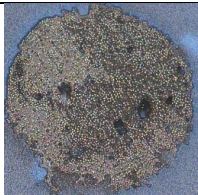
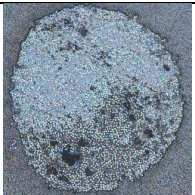
Table A.1: Cross-sectional images under each condition

| | | | |
|-------------|---|--|---|
| 0.5 mm/s | Sample 1 | Sample 2 | Sample 3 |
| 350°C |  |  |  |
| | Sample 4 | Sample 5 | Sample 6 |
| |  |  |  |
| | Sample 7 | | |
| |  | | |
| 0.5 mm/s | Sample 1 | Sample 2 | Sample 3 |
| 360°C |  |  |  |
| | Sample 4 | Sample 5 | Sample 6 |

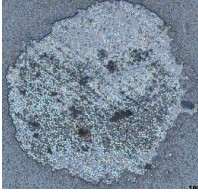


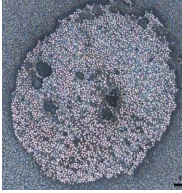

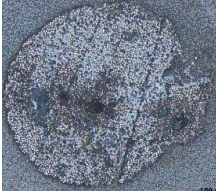

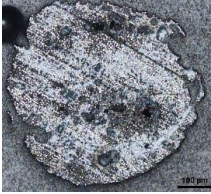


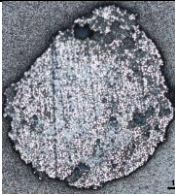
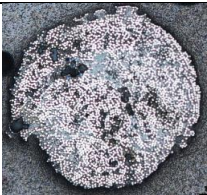
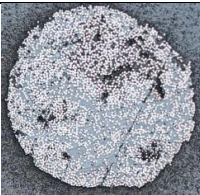

Appendix A Cross Sectional Images of CF/PEEK Filament

| | | | |
|-------------|---|--|---|
| |  |  |  |
| | Sample 7 | | |
| |  | | |
| 0.5 mm/s | Sample 1 | Sample 2 | Sample 3 |
| 370°C |  |  |  |
| | Sample 4 | Sample 5 | Sample 6 |
| |  |  |  |
| | Sample 7 | | |
| |  | | |
| 0.5 mm/s | Sample 1 | Sample 2 | Sample 3 |
| 380°C |  |  |  |
| | Sample 4 | Sample 5 | Sample 6 |





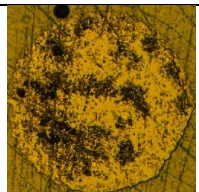
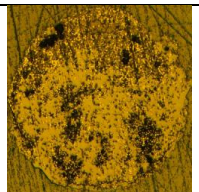
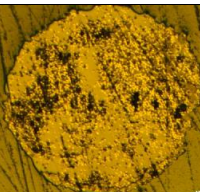
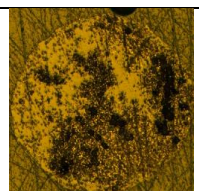
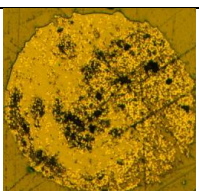
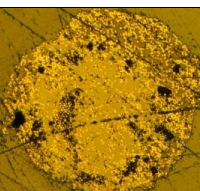
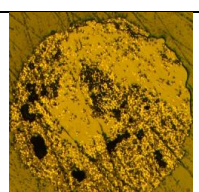
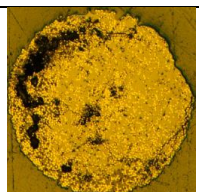
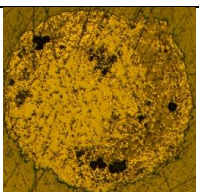
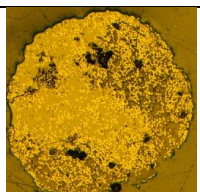
Appendix A Cross Sectional Images of CF/PEEK Filament

| | | | |
|-------------|---|--|---|
| |  |  |  |
| | Sample 7 | | |
| |  | | |
| 0.5 mm/s | Sample 1 | Sample 2 | Sample 3 |
| 390°C |  |  |  |
| | Sample 4 | Sample 5 | Sample 6 |
| |  |  |  |
| | Sample 7 | | |
| |  | | |
| 0.5 mm/s | Sample 1 | Sample 2 | Sample 3 |
| 400°C |  |  |  |
| | Sample 4 | Sample 5 | Sample 6 |

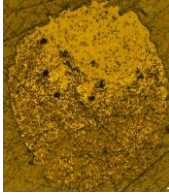
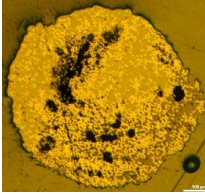
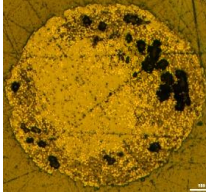
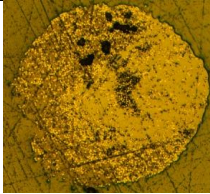
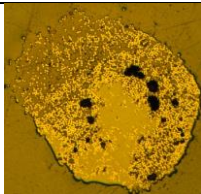
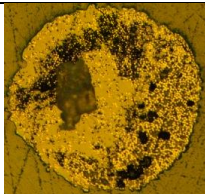
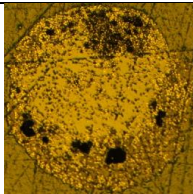
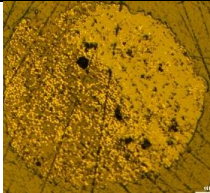
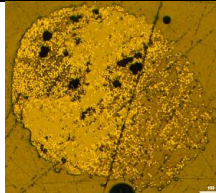
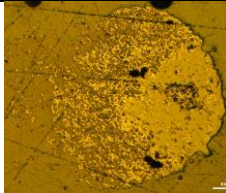
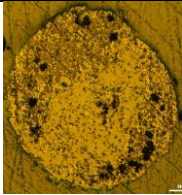
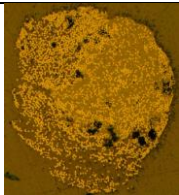
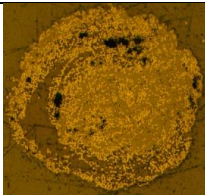
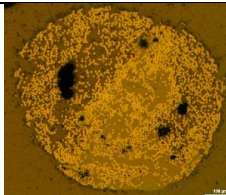
Appendix A Cross Sectional Images of CF/PEEK Filament

| | | | |
|-------------|---|--|---|
| |  |  |  |
| | Sample 7 | | |
| |  | | |
| 0.5 mm/s | Sample 1 | Sample 2 | Sample 3 |
| 410°C |  |  |  |
| | Sample 4 | Sample 5 | Sample 6 |
| |  |  |  |
| | Sample 7 | | |
| |  | | |
| 0.5 mm/s | Sample 1 | Sample 2 | Sample 3 |
| 420°C |  |  |  |
| | Sample 4 | Sample 5 | Sample 6 |

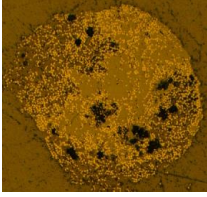
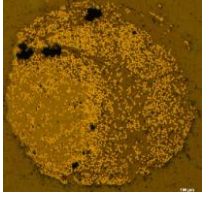
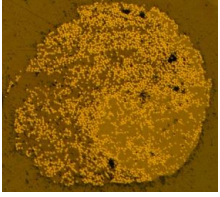
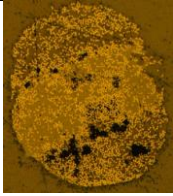
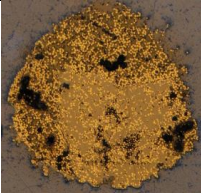
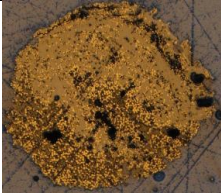
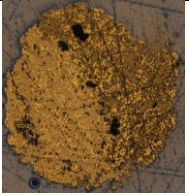
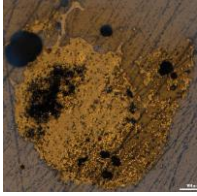
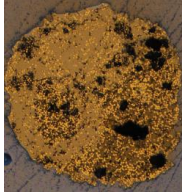
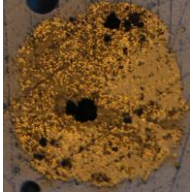
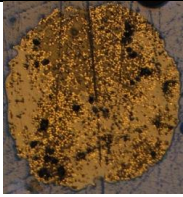
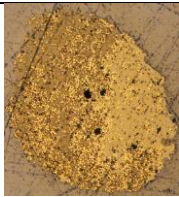
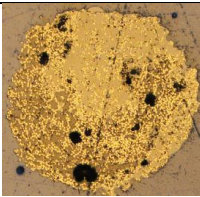
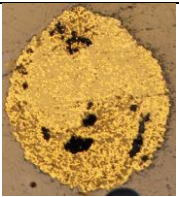
Appendix A Cross Sectional Images of CF/PEEK Filament

| | | | |
|-----------|---|--|---|
| |  |  |  |
| | Sample 7 | | |
| |  | | |
| 1 mm/s | Sample 1 | Sample 2 | Sample 3 |
| 350°C |  |  |  |
| | Sampe 4 | Sample 5 | Sample 6 |
| |  |  |  |
| | Sample 7 | | |
| |  | | |
| 1 mm/s | Sample 1 | Sample 2 | Sample 3 |
| 360°C |  |  |  |
| | Sample 4 | Sample 5 | Sample 6 |

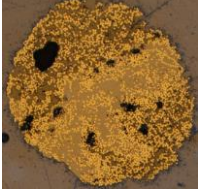
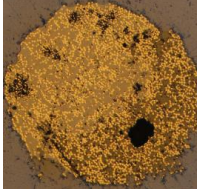
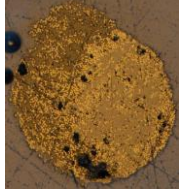
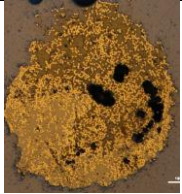
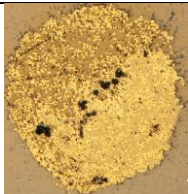
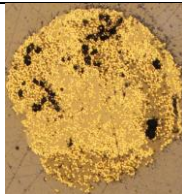

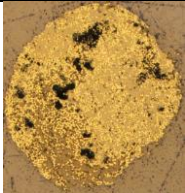
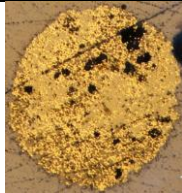
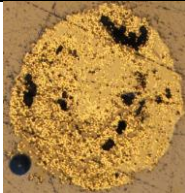
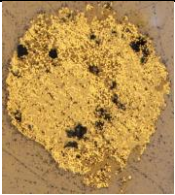
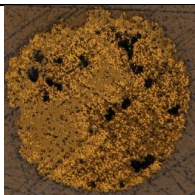
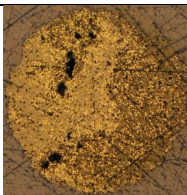
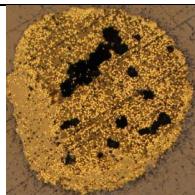
Appendix A Cross Sectional Images of CF/PEEK Filament

| | | | |
|-----------|---|--|---|
| |  |  |  |
| | Sample 7 | | |
| |  | | |
| 1 mm/s | Sample 1 | Sample 2 | Sample 3 |
| 370°C |  |  |  |
| | Sample 4 | Sample 5 | Sample 6 |
| |  |  |  |
| | Sample 7 | | |
| |  | | |
| 1 mm/s | Sample 1 | Sample 2 | Sample 3 |
| 380°C |  |  |  |
| | Sample 4 | Sample 5 | Sample 6 |

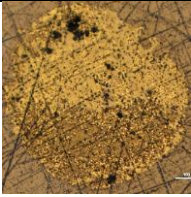
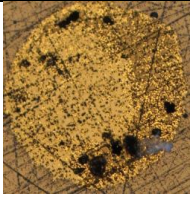
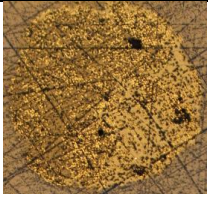
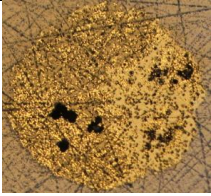
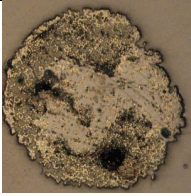
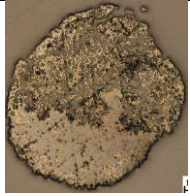
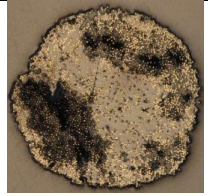
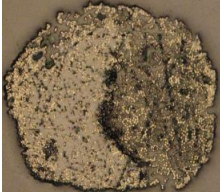
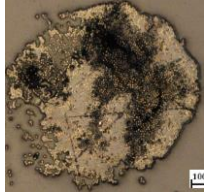

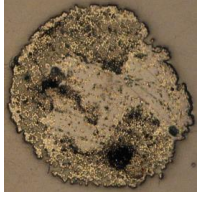
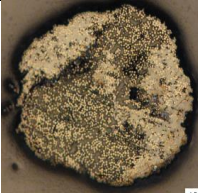

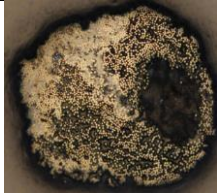
Appendix A Cross Sectional Images of CF/PEEK Filament

| | | | |
|-----------|---|--|---|
| |  |  |  |
| | Sample 7 | | |
| |  | | |
| 1 mm/s | Sample 1 | Sample 2 | Sample 3 |
| 390°C |  |  |  |
| | Sample 4 | Sample 5 | Sample 6 |
| |  |  |  |
| | Sample 7 | | |
| |  | | |
| 1 mm/s | Sample 1 | Sample 2 | Sample 3 |
| 400°C |  |  |  |
| | Sample 4 | Sample 5 | Sample 6 |

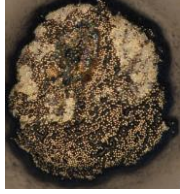
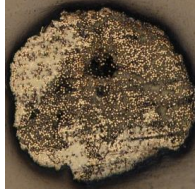
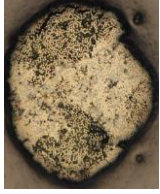
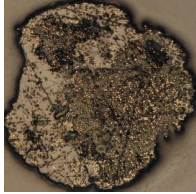
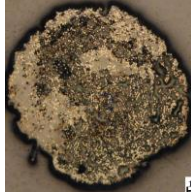
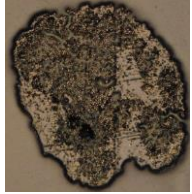
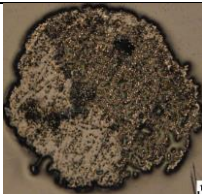
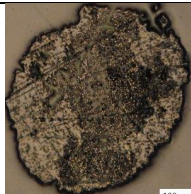
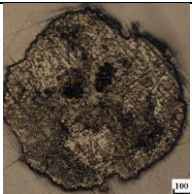
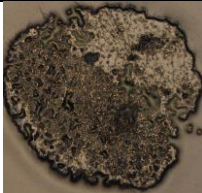
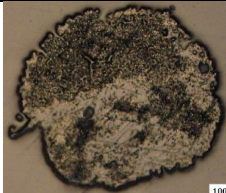
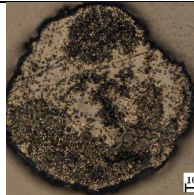
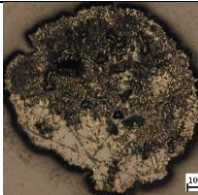

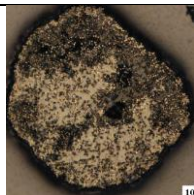
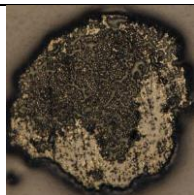
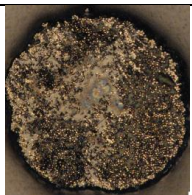
Appendix A Cross Sectional Images of CF/PEEK Filament

| | | | |
|-----------|---|--|---|
| |  |  |  |
| | Sample 7 | | |
| |  | | |
| 1 mm/s | Sample 1 | Sample 2 | Sample 3 |
| 410°C |  |  |  |
| | Sample 4 | Sample 5 | Sample 6 |
| |  |  |  |
| | Sample 7 | | |
| |  | | |
| 1 mm/s | Sample 1 | Sample 2 | Sample 3 |
| 420°C |  |  |  |
| | Sample 4 | Sample 5 | Sample 6 |

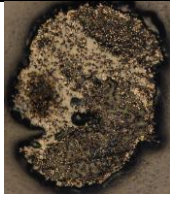
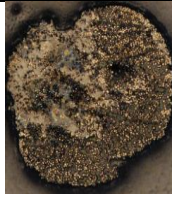
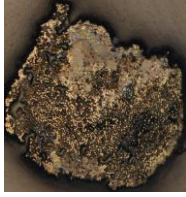
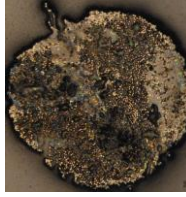
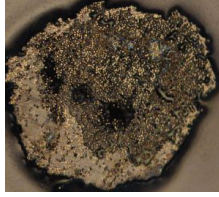
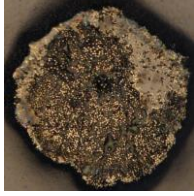


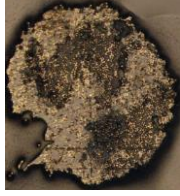




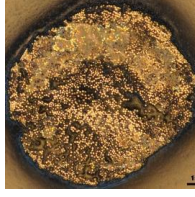

Appendix A Cross Sectional Images of CF/PEEK Filament

| | | | |
|-----------|---|--|---|
| |  |  |  |
| | Sample 7 | | |
| |  | | |
| 3 mm/s | Sample 1 | Sample 2 | Sample 3 |
| 350°C |  |  |  |
| | Sample 4 | Sample 5 | Sample 6 |
| |  |  |  |
| | Sample 7 | | |
| |  | | |
| 3 mm/s | Sample 1 | Sample 2 | Sample 3 |
| 360°C |  |  |  |
| | Sample 4 | Sample 5 | Sample 6 |


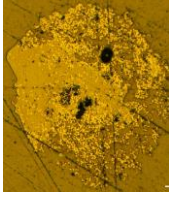
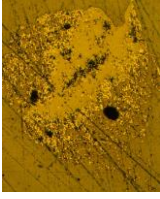
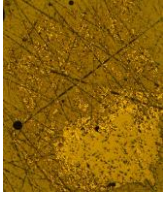
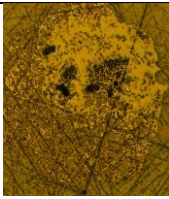
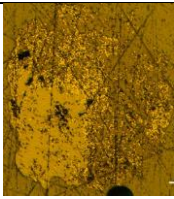
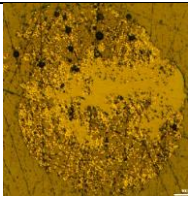
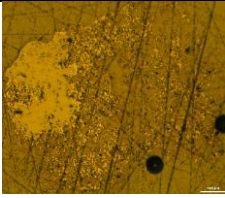
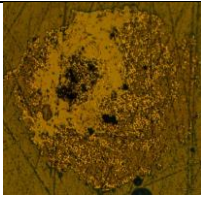
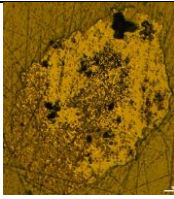
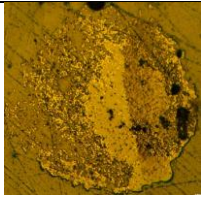
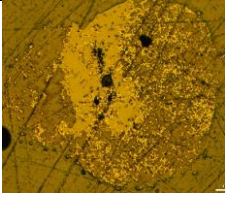
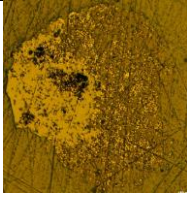
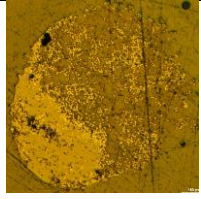
Appendix A Cross Sectional Images of CF/PEEK Filament

| | | | |
|-----------|---|--|---|
| |  |  |  |
| 3 mm/s | Sample 1 | Sample 2 | Sample 3 |
| 370°C |  |  |  |
| | Sample 4 | Sample 5 | Sample 6 |
| |  |  |  |
| | Sample 7 | Sample 8 | |
| |  |  | |
| 3 mm/s | Sample 1 | Sample 2 | Sample 3 |
| 380°C |  |  |  |
| | Sample 4 | Sample 5 | Sample 6 |
| |  |  |  |
| | Sample 7 | Sample 8 | |

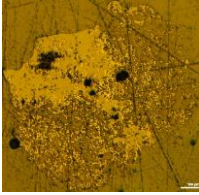
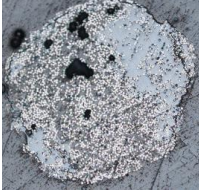
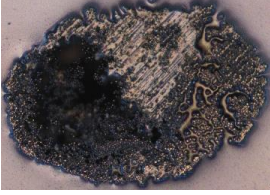
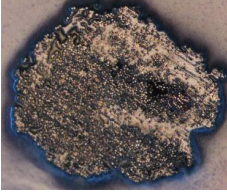
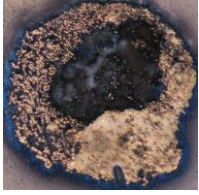
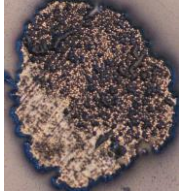
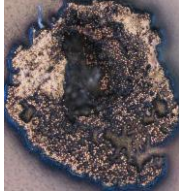
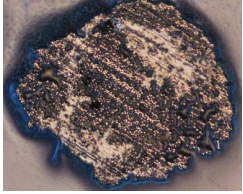
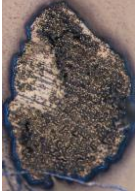
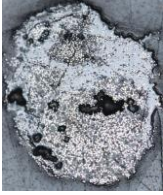
Appendix A Cross Sectional Images of CF/PEEK Filament

| | | | |
|-----------|---|--|---|
| |  |  | |
| 3 mm/s | Sample 1 | Sample 2 | Sample 3 |
| 390°C |  |  |  |
| | Sample 4 | Sample 5 | Sample 6 |
| |  |  |  |
| | Sample 7 | | |
| |  | | |
| 3 mm/s | Sample 1 | Sample 2 | Sample 3 |
| 400°C |  |  |  |
| | Sample 4 | Sample 5 | Sample 6 |
| |  |  |  |
| | Sample 7 | | |

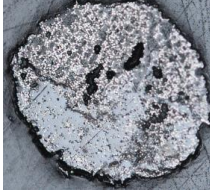
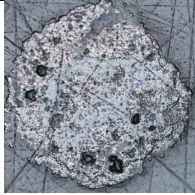
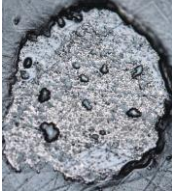
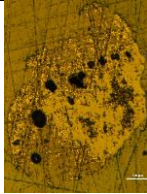
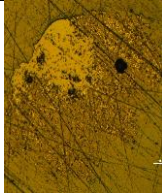
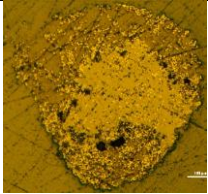
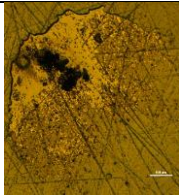
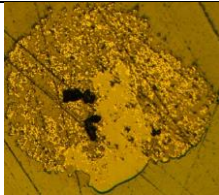
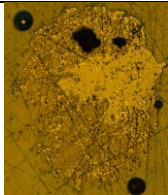
Appendix A Cross Sectional Images of CF/PEEK Filament

| | | | |
|-----------|---|--|---|
| |  | | |
| 3 mm/s | Sample 1 | Sample 2 | Sample 3 |
| 410°C |  |  |  |
| | Sample 4 | Sample 5 | Sample 6 |
| |  |  |  |
| | Sample 7 | | |
| |  | | |
| 3 mm/s | Sample 1 | Sample 2 | Sample 3 |
| 420°C |  |  |  |
| | Sample 4 | Sample 5 | Sample 6 |
| |  |  |  |
| | Sample 7 | | |

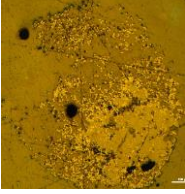
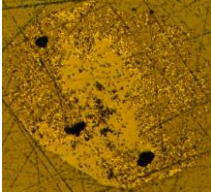
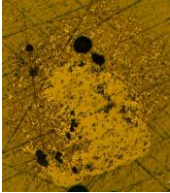

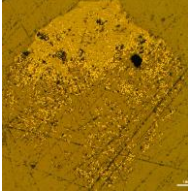
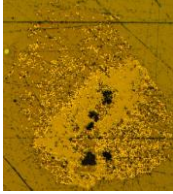
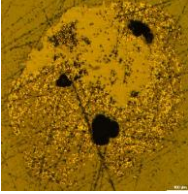
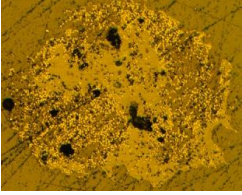
Appendix A Cross Sectional Images of CF/PEEK Filament

| | | | |
|--------|---|--|---|
| |  | | |
| 5 mm/s | Sample 1 | | |
| 350°C |  | | |
| 5 mm/s | Sample 1 | Sample 2 | Sample 3 |
| 360°C |  |  |  |
| | Sample 4 | Sample 5 | Sample 6 |
| |  |  |  |
| | Sample 7 | | |
| |  | | |
| 5 mm/s | Sample 1 | | |
| 370°C |  | | |

Appendix A Cross Sectional Images of CF/PEEK Filament

| | | | |
|-----------|---|--|---|
| 5 mm/s | Sample 1 | | |
| 380°C |  | | |
| 5 mm/s | Sample 1 | | |
| 390°C |  | | |
| 5 mm/s | Sample 1 | | |
| 400°C |  | | |
| 5 mm/s | Sample 1 | Sample 2 | Sample 3 |
| 410°C |  |  |  |
| | Sample 4 | Sample 5 | Sample 6 |
| |  |  |  |
| | Sample 7 | | |

Appendix A Cross Sectional Images of CF/PEEK Filament

| | | | |
|-----------|---|--|---|
| |  | | |
| 5 mm/s | Sample 1 | Sample 2 | Sample 3 |
| 420°C |  |  |  |
| | Sample 4 | Sample 5 | Sample 6 |
| |  |  |  |
| | Sample 7 | | |
| |  | | |

Appendix B

A Numerical Model Theory of Crystal Growth

B.1 Overview

The model is introduced based on the work of McIlroy *et al* [264]. In line with the hypothesis, a model is developed to predict the crystallisation kinetics of a singly-deposited filament of PEEK under typical printing conditions, based on the Schneider rate equations. Since the process is non-isothermal, the spatial variations are accounted for in the temperature evolution via the axisymmetric heat equation, together with a boundary condition informed by the IR-imaging measurements.

In particular, the predictions are made of the final crystal fraction at the centre of a deposited filament, ϕ_f , and at the surface of a deposited filament, ϕ_w , which corresponds to a weld region within a fully constructed wall. These predictions of crystallinity are related to the storage moduli in the filament and in the weld, denoted E_f and E_w , respectively, via the composite solid theory of Halpin & Kardos *et al* [160].

In order to compare the DMA measurements to the crystallisation model we must relate E_f and E_w to the sample-averaged measurements E_{par} and E_{perp} . By considering the stiffness of heterogeneous structures, it can be formed as:

$$\frac{1}{E_{perp}} = \frac{1}{z} \left(\frac{z-z_w}{E_f} + \frac{z_w}{E_w} \right), \quad (\text{B.1})$$

and

$$E_{par} = \frac{1}{z} (E_f(z - z_w) + E_w z_w), \quad (\text{B.2})$$

where z is the height of a single filament and z_w is the height of a single weld region. Note that since the samples are single-filament walls, the porosity here is neglected. Also, Eqs (D.1) and (D.2) highlight how variations in z_w along the print direction may lead to significant deviations within a sample.

B.2 Modelling Quiescent Crystallisation

This model considers the homogeneous growth of spherulitic structures via the Schneider rate equations. To account for space filling, the Avrami equation is employed. The Schneider rate equations are solved via Euler's method with a non-isothermal temperature evolution measured via IR-imaging measurement. The temperature dependence of the crystal growth and nucleation rates are informed by experimental measurements found in the literature [9].

B.3 Modelling Temperature Profile

The IR-imaging technique discussed in Chapter 6, Section 6.3.1 provides a surface measurement of the filament temperature. Whilst this is sufficient to make predictions for the crystallisation kinetics in the weld region, understanding properties within the filament requires knowledge of the temperature evolution at the filament centre. The axisymmetric heat equation is employed to make a prediction of the temperature evolution at the filament centre. In this way, the temperature evolution profile at the centre of the filament is obtained. This temperature profile can then be employed in the Schneider rate equations to make predictions of the degree of space filling at the filament centre and consequently the properties originating from the filament core (E_f). Note that the temperature profile at the weld is provided directly by the IR-imaging measurement, whereas the temperature at the centre of the filament is obtained from the calculation described above.

Appendix C

IR-Imaging Measurement Results

C.1 Temperature profile loaded with PEEK

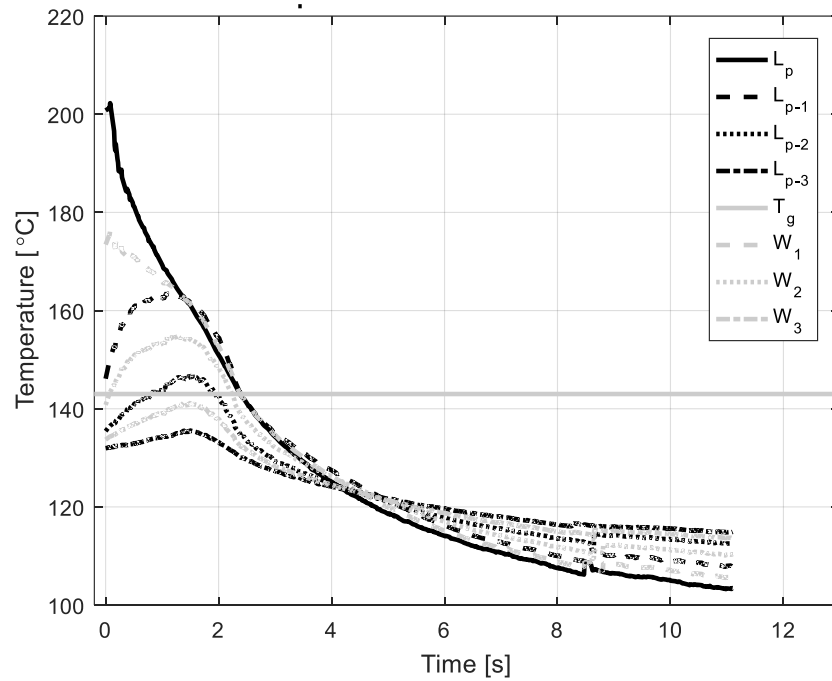


Figure C.1: Temperature profile of loaded PEEK at 3 mm/s 390°C

Appendix C IR-Imaging Measurement Results

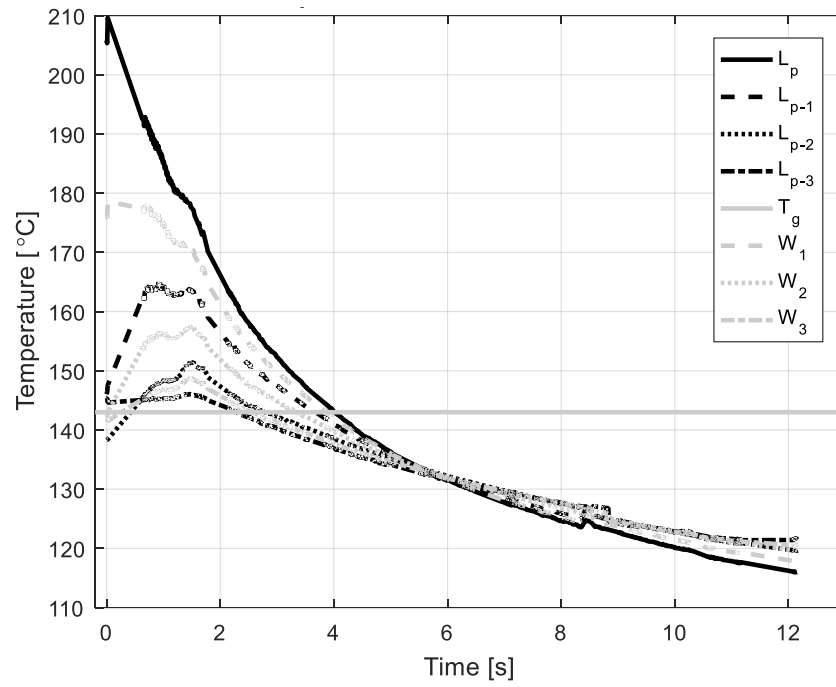


Figure C.2: Temperature profile of loaded PEEK at 3 mm/s 400°C

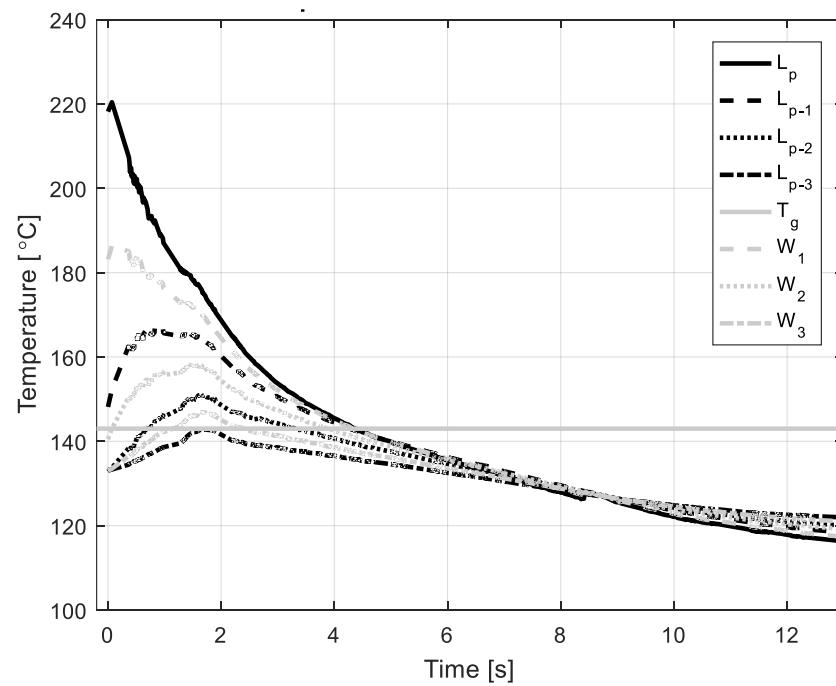


Figure C.3: Temperature profile of loaded PEEK at 3 mm/s 410°C

Appendix C IR-Imaging Measurement Results

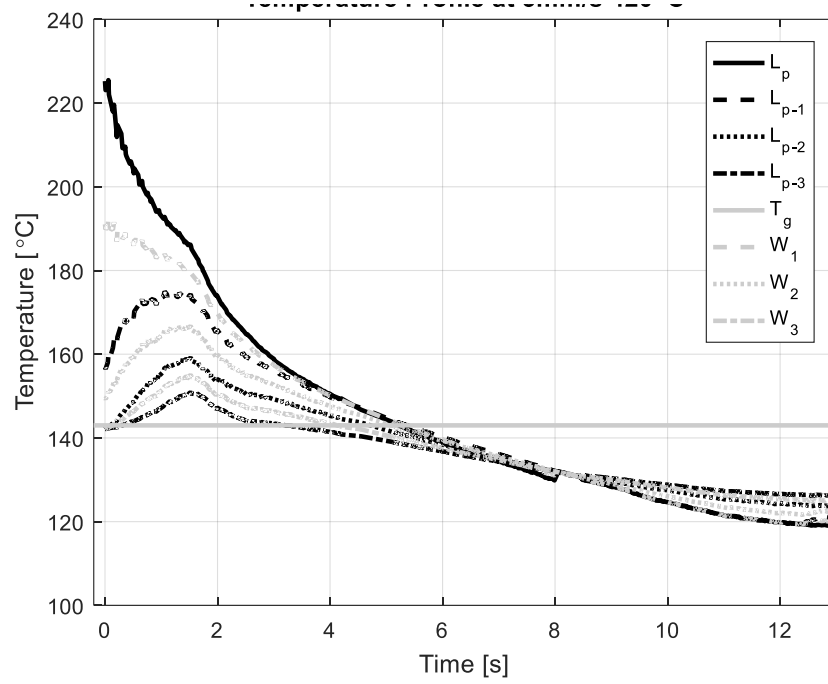


Figure C.4: Temperature profile of loaded PEEK at 3 mm/s 420°C

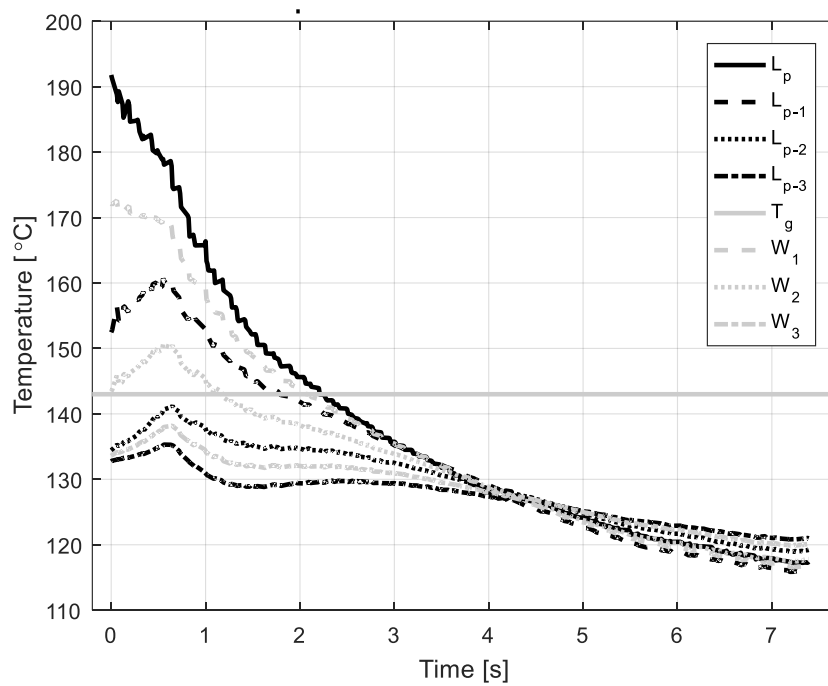


Figure C.5: Temperature profile of loaded PEEK at 6 mm/s 390°C

Appendix C IR-Imaging Measurement Results

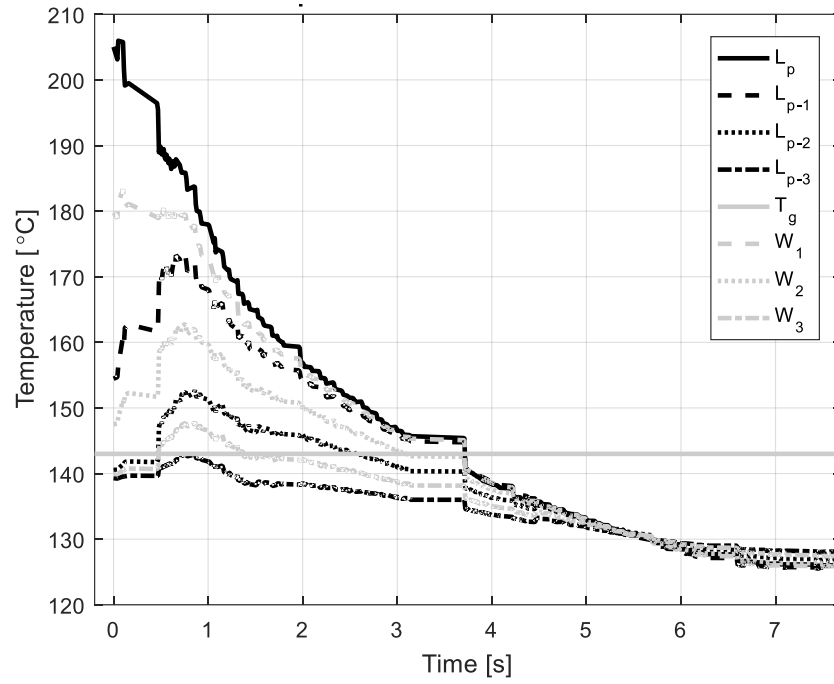


Figure C.6: Temperature profile of loaded PEEK at 6 mm/s 400°C

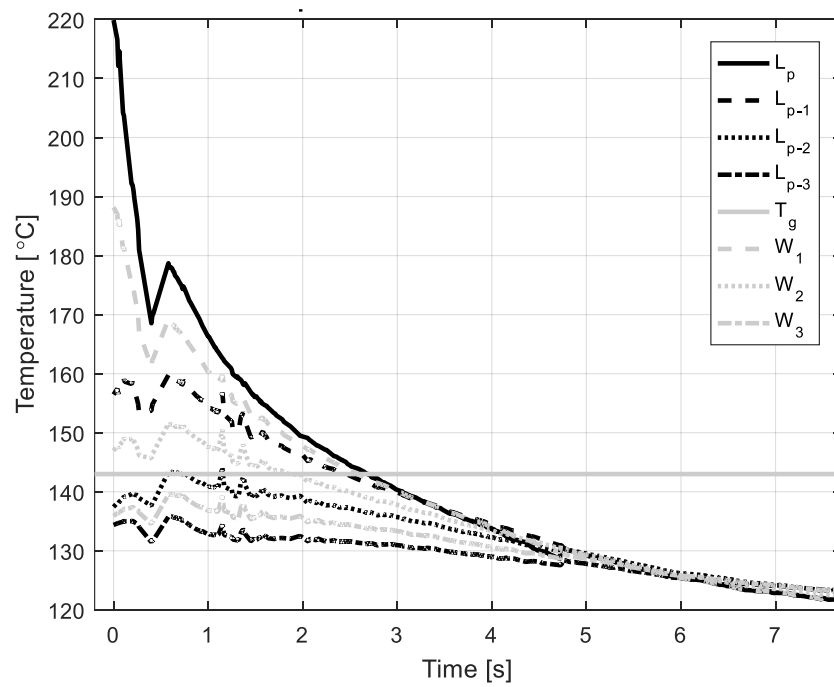


Figure C.7: Temperature profile of loaded PEEK at 6 mm/s 410°C

Appendix C IR-Imaging Measurement Results

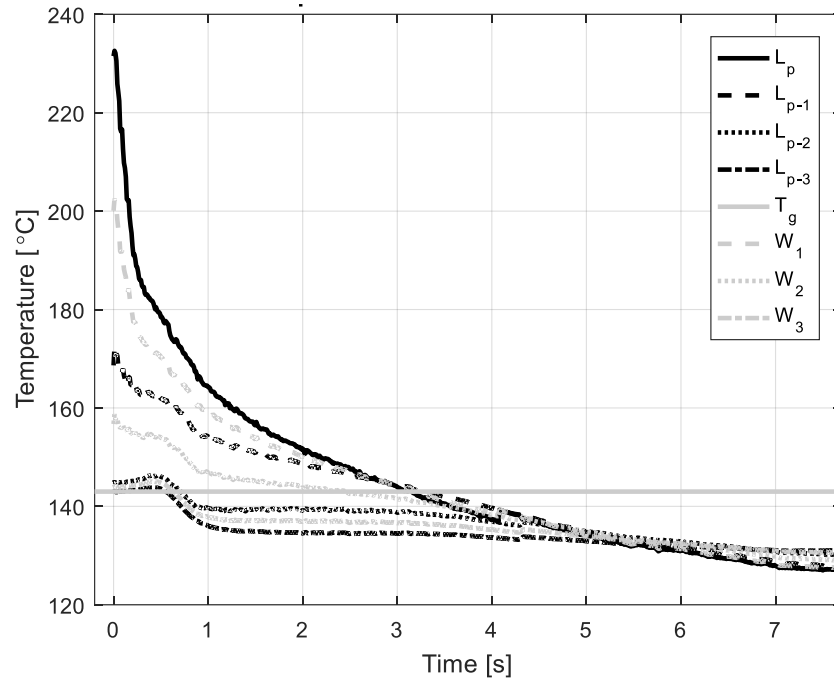


Figure C.8: Temperature profile of loaded PEEK at 6 mm/s 420°C

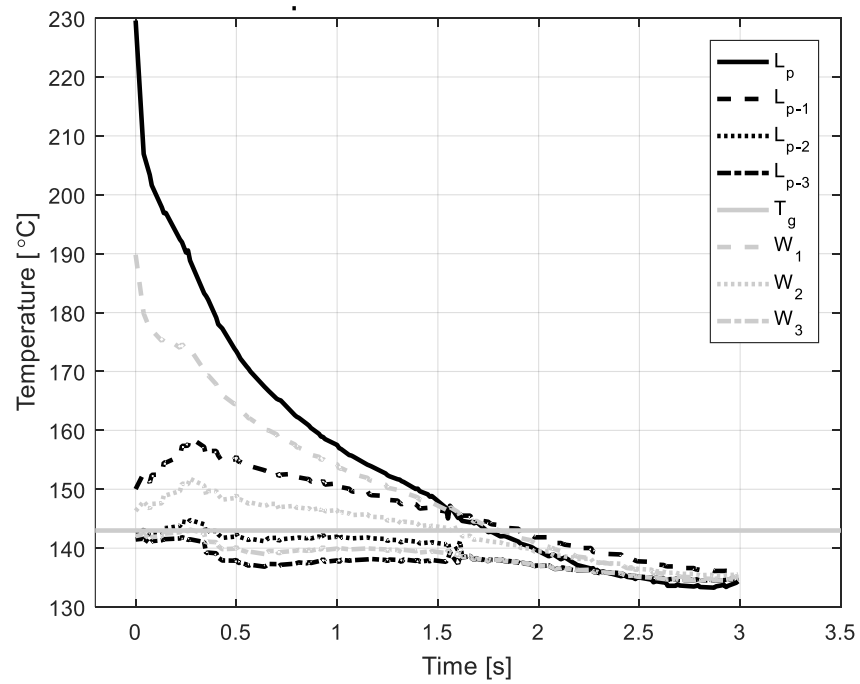


Figure C.9: Temperature profile of loaded PEEK at 18 mm/s 400°C

Appendix C IR-Imaging Measurement Results

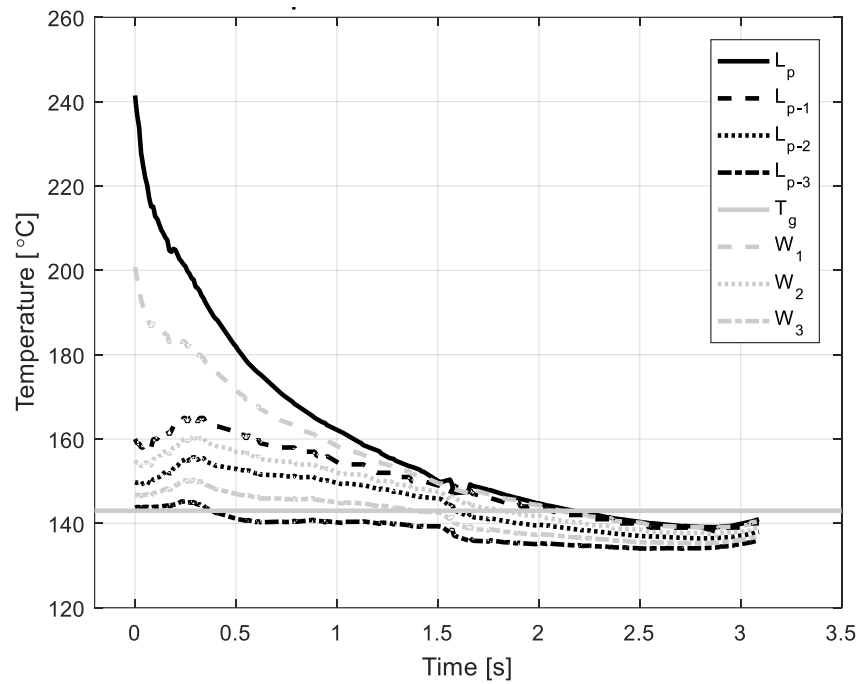


Figure C.10: Temperature profile of loaded PEEK at 18 mm/s 410°C

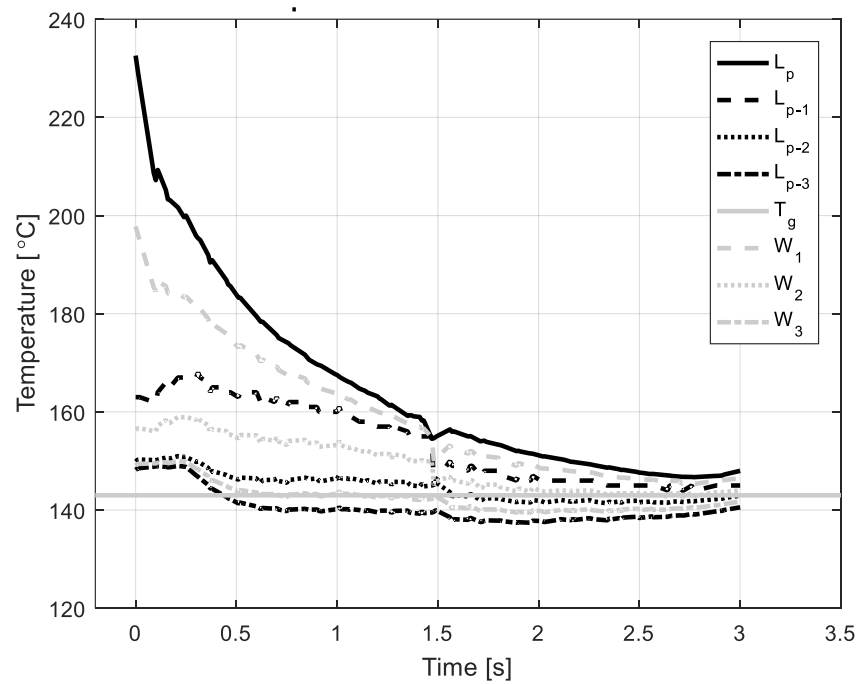


Figure C.11: Temperature profile of loaded PEEK at 18 mm/s 420°C

C.2 Temperature profile without load

Appendix C IR-Imaging Measurement Results

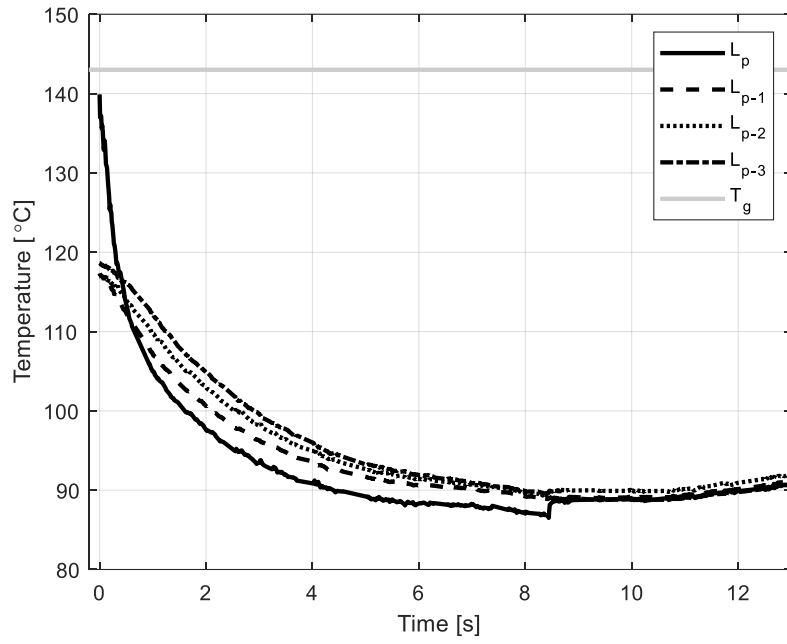


Figure C.12: Temperature profile without loaded PEEK at 3 mm/s 390°C

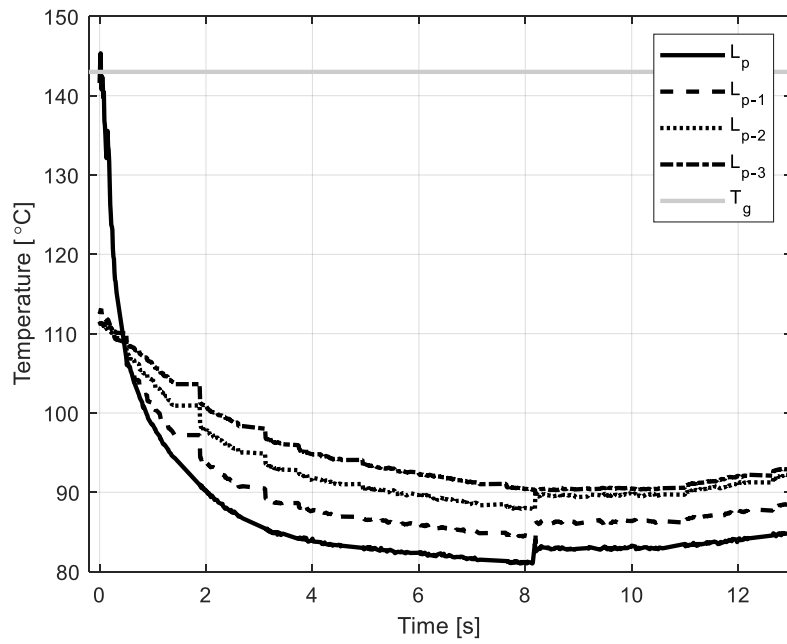


Figure C.13: Temperature profile without loaded PEEK at 3 mm/s 400°C

Appendix C IR-Imaging Measurement Results

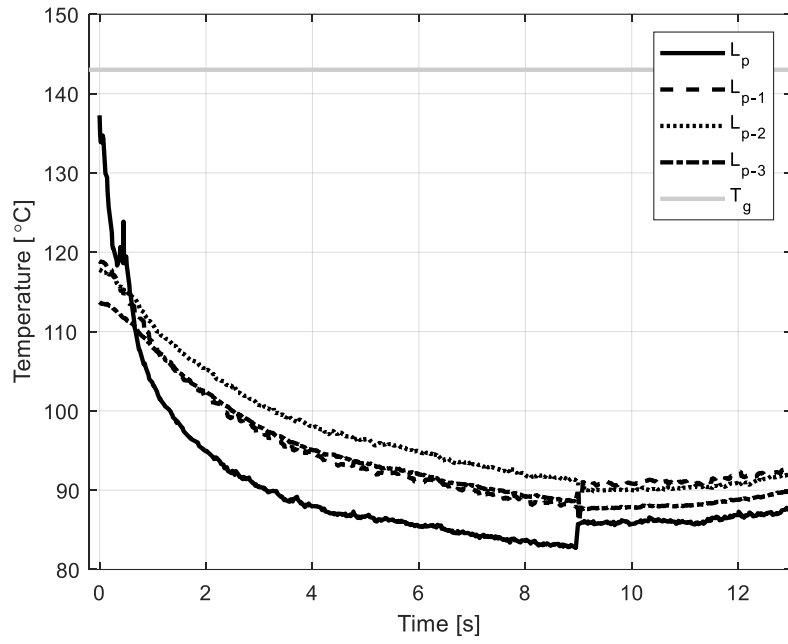


Figure C.14: Temperature profile without loaded PEEK at 3 mm/s 410°C

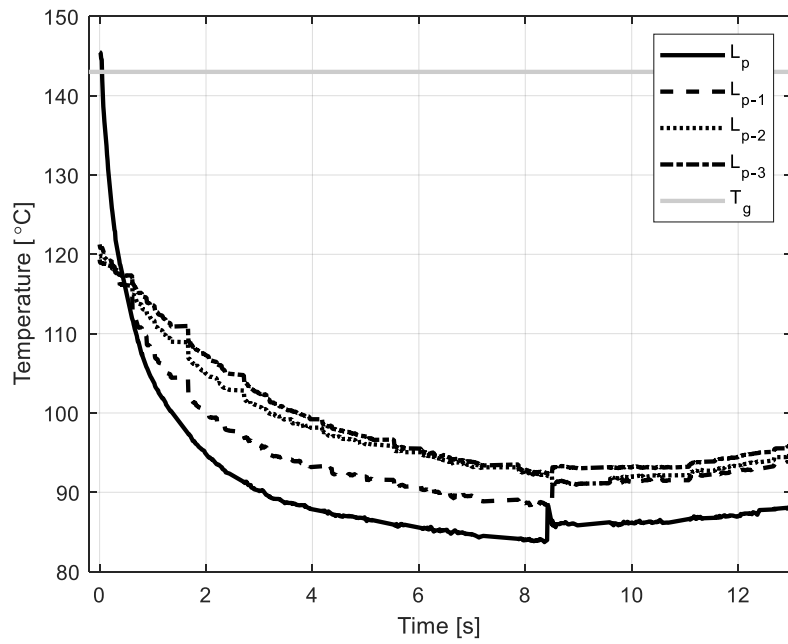


Figure C.15: Temperature profile without loaded PEEK at 3 mm/s 420°C

Appendix C IR-Imaging Measurement Results

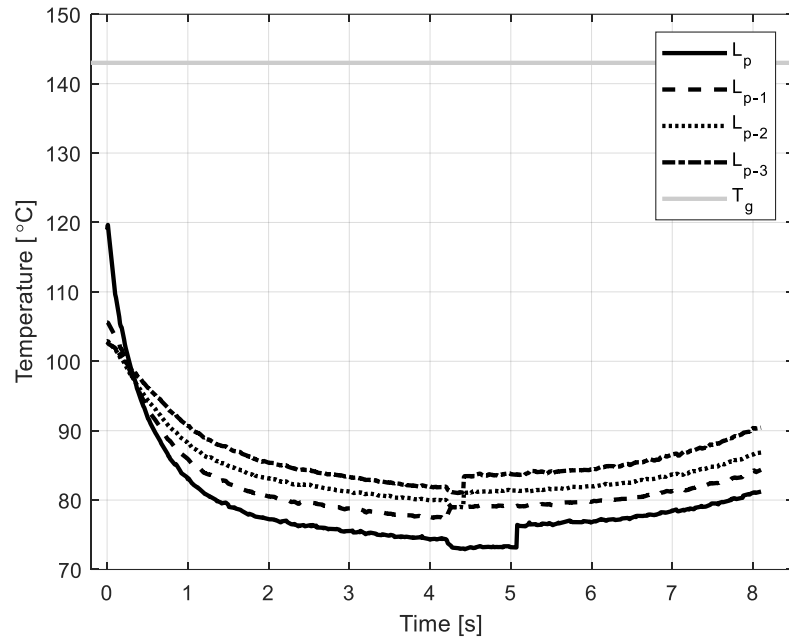


Figure C.16: Temperature profile without loaded PEEK at 6 mm/s 390°C

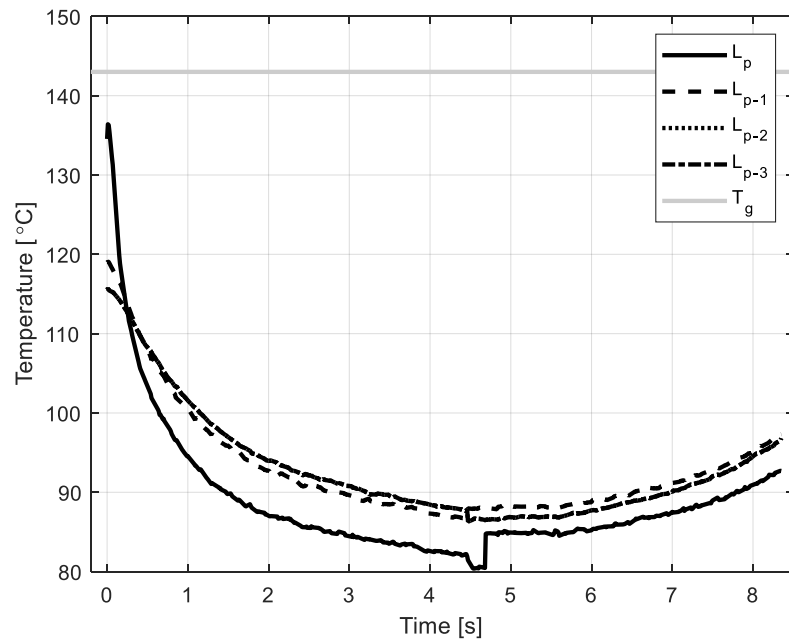


Figure C.17: Temperature profile without loaded PEEK at 6 mm/s 400°C

Appendix C IR-Imaging Measurement Results

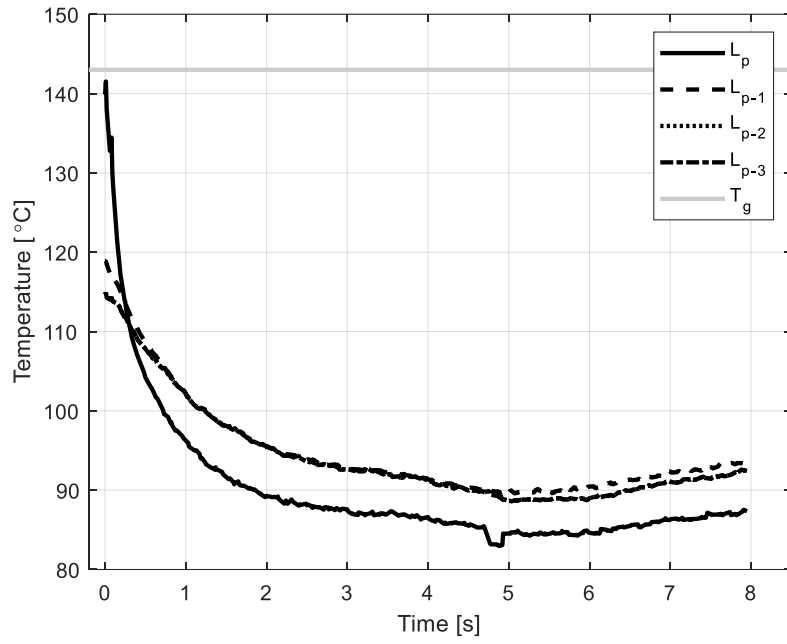


Figure C.18: Temperature profile without loaded PEEK at 6 mm/s 410°C

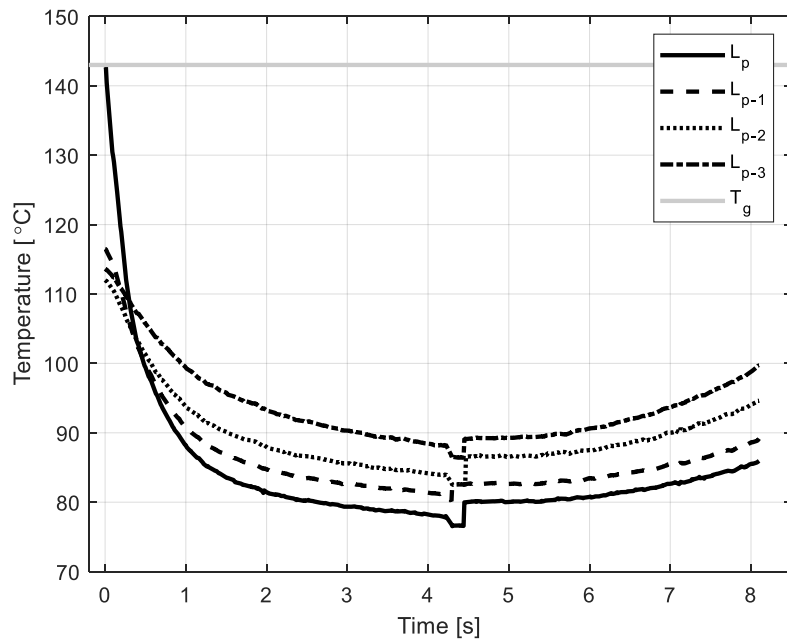


Figure C.19: Temperature profile without loaded PEEK at 6 mm/s 420°C

Appendix C IR-Imaging Measurement Results

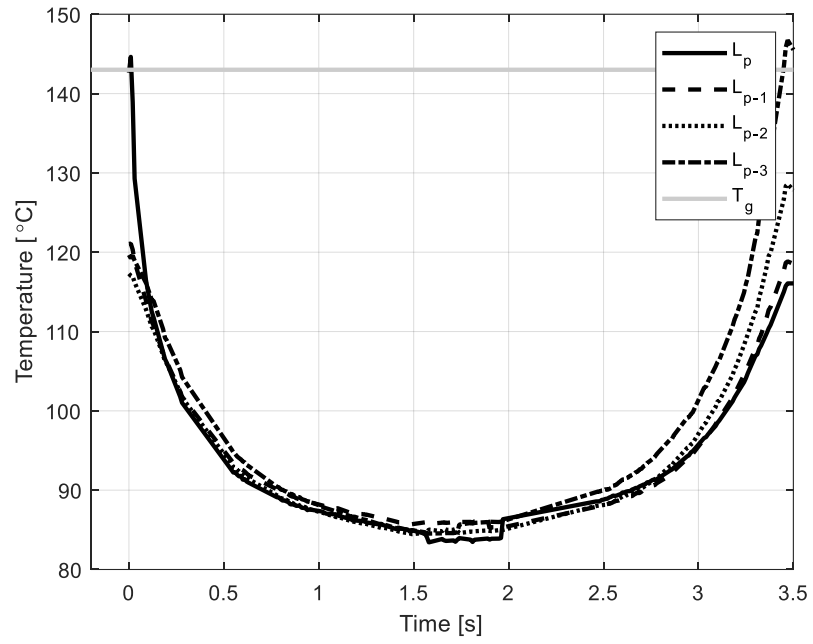


Figure C.20: Temperature profile without loaded PEEK at 18 mm/s 400°C

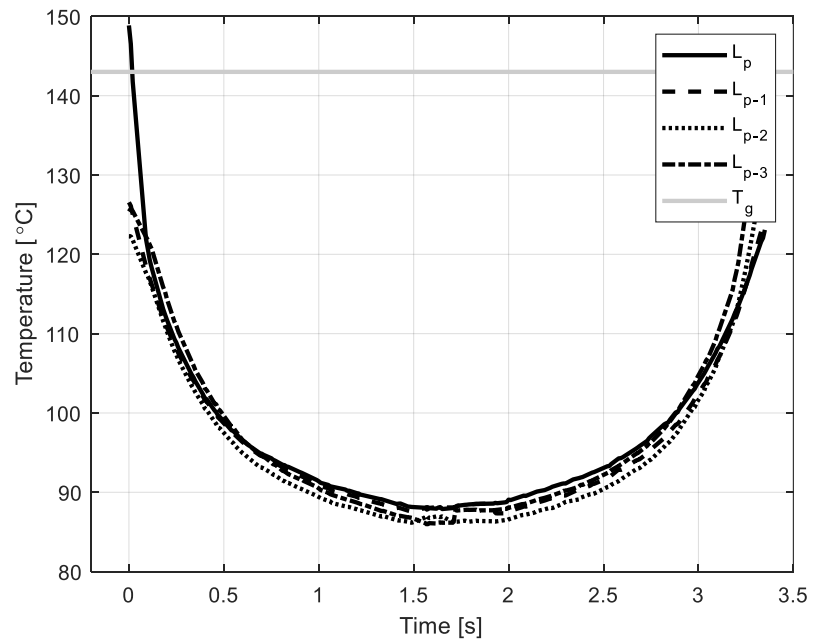


Figure C.21: Temperature profile without loaded PEEK at 18 mm/s 410°C

Appendix C IR-Imaging Measurement Results

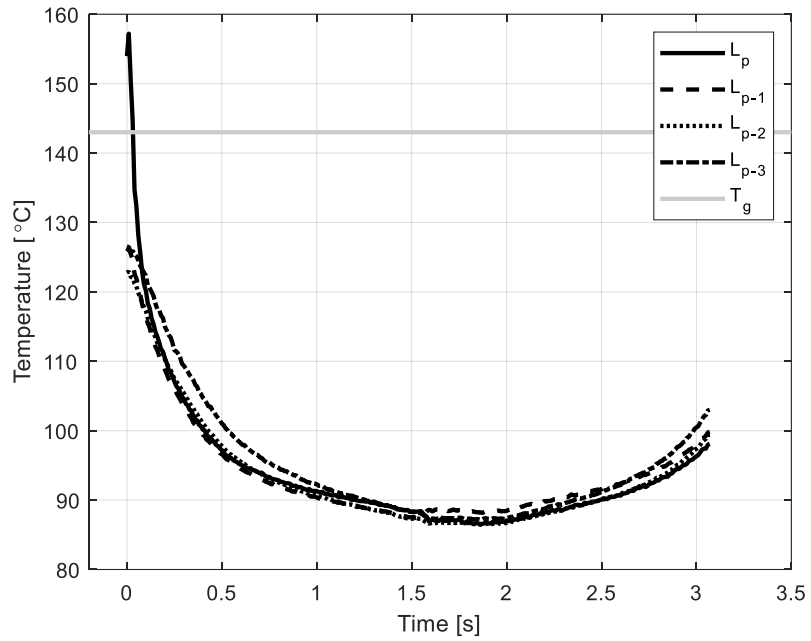


Figure C.22: Temperature profile without loaded PEEK at 18 mm/s 420°C

C.3 Temperature profile with correction

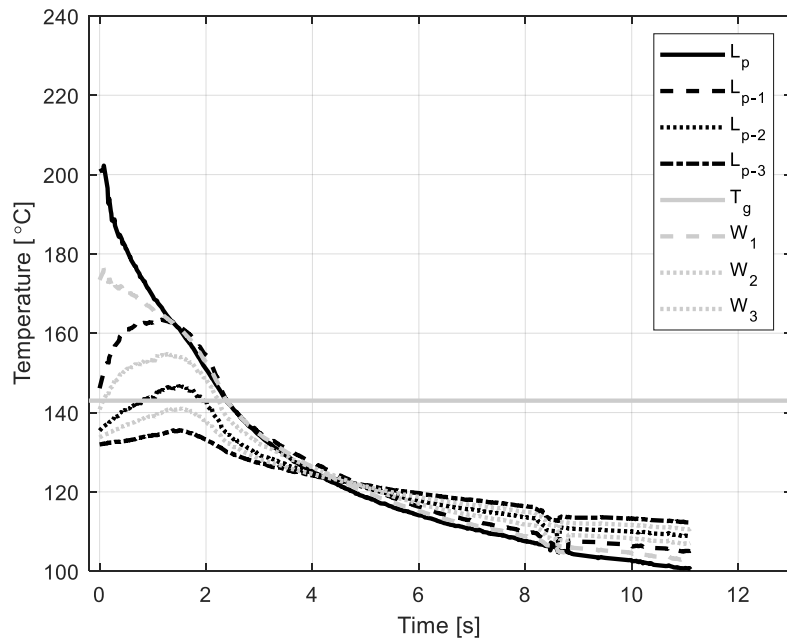


Figure C.23: Corrected temperature profile of PEEK at 3 mm/s 390°C

Appendix C IR-Imaging Measurement Results

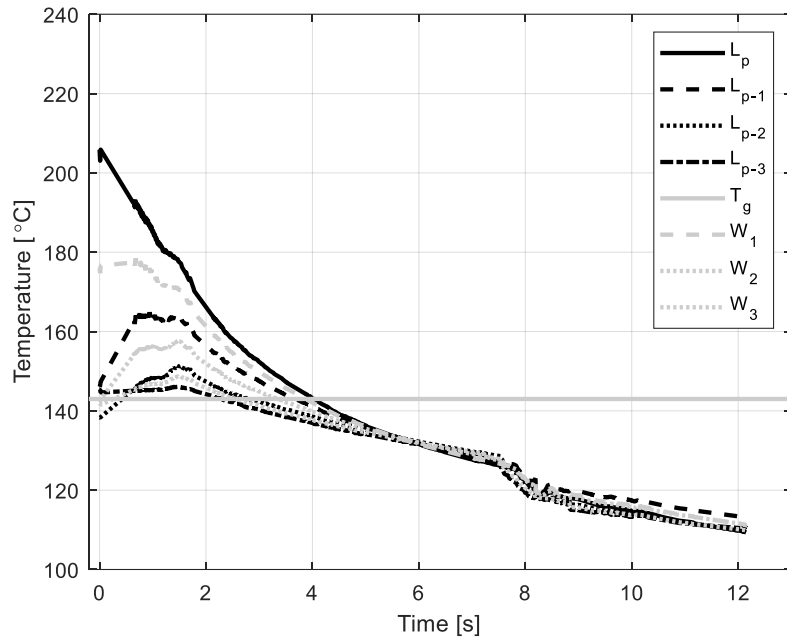


Figure C.24: Corrected temperature profile of PEEK at 3 mm/s 400°C

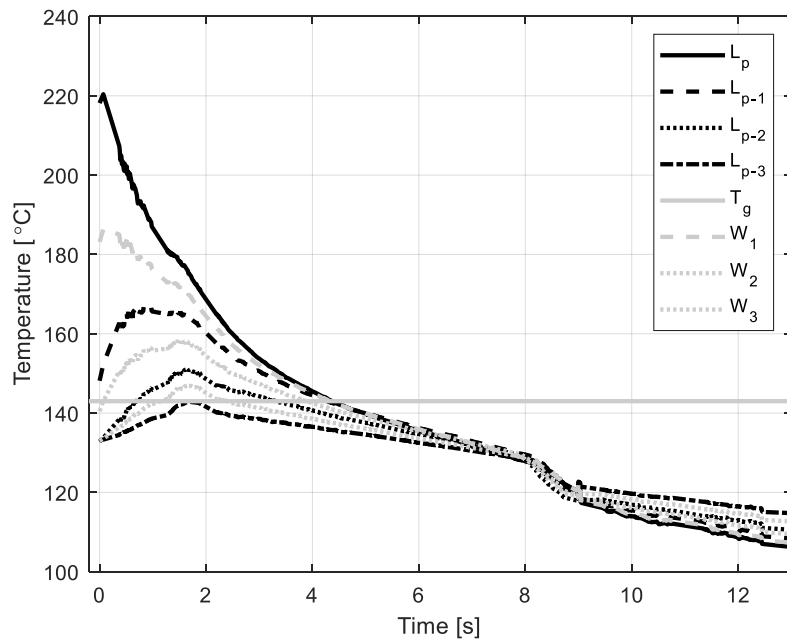


Figure C.25: Corrected temperature profile of PEEK at 3 mm/s 410°C

Appendix C IR-Imaging Measurement Results

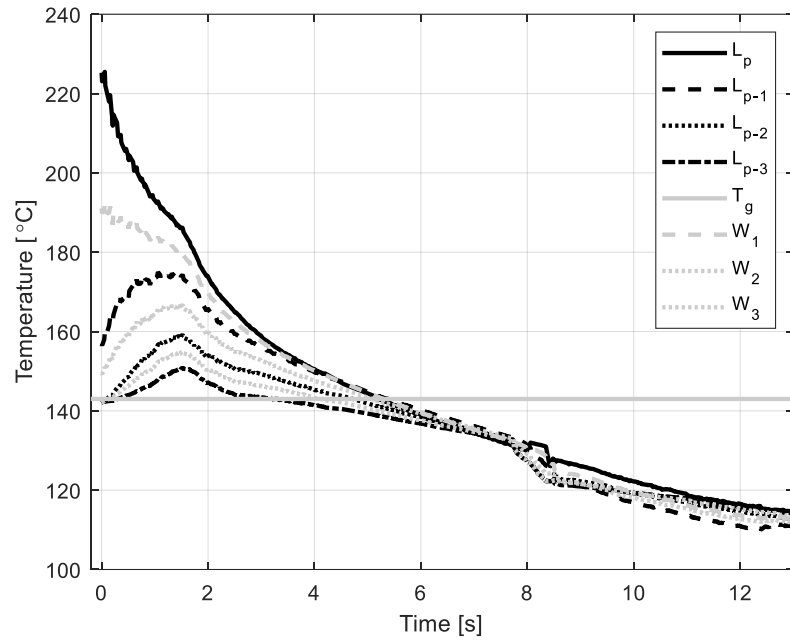


Figure C.26: Corrected temperature profile of PEEK at 3 mm/s 420°C

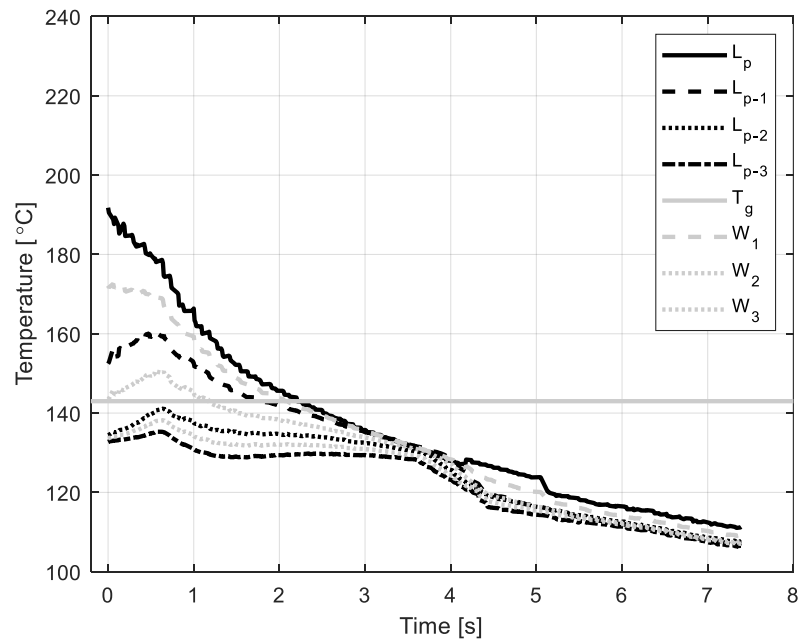


Figure C.27: Corrected temperature profile of PEEK at 6 mm/s 390°C

Appendix C IR-Imaging Measurement Results

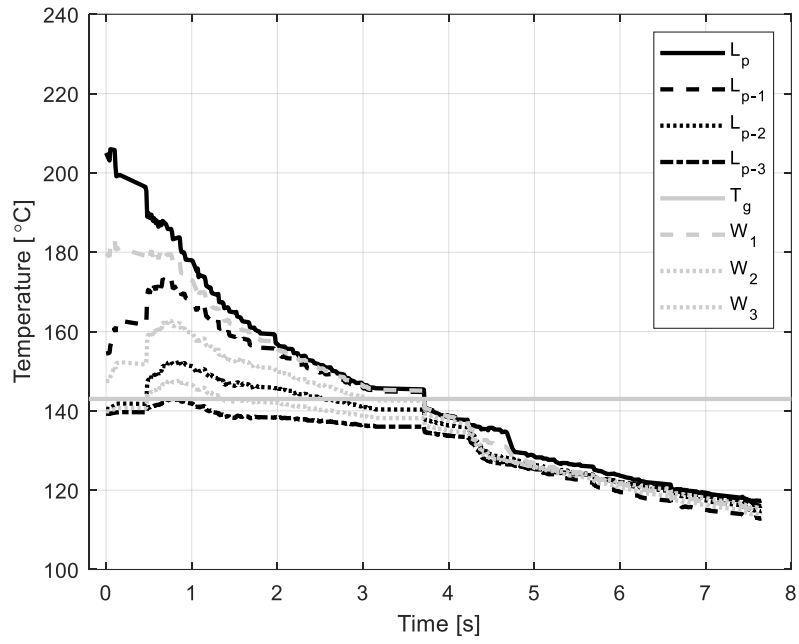


Figure C.28: Corrected temperature profile of PEEK at 6 mm/s 400°C

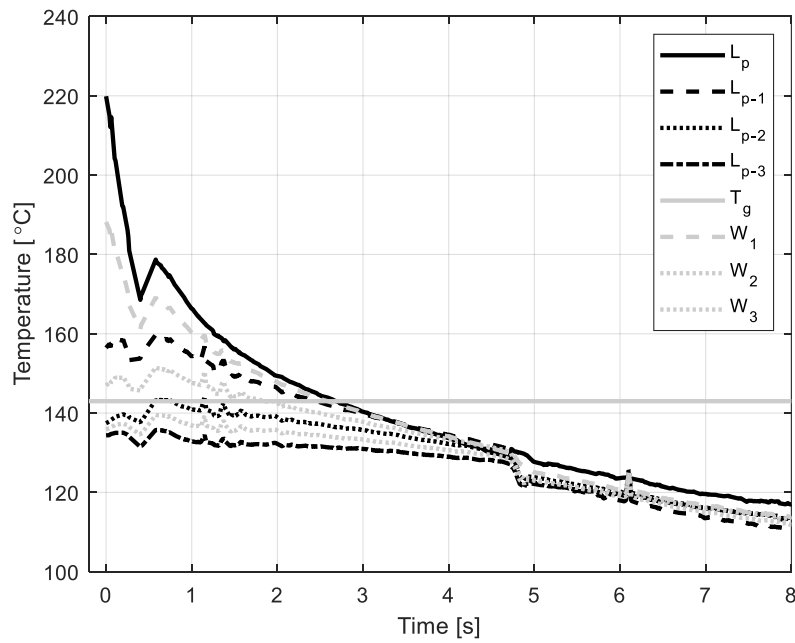


Figure C.29: Corrected temperature profile of PEEK at 6 mm/s 410°C

Appendix C IR-Imaging Measurement Results

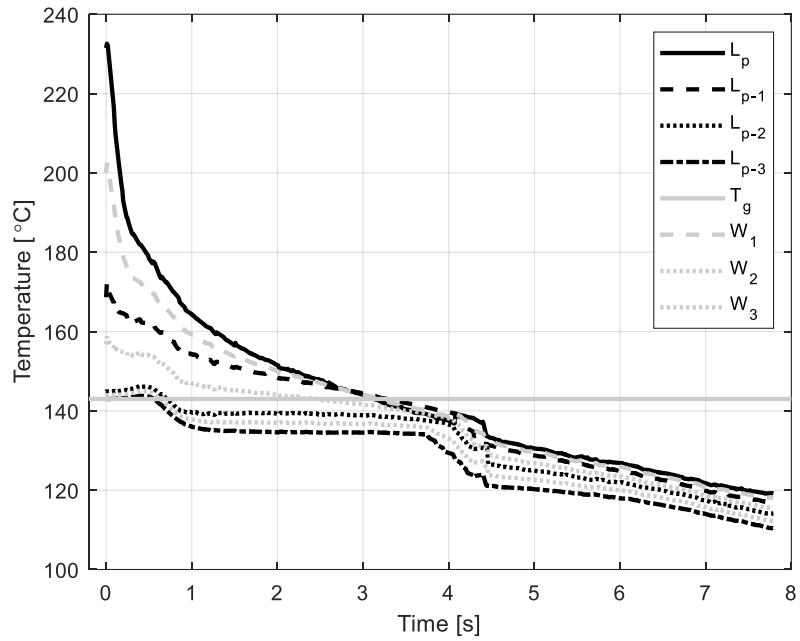


Figure C.30: Corrected temperature profile of PEEK at 6 mm/s 420°C

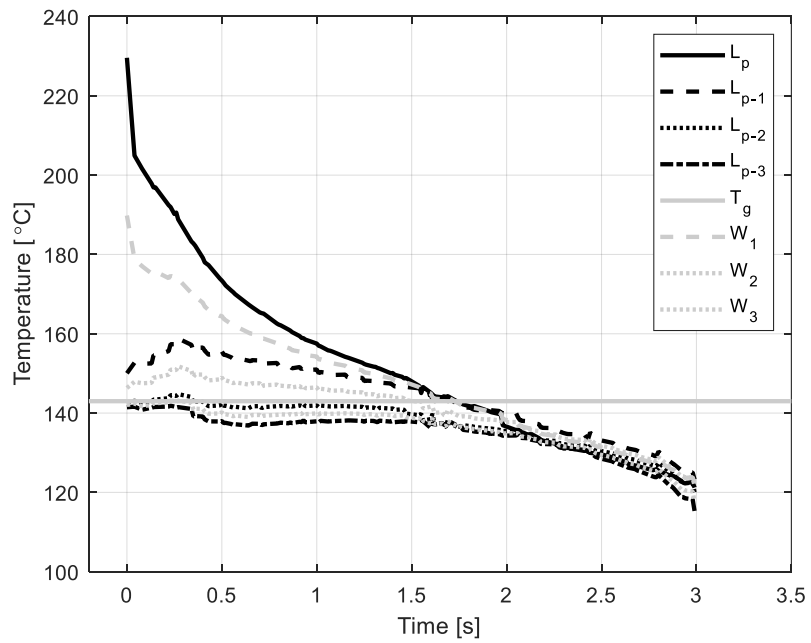


Figure C.31: Corrected temperature profile of PEEK at 18 mm/s 400°C

Appendix C IR-Imaging Measurement Results

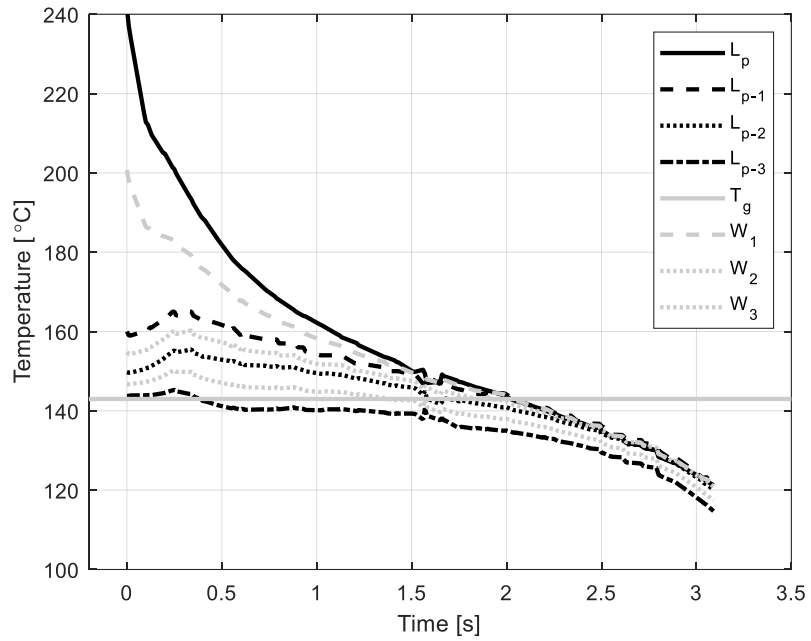


Figure C.32: Corrected temperature profile of PEEK at 18 mm/s 410°C

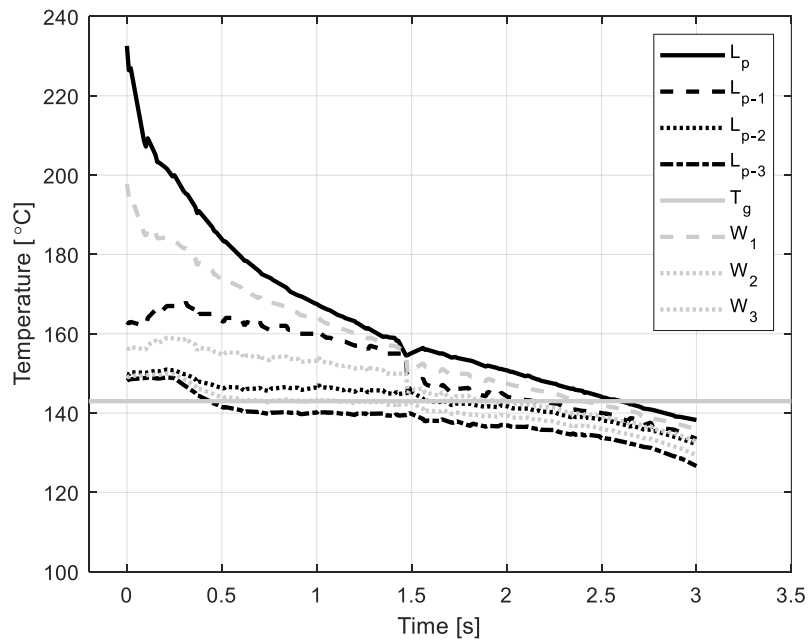


Figure C.33: Corrected temperature profile of PEEK at 18 mm/s 420°C

Appendix D

Temperature Control Correction of CF/PEEK

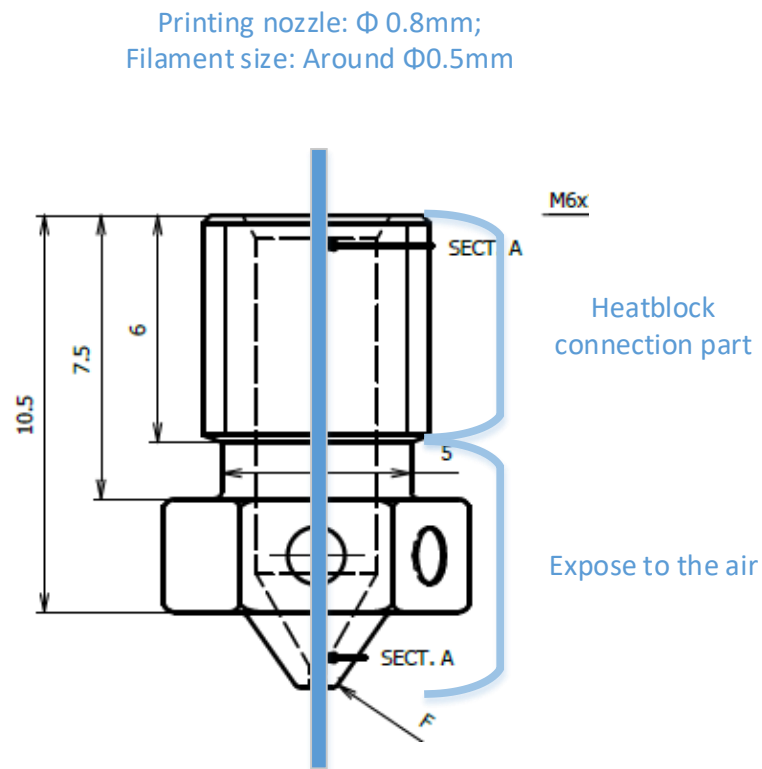


Figure D.1: Schematic printing nozzle of CF/PEEK

Based on the schematic of the printing nozzle of CF/PEEK in Figure D.1, the 1D axisymmetric heat equation describing the heat flow in the nozzle is given by:

$$\frac{\partial T}{\partial t} = \alpha \frac{1}{r} \frac{\partial}{\partial r} \left(r \frac{\partial T}{\partial r} \right) \quad (\text{D.1})$$

With the boundary conditions of:

$$(1) T = T_N \text{ at } r = R_0,$$

Appendix D Temperature Control Correction of CF/PEEK

where T_N is the print temperature, and R_0 is the hotend radius which is 1 mm here.

(2) T is finite at $r = 0$ (symmetry condition).

$$\alpha = \begin{cases} \alpha_{fill}, & 0 < r \leq R_{fill} \\ \alpha_{air}, & R_{fill} < r \leq R_0 \end{cases}$$

Where $\alpha_{fill} = 4.2 \times 10^{-7} \text{ m}^2\text{s}^{-1}$ is the thermal diffusivity of the CF/PEEK filament calculated based on the thermal conductivity, specific heat capacity and the CF/PEEK density (obtained from Chapter 4). $\alpha_{air} = 1.9 \times 10^{-5} \text{ m}^2\text{s}^{-1}$ is the thermal diffusivity of the air. R_{fill} is the filament radius which is 0.25 mm.

The relationship between temperature and material distance to the exit of the nozzle at fibre volume fraction of 50% is shown in Figure D.2:

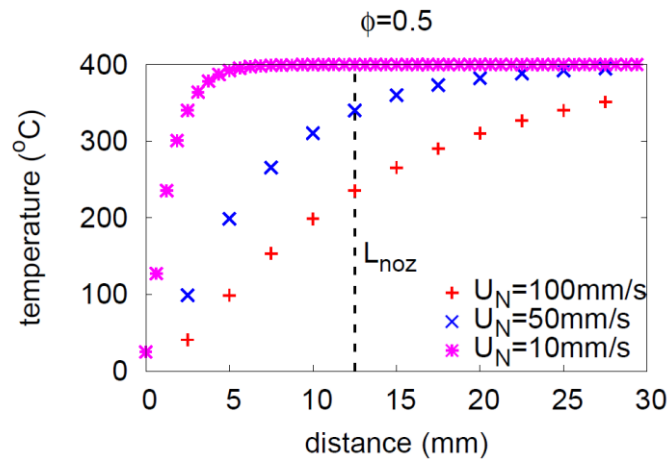


Figure D.2: Effect of print speed and the filament temperature

This result can be used as a comparison of this PhD thesis, Chapter 6, Section 6.4.3.2 and Appendix F. as to control the operation temperature when print the CF/PEEK filament.

Appendix E

On the Nielsen Model for the Prediction of Thermal Conductivity of Composites

Using the equations states in Section 6.4.3.1:

$$B = \frac{\frac{k_f}{k_m} - 1}{\frac{k_f}{k_m} + A} \quad (\text{E.1})$$

$$\varphi = 1 + \frac{(1 - \varphi_{max})\varphi}{\varphi_{max}^2} \quad (\text{E.2})$$

As the composites thermal conductivity is defined as [285]:

$$k_c = (1 - \varphi)k_m + \varphi k_f \quad (\text{E.3})$$

Plug (E.1) and (E.2) into (E.3), k_c is obtained as:

$$k_c = \frac{k_m(A(k_f - k_m)\varphi + Ak_m + k_f)\varphi_{max}^2}{(-1 + \varphi_{max})(k_f - k_m)\varphi - \varphi_{max}^2(k_f - k_m)\varphi + (Ak_m + k_f)\varphi_{max}^2} \quad (\text{E.4})$$

Input the selected values states in Section 6.4.3.1. The CF/PEEK thermal conductivity in lateral direction can be predicted shown in Figure 6.13.

Appendix F

Halpin & Kardos Theory

In the theory of Halpin & Kardos [160], semi-crystalline polymers are assumed to behave as a multi-phase composite solid to develop an equation to link the crystal fraction to the storage modulus of the material. It is shown that the modulus of a semi-crystalline polymer is comparable to that of a randomly-reinforced polymer, where the geometry of the reinforcement is similar in structure to the crystal morphology. Morphology ranges from spherulites consisting of extended fibrils at low volume fractions, to densely packed lamellae at high volume fractions.

Consider a volume fraction of reinforcement fibres, ν_f , with aspect ration l/d , stiffness S_r , modulus E_r , and Poisson ratio ν_r . The fibres sit within a matrix of stiffness S_m , modulus E_m , and Poisson ratio ν_m . Typically $S_r \sim 10^3 S_m$ and $E_r = 10^3 E_m$.

The stiffness of the material in the fibre direction, S_{11} , is given by

$$\frac{S_{11}}{S_m} = \frac{1+2(l/d)\eta S_1 \nu_r}{1-\eta S_1 \nu_r}, \quad (\text{F.1})$$

Where

$$\eta S_1 = \frac{S_f/S_m - 1}{S_r/S_m + 2(l/d)}. \quad (\text{F.2})$$

Furthermore, the in-plane shear modulus, E_{12} , is given by:

$$\frac{E_{12}}{E_m} = \frac{1+\eta S_2 \nu_r}{1-\eta S_2 \nu_r}, \quad (\text{F.3})$$

Where

$$\eta E = \frac{E_r/E_m - 1}{E_r/E_m + 1}. \quad (\text{F.4})$$

Appendix F Halpin & Kardos Theory

The stiffness transverse to the fibre direction is given by

$$\frac{S_{22}}{S_m} = \frac{1+2\eta S_2 \nu_r}{1-\eta S_2 \nu_r}, \quad (\text{F.5})$$

where

$$\eta S_2 = \frac{S_r/S_m - 1}{S_r/S_m + 2}. \quad (\text{F.6})$$

The Poisson coefficient is given by the rule of mixtures

$$\nu_{12} = \nu_f \nu_f + \nu_m (1 - \nu_r). \quad (\text{F.7})$$

Where

$$\nu_f = \frac{S_r}{2E_r} - 1, \quad (\text{F.8})$$

$$\nu_m = \frac{S_m}{2E_m} - 1. \quad (\text{F.9})$$

It is shown that the elastic coefficients for a randomly reinforced solid can be expressed as

$$\bar{S} = \frac{4U_5(U_1 - U_5)}{U_1}, \quad (\text{F.10})$$

$$\bar{\nu} = \frac{U_1 - 2U_5}{U_1}, \quad (\text{F.11})$$

$$\bar{E} = U_5, \quad (\text{F.12})$$

Where the invariant terms are given by

$$U_1 = \frac{1}{8}(3Q_{11} + 3Q_{22} + 2Q_{12} + 4Q_{66}), \quad (\text{F.13})$$

$$U_5 = \frac{1}{8}(Q_{11} + Q_{22} - 2Q_{12} + 4Q_{66}). \quad (\text{F.14})$$

With

$$Q_{11} = \frac{S_{11}}{1 - \nu_{12}\nu_{21}}, \quad (\text{F.15})$$

$$Q_{22} = \frac{S_{22}}{1 - \nu_{12}\nu_{21}}, \quad (\text{F.16})$$

Appendix F Halpin & Kardos Theory

$$Q_{12} = \nu_{12}Q_{22} = \nu_{21}Q_{11}, \quad (\text{F.17})$$

$$Q_{66} = G_{12}. \quad (\text{F.18})$$